

UNIVERSITÀ DEGLI STUDI DI TRIESTE

Facoltà di Scienze Matematiche, Fisiche e Naturali

Dottorato di Ricerca in Fisica - XXI Ciclo

**Galactic Population
in
Cosmological Hierarchical Models**

DOTTORANDO

Alexandro Saro

COORDINATORE DEL COLLEGIO DEI DOCENTI

Prof. Gaetano Senatore, Università di Trieste

TUTORE

Prof. Stefano Borgani, Università di Trieste

RELATORE

Prof. Stefano Borgani, Università di Trieste

a.a. 2007/2008

Contents

1	INTRODUCTION	21
2	CLUSTERS OF GALAXIES: AN OVERVIEW	27
2.1	X-Ray properties of clusters of galaxies	29
2.1.1	The Sunyaev–Zel’dovich effect (SZ)	31
2.2	Optical and near infra-red properties of clusters of galaxies	34
2.2.1	The number–density profile of cluster galaxies	36
2.2.2	The colour–magnitude relation	37
2.2.3	The mass–luminosity ratio	42
2.2.4	Number of galaxies versus cluster’s mass	43
2.2.5	The luminosity functions	44
2.3	Clusters of galaxies at redshift $z \gtrsim 1$	45
2.4	High–redshift proto–clusters	49
3	NUMERICAL COSMOLOGY AND GALAXY FORMATION	57
3.1	Gravitational dynamics: the N–body TREE code	58
3.2	Initial conditions	63
3.3	Hydrodynamical methods: The Smoothed Particle Hydrodynamics (SPH) technique	64
3.4	The GADGET-2 code	67
3.4.1	Radiative cooling	68
3.4.2	Star formation	70
3.4.3	The chemical evolution model	71
3.4.4	Feedback from galactic winds	73
3.5	Spectro-photometric codes	74
3.5.1	Basic principles	75
3.5.2	The GALAXEV code	76
3.6	Identifying galaxies	76
3.6.1	The SKID algorithm	77
3.6.2	The SUBFIND algorithm	78

Contents

3.7	Semi-Analytic Models: an overview	81
3.7.1	Dark matter haloes	81
3.7.2	Astrophysical gas processes	84
3.7.3	The cooling of gas	84
3.7.4	Star formation	85
3.7.5	Feedback processes	86
3.7.6	Galaxy mergers	87
4	SIMULATIONS OF THE GALAXY POPULATION IN NEARBY CLUSTERS	91
4.1	The simulations	94
4.1.1	The simulated clusters	94
4.1.2	The code	96
4.2	Assigning luminosities to galaxies	100
4.3	Results	101
4.3.1	The number-density profile of cluster galaxies	101
4.3.2	The colour–magnitude relation	103
4.3.3	The mass–luminosity ratio	106
4.3.4	The luminosity function	108
4.3.5	Radial dependence of the galaxy population	112
4.3.6	The SN-Ia rate	114
4.4	Testing numerical effects on the galaxy stellar mass function	116
4.5	Summary and discussion	118
5	SIMULATING THE CORE OF A PROTO-CLUSTER REGION AT $z \simeq 2$	123
5.1	The simulated proto-clusters	124
5.2	Mass and luminosity of proto-cluster galaxies	125
5.3	Star formation	130
5.4	Are the proto-clusters in virial equilibrium?	131
5.5	Predicted X-ray properties	133
5.6	Conclusions	134
6	THE EFFECT OF GAS-DYNAMICS ON SEMI-ANALYTIC MODELING OF CLUSTER GALAXIES	137
6.1	The simulations	139
6.2	The semi-analytic model	142
6.3	Results	144
6.3.1	The stellar mass function	146
6.3.2	The number density profiles	146
6.3.3	Merging times	147
6.3.4	The brightest cluster galaxies	153
6.4	Summary and discussion	158

7	SPH AND SEMI-ANALYTIC MODELING OF CLUSTER GALAXIES	161
7.1	The simulation	162
7.2	The semi-analytic model	162
7.3	Comparing predictions on the galaxy population	164
7.3.1	Radial distribution of galaxies	164
7.3.2	Mass function of galaxies	167
7.4	Comparing predictions on single galaxies	169
7.4.1	General behaviour	169
7.4.2	Evolution of galaxies	171
7.4.3	Effect of the environment	176
7.5	Summary and discussion	178
8	CONCLUSIONS	183
8.1	Discussion and Conclusions	183
8.2	Future Perspectives	186
A	APPENDIX - Basics of Cosmology	189
A.1	Basic Equations for an expanding universe	189
A.2	Structure Formation	191
A.3	Key Observations	197

List of Figures

2.1	The X-ray emission from a thin plasma with 0.35 solar abundance at different temperatures, $T = 1, 2$ and 8 keV (from Arnaud et al. 2005).	31
2.2	The CMB spectrum, undistorted (dashed line) and distorted by the tSZ effect (solid line). The tSZ distortion shown is for a model cluster 1000 times more massive than a typical massive galaxy cluster (from Carlstrom et al. 2002). .	33
2.3	Left panel: composite X-ray/optical image of the galaxy cluster Abell 1689, located at redshift $z \simeq 0.18$. The map shows area of 556 kpc on a side. The purple diffuse halo shows the distribution of gas at a temperature of about 10^8 K, as revealed by the Chandra X-ray Observatory. Images of galaxies in the optical band, coloured in yellow, are from observations performed with the Hubble Space Telescope. The long arcs in the optical image are caused by gravitational lensing of background galaxies by matter in the galaxy cluster, the largest system of such arcs ever found (Credit:X-ray: NASA/CXC/MIT; Optical: NASA/STScI). Right panel: optical image of cluster Abell 1914 from the Sloan Digital Sky Survey with the superimposed map of the temperatures of the Cosmic Microwave Background observed by the Sunyaev-Zel'dovich array (SZA). The image illustrates the effect of up-scattering of the CMB photons by the hot ICM from low frequencies to higher frequencies. At the frequency of observation, the cluster appears as a temperature decrement in the CMB temperature map. (Credit: John Carlstrom and SZA collaboration). Figure from Borgani & Kravtsov (2009) in preparation. . . .	35
2.4	Number–density profile of galaxies as a function of the cluster-centric distance (from Popesso et al. 2005).	37
2.5	Colour magnitude relation for the Virgo cluster (empty symbol) and for the Coma cluster (filled symbols): (a) CMR for the $U - V$ colours; (b) CMR for the $V - K$ colours. Triangles are S0 galaxies, circles ellipticals and stars S0/a or s0 ₃ galaxies. Dashed line shows the CMR predicted for the Coma cluster starting from the Virgo cluster (from Bower et al. 1992).	38
2.6	CMR in the $B - R$ as a function of M_R respectively for :a) A21; b) A690; c) A1213; d) A1656 (Coma); e) A2152; f) A2399 (from López-Cruz et al. 2004).	39

List of Figures

- 2.7 Upper panels: Comparison between numerical predictions from semi-analytic models and observational results from Prugniel & Simien (1996) regarding the CMR in $B-V$ as a function of the M_B magnitude. Numerical predictions are shown in the left panel, while observations are shown in the right panel, where the continuous line shows the median, from Lanzoni et al. (2005). Lower panels: As in the upper panels but for the CMR in the $V-K$ as a function of the M_V compared with observations from Bower et al. (1992). Plots from Lanzoni et al. (2005). 40
- 2.8 Comparison between numerical predictions from N-body hydro-dynamical simulations and observational results from Bower et al. (1992) (continuous line). CMR in $U-V$ (a) and $V-K$ (b) as a function of M_V , colour coded in metallicity. (c) Relation between mean metallicity of galaxies and M_V magnitude and (d) between age of galaxies and M_V magnitude, averaged in mass (filled symbols) and luminosity (empty violet symbols), from Romeo et al. (2004). 41
- 2.9 Left panel: Mass to light ratio as a function of the cluster's mass in the K band (from Lin et al. 2004). Right panel: Same as left panel but in i band within r_{500} (from Popesso et al. 2004). 43
- 2.10 Left panel: Relation between the number of galaxies with $M_K < -21$ and the cluster's mass (from Lin et al. 2004). Right panel: Relation between the number of galaxies with $M_r < -20$ and the cluster's mass within r_{200} (from Popesso et al. 2006b). 44
- 2.11 Luminosity function in the four SLOAN bands u, r, i, z computed within r_{200} . Dots: Observational data. Continuous line: Best fit (from Popesso et al. 2006a). 46
- 2.12 Composite NDWFS and *Spitzer* IRAC $B_W, I, [4.5]$ colour image of cluster ICS J1438.1+3414 at $\langle z_{sp} \rangle = 1.413$. North is up and east is left, and the field size is $5'$ square ($\sim 2.4 - 2.5$ Mpc for $z = 1 - 1.5$). Objects with yellow circles are photometric redshift members, i.e., they have integrated $P(z) > 0 : 3$ in the range $z_{est} \pm 0.06(1 + z_{est})$, where z_{est} is the mean estimated photometric redshift for the cluster. Spectroscopically confirmed cluster members are denoted by yellow squares. Not all spectroscopic members fall within the $5'$ field shown here. Blue diamonds indicate photometric redshift members whose spectroscopic redshifts are not in the range $z_{sp} \pm 2000(1 + z_{sp}) \text{ km s}^{-1}$ (from Eisenhardt et al. 2008). 48

2.13 Composite image of a $23'' \times 18''$ region at the core of the MRC 1138-262 proto-cluster taken with the ACS through the $g_{475} + I_{814}$ filters, using a total of 19 orbits. Also shown are rest-frame Ly_{α} emission velocities in kilometres per second, measured through $1''$ wide spectrograph slits in three position angles indicated by the dashed lines. These were obtained using the FORS at the VLT Kurk et al. 2003). The velocities were measured at the peaks of the Ly_{α} emission profiles and are relative to the median velocity of Ly_{α} absorption. Following Kurk et al. (2003) the nucleus is taken to be the position of the peak Ha. This coincides with the peak in ACS continuum emission, indicated by the extrapolation of the arrow corresponding to 730 km s^{-1} , the velocity of the nuclear Ly_{α} emission. Eight of the satellite galaxies (flies) that have chain, tadpole, or clumpy morphologies are indicated by numerals 18 (from Miley et al. 2006) 50

2.14 g_{475} image of MRC 1138-262 and surrounding 15×18.5 region, smoothed with a Gaussian of $s = 0.05$ arcsec. All regions identified as galaxies have been removed and are coloured white. The intergalactic light is clearly visible between the radio and satellite galaxies (from Hatch et al. 2008). 53

2.15 The luminosity function of the galaxies within the Spiderweb complex. The solid line is a Schechter function fit to the data. The dotted line indicates how much of the luminosity function is missing if the intergalactic light results from a population of fainter galaxies; approximately 15 galaxies with absolute I_{814} magnitude (rest frame NUV) between $19.5 < \text{mag} < 18.1$ would provide the necessary light (from Hatch et al. 2008). 54

2.16 Slope β of UV spectrum of galaxies and intergalactic light of the Spiderweb system. Data has been binned in 2D as described in the text. Galaxies are outlined in black. The Ly_{α} flux peaks on the galaxy that lies ~ 3 arcsec West of the radio galaxy which has the bluest colour compared to the other satellite galaxies. Image is rotated 5 degrees East from North, with North Up and East left (from Hatch et al. 2008). 55

3.1 Schematic illustration of the TREE code scheme in two dimensions (Springel et al. 2001). The particles on the left are enclosed in a first level cell (main node) that is iteratively split into 4 squares (8 cubes for the three-dimensional case) until one particle remains (the leaf of the tree). 59

List of Figures

- 3.2 The dark matter density field on various scales from the Millennium simulation. Each individual image shows the projected dark matter density field in a slab of thickness $15 h^{-1}\text{Mpc}$ (sliced from the periodic simulation volume at an angle chosen to avoid replicating structures in the lower two images), colour-coded by density and local dark matter velocity dispersion. The zoom sequence displays consecutive enlargements by factors of four, centred on one of the many galaxy cluster halos present in the simulation (from Springel et al. 2005). 61
- 3.3 A $64h^{-1}$ Mpc-thick slice through this simulation showing the matter density field in the past light cone as a function of look-back time all the way to the horizon from the Horizon simulation. The thickness of the wedge is constant and the opening angle is 45 degrees. The Earth is at the vertex and the upper boundary is the Big Bang surface at a look-back time of 13.6 billion years (from Kim et al. 2008). 62
- 3.4 The particle distribution with the imposed displacements, taken from the same cosmological initial conditions, once based on an originally regular grid (left panel) and once based on a glass like particle distribution (right panel). Credits: Dolag et al. (2008). 63
- 3.5 Evolution at $z = 9, 5$ and 0 of a TREE-SPH simulation realised with the GADGET-2 code for a ΛCDM within a cosmological box of $192 h^{-1}$ Mpc (from Borgani et al. 2004). 68
- 3.6 The formation of a galaxy cluster in a cosmological context, as described by a hydrodynamical simulation carried out with the Tree-SPH GADGET-2 code Springel (2005). Upper, central and bottom panels refer to the density maps of dark matter, gas and star distributions, respectively. From left to right we show the snapshots at $z = 4$, where putative proto-cluster regions are traced by the observed concentrations of Lyman-break galaxies and Lyman- α emitters Overzier et al. (2008), at $z = 2$, where highly star-forming radio-galaxies should trace the early stage of cluster formation Miley et al. (2006); Saro et al. (2009); see Chapter 5, and at $z = 0$. This cluster has a total virial mass $M_{vir} \simeq 10^{15} h^{-1} M_{\odot}$ at $z = 0$ (Dolag et al. 2008). Each panel covers a comoving scale of about $24 h^{-1}\text{Mpc}$, while the cluster virialised region at $z = 0$ is nearly spherical with a radius of about $3 h^{-1}\text{Mpc}$ (from Borgani & Kravtsov 2009, in preparation). 69
- 3.7 This picture shows the evolution of the M/L ratio in B, V and K band for a Salpeter IMF with solar metallicity computed with the GALAXEV code. . . 77

3.8	<p>Example for a sub-halo identification with SUBFIND. The top left panel shows a small FOF-group (44800 particles). SUBFIND identifies 56 sub-haloes within this group, the largest one forms the background halo and is shown on the top right, while the other 55 sub-haloes are plotted on a common panel on the lower left. Particles not bound to any of the sub-haloes form “fuzz”, and are displayed on the lower right (from Springel et al. 2001).</p>	79
3.9	<p>A comparison between the galaxy population of a simulated massive ($M_{200} \sim 10^{15} h^{-1} M_{\odot}$) cluster at $z = 0$ as it is identified by the SKID and by the SUBFIND algorithms. The simulation is based on the GADGET-2 code and includes radiative cooling, star formation but no feedback, in a similar way as described in Chapter 7. Left panel shows the cumulative stellar mass functions of galaxies identified within r_{200} by both the SKID and the SUBFIND codes. Right panel shows a map in the plane x-y of the position of the identified galaxies in cluster-centric coordinates.</p>	80
3.10	<p>Left panel: A schematic merger tree for a dark matter halo. The horizontal lines represent snapshots in the evolution of the history of the halo, corresponding to time-steps in an N-body simulation or Monte-Carlo realisation of the merger tree ($t_1 < t_2$). The size of the circle indicates the mass of the halo. The haloes grow through merger events between haloes and by accretion of objects below the (halo) mass resolution (e.g. as depicted between steps t_3 and t_4). The final halo is shown at t_5 (from Baugh 2006). Right panel: A merging tree from a Monte Carlo simulation, showing the formation history of a central dominant galaxy in a large DM halo with present mass $10^{13} M_{\odot}$. Time runs from top to bottom, from $z = 10$ to the present. Each branch represents a progenitor of the final galaxy, and the colour code (shown on the right in units of $5 \times 10^{11} M_{\odot}$) quantifies the mass of the corresponding progenitor. A total of some 10^3 progenitors are involved, with the main one being represented on the rightmost branch (from Cavaliere & Menci 2007).</p>	82
3.11	<p>A schematic overview of the ingredients of a hierarchical galaxy formation model (from Baugh 2006).</p>	83
3.12	<p>A schematic of the basic cooling model used in semi-analytical models (from Baugh 2006).</p>	85

List of Figures

3.13 The K-band luminosity function of galaxies. The points show the observational determinations of Cole et al. (2001, circles), Kochanek et al. (2001, squares) and Huang et al. (2003, $z < 0.1$, stars). Lines show results from different GALFORM models. Model 1 (dashed line) shows the result of converting the dark matter halo mass function into a galaxy luminosity function by assuming a fixed mass-to-light ratio chosen to match the knee of the luminosity function. Model 2 (dotted line) shows the result from GALFORM when no feedback, photoionization suppression, galaxy merging or conduction are included. Models 3 and 4 (long dashed and solid lines respectively) show the effects of adding photoionization and then galaxy merging (from Benson et al. 2003). 88

3.14 A schematic view of a merger between two dark matter haloes. The progenitors of the final halo each contain a galaxy. After the haloes merge, the more massive galaxy is placed at the centre of the newly formed halo. Any hot gas that cools would be directed onto the central galaxy (for simplicity, in this illustration, the haloes have exhausted their supply of hot gas). The smaller galaxy becomes a satellite of the central galaxy. The orbit of the satellite galaxy decays due to dynamical friction. The satellite may eventually merge with the central galaxy (from Baugh 2006). 89

4.1 We show in these panels a representation of the gas density for a sample of 8 analysed clusters. The brighter the colours are, the larger the density is. 96

4.2 We show in these panels a representation of the gas temperature for a sample of 8 analysed clusters. Brighter colours are for colder gas and redder colours are for hotter gas. 97

4.3 The number density profile of cluster galaxies. Left panel: the profiles of galaxies of different stellar mass, averaged over all clusters, for the runs with Salpeter IMF (filled symbols). Shown with the solid curve is the average DM profile. All profiles are normalised to the total number density within the virial radius. Right panel: The number density of galaxies, brighter than $r = -18.5$, contained within a given radius, normalised to the total number density found within the r_{200} . Filled squares and open circles are by combining all the simulated clusters, for the Salpeter and for the top-heavy IMF, respectively. The solid curve is the best-fit King model to the number density profiles of cluster galaxies from the analysis of RASS-SDSS data by Popesso et al. (2006b), here plotted with arbitrary normalisation. Error-bars in the simulation profile correspond to Poissonian uncertainties. For reasons of clarity they have been plotted only for the Salpeter runs. 100

4.4 The $V-K$ vs. V colour–magnitude relation by combining all the galaxies within the virial radii of the simulated clusters, for the Salpeter IMF (top panel) and for the top–heavy IMF with normal feedback (bottom panel). Straight lines in each panel show the observed CMR relations by Bower et al. (1992), with the corresponding intrinsic standard deviations. Big filled dots mark the BCG of each cluster. Different symbols and colours are used for galaxies having different metallicities. Magenta open circles: $Z > 1.5Z_{\odot}$; blue filled triangles: $1.5 < Z/Z_{\odot} < 1$; red open squares: $1 < Z/Z_{\odot} < 0.7$; black open triangles: $0.7 < Z/Z_{\odot} < 0.4$; green filled squares: $Z < 0.4Z_{\odot}$ 103

4.5 The same as the top panel of Figure 4.4, but only including in the computation of the luminosities the star particles having redshift of formation $z_f > 1$ 104

4.6 The comparison between simulated and observed relation between mass and luminosity in the i band (left panel) and in the K band (right panel). In each panel, squares are for the Salpeter IMF, circles for the top–heavy IMF with normal feedback, triangles for the top–heavy IMF with strong feedback and asterisks for the Salpeter IMF with no feedback. Filled squares and circles are for the g676 and g51 runs, so as to make clear the effect of changing the feedback strength. The straight solid lines are the best fitting results from Popesso et al. (2005) for the i band and from Lin et al. (2004) for the K band, with the dashed lines marking the corresponding observational scatter. 105

4.7 The number of galaxies within clusters above a given luminosity limit. Left panel: results in the r band, compared to the observational best–fitting result from SDSS data by Popesso et al. (2006b) (the dashed lines mark the intrinsic scatter of the observational relation). Right panel: results in the K band, compared to the observational best–fitting result from 2MASS data by Lin et al. (2004). Symbols for the simulations have the same meaning as in Figure 4.6. 108

4.8 The Comparison between the simulated (histograms) and the observed (curves) luminosity functions of cluster galaxies in the Sloan- r (left panel) and z (right panel) bands. The smooth curves are the best fit to the SDSS data analysed by Popesso et al. (2006a). In each panel, the solid and the dashed histograms are for the Salpeter and for the top–heavy IMF, respectively. Normalisation of the simulated LF are chosen to match the observed one at $r = -20$ and $z = -20$ with the Salpeter LF. Consistent with the observational analysis, the brightest cluster galaxies (BCGs) are not included in the computation of the luminosity function. 109

4.9 The combined stellar mass function for the galaxies identified within r_{200} of all clusters. The solid and the dashed histograms correspond to the Salpeter and to the top-heavy IMF, respectively. 111

List of Figures

- 4.10 The effect of a stronger feedback on the z -band luminosity function. The histograms show the combined luminosity function for the g51 and g676 clusters in the case of standard feedback ($v_w = 500 \text{ km s}^{-1}$, dashed line) and of strong feedback ($v_w = 1000 \text{ km s}^{-1}$, solid line). The smooth curve is the best-fit to the SDSS data by Popesso et al. (2006a). 111
- 4.11 Left panel: The radial dependence of galaxy colours, averaged over all simulated clusters. In each panel, solid lines with filled squares are for the Salpeter IMF, while dashed line with open circles are for the top-heavy IMF. The reported results are the average over all the simulated clusters. Right panel: The fraction of galaxies younger than 8.5 Gyr, as a function of cluster-centric distance, in units of r_{vir} . Symbols and line types have the same meaning as in the left panel. 113
- 4.12 The specific mean star formation rate, averaged over all the simulated clusters, as a function of the cluster-centric distance. Symbols and line types have the same meaning as in Figure 4.11. In the central bin we have excluded the contribution from the BCGs. 114
- 4.13 Comparison between the observed and the simulated evolution of the SN-Ia rate per unit B-band luminosity (SNU_B). In both panels, filled symbols with error-bars refer to observational data from Mannucci et al. (2008) (triangle), Gal-Yam et al. (2002) (squares) and Sharon et al. (2007) (pentagon). Left panel: the effect of changing the IMF. The open squares are for the Salpeter (1955) IMF, the open triangles are for the top-heavy IMF by Arimoto & Yoshii (1987a) and the open circles for the IMF by Kroupa (2001). For the Salpeter IMF, the shaded area show the r.m.s. scatter evaluated over the four simulated clusters, while for the other two IMFs only the result for the g51 cluster is shown. Right panel: the effect of suppressing low-redshift star formation and of changing the binary fraction on the SNU_B evolution of the g51 cluster. The open squares and the open circles are for the reference run with Salpeter (1955) IMF and for the same run with cooling and star formation stopped at $z = 1$ (CS run), respectively. The filled and the open triangles are for the runs with Arimoto & Yoshii (1987a) IMF, using $A = 0.1$ and $A = 0.05$ for the fraction of binary stars, respectively. 115
- 4.14 The cumulative stellar mass function of the galaxies identified within the virial radii of the most massive among the three simulated clusters described in this Section (see also Borgani et al. 2006). All the simulations have been done at fixed mass resolution, which correspond to an increase by a factor 10 with respect to the basic resolution (i.e., $m_{gas} \simeq 6.9 \times 10^7 M_\odot$; see text). The four curves correspond to the different choices for the gravitational softening. The labels indicate the factor by which the softening has been changed, with respect to the standard choice of $3.5h^{-1}\text{kpc}$ 118

4.15	The combined cumulative stellar mass function of the galaxies identified within the virial radii of the three clusters. The four curves correspond to the different resolutions at which the clusters have been simulated. Continuous, long-dashed, short-dashed and dotted curves are for the simulations at progressively increasing resolution. The labels indicate the factor by which mass resolution is increased, with respect to the lowest resolution run (1x).	119
5.1	The projected stellar mass density for the C1 (left panel) and C2 (right panel) clusters at $z \simeq 2.1$, within a region of $150 h^{-1}\text{kpc}$ on a side, centred on the most massive galaxy.	126
5.2	The computed optical depth τ_V map in logarithmic scale for the C1 (left panel) and C2 (right panel) clusters at $z \simeq 2.1$, within a region of $150 h^{-1}\text{kpc}$ on a side, centred on the most massive galaxy.	127
5.3	The computed reddening $E(B - V)$ map in logarithmic scale for the the C1 (left panel) and C2 (right panel) clusters at $z \simeq 2.1$, within a region of $150 h^{-1}\text{kpc}$ on a side, centred on the most massive galaxy.	128
5.4	Galaxy luminosity function within the region shown in Figure 5.1, in the F814W(I_{814}) ACS filter band. Results for the C1 and for the C2 simulated clusters are shown as solid and dashed histograms respectively. The dotted blue histogram shows the observed luminosity function by Hatch et al. (2008) within the same region. The shaded regions show the luminosity of the observed and of the simulated BCGs, with the same colour code described above.	129
5.5	The projected surface brightness map in the I_{814} band for the C1 (left panel) and C2 (right panel) clusters at $z \simeq 2.1$, within a region of $150 h^{-1}\text{kpc}$ on a side, centred on the most massive galaxy.	130
5.6	The projected surface brightness map in the g_{475} band for the C1 (left panel) and C2 (right panel) clusters at $z \simeq 2.1$, within a region of $150 h^{-1}\text{kpc}$ on a side, centred on the most massive galaxy.	131
5.7	The map of star formation rate density for the C1 (left) and C2 (right) cluster, within the same region shown in Figure 5.1. Red crosses mark the positions of the 50 per cent most massive galaxies identified in projection within this region.	132
5.8	Histogram of line-of-sight galaxy velocities the C1 (solid line) and C2 (dashed line) clusters. Each histogram shows the average over three independent projections of a square region of $150 h^{-1}\text{kpc}$ on a side.	133

- 6.1 Mean differential (left) and cumulative (right) mass functions of all subhaloes identified within r_{200} and at $z = 0$, averaged over the four simulated clusters used in this study. Solid black lines are for the DM runs, while dot-dashed red lines are for GAS runs. For each cluster, we also show the main halo, using the corresponding value of M_{200} . For all other substructures, masses are given by the sum of the masses of all their bound particles. . . . 141

- 6.2 Density map of the g51 cluster for the DM run (left panels) and for the GAS run (right panels), at $z = 0$ (upper panels) and at $z = 2$ (lower panels). Positions are in comoving units. In the upper panels, the positions of all galaxies with stellar mass larger than $10^{11}h^{-1}M_{\odot}$ are marked by circles whose radii are proportional to the galaxy stellar mass. Different colours are used for different galaxy types: blue for Type-0, white for Type-1, and green for Type-2 galaxies. In the lower panels, we have marked by circles all galaxies more massive than $5 \times 10^{10}h^{-1}M_{\odot}$, and used the same colour-coding. 143

- 6.3 Differential (left panels) and cumulative (right panels) stellar mass functions for all galaxies within r_{200} at $z = 0$, in the four simulated clusters used in this study. The differential mass functions have been normalised to the total number of galaxies within r_{200} in each cluster. The solid histograms show the mean of the distributions from the four clusters, while the shaded region indicate, for each value of the stellar mass, the minimum and maximum number of galaxies. Solid black lines are for the DM runs, while dot-dashed red lines are for GAS runs. We show separately the stellar mass functions of the whole galaxy population (upper panels), of the Type-2 satellite galaxy population (central panels) and the Type-0 and Type-1 galaxies (lower panels). 145

- 6.4 Averaged radial density of galaxies identified $z = 0$ and within r_{200} for the four clusters used in our study. The distribution is normalised to the mean density of galaxies within r_{200} . Histograms show the mean of the four clusters, while their dispersion is indicated by the shaded regions. Solid black lines are for DM runs, while dashed-dotted red lines are for GAS runs. The dashed green line in each panel shows the mean density profile of dark matter. The three panels show separately the radial density of the whole galaxy population (upper left panel), of the Type-2 satellite galaxy population (upper right panel), and of the Type-0 and Type-1 satellite galaxies (lower panel). 148

- 6.5 Distribution of lifetimes of Type-1 galaxies. The lifetime is defined here as the time elapsed between the last time the galaxy was a Type-0 galaxy and the time the substructure mass was reduced below the resolution limit of the simulation (the galaxy becomes a Type-2). Results from the four simulated clusters have been stacked together. The solid black line is for the DM runs, and the red dashed line corresponds to the GAS runs. 150

6.6	Upper left panel: distributions of the merging times assigned to the Type-2 galaxies identified at $z = 1$ in the four simulated clusters. The solid black line shows the result from the DM runs, while the dot-dashed red line is for the GAS runs. The vertical green dotted line marks the value of the lookback time at $z = 1$. All galaxies whose merging time is smaller than this value will merge by $z = 0$. Upper right panel: distribution of the formation times of the Type-2 galaxies, i.e. the lookback times when the galaxies first become Type-2. Lower panel: distribution of the differences between the formation and the merging times (T_{delay}) of the Type-2 galaxies identified $z = 1$ (see text).	151
6.7	Dependence of satellite mass (upper left panel), distance from the centre of the accreting halo (upper right panel), circular velocity of the accreting halo at the virial radius (lower left panel), and ratio between the mass of the accreting halo and the satellite mass (lower right panel) on T_{delay} . In all panels, solid lines show the median of the distributions, while dot-dashed lines show the 25th and 75th percentile of the distributions. Black lines are used for the DM runs and red lines for the GAS runs. Quantities refer to Type-2 galaxies identified at $z = 1$	152
6.8	Satellite mass as a function of T_{delay} (as in the upper left panel of Figure 6.7), for all Type-2 galaxies identified at $z = 3.4$	154
6.9	Evolution of the Type-0 progenitors of the BCG for the four simulated clusters used in this study. In each panel, the solid black lines and the dashed red lines show the integral of the SFR associated with the progenitors of the BCG for the DM runs and for the GAS runs respectively. The black and the red dotted lines show the total stellar mass of all Type-0 progenitors of the BCGs.	156
6.10	Left panel: comparison between the trajectories of a sub-halo merging with the g51 cluster, projected on the x - y plane. Open black diamonds are for the DM run, while filled red circles are for the GAS run. At each redshift, the coordinates of the merging sub-halo are computed with respect to the cluster centre at the corresponding redshift. The big black circle shows the centre of the cluster at each snapshot, and its radius is equal to the corresponding value of r_{200} at the last snapshot in which the sub-halo was identified in the DM run. Right panel: evolution of the cluster-centric distance of the same sub-halo in the DM (black solid line) and GAS (red dot-dashed line) run. . .	157
6.11	Same as for the upper right panel of Figure 6.7, but only for Type-2 galaxies with stellar masses larger than $10^{11} M_{\odot}$	157
6.12	Total mass in the main progenitor of the BCG of the cluster g8 (dotted lines) for the DM (black) and GAS (red) runs. The black solid line and the red dot-dashed line show the integral of the SFR in the main progenitor of the BCG.	158

List of Figures

- 7.1 Example of a merger tree of the fourth most massive in stellar mass galaxy found in the simulation within r_{200} . Upper panel shows the merger tree of the synthetic galaxy as computed in the SAM. Lower panel shows the merger tree of the same galaxy as results directly from the simulation. Size of circles are proportional to square root of the galaxy stellar mass. Different colours are used for different galaxy types. Black is for Type-0 central galaxies, green for Type-1 satellite galaxies and red for Type-2 satellite galaxies. Final stellar mass of this galaxy is shown in the upper left corner of each panel. 165
- 7.2 Stellar density map of a box placed at the centre of the analysed cluster and of size $10r_{200}$ (upper panels) and $2r_{200}$ (lower panels). Positions are in comoving units. The positions of all galaxies with stellar mass larger than $10^{11} h^{-1} M_{\odot}$ are marked by circles with larger radii corresponding to larger stellar mass as computed in the simulation (left panels) and in the SAM (right panels). Different colours are used for different galaxy types: red for Type-0, black for Type-1, and green for Type-2 galaxies. 166
- 7.3 Radial density of galaxies identified at $z = 0$ and within $5r_{200}$ of the analysed cluster used in our study. Solid black lines show the radial density of galaxies directly identified in the simulation, while dashed-dotted red lines show the SAM predictions. The dashed green line in each panel shows the density profile of matter, normalised to match the radial density of SAM galaxies in the inner regions of the cluster. The three panels show separately the radial density of the whole galaxy population (upper panel), of the Type-2 satellite galaxy population (lower left panel), and of the Type-0 and Type-1 satellite galaxies (lower right panel). 168
- 7.4 Differential (left panels) and cumulative (right panels) stellar mass functions for all galaxies within $1.5r_{200}$ at $z = 0$ in the analysed simulated cluster as predicted by the SPH simulation (black continuous lines) and by the SAM (red dashed lines). We show separately the stellar mass functions of the whole galaxy population (upper panels), of the Type-2 satellite galaxy population (central panels) and the Type-0 and Type-1 galaxies (lower panels). SAM galaxies with a stellar mass lower than $10^6 h^{-1} M_{\odot}$ are shown in the $10^6 h^{-1} M_{\odot}$ bin 170
- 7.5 Comparison between the galaxy stellar masses as predicted by the SPH simulations (x axis) and by the SAM (y axis) at redshift $z = 0$ in different radial bins. Each symbol represent a galaxy which has the same position in both analysis, thus it is considered as *same galaxy*. The cyan continuous line represent the one to one correspondence. Black crosses are Type-0 central galaxies and red diamonds are Type-1 satellite galaxies. 172

- 7.6 We show in this Figure the evolution of the BCG of the analysed cluster as predicted by the SPH simulation (continuous black lines) and by the SAM (dashed red lines). *Upper right panel:* The number of identified galaxies which will eventually merge with the BCG by redshift $z = 0$ as a function of the lookback time. *Upper left panel:* The total star formation rate in the identified progenitors of the BCG at redshift $z = 0$ as a function of the lookback time. *Lower right panel:* The total stellar mass in the identified progenitors of the BCG at redshift $z = 0$ as a function of the lookback time. *Lower left panel:* A comparison between the total stellar mass (dashed-dotted (SPH) and continuous (SAM) lines) and the integral of the star formation rate (dotted lines) in the identified progenitors of the BCG at redshift $z = 0$ as a function of the lookback time. 175
- 7.7 We show in this Figure the evolution of the fourth most massive galaxy within r_{200} at $z = 0$ as predicted by the SPH simulation (continuous black lines) and by the SAM (dashed red lines). Merger trees of this galaxy were shown in Fig. 7.1. *Upper right panel:* Distance between the main progenitor of the studied galaxy and the centre of the cluster as a function of the lookback time in units of the corresponding r_{200} of the cluster at that time. *Upper left panel:* The number of identified progenitors of the galaxy as a function of the lookback time. *Lower left panel:* The total star formation rate in the identified progenitors of the galaxy as a function of the lookback time. *Lower right panel:* A comparison between the total stellar mass (dashed-dotted (SPH) and continuous (SAM) lines) and the integral of the star formation rate (dotted lines) in the identified progenitors of the galaxy as a function of the lookback time. Dashed blue vertical line is placed at the lookback time corresponding to the transition between Type-0 and Type-1 galaxy of the galaxy main progenitor. 177
- 7.8 We show in this Figure the evolution of the cluster-centric distance between the main progenitor a central Type-0 galaxy (right panel) and of a satellite Type-1 galaxy (left panel) as a function of the lookback time in units of the corresponding r_{200} of the cluster at that time. Both galaxies have a predicted stellar mass at $z = 0$ of $\sim 6 \times 10^{11} h^{-1} M_{\odot}$ in the SAM run. The dashed vertical blue line is placed at the position of transition between central Type-0 and satellite Type-1 of the main progenitor of the galaxy. 179

List of Figures

7.9	We show in this Figure the evolution of a central Type-0 galaxy (right panels) and of a satellite Type-1 galaxy (left panels) as predicted by the SPH simulation (continuous black lines) and by the SAM (dashed red lines). Both galaxies have a predicted stellar mass at $z = 0$ of $\sim 60 \times 10^{10} h^{-1} M_{\odot}$ in the SAM run. <i>Upper panels:</i> The total star formation rate in the identified progenitors of the galaxy as a function of the lookback time. <i>Lower panels:</i> A comparison between the total stellar mass (dashed-dotted (SPH) and continuous (SAM) lines) and the integral of the star formation rate (dotted lines) in the identified progenitors of the galaxy as a function of the lookback time. Dashed blue vertical line is placed at the lookback time corresponding to the transition between Type-0 and Type-1 galaxy of the satellite galaxy main progenitor.	180
A.1	z -evolution of the Comoving Number Density of DM Haloes	197
A.2	Confidence regions for Ω_M and Ω_{Λ}	198

List of Tables

4.1	Characteristics of the clusters identified within the simulated regions at $z = 0$. Col. 1: name of the simulated region; Col. 2: name of the clusters within each region; Col. 3: value of the total mass, M_{200} , contained within the radius r_{200} encompassing an average density 200 times larger than the critical cosmic density ρ_c (units of $10^{14} M_{\odot}$); Col. 4: total number of galaxies, N_{200} , within r_{200} , having a minimum number of 32 star particles.	95
4.2	Characteristics of the simulations. Col. 1: simulation name; Col. 2: IMF slope; Col 3: wind speed, v_w (units of km s^{-1}).	100
5.1	Characteristics of the two simulated proto-clusters at $z \simeq 2$. Col. 2: mass contained within r_{200} (in units of $10^{13} M_{\odot}$). Col. 3: r_{200} (in physical $h^{-1}\text{kpc}$). Col. 3 and 4: total stellar mass (in units of $10^{12} M_{\odot}$), and number of identified galaxies within r_{200} . Col. 5: X-ray luminosity in the [0.5–2.0] keV observer-frame energy band (units of $10^{43} \text{erg s}^{-1} \text{cm}^{-2}$). Col. 6: spectroscopic-like temperature. Col. 7: emission weighted Iron metallicity within r_{200}	125
6.1	Some numerical information about the four clusters used in this study. Column 1: name of the run; Column 2: M_{200} , in units of $10^{14} M_{\odot}$; Column 3: r_{200} , in units of $h^{-1}\text{Mpc}$; Column 4: total number of sub-haloes within r_{200}	140
7.1	Characteristics of the analysed cluster used in this study within r_{200} at $z = 0$. Column 1: name of the run; Column 2: number of identified galaxies; Column 3: total stellar mass M_* in units of $10^{13} h^{-1} M_{\odot}$; Column 4: total gas mass M_{gas} in units of $10^{13} h^{-1} M_{\odot}$; Column 5: total star formation rate (SFR) in units of $10^3 M_{\odot} \text{yr}^{-1}$. In the last row we show values for the Type-0 and Type-1 SAM galaxy population only.	163
A.1	Equations of state for different matter–energy components in the Universe	190

CHAPTER 1

INTRODUCTION

The Universe is currently thought to originate from a singularity in the space–time which began to expand – giving raise to the so–called *Big Bang* – about ~ 14 Gyr ago. Theoreticians succeed in conjecturing on the physics of the universe up to 10^{-9} seconds after the time zero; from these speculations we are able to make precise predictions on the pristine abundance of cosmic elements (e.g. Burles & Tytler 1998) formed at $t = 3$ minutes. Such a prediction turns out to be in excellent concordance with estimates drawn from the signature left by the recombination of free electrons and nuclei on the Cosmic Microwave Background (CMB) – the relic of the pristine energy bath – , about 4×10^5 yrs later (Komatsu et al. 2008). This is probably one of the most important confirmations of the current Standard Cosmological Model. Beside the study of the CMB anisotropies, other independent observations confirm the well established so-called *Λ CDM Concordance Model*.

- Baryonic Acoustic oscillations arise from the competition between gravitational attraction and gas pressure in the primordial plasma. These oscillations leave their imprint on very large scales ($\sim 100 h^{-1}\text{Mpc}$) on structures at every epoch of the evolution of the Universe, providing a robust standard ruler from which the expansion history of the Universe can be inferred (Percival et al. 2007a).
- Supernovae Ia (SN-Ia) are thought to be nuclear explosions of carbon/oxygen white dwarfs in binary systems. The value of SN-Ia as cosmological probes arises from the high peak luminosity as well as the observational evidence (locally) that this peak luminosity is the sought-after standard candle. In fact, the absolute magnitude, at peak, varies by about 0.5 magnitudes which corresponds to a 50%-60% variation in luminosity; this, on the face of it, would make them fairly useless as standard candles. However, the peak luminosity appears to be well-correlated with decay time: the larger L_{peak} , the slower the decay (Kowalski et al. 2008).
- The term large-scale structure (LSS) refers to the characterisation of observable distributions of matter and light on the largest scales. Clustering properties of large-

INTRODUCTION

scale structures as voids, filaments and clusters of galaxies depend on the cosmological models and can be thus used to constrain cosmological parameters (see, e.g., Borgani 2006).

All together, these independent observables, confirm that we are living in a Universe where only a tiny fraction ($\sim 4 \div 5\%$) of the total amount of energy-mass of the Universe is in the form of common known baryonic matter (see Appendix A). The rest of the matter of the Universe is in the form of an yet unknown non-baryonic matter which seems to interact only gravitationally with baryons and energy, then not emitting any kind of radiation. It is thus called *Dark Matter* (DM). Nevertheless, we know it must be there by a number of observations: among others, the rotation curves of spiral galaxies, the mass-over-light ratio for galaxy clusters, the velocity dispersion of galaxies in clusters, the large scale velocity field, the power spectrum of CMB (for reviews see e.g. Sellwood 2004, Ellis 2003). All together, baryonic and Dark Matter can account only for almost a $25 \div 30\%$ of the total content of energy-mass of the Universe. The remaining $\sim 70 \div 75$ percent is in the form of an even more unknown energy field (usually known as *Dark Energy*, DE) which causes the acceleration of the expansion of the Universe (see, e.g., Kowalski et al. 2008).

After the recombination, baryons – no longer impeded by the radiation pressure of photon which were coupled to them – were able to collapse and rest in the potential well created by DM. From that moment on, the Cosmology become the study of structure formation, that is to say the infall of dark matter halos and baryons in those potential wells. It is believed that a pristine field of very tiny fluctuations were superimposed to the otherwise homogeneous density field by some yet uncertain quantum mechanism; in this framework, with the additional assumption of the Cold Dark Matter scenario, the structure formation proceed in a *Bottom-Up* direction, the smallest structures forming first from the peaks of the primordial density fluctuations and then merging as building-blocks for larger ones. The collapse of matter can be described with linear perturbation theory until the contrast with respect to the mean density approaches unity, $(\rho - \bar{\rho})/\bar{\rho} \sim 1$; then, the collapse enters in the *non-linear* regime (see Appendix A).

At the top of the hierarchy of non-linear structures there are the Clusters of Galaxies, which are the greatest virialised objects in the universe, collecting matter from regions of about ~ 10 Mpc ($1\text{pc} \simeq 3.26$ light years). Most of the baryons in clusters are in the form of a hot, ionised gas which emits by thermal bremsstrahlung in the X-ray band, so that they can be detected at large redshifts, probing the large scale structure in the universe. Originating from the rare high peaks of primordial density perturbations, they probe the high-density tail of the cosmic density field and thereby their evolution is very sensitive to the details of the cosmological model. This is the reason why Galaxy Clusters are thought to be very useful cosmological laboratories. Moreover, they can be considered as fair tracers for the baryon's history in the universe, thereby being also invaluable astrophysical laboratories.

Owing to the continuous improvement in both spatial and spectral resolution power of modern X-ray, Optical and Infrared (IR) telescopes (as for example Chandra and XMM-

Newton in the X-band, Hubble Space Telescope (HST) and Very Large Telescope (VLT) in Optical bands and Spitzer in IR bands), more and more details on the inner properties of galaxy clusters have been unveiled in the last decade. These objects, that in a first approximation were thought to be virialised and spherically symmetric, have very complex dynamical features – such as strong asymmetries and clumpiness – witnessing for violent processes being acting or having just played a role. They exhibit luminosity and temperature functions which are not trivially related to their mass function, as one would expect for virialised gravitation–driven objects. Moreover, the radial structure of baryons’ properties is far to be completely understood: a number of observational facts pose a real challenge to our ability in modelling the physics of the Intra Cluster Medium (ICM) and the closely related physics of the galaxy population. Indeed a number of different physical processes are acting together during the formation and evolution of galaxy clusters. Gas cooling, star formation, chemical enrichment, feedback from Supernovae explosions (SN) and from Active Galactic Nuclei (AGN), etc are physical processes at the base of galaxy formation, which are difficult to disentangle. In addition to this, galaxy formation and evolution in clusters take place in extreme environments. Merging of galaxies, tidal interactions, ram pressure stripping, galaxy harassment and galaxy strangulation are physical processes which act preferentially in high-dense environments such as galaxy clusters.

A comprehensive description of the physics of baryons in a cosmological framework needs both a very high resolution and efficient and detailed codes to take into account all the complex interplay among different physical processes and reproduce reasonable galactic populations. This is why, traditionally, galaxy formation was studied through the use of semi-analytic models (SAMs) (see, e.g., Baugh 2006 for a review of semi-analytic models of galaxy formation). These models assume that baryons follow the dynamics of Dark Matter (computed either via numerical simulations or analytically). Then, within the DM haloes of galaxies, physics of baryons is followed with “physical motivated recipes”. Thanks to the enormous increase in the last decade in both the computational power and code efficiencies, recent direct hydrodynamical cosmological simulation achieved a sufficient numerical resolution and detailed description of the physical processes that allows one to predict and describe the cluster galaxy population with a reasonable realism (see, e.g., Dolag et al. 2008b and Borgani & Kravtsov 2009 in preparation, for recent reviews).

The aim of this Thesis is to explore the potentiality of direct hydrodynamical cosmological simulations and to study the complementarity of direct simulations and semi-analytic models on the formation and evolution of the cluster galaxy population within the hierarchical cosmological framework.

This Thesis is structured as follow.

Chapter 2 provides an introduction to cluster studies. It first describes the properties of the ICM in the X-ray band and through observations of SunyaevZeldovich (SZ) effect. Then we describe in more detail the properties of the cluster galaxy population in the optical and

near infrared bands. A picture of the evolution of galaxy clusters is also given. In particular we reviewing observations of proto-cluster regions at $z \sim 2$.

We provide in **Chapter 3** a brief overview of numerical methods developed to study the process of cosmic structure formation. More in detail we first describe some numerical algorithms to perform N-body cosmological hydrodynamical simulations, with particular emphasis on the TREE-SPH code GADGET-2 (Springel et al., 2005), widely used in this Thesis work. A brief description of the main features of two codes used to identify gravitationally bound structures in simulations [SUBFIND (Springel, 2001) and SKID (Stadel, 2000)] and of a spectro-photometric code aimed at computing luminosities of the simulated galaxies in different bands [GALAXEV (Bruzual & Charlot, 2003)] is also given. At the end of this Chapter we provide a general description of another complementary technique widely used to study galaxy formation within the hierarchical cosmological framework: the semi-analytic model (SAM) approach. Indeed, on one hand direct simulations allow us to follow the dynamics and physical processes with great accuracy, while on the other hand SAM allow us to explore the parameter space and reach statistics which are un-comparable to the direct simulation approach.

We have compared in **Chapter 4** the observed properties of the nearby cluster galaxy population presented in Chapter 2 with the synthetic galaxies predicted by numerical hydrodynamical cosmological simulations. We will show how numerical predictions are in reasonable agreement with observed properties as the colour-magnitude relation for the bulk of the galaxy population, whereas brighter central galaxies appear far too massive, star forming and bluer than the observed ones. Furthermore the number of galaxies brighter than a magnitude limit as a function of the cluster's mass turns out to be underestimated by about a factor of three in numerical simulations compared to the observed ones. The main results reported in this Chapter have been published in Saro et al. (2006) and Fabjan et al. (2008).

A comparison between the observed properties of the "Spiderweb system" briefly discussed in Chapter 2 and numerical predictions of high-resolution hydrodynamical cosmological simulations are reported in **Chapter 5**. We analyse two high-resolution proto-clusters at $z \sim 2.1$, one having a mass of $M_{200} \sim 10^{14} h^{-1} M_{\odot}$ ¹ at $z = 0$ and the other on the mass class of $M_{200} \sim 10^{15} h^{-1} M_{\odot}$ at $z = 0$. We conclude that the "Spiderweb complex" could correspond to the high-redshift progenitor of a rich galaxy cluster, whose BCG may have already been partially quenched by a 'radio mode' AGN feedback by $z \sim 2$. The main results reported in this Chapter have been published in Saro et al. (2009).

The effect of gas-dynamics on semi-analytic modelling of cluster galaxies is treat in **Chapter 6**. Here, we will use a hybrid SAM (De Lucia & Blaizot 2007) to compare numerical predictions of four massive cluster simulated with only dark matter particles and with both dark matter and gas particles. Our results show that gas dynamics has only a marginal

¹We define M_{Δ} as the mass contained within a radius encompassing a mean density equal to $\Delta\rho_c$, with ρ_c the critical cosmic density. Thus M_{200} is the mass within a radius r_{200} which encompass a mean density equal $200 \times \rho_c$. See Appendix A.

impact on the statistical properties of the galaxy population, but that its impact on the orbits and merging times of haloes strongly influences the assembly of the most massive galaxies. The main results reported in this Chapter have been published in Saro et al. (2008).

A detailed comparison between stripped-down versions of SAM and direct simulation is reported in **Chapter 7**. We study here the synthetic cluster galaxy population in a massive cluster predicted by these two techniques when a "simplified" physics is implemented in both techniques, so as to reduce the number of degrees of freedom in the comparison. We include only gravitational dynamics, radiative cooling and star formation. We conclude that while a good agreement is found in the predicted star formation histories of galaxies lying in low density environment, the discrepancy is larger for galaxies sitting at the centre of deep potential wells. In particular the direct simulated and SAM predicted star formation histories for the BCG substantially differs. Furthermore tidal stripping removes a non negligible fraction of SPH-simulated satellite galaxies. These stellar material lost by the satellite galaxy population is accreted by central galaxies in the form of a diffuse stellar component. The main results reported in this Chapter will be published in a paper in preparation (Saro et al. 2009).

A detailed comparison between stripped-down versions of SAM and direct simulation is reported in **Chapter 7**. We study here the synthetic cluster galaxy population in a massive cluster predicted by these two techniques when a "simplified" physics is implemented in both techniques, so as to reduce the number of degrees of freedom in the comparison

Chapter 8 contains the main conclusions from this work and outlines the future directions of investigation.

Finally, the **Appendix** describe the basic concepts of cosmology, which are used through the Thesis. In particular, we briefly review the cosmological model and the process of formation of the large scale structure.

CHAPTER 2

CLUSTERS OF GALAXIES: AN OVERVIEW

In this Chapter we will present an introduction to clusters of galaxies, with particular attention to observations in the optical and near infrared bands. Providing a comprehensive outline of that matter is far beyond the scope of this brief introduction, so that we address the reader to other reviews (Rosati et al., 2002; Carlstrom et al., 2002; Yee & Gladders, 2002; Demarco et al., 2005; Birkinshaw & Lancaster, 2007; Biviano, 2008; Diaferio et al., 2008; Kaastra et al., 2008; Miley & De Breuck, 2008; Plionis et al., 2008), while in the following we give only few basic ideas.

In Section 2.1 we will present a short introduction to observations of galaxy clusters in the X-ray band and through the Sunyaev Zel'dovich effect. Then we will present in Section 2.2 some of the main observables in the optical and near infrared bands. We will discuss in Chapter 4 how our numerical predictions compare with these observations. Finally, in Section 2.4 we will briefly present some observational results about high-redshift progenitors of galaxy clusters that we have compared with our numerical predictions in Chapter 5.

A first complete sample of clusters of galaxies was first provided by Abell (1958), who identified clusters as over-dense regions in the projected number counts of galaxies. Indeed they can include from tens to even few thousands of galaxies with velocity dispersion along the line of sight as high as $\sigma_v \sim 10^3 \text{ km s}^{-1}$ within the Mpc scale. Their corresponding typical masses are of the order of $10^{14} \div 10^{15} M_\odot$, dominated by the dark matter component ($\sim 80\%$, Zwicky 1937), while baryons only constitute $\sim 15 \div 20\%$ of the total mass budget. Most of these baryons are in the form of a hot and diffuse gas, the Intra-Cluster Medium (ICM). During the process of cluster formation, this gas is shocked by merging and heated by adiabatic compression, thus reaching the virial temperature (from $\sim 1 \text{ keV}$ to $\sim 10 \text{ keV}$) and densities of the order of one particle per 10^{-3} cm^{-3} . Only a very small fraction of baryon gas ($\sim 3\%$ of the total mass) cools to form stars and galaxies, which are the only component visible at optical wavelengths. Due to their high luminosity, it is possible to identify clus-

CLUSTERS OF GALAXIES: AN OVERVIEW

ters of galaxies even to very large distances, corresponding to high redshifts of the order of $z \sim 1.5$ (Mullis et al. 2005, Stanford et al. 2006, Eisenhardt et al. 2008a).

Relaxed galaxy clusters have regular structures, suggesting that they have reached an equilibrium dynamical state. Indeed, the resulting crossing time t_{cr} for a cluster of galaxies with radius D and velocity dispersion of galaxies σ_v is:

$$t_{cr} = \frac{D}{\sigma_v} \simeq 1 \left(\frac{D}{1Mpc} \right) \left(\frac{10^3 km/s}{\sigma_v} \right) Gyr, \quad (2.1)$$

This is significantly shorter than the age of the Universe which is of the order of the Hubble time $t_H \simeq 10 h^{-1} Gyr$ (see Appendix A).

It is worthwhile noticing that the first historical observational evidence for the existence of dark matter is related to clusters of galaxies. Already Smith (1936) and Zwicky (1933, 1937) have found that the inferred mass from the velocity dispersion of galaxies assuming the virial equilibrium was higher than the estimated mass from optical observations.

Galaxy clusters represent powerful probes for cosmology for many reasons (Borgani 2006). For example:

- The mass function of nearby galaxy clusters provides constraints on the amplitude of the power spectrum at the cluster scale (e.g., Rosati et al. 2002; Voit 2005 and references therein). At the same time, its evolution provides constraints on the linear growth rate of density perturbations, which translate into dynamical constraints on the matter and Dark Energy (DE) density parameters.
- The clustering properties (i.e., correlation function and power spectrum) of the large-scale distribution of galaxy clusters provide direct information on the shape and amplitude of the underlying DM distribution power spectrum. Furthermore, the evolution of these clustering properties is again sensitive to the value of the density parameters through the linear growth rate of perturbations (e.g., Borgani & Guzzo 2001; Moscardini et al. 2001 and references therein).
- The mass-to-light ratio in the optical band can be used to estimate the matter density parameter, Ω_M , once the mean luminosity density of the Universe is known and under the assumption that mass traces light with the same efficiency both inside and outside clusters (see Bahcall et al. 2000; Girardi et al. 2000; Carlberg et al. 1996, as examples of the application of this method).
- The baryon fraction in nearby clusters provides constraints on the matter density parameter, once the cosmic baryon density parameter is known, under the assumption that clusters are fair containers of baryons (e.g., Fabian 1991; White et al. 1993). Furthermore, the baryon fraction of distant clusters provide a geometrical constraint on

the DE content and equation of state, under the additional assumption that the baryon fraction within clusters does not evolve (e.g., Allen et al. 2002; Ettori et al. 2003).

However, to fully exploit the potential of galaxy clusters as cosmological probes it is necessary to achieve an accurate knowledge of their structure and properties. In a simple picture of structure formation, baryonic and dark matter collapse under the only action of the gravitational attraction. As we mentioned, during this process, the gas is shocked in accretion and/or merging events and heated by adiabatic compression. Since gravity does not have any preferred scale, this scenario predicts the formation of self-similar systems which basically appear as scaled versions of each other. By assuming that the gas lies in hydrostatic equilibrium within the dark matter potential wells, this scenario predicts well defined scaling relations between gas properties and total mass (see Kaiser 1991; Rosati et al. 2002; Voit 2005, for reviews). However, the observed scaling relations deviate from those predicted by self-similar scaling. This is a clear indication that non-gravitational processes, like radiative cooling, star formation and consequent heating from SNe or feedback from AGNs, are acting in the core of galaxy clusters. The correct interpretation of these processes makes galaxy clusters interesting astrophysical laboratories, where to study, among other things, the complex interplay between the ICM and the galaxies. At the same time, it indicates that an accurate study of the thermo-dynamical structure of the ICM is required in order to use galaxy clusters as precision tools for cosmology. In this Chapter we provide an introduction to cluster studies with particular emphasis on their galaxy population.

2.1 X-RAY PROPERTIES OF CLUSTERS OF GALAXIES

For a further and wider investigation of the topics developed in this section, we address the reader to more comprehensive reviews such as for example Rosati et al. (2002), Kaastra et al. (2008) and Plionis et al. (2008).

The first X-ray mapping of the sky was performed by the satellite telescope *UHURU* (Giacconi et al. 1972) which has shown that at the position of rich galaxy clusters already identified in optical bands there was a enhancement of diffuse X-ray emission with a power of $10^{43} \div 10^{45} \text{ erg s}^{-1}$. Later, Felten et al. (1966) and more explicitly Cavaliere et al. (1971) suggested that this radiation in the X-band was due to the thermal emission from the hot Intra Cluster Medium. This prediction was later confirmed by the first clusters' high quality spectra in the X-band (HEAO-1 AA2 Experiment Henriksen & Mushotzky 1986).

Dynamics of baryons is determined by the the dark matter potential wells, which gravitationally dominates. Gravitational collapse produces an adiabatic compression of the gas. This compression heats the gas, as well as shock processes. For example, if the collapsing mass is on the order of $10^{15} M_{\odot}$, the resulting temperature of the ICM can reach values of the order of $2 \times 10^7 - 10^8 K$ (even more than 10 keV). At these temperatures the gas component is completely ionised and emits in the X-band through thermal bremsstrahlung.

For a gas temperature T , the emissivity per unit frequency ν is given by (e.g. Rybicki & Lightman 1986):

$$\epsilon_\nu = n_e n_H \Lambda(T, Z, \nu) \simeq n_e^2 \Lambda(T, Z, \nu) \simeq 5.44 \cdot 10^{-52} \overline{Z^2} T^{1/2} n_e^2 \overline{g} e^{-h\nu/kT} \quad \text{W m}^{-3} \text{ Hz}^{-1} \quad (2.2)$$

where $\overline{Z^2}$ is the meansquared atomic charge on the ions. The Gaunt factor, $\overline{g} \sim 1.2$ is a dimensionless quantity which depends on the range of distances between electrons and ions at which the scatter process occurs, with a weak dependence on ν . The quadratic term in density of particles n_e is due to the fact that the energy emitted from a volume is proportional to both the number of electrons and the number of ions, and the *cooling function* $\Lambda(T)$ depends only on the chemical composition and temperature of the gas and it's normalised to the density of electrons and protons. Examples of X-ray spectra for typical cluster temperatures are shown in Fig. 2.1. Due to the high temperature, the continuum emission is dominated by thermal Bremsstrahlung, the main species by far contributing to the emission being H and He. The emissivity of this continuum is very sensitive to temperature for energies greater than kT and rather insensitive to it below. This is due to the exponential cut-off of the Bremsstrahlung emission. Indeed, it scales as $\overline{g} T^{-1/2} \exp(-h\nu/kT)$. The only line that clearly stands out at all temperatures is the Iron K line complex around 6.7 keV (see Fig. 2.1). We can also observe the K lines of other elements ($Z > 8$, H and He-like ionisation states), as well as the L-shell complex of lower ionisation states of Iron. However the intensity of these lines rapidly decreases with increasing temperature. Except for the cool clusters ($kT \lesssim 4 \text{ keV}$) or in the cool core present in some clusters, one cannot expect to measure the abundance of elements other than Iron because they are completely ionised. Most of the heavy elements with the exception of Iron are synthesised by Supernovae (SN) Type-II, while Iron production has a substantial contribution from SN Type-Ia supernovae (see e.g. Matteucci 2003). A detailed treatment of the chemical and stellar evolution of galaxies together with a fair description of feedback processes which pollute the ICM is thus needed for a comprehensive description of the metal enrichment of the intra-cluster medium.

The surface brightness of clusters of galaxies in the X-band is thus given by the following integral along the line of sight:

$$S_X = \frac{1}{4\pi(1+z)^4} \int n_e n_H \Lambda(T) dl. \quad (2.3)$$

The study of the X-ray properties of clusters of galaxies has sustained a rapid growth since the 90s, with the realisation of missions such as ROSAT, ASCA and Beppo-SAX and later with the Chandra and Newton-XMM missions since 1999. As a result wider and deeper fields together with better calibrations of the L_X/M ratio are now established. Recently, for example, Rykoff et al. (2008) analysed a sample of 17,000 optical selected galaxy clusters in the max-BCG cluster sample and found the following correlation between the mean 0.1-2.4 keV X-ray luminosity, $\langle L_X \rangle$, from the ROSAT All-Sky Survey and the inferred mean

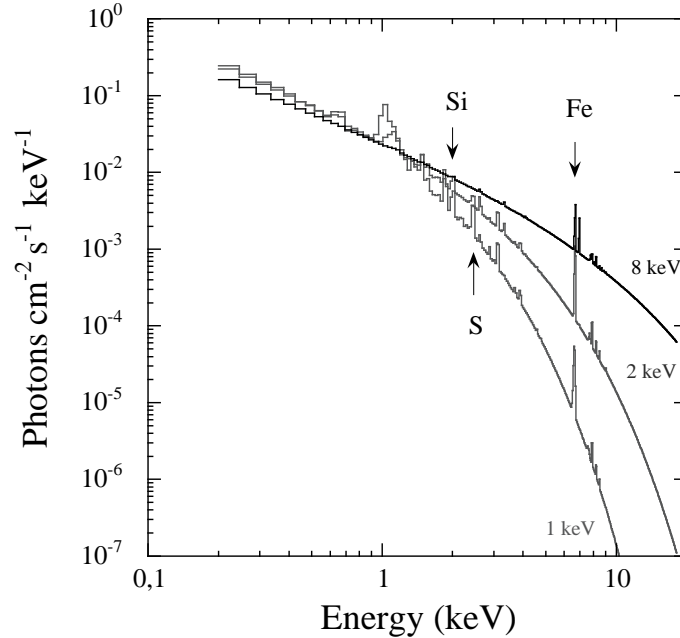


Figure 2.1: The X-ray emission from a thin plasma with 0.35 solar abundance at different temperatures, $T = 1, 2$ and 8 keV (from Arnaud et al. 2005).

mass $\langle M_{200} \rangle$, measured from weak gravitational lensing of *SLOAN DIGITAL SKY SURVEY* (*SDSS*) background galaxies (Johnston et al. 2007):

$$\langle L_X \rangle / 10^{42} \text{ erg s}^{-1} = (12.6_{-1.3}^{+1.4} (\text{stat}) \pm 1.6 (\text{sys})) (\langle M_{200} \rangle / 10^{14} h^{-1} M_{\odot})^{1.65 \pm 0.13}, \quad (2.4)$$

in reasonable agreement with previous results (e.g. Reiprich & Böhringer 2002; Stanek et al. 2006). Therefore, thanks to their X-ray properties, clusters of galaxies are fair mass estimator and can be used to constrain cosmological parameters (see also Appendix A and Rosati et al. 2002).

2.1.1. The Sunyaev–Zel’dovich effect (SZ)

For a further and wider investigation of the topics presented in this section, we particullary suggest to the reader the reviews by, e.g., Carlstrom et al. (2002); Birkinshaw & Lancaster (2007).

Another interesting approach to the study of the extensive atmosphere of hot gas in clusters of galaxies is provided by the Sunyaev–Zel’dovich effect (Sunyaev & Zeldovich 1970, 1972). We can separate into two different aspects of the Sunyaev–Zel’dovich effect:

- The Thermal Sunyaev–Zel’dovich effect (tSZ)
- The Kinetic Sunyaev–Zel’dovich effect (kSZ)

■ **The Thermal Sunyaev-Zel'dovich effect**

As the cosmic microwave background radiation propagates through a cluster of galaxies towards us, photons have a small probability of being inverse-Compton scattered by electrons in the cluster gas. Since the CMB radiation has a temperature of about $T_\gamma = 2.73$ K, while as we have seen the gas in a galaxy cluster may have temperatures as high as $T_{el} \sim 10^8$ K, scattering tend to increase the photon energies, so causing a change in the microwave background radiation intensity and spectrum towards the cluster. The resulting energy variation of each single photon can be expressed in the case of $E_\gamma \ll m_e c^2$ as:

$$\frac{\Delta E}{E} \approx \frac{k_B T_e}{m_e c^2}, \tag{2.5}$$

A photon crossing a region of the ionised plasma, will thus experience a number of collisions N_u defined as:

$$N_u = n_e \sigma_T \tag{2.6}$$

where n_e is the electron's density and σ_T is the Thompson cross-section

Thus we can define the parameter y of Comptonisation which measures the entity of the effect as:

$$y = \int n_e \frac{k_B T_e}{m_e c^2} \sigma_T d\ell, \tag{2.7}$$

where the integral is along the line of sight.

As a consequence, there is an increase of the photons' energy, which causes a deformation of the CMB spectra. The net observable result is that there is decrease of the intensity of the CMB radiation at frequencies lower than $\nu_{cr} \simeq 218$ GHz, and an increase of intensity for frequencies higher than ν_{cr} . The distortion is represented in Fig.2.2 as computed for a model cluster being 1000 times more massive than a typical massive cluster, to make it clearly visible.

Typical values of the parameter y of Comptonisation observed from the Sunyaev-Zel'dovich effect are between $10^{-6} \leq y \leq 10^{-4}$ (Silverberg et al. 1997; Enßlin & Kaiser 2000; LaRoque et al. 2006; Bonamente et al. 2008), depending on the plasma's temperature.

■ **The Kinematic Sunyaev-Zel'dovich effect**

Beside the thermal Sunyaev-Zel'dovich effect, there is the so called kinetic Sunyaev-Zel'dovich effect. The kinematic effect is produced by clusters which are in motion relative to the frame in which the CMB has a zero dipole. In the cluster frame, the CMB develops a dipole term proportional to the cluster's speed, and the scattering of this anisotropic radiation field causes it to become slightly more isotropic.

Temperature variations are proportional to the plasma velocity v_p ,

$$\frac{\Delta T}{T} = -\tau_e \frac{v_p}{c}, \tag{2.8}$$

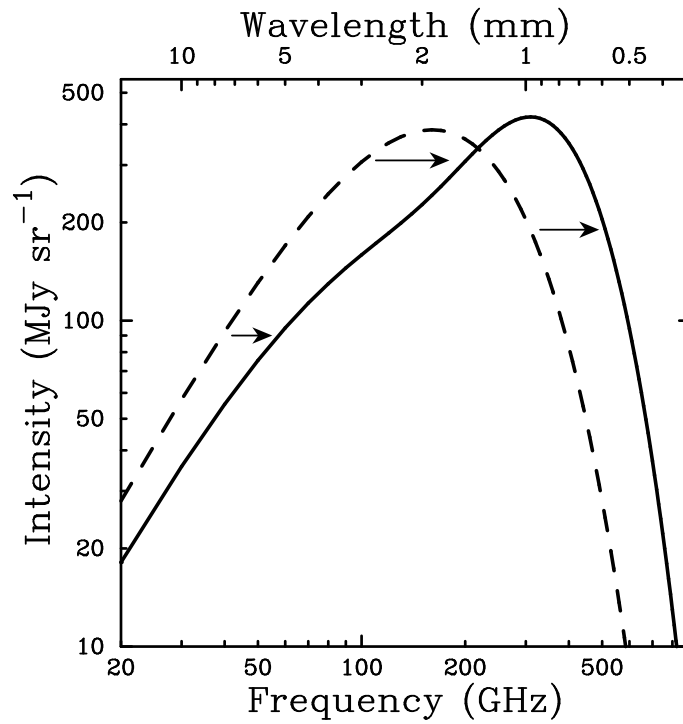


Figure 2.2: The CMB spectrum, undistorted (dashed line) and distorted by the tSZ effect (solid line). The tSZ distortion shown is for a model cluster 1000 times more massive than a typical massive galaxy cluster (from Carlstrom et al. 2002).

where τ_e is the optical depth of the electronic cloud producing the distortion.

Typical values of distortions of the CMB induced by the kSZ are about one order of magnitude lower than those from the tSZ. From the analyses of the kinematic Sunyaev-Zel'dovich effect, it is thus possible to obtain informations about the peculiar velocities of clusters of galaxies, in a redshift independent way.

The power of the SZ effect comes about because the effect is caused by scattering, rather than emission, and so it scales with the density of the scattering electrons. A cluster of galaxies may therefore appear quite different in its X-ray and SZ structures, and a comparison of those structures can provide interesting informations on the physics of clusters and their atmospheres.

As an example, we shows in Figure 2.3 an overlay of the optical, X-ray and SZ effect images of Abell 1689 and 1914 massive clusters and illustrates all of the main components of the clusters: the luminous stars, hot ICM observed via its X-ray emission and the SZ effect, and even the presence of the unseen dark matter manifesting itself through gravitational lensing of background galaxies. The figure shows several bright elliptical galaxies that are typically located near the cluster centres. A salient feature of such central galaxies is that they show little evidence of ongoing star formation, despite their extremely large masses. Furthermore, a large amount of DM, extending well beyond the region traced by the X-ray emission, leaves its imprint in the pattern of gravitational lensing, which causes the distortion of the images of background galaxies. In the inner regions of clusters the gravitational lensing can be easily seen in the long thin arcs curved around the cluster centre. At larger radii, the effect is weaker. Although not easily visible by eye, it can still be reliably measured by estimating shapes of many background galaxies and comparing their statistical average with the expected value for an isotropic distribution of shapes. The gravitation lensing is a direct probe of the total mass distribution in clusters, which makes it both extremely powerful in its own right and a very useful check for other methods for measuring cluster masses.

2.2 OPTICAL AND NEAR INFRA-RED PROPERTIES OF CLUSTERS OF GALAXIES

We will now review in this Section the observed optical and near infra-red (NIR) properties of the galaxy population within nearby clusters. To give a comprehensive outline of that matter is far beyond the scope of this brief introduction, so that we address the reader to recent review (e.g. Yee & Gladders 2002; Plionis et al. 2008; Biviano 2008), while in the following we restrict our analyses to only few observed properties of the cluster galaxy population. In Chapter 4 we will present a detailed comparison between these observations and the numerical predictions of our cosmological hydro-dynamical simulations. More in detail, we will focus on:

- The number-density profile of cluster galaxies;



Figure 2.3: Left panel: composite X-ray/optical image of the galaxy cluster Abell 1689, located at redshift $z \simeq 0.18$. The map shows area of 556 kpc on a side. The purple diffuse halo shows the distribution of gas at a temperature of about 10^8 K, as revealed by the Chandra X-ray Observatory. Images of galaxies in the optical band, coloured in yellow, are from observations performed with the Hubble Space Telescope. The long arcs in the optical image are caused by gravitational lensing of background galaxies by matter in the galaxy cluster, the largest system of such arcs ever found (Credit: X-ray: NASA/CXC/MIT; Optical: NASA/STScI). Right panel: optical image of cluster Abell 1914 from the Sloan Digital Sky Survey with the superimposed map of the temperatures of the Cosmic Microwave Background observed by the Sunyaev-Zel'dovich array (SZA). The image illustrates the effect of up-scattering of the CMB photons by the hot ICM from low frequencies to higher frequencies. At the frequency of observation, the cluster appears as a temperature decrement in the CMB temperature map. (Credit: John Carlstrom and SZA collaboration). Figure from Borgani & Kravtsov (2009) in preparation.

- The colour–magnitude relation;
- The mass–luminosity ratio;
- The number of galaxies as a function of the cluster’s mass;
- The luminosity function.

2.2.1. The number–density profile of cluster galaxies

Popesso et al. (2005) have analysed a sample of 217 galaxy clusters from the Sloan Digital Sky Survey (SDSS) catalogues and have computed the number of galaxies as a function of the cluster–centric distance. They have considered all galaxies with magnitude in r band $r < -18.5$. To stack all the clusters together uniformly they have compute distances in units of r_{200} ¹ of each cluster. They have found a best fit of their data by comparing their results with two different theoretical distributions.

They have first compared their results with a King profile (King 1962), which describes the mass distribution of relaxed galaxy clusters. We recall that by relaxed clusters we mean all those clusters that have not experienced major merging processes for a sufficiently long time. The King profile can be expressed in its 3D and projected formulation with the following expressions:

$$n(r) = \frac{n_0}{(1 + (r/r_c)^2)^{3/2}} \quad (2.9)$$

$$\sigma(b) = \frac{\sigma_0}{(1 + (b/r_c)^2)}, \quad (2.10)$$

where r_c is the so–called *core radius* and $\sigma_0 = 2n_0r_c$ is a normalising factor.

The second theoretical profile they have compared with is the NFW profile (Navarro et al. 1997), which describes the density profile of dark matter haloes predicted by cosmological N–body simulations and can be expressed as:

$$\rho(r) = \frac{\delta_0}{(r/r_s)(1 + (r/r_s)^2)} \quad (2.11)$$

where δ_0 is a normalisation factor and r_s is a characteristic radius which is usually defined as a function of the concentration parameter c in the form $r_s = r_{200}/c$.

Popesso et al. (2005) have found that the best fit to their results is given by a King profile with a core radius of $r_c/r_{200} = 0.224 \pm 0.005$ and $\sigma_0 = 0.153 \pm 0.004$, while for a NFW profile they have found a concentration parameter $3.9 < c < 4.2$. Figure 2.4 shows the observed number–density profile of galaxies and the best fits found by Popesso et al. (2005) of the two different theoretical distributions of Eq. 2.9 and Eq. 2.11. It is worth to notice that

¹We define r_{200} as the mass contained within a radius encompassing a mean density equal to $200 \times \rho_c$, with ρ_c the critical cosmic density. See Appendix A.

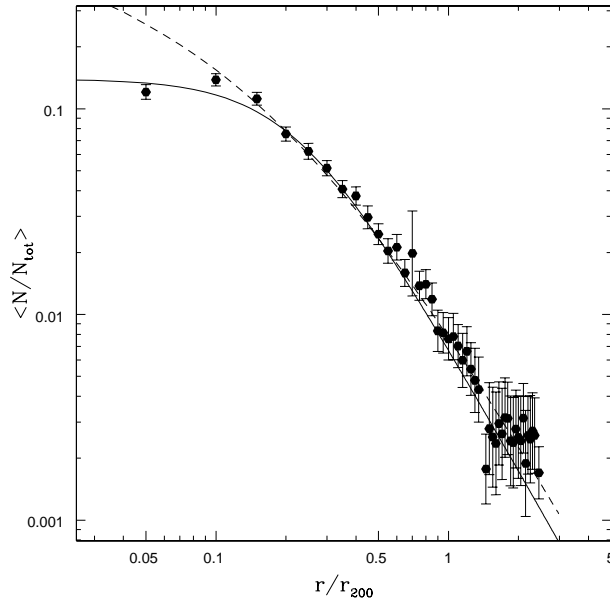


Figure 2.4: Number-density profile of galaxies as a function of the cluster-centric distance (from Popesso et al. 2005).

the number density profile of galaxies in the central regions of the clusters has a shallower distribution than the density profile of dark matter haloes predicted by NFW profiles (see also discussion in Section 4.3.1).

2.2.2. The colour-magnitude relation

By Colour Magnitude Relation (CMR) we mean the reddening of the integrated colours of galaxies with the increase of their luminosity, which was first observed by Baum (1959).

It is usually interpreted as a metallicity effect (Kauffmann & Charlot 1998, see also De Lucia et al. 2004, 2007), whereas its scatter would mirror the natural spread in galaxy ages (Kodama & Arimoto 1997). The more massive the galaxy is, the more metal rich is. Thus, as a net result, galaxies more massive and older tend to be redder than the younger and less massive ones. A good description of all processes related to the metal enrichment is therefore a crucial ingredient for a realistic description of the CMR.

The CMR is also useful to determine distances, as highlighted by Bower et al. (1992). Indeed, by knowing differences in colours, one can recover absolute magnitudes of cluster galaxies, and therefore their distances. In the same work, by analysing the Coma and the Virgo clusters, they have shown the universality of the CMR.

For example, from a sample of 50 elliptical and lenticular galaxies in the Coma cluster Bower et al. (1992) found a best fit for $V - K$ as function of M_V and $U - V$ as a function of

M_V :

$$V - K = -0.0743 \pm 0.0011(M_V + 34.92) + 4.21 \pm 0.16 \quad (2.12)$$

and

$$U - V = -0.0819 \pm 0.008(M_V + 34.92) + 2.61 \pm 0.11. \quad (2.13)$$

In Fig.2.5 we report the colour magnitude diagrams found by Bower et al. (1992) for the Virgo cluster (empty symbols) and for the Coma cluster (filled symbols). The continuous line shows the median fit. Dashed line shows the CMR predicted for the Coma cluster starting from the Virgo cluster, shifted by a constant distance modulus of 3.6, thus showing the CMR universality.

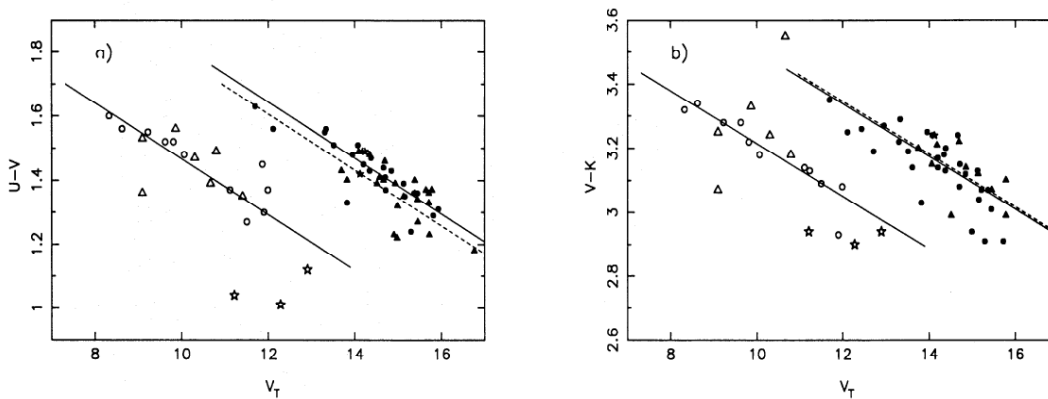


Figure 2.5: Colour magnitude relation for the Virgo cluster (empty symbol) and for the Coma cluster (filled symbols): (a) CMR for the $U - V$ colours; (b) CMR for the $V - K$ colours. Triangles are S0 galaxies, circles ellipticals and stars S0/a or s0₃ galaxies. Dashed line shows the CMR predicted for the Coma cluster starting from the Virgo cluster (from Bower et al. 1992).

More recently López-Cruz et al. (2004) have analysed the CMR from a sample of 57 clusters in the Einstein IPC database (Jones & Forman 1999) identified in the X-band in the redshift range $0.02 \leq z \leq 0.18$. They have confirmed the universality of the CMR at low redshift in $B - R$ as a function of the M_R magnitude. They also have studied the redshift dependence of the CMR. Fig.2.6 shows this relation for a subsample of six galaxy clusters.

A number of theoretical predictions have been compared to these observations. For example Lanzoni et al. (2005) and Romeo et al. (2004), have compared their semi-analytic model (SAM) and hydro-dynamical N-body simulation predictions respectively with observational results from Prugniel & Simien (1996) and Bower et al. (1992).

Figure 2.7 from Lanzoni et al. (2005), indeed shows their semi-analytic prediction for the CMR in $B - V$ as a function of M_B and $V - K$ as a function of M_V compared with observational data from Prugniel & Simien (1996) and Bower et al. (1992).

2.2. Optical and near infra-red properties of clusters of galaxies

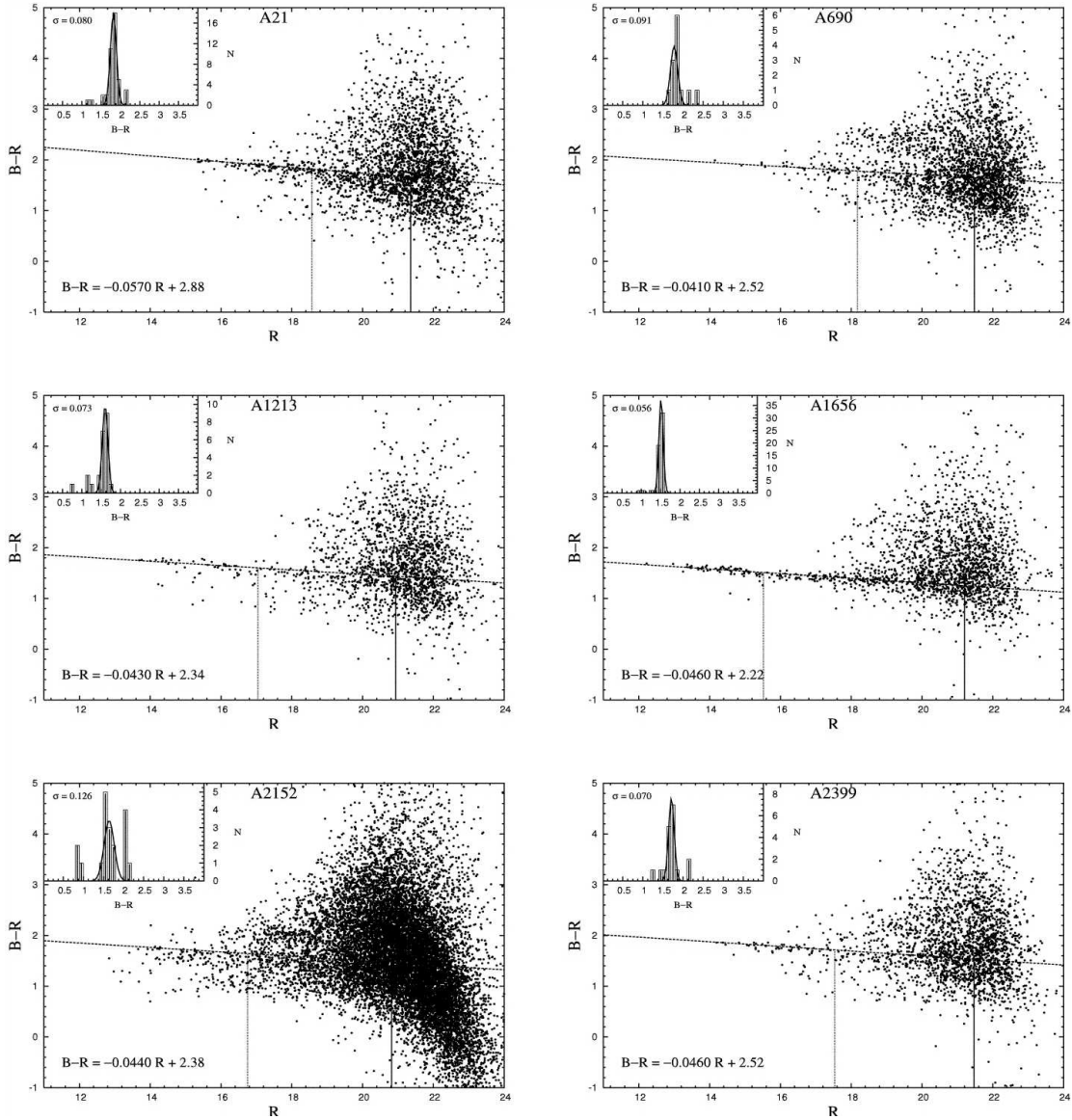


Figure 2.6: CMR in the $B - R$ as a function of M_R respectively for :a) A21; b) A690; c) A1213; d) A1656 (Coma); e) A2152; f) A2399 (from López-Cruz et al. 2004).

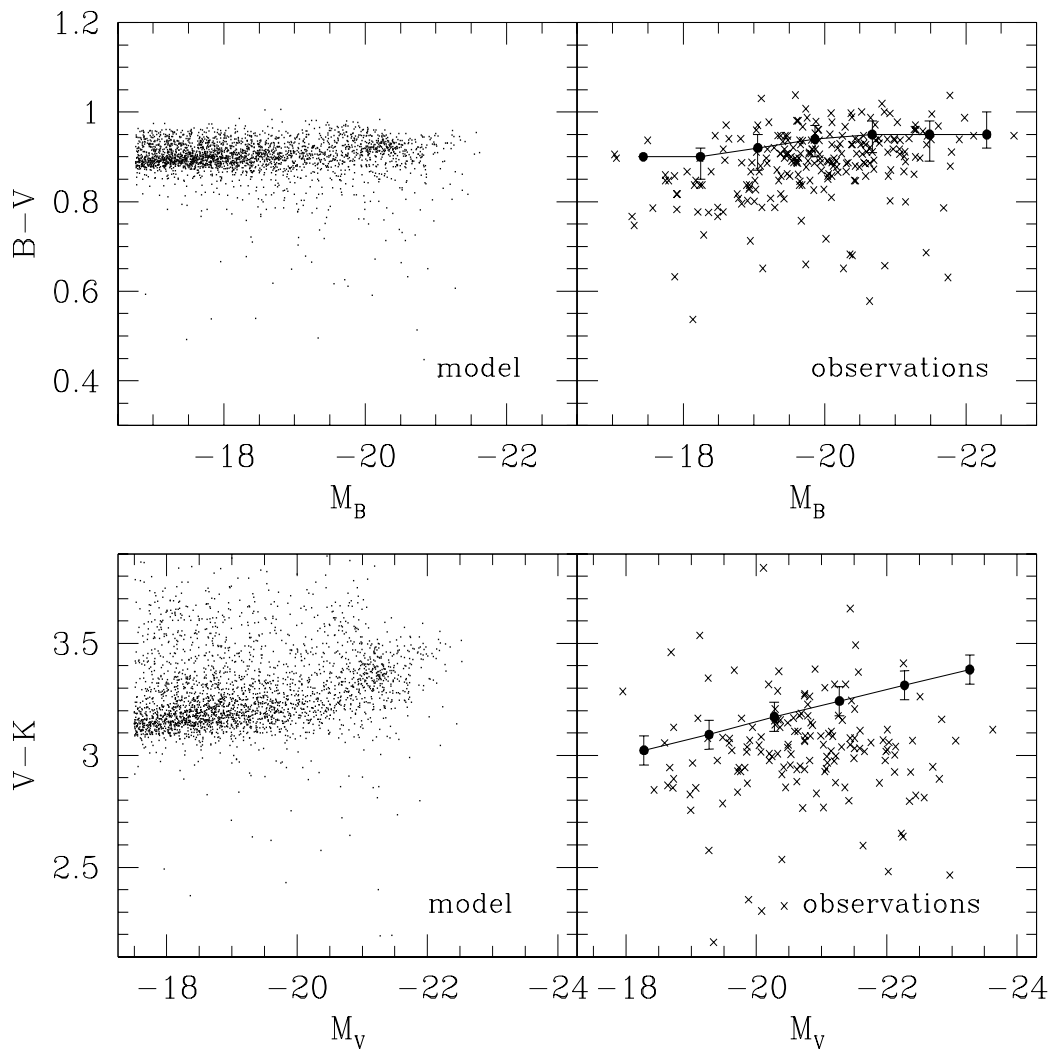


Figure 2.7: Upper panels: Comparison between numerical predictions from semi-analytic models and observational results from Prugniel & Simien (1996) regarding the CMR in $B - V$ as a function of the M_B magnitude. Numerical predictions are shown in the left panel, while observations are shown in the right panel, where the continuous line shows the median, from Lanzoni et al. (2005). Lower panels: As in the upper panels but for the CMR in the $V - K$ as a function of the M_V compared with observations from Bower et al. (1992). Plots from Lanzoni et al. (2005).

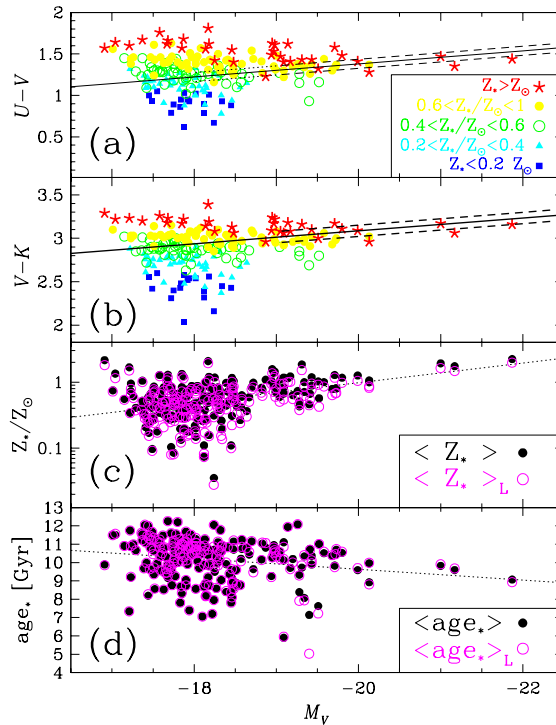


Figure 2.8: Comparison between numerical predictions from N-body hydro-dynamical simulations and observational results from Bower et al. (1992) (continuous line). CMR in $U - V$ (a) and $V - K$ (b) as a function of M_V , colour coded in metallicity. (c) Relation between mean metallicity of galaxies and M_V magnitude and (d) between age of galaxies and M_V magnitude, averaged in mass (filled symbols) and luminosity (empty violet symbols), from Romeo et al. (2004).

Figure 2.8 shows instead a comparison with predictions from hydro-dynamical cosmological simulations of Romeo et al. (2004) with the observational results from Bower et al. (1992). More in detail they have compared the CMR in $U - V$ as a function of M_V and $V - K$ as a function of M_V , by distinguishing between different contribution from galaxies with different metallicities. Furthermore they have studied the relation of mean age and metallicity of galaxies as a function of magnitude in the V band.

We will discuss more in detail the different assumptions and implementations of both SAM and direct hydro-dynamical simulations in Chapter 3.

The presence, as early as $z \sim 1.5$, of a prominent and low-scatter red sequence in galaxy clusters places useful constraints on the possible evolutionary pathways in galaxy colour and luminosity (Mullis et al. 2005; Stanford et al. 2005, 2006; Bell et al. 2004; Faber et al. 2007;

De Lucia et al. 2004c, 2007). Indeed both the low-scatter of the CMR and its little evolution with redshift are challenging properties to be reproduced by numerical models of galaxy formation (see e.g. Diaferio et al. 2001a; De Lucia et al. 2004c; Menci et al. 2008; Romeo et al. 2008 and references therein).

2.2.3. The mass–luminosity ratio

From the cluster’s mass to light ratio, assuming that it is representative of the Universe, is possible to compute Ω_M by multiplying it by the observed mean luminosity density of the Universe (see e.g. Bahcall et al. 2000; Girardi et al. 2000; Carlberg et al. 1996):

$$\Omega_M = M/L \times \rho_L. \quad (2.14)$$

Assuming a mass to light ratio $M/L \propto M^\alpha$, a number of authors have found a value of α between 0.2 and 0.4. For example Girardi & Mezzetti (2001) have analysed a sample of 141 clusters, 36 poor clusters, seven rich groups and two samples of ~ 500 groups of galaxies from the Nearby Optical Galaxy catalogue finding $M \propto L_B^{1.34 \pm 0.03}$ which implies a values of $\alpha \sim 0.25$. A possible explanation of this shallower dependence of the luminosity from the cluster’s mass is that the more massive clusters are also the older, thus a lower luminosity especially in the bluer and optical bands is expected.

Another possible explanation given by Lin et al. (2003) is that systems with virial temperatures higher than $10^7 K$ have a lower efficiency of forming cooling flows at cluster’s cores. thus possibly implying a relatively lower stellar mass fraction:

$$M_{star}/M_{tot} \propto M_{tot}^{-0.26}. \quad (2.15)$$

This also may explain the fact that the M/L is higher in the K band, which is dominated by old red–giant stars.

In another work Lin et al. (2004) have observed the relation between the M/L ratio and the cluster’s mass in the NIR K band (left panel of Fig. 2.9). They have analysed a sample of 93 clusters and groups of galaxies of the Two Micron All Sky Survey (2MASS) finding a value of α for the best fit of $\alpha = 0.26 \pm 0.04$ within r_{200} . In a similar way Popesso et al. (2004) have analysed a sample of 130 clusters of the RASS-SDSS catalogue focusing on the red galaxy population finding $M/L \propto M^{0.2 \pm 0.08}$ in the i band within r_{500} . As shown in the right panel of Fig. 2.9, for the whole galaxy population they have found a best fit of:

$$\log(L/10^{12}L_\odot) = (0.90 \pm 0.05) \times \log(M_{500}/10^{14}M_\odot) - 0.06 \pm 0.03. \quad (2.16)$$

Rines et al. (2004a) analysed nine nearby rich, X-ray luminous clusters from the Cluster And Infall Region Nearby Survey (CAIRNS) catalogue. CAIRNS is a spectroscopic survey of the infall regions surrounding nine nearby rich clusters of galaxies. They observed the relation between the M/L ratio and the cluster’s mass in the NIR K band. They found a large

2.2. Optical and near infra-red properties of clusters of galaxies

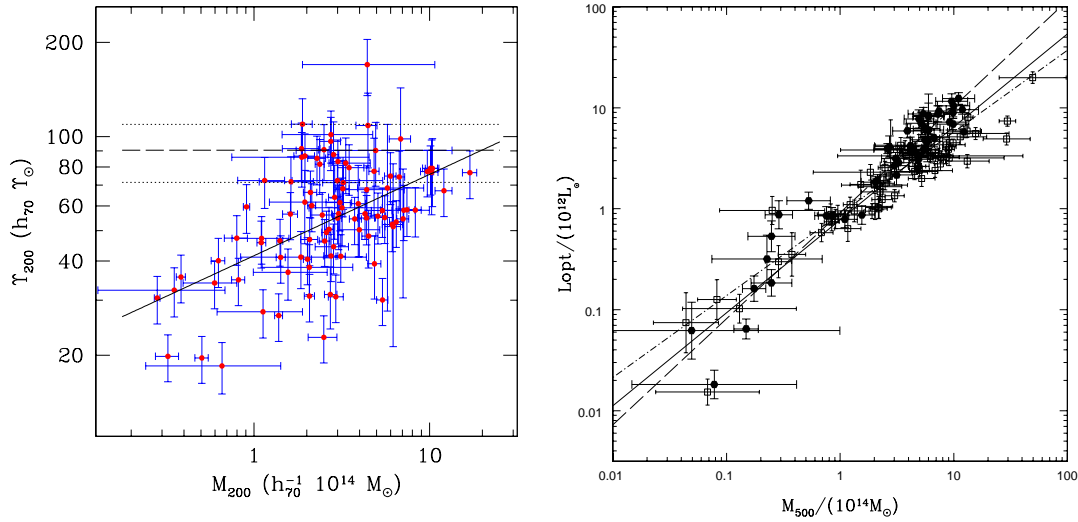


Figure 2.9: Left panel: Mass to light ratio as a function of the cluster’s mass in the K band (from Lin et al. 2004). Right panel: Same as left panel but in i band within r_{500} (from Popesso et al. 2004).

scatter but the CAIRNS clusters show an increase in M/L (evaluated at r_{200}) with increasing mass. Rines et al. (2004) found a similar correlation between X-ray mass and near-infrared mass-to-light ratios to the one found by Lin et al. (2004); more massive clusters have larger mass-to-light ratios with a best-fit relation:

$$(M/L_{K_s})(< r_{500}) = (67 \pm 4)h \left(\frac{M_{500}}{2.1 \times 10^{14} M_{\odot}} \right)^{0.31 \pm 0.09}. \quad (2.17)$$

2.2.4. Number of galaxies versus cluster’s mass

Another property that is possible to observe and gives important informations on both physics of galaxy formation and merging rate of galaxies is the number of galaxies as a function of the cluster mass. For example, Lin et al. (2004) have shown that the number of galaxies within r_{500} , N_{500} , with magnitude $M_K \leq -21$ is proportional to $M_{500}^{0.84}$ (see left panel of Fig. 2.10). More in detail they have found that:

$$N_{500}(M_K \leq -21) = 56 \pm 2 \left(\frac{M_{500}}{2 \times 10^{14} \times 0.7 h^{-1} M_{\odot}} \right)^{0.84 \pm 0.04}. \quad (2.18)$$

In a similar way Popesso et al. (2006b) have found that the number of galaxies increases slower than the cluster’s mass. More in detailed they found in the r band that the number of galaxies with magnitude less than -20 lies on the relation:

$$N = 10^{-11.60 \pm 0.59} (M_{200}/M_{\odot})^{0.91 \pm 0.04}, \quad (2.19)$$

as shown in the right panel of Fig. 2.10.

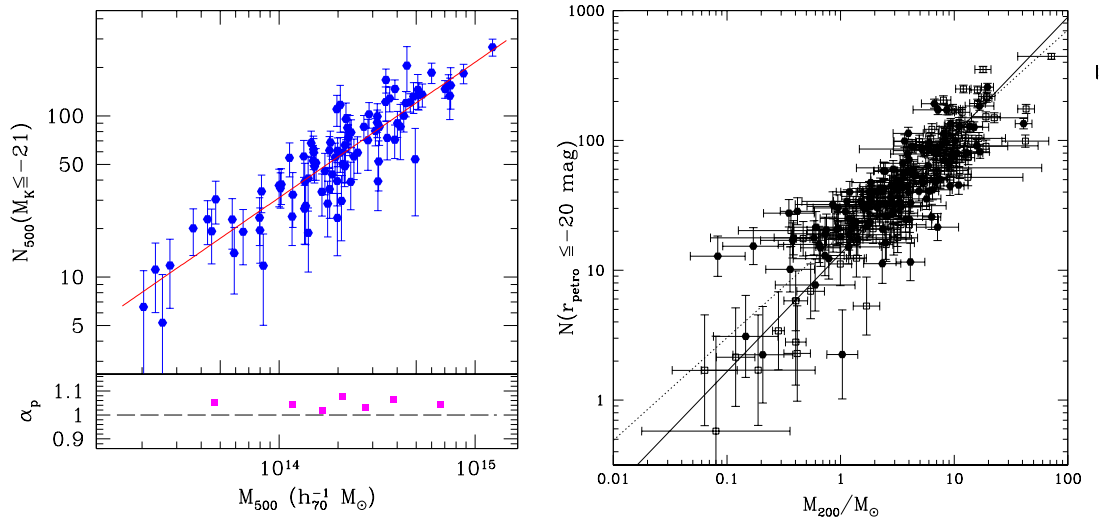


Figure 2.10: Left panel: Relation between the number of galaxies with $M_K < -21$ and the cluster’s mass (from Lin et al. 2004). Right panel: Relation between the number of galaxies with $M_r < -20$ and the cluster’s mass within r_{200} (from Popesso et al. 2006b).

2.2.5. The luminosity functions

One of the most studied property of the cluster galaxy populations is their luminosity function, which is defined as the number of galaxies per unit volume within a given magnitude bin.

Despite (or because of) its conceptual simplicity the LF has been for many years one of the most popular tools for the interpretation of galaxy observations at all redshifts and in very different environments. The comparison of the LF at different redshifts constrains models of galaxy formation and evolution (Kauffmann & Charlot 1998), while the comparison of the LF in low and high density environments probes the relevance of the environmental effects on the galaxy populations. The LF is historically best studied in rich clusters of galaxies, which provide large numbers of galaxies at the same distance and, at low redshift, with high contrast against the background, allowing an efficient identification of cluster members with small contamination from background galaxies.

The most widely used expression for the luminosity function is the one presented by Schechter (1976):

$$\phi(L)dL = \phi_*(L/L_*)^\alpha e^{-(L/L_*)} d(L/L_*). \quad (2.20)$$

Where L_* is a characteristic luminosity, ϕ_* is the density of galaxies per units of magnitude at the luminosity L_* and α is a constant which indicates the slope of the relation at the faint

end. Typical values of ϕ_* , the characteristic magnitude M_* and α for field galaxies in the B-band are $\phi_* = 0.0156 \pm 0.004$, $M_* = -19.2 \pm 0.27$ and $\alpha = -1.30 \pm 0.069$ (Fried et al. 2001).

Recently, with the increase of the accuracy and completeness of samples, observations have started to show a bimodal behaviour in the luminosity function. For example Popesso et al. (2006a) have studied a sample of 97 clusters of galaxies from the ROSAT All-Sky Survey in the X-band and from the RASS-SDSS in the optical bands (York et al. 2000, Stoughton et al. 2002, Abazajian et al. 2004) with redshift distribution $z \leq 0.25$. Popesso et al. (2006a) have computed the combined luminosity functions in the g, r, i and z . Their results are shown in Fig. 2.11. It clearly exhibits the bimodal behaviour of the luminosity function (LF), well described by the following equation:

$$\phi(L)dL = \phi_* \left[\left(\frac{L}{L_b^*} \right)^{\alpha_b} \exp \left(\frac{-L}{L_b^*} \right) + \left(\frac{L}{L_f^*} \right)^{\alpha_f} \exp \left(\frac{-L}{L_f^*} \right) \right] d(L/L_*). \quad (2.21)$$

The large uncertainties associated to the exponential cut-off at the bright end of the LF is due to the low statistics of galaxies at this magnitudes. Popesso et al. (2006) have also computed the separate contribution of the early type and late type populations of galaxies to the LF, based on a colour cut. They have found that the bluer population is well described by a simple Schechter function, while the bimodal behaviour of the LF is mainly due to the redder population of galaxies. Furthermore the exponential cut-off at the bright end is similar in both early and late type galaxies. They have therefore argued that the differences in the faint end are not due to merging processes associated to the central galaxies, but may lie in the transformation of spiral and irregular galaxies into early type dwarf galaxies. However, these results is at variance with other analyses. For instance, Adami et al. (2000) and Mobasher et al. (2003) performed deep spectroscopic survey of the Coma cluster and found no evidence for an upturn of the LF at faint magnitudes.

2.3 CLUSTERS OF GALAXIES AT REDSHIFT $z \gtrsim 1$

Despite the advent of the era of precision cosmology ushered in by observations of SNe and the cosmic microwave background (see Appendix A), significant uncertainty remains in the expected numbers of galaxy clusters at $z > 1$. Moreover, the CMB temperature anisotropies on scales corresponding to clusters are not accurately known, leading to values for σ_8 , the rms matter fluctuation in a sphere of radius $8h^{-1}$ Mpc at $z = 0$ (Appendix A), which cover the range $0.67_{-0.13}^{+0.18}$ (Gladders et al. 2007) to 0.98 ± 0.10 (Bahcall et al., 2003).

The range $\sigma_8 = 0.7$ to 1 corresponds to a variation of a factor of nearly 20 in the predicted numbers of $z > 1$ clusters with $M_{\text{tot}} > 10^{14} M_{\odot}$ (e.g. Sheth & Tormen, 1999). Obtaining substantial samples of galaxy clusters at $z > 1$ has proved challenging, largely because such objects are difficult to detect using only optical data. Due to their greatly enhanced rate of

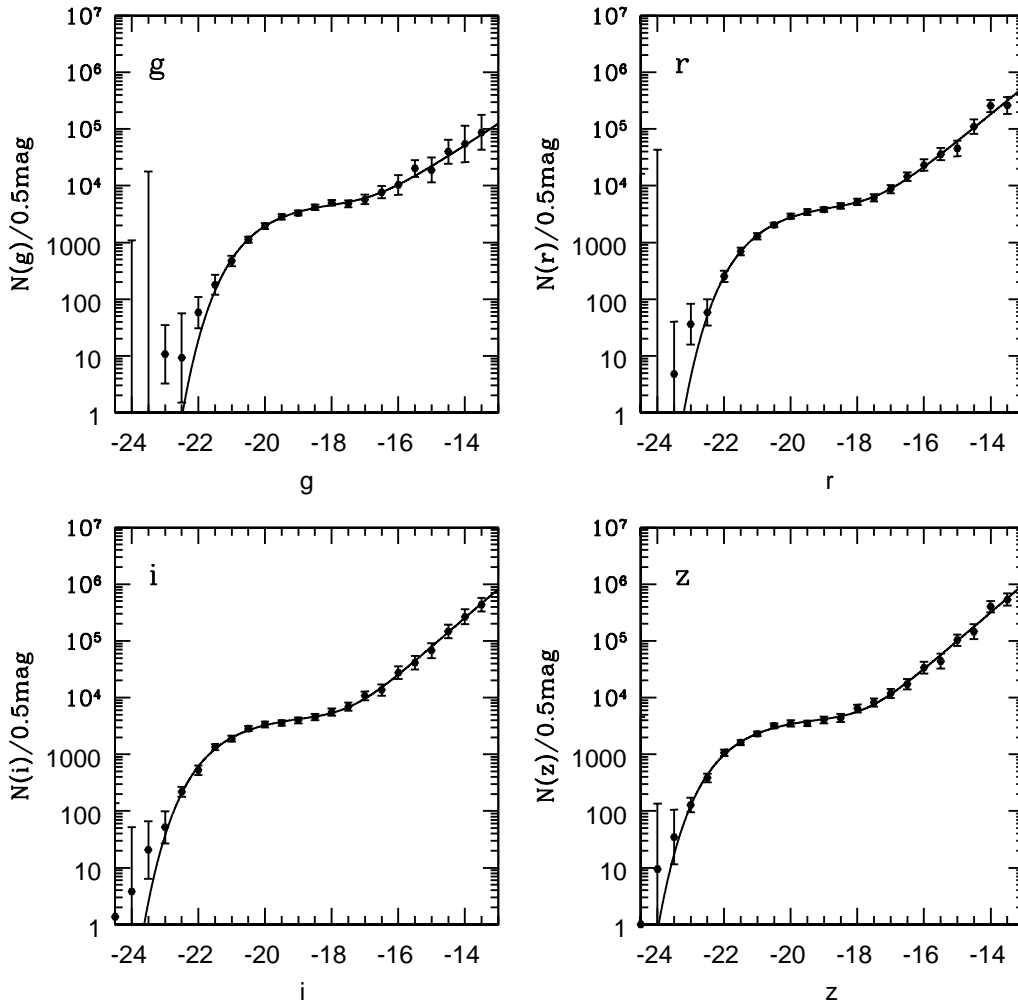


Figure 2.11: Luminosity function in the four SLOAN bands u, r, i, z computed within r_{200} . Dots: Observational data. Continuous line: Best fit (from Popesso et al. 2006a).

star formation by $z \sim 1$, the UV emission from modest sized field galaxies overwhelms that from the intrinsically red spectra of quiescent, early type galaxies preferentially found in clusters. The Red Sequence Cluster Survey (Gladders & Yee, 2000, 2005) uses the observed colour-magnitude relationship in cluster galaxies to improve the contrast and has proven highly efficient to $z \sim 1$, but the optical colours of the red sequence become increasingly degenerate at higher redshifts, as they no longer span the rest 4000\AA break. Wilson et al. (2008) describe a program to extend the red sequence technique to higher redshift using Spitzer data, but it is also important to *test* for the existence of red sequences in $z > 1$ clusters

rather than preselecting for them, if possible. Another powerful approach is to target for IR followup extended sources in deep X-ray surveys lacking prominent optical counterparts. This technique yielded confirmed clusters at $z = 1.10, 1.23,$ and 1.26 (Stanford et al., 2002; Rosati et al., 1999, 2004) and more recently at $z = 1.39$ (Mullis et al., 2005) and 1.45 (Stanford et al., 2006). The UKIDSS Ultra Deep Survey provides another recent example, finding 13 cluster candidates with $0.6 < z < 1.4$ in a 0.5 deg^2 survey (van Breukelen et al., 2006), one of which has 4 spectroscopic redshifts at $z = 0.93$ (Yamada et al., 2005). Eisenhardt et al. (2008a) identified 335 galaxy cluster and group candidates from a $4.5\mu\text{m}$ selected sample of galaxies in the IRAC Shallow Survey. Candidates were identified by searching for over-densities in photometric redshift slices, and 106 clusters are at $z > 1$. They claimed that roughly 10% of these candidates may be expected to arise by chance or from projection effects. Nevertheless, 12 clusters have been spectroscopically confirmed at $z > 1$, as have 61 of the 73 clusters observed with AGES at $z < 0.5$. For the two $z > 1$ clusters with 20 or more spectroscopic members, they have estimated total cluster masses of several $10^{14}M_{\odot}$, and the total mass estimated from the stellar luminosity yields comparable values. They also found colour-magnitude diagrams in $I - [3.6]$ vs. $[3.6]$ for the $z > 1$ spectroscopically confirmed clusters, revealing that a red sequence is generally present, even though clusters were not selected for this (see also Zirm et al. 2008). Moreover they found that for the full cluster sample, the mean colour of brighter galaxies within each cluster is systematically redder than the mean colour of all probable cluster member galaxies, implying that the mass-metallicity relation is already in place at $z \sim 1.5$. We report as example in Figure 2.12 by Eisenhardt et al. (2008) the cluster ISCS J1438.1+3414 at $\langle z_{\text{sp}} \rangle = 1.413$. It clearly exhibits a large concentration of red galaxies in the region. Both photometric redshift members and spectroscopically confirmed cluster members are shown in the picture. Presence of photometric redshift members which are not spectroscopically confirmed are also shown as blue diamonds.

Recently, Castellano et al. (2007) discovered a localised over-density at $z \sim 1.6$ in the GOODS-South Field. They compared the properties of the member galaxies to those of the surrounding field and they found that the two populations are significantly different, supporting the reality of the structure. Castellano et al. (2007) showed that the reddest galaxies, once evolved according to their best fit models, have colours consistent with the red sequence of lower redshift clusters. The estimated M_{200} total mass of the cluster they found is in the range $1.3 \times 10^{14} - 5.7 \times 10^{14} M_{\odot}$, depending on the assumed bias factor b . Castellano et al. (2007) provided also an upper limit for the 2-10 keV X-ray luminosity, based on the 1Ms Chandra observations. They found $L_X = 0.5 \cdot 10^{43} \text{ erg s}^{-1}$, suggesting that the cluster has not yet reached the virial equilibrium.

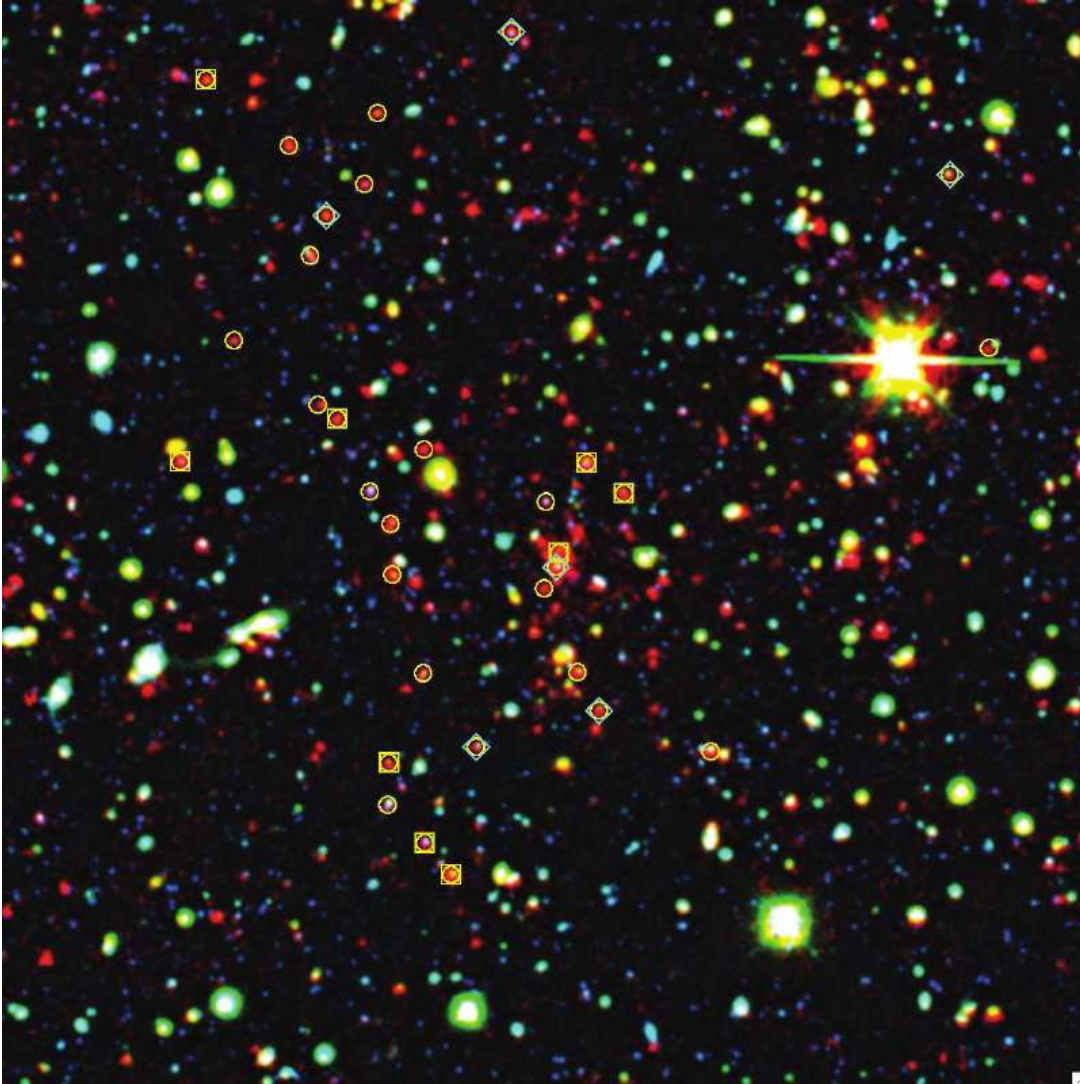


Figure 2.12: Composite NDWFS and *Spitzer* IRAC B_W , I , $[4.5]$ colour image of cluster ISCS J1438.1+3414 at $\langle z_{sp} \rangle = 1.413$. North is up and east is left, and the field size is $5'$ square ($\sim 2.4 - 2.5$ Mpc for $z = 1 - 1.5$). Objects with yellow circles are photometric redshift members, i.e., they have integrated $P(z) > 0 : 3$ in the range $z_{est} \pm 0.06(1 + z_{est})$, where z_{est} is the mean estimated photometric redshift for the cluster. Spectroscopically confirmed cluster members are denoted by yellow squares. Not all spectroscopic members fall within the $5'$ field shown here. Blue diamonds indicate photometric redshift members whose spectroscopic redshifts are not in the range $z_{sp} \pm 2000(1 + z_{sp}) \text{ km s}^{-1}$ (from Eisenhardt et al. 2008).

2.4 HIGH-REDSHIFT PROTO-CLUSTERS

We will now focus our attention on the observed properties of high redshift proto-clusters. As we discussed in previous Section, in recent years a number of observations has shed a light to the evolution of clusters with redshift up to $z \sim 1.5$ (e.g. Mullis et al. 2005, Eisenhardt et al. 2008b, Stanford et al. 2005 and references therein). A common technique for the search of over-dense regions to even higher redshift is to look for over-densities of emission line galaxies in the neighbourhood of luminous high-redshift radio galaxies (e.g. Pentericci et al. 1998). These regions likely trace proto-clusters and present merging and putative BCG assembly processes located at the peaks of the density fields, which are usually associated to the radio-galaxy. We will discuss here some observational results concerning the radio-galaxy MRC-1138-262 at redshift $z \sim 2$. This is probably the most studied putative proto-cluster region in literature (e.g. Pentericci et al. 1997, 1998, 1999, 2000; Carilli et al. 2002; Kurk et al. 2000, 2004; Miley et al. 2006; Venemans et al. 2007; Hatch et al. 2008; Zirm et al. 2008 and references therein). For a comprehensive discussion about distant radio galaxies and their environment we address the reader to the review by Miley & De Breuck (2008). In Chapter 5 we will present a detail comparison between these observations and the predictions of our cosmological hydro-dynamical simulations.

Figure 2.13 shows a deep image taken with the Advanced Camera for Surveys (ACS) of the *Hubble Space Telescope* (HST). The morphology of the galaxy distribution shown on this deep HST ACS image is reminiscent of what has been called a *Spiderweb*. More than 10 individual clumpy features are observed, apparently star-forming satellite galaxies in the process of merging with the progenitor of a dominant cluster galaxy, at a look-back time of about 11 Gyr. There is an extended emission component, implying that a high star formation rate was occurring within a 40 – 50 kpc region surrounding the most luminous galaxy. A striking feature of the Spiderweb complex is the presence of several faint linear galaxies within the merging structure. The dense environments and fast galaxy motions at the centers of proto-clusters may stimulate the formation of these structures, which dominate the faint resolved galaxy populations in the Hubble Ultra Deep Field. We address the attention's reader to the very high velocities associated to the satellite galaxies (the flies of the Spiderweb), reaching velocities along the line of sight of roughly 2000 km s^{-1} . Another important feature is the presence of an evident diffuse stellar component surrounding the disturbed morphology of the central radio galaxy.

In Fig. 2.14 by Hatch et al. (2008), an image of the region around the Spiderweb galaxy is shown in the g_{475} band. Galaxies were identified with the SEXTRACTOR algorithm (Bertin & Arnouts 1996) and are shown as white regions. This picture clearly exhibit the difficulties of deciding whether assigning pixels to galaxies or to the diffuse component. Hatch et al. (2008) examined the possibility that the intergalactic UV light may be caused by a fainter population of cluster galaxies that lie between the detected satellite galaxies.

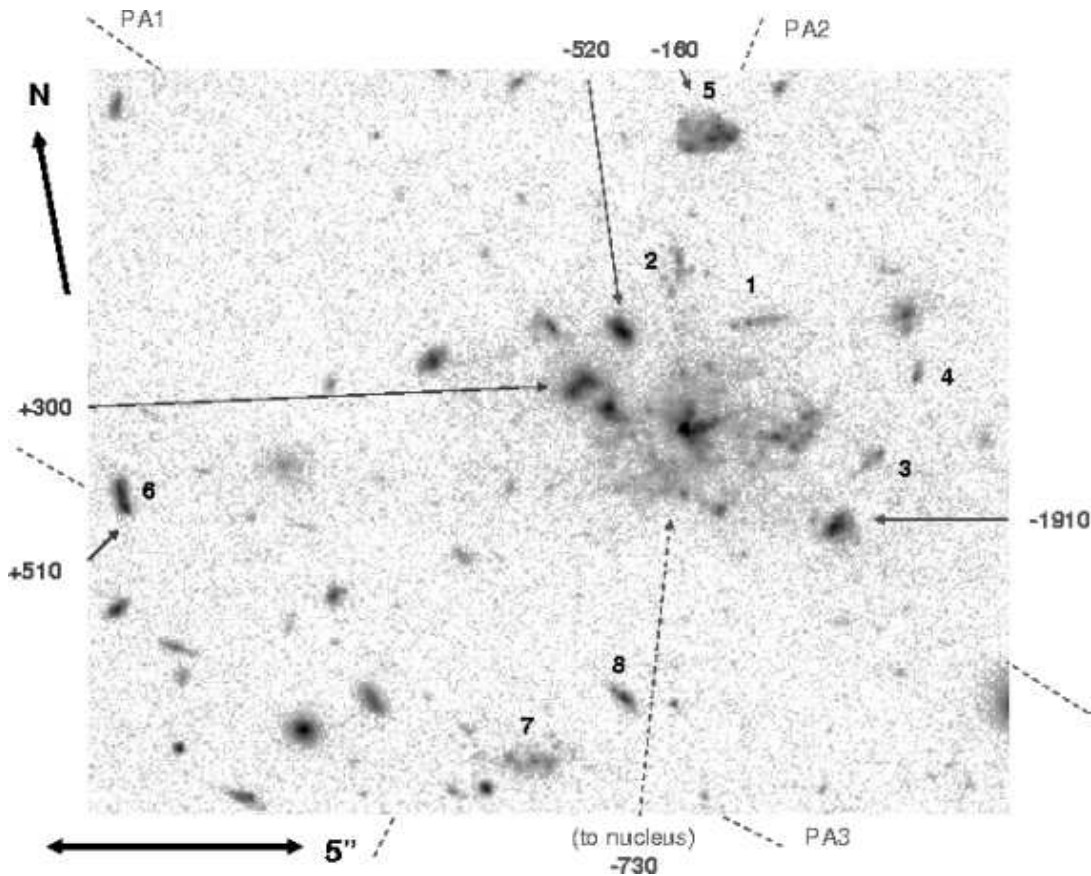


Figure 2.13: Composite image of a $23'' \times 18''$ region at the core of the MRC 1138-262 proto-cluster taken with the ACS through the $g_{475} + I_{814}$ filters, using a total of 19 orbits. Also shown are rest-frame Ly_{α} emission velocities in kilometres per second, measured through $1''$ wide spectrograph slits in three position angles indicated by the dashed lines. These were obtained using the FORS at the VLT Kurk et al. 2003). The velocities were measured at the peaks of the Ly_{α} emission profiles and are relative to the median velocity of Ly_{α} absorption. Following Kurk et al. (2003) the nucleus is taken to be the position of the peak Ha. This coincides with the peak in ACS continuum emission, indicated by the extrapolation of the arrow corresponding to 730 km s^{-1} , the velocity of the nuclear Ly_{α} emission. Eight of the satellite galaxies (flies) that have chain, tadpole, or clumpy morphologies are indicated by numerals 1-8 (from Miley et al. 2006)

Fig. 2.15 by Hatch et al. (2008)² plots the rest-frame NUV (I_{814} band) luminosity function of the detected galaxies with the solid line showing the best fitting Schechter function $\phi(M) = 0.4\phi^* \log_{10}[10^{0.4(M^*-M)}]^{-\alpha-1} \exp[-10^{0.4(M^*-M)}]$ (Schechter, 1976). The best fit-

²The luminosity function published by Hatch et al. (2008) did not include the correction factor $2.5 \times \log_{10}(1+z)$ (R.A. Overzier, private communication).

ting parameters were found to be $M^* = -24.3$, $\phi^* = 198.3 \text{ mag}^{-1} \text{ Mpc}^{-3}$ and the slope $\alpha = -1.26$. The slope of the faint end, α , is found to be similar to that of a sample of $z = 2.2$ galaxies from Sawicki & Thompson (2006). The bright M^* and large ϕ^* are a direct consequence of the fact that the region of interest is associated with a massive galaxy at the centre of a forming cluster, and should not be taken as a measure of the luminosity function beyond this region. The luminosity function is complete to -19.5 mag and encompasses almost all of the galaxies detected, therefore the integral of the Schechter function from -19.5 to -24.5 results in the total I_{814} flux from the galaxies in the Spiderweb complex. The intergalactic UV light in this bandpass accounts for 39% of the total flux above a surface brightness of $27.0 \text{ mag arcsec}^{-2}$. The authors argued therefore that if the IGL resulted from a population of fainter cluster galaxies, the missing galaxies would fill up the Schechter function up to -18.1 mag (indicated by the dotted line in Fig. 2.15). Therefore the IGL would comprise of approximately 15 galaxies with absolute magnitudes between -19.5 mag and -18.1 mag . The IGL extends across a region 4243 kpc^2 ($\sim 60 \text{ arcsec}^2$). Therefore each of the 15 faint galaxies would have to extend across $\sim 4 \text{ arcsec}^2$ – larger than the massive radio galaxy, or be distributed in a very ordered arrangement around the radio galaxy. Hatch et al. (2008) claimed that such an ordered distribution is unlikely and any faint galaxies are not likely to have such a large extent, therefore the IGL cannot be caused by a non-detected faint cluster galaxy population, but rather it must be due to an intrinsically diffuse source or very many unresolved radiation sources. In a previous work, Pentericci et al. (1998) have estimated the total stellar mass of the central radio galaxy from the K band luminosity and found $M_* \sim 10^{12} M_\odot$.

Hatch et al. (2008) have also computed the UV slope β which measures the UV continuum through

$$\beta = \frac{0.4 \times (g_{475} - I_{814})}{\log \frac{\lambda_{475}}{\lambda_{814}}} - 2. \quad (2.22)$$

Figure 2.16 shows the resulting map of the UV slope β . Data has been binned in 2D so that each bin within a galaxy has a S/N greater than 10, and each bin outside a galaxy has a S/N of ~ 5 . Hatch et al. (2008) have found that for the majority of the intergalactic light component a value of $-2 < \beta < -1$, which implies a reddening value of $E(B - V) \sim 0.1 - 0.25$. They have also found a trend in the IGL to be bluer with the increasing distance from the nearest galaxies. They have therefore argued that a process of diffuse star formation was taking place in the Spiderweb region. They have computed a total SFR from the UV continuum in the whole region of $\sim 142 M_\odot \text{ yr}^{-1}$ without dust correction. When applying a minimum dust correction of $E(B - V) = 0.1$ they have put a lower limit on the total SFR of $\sim 325 M_\odot \text{ yr}^{-1}$, 44% of which is due to the IGL, implying a vigorous star formation, before it is quenched by AGN feedback.

Pentericci et al. (2000) performed VLT spectroscopic observations of Ly_α -excess objects in the field of the Spiderweb complex within a projected physical distance of 1.5 Mpc from the radio-galaxy. They found 14 galaxies and one QSO at approximately the same dis-

tance as the Spiderweb galaxy. All identified galaxies have redshifts in the range 2.16 ± 0.02 , centred around the redshift of the radio galaxy. The velocity distribution found by Pentericci et al. (2000) suggested that there are two galaxy subgroups having velocity dispersions of $\sim 500 \text{ km s}^{-1}$ and $\sim 300 \text{ km s}^{-1}$ and a relative velocity of 1800 km s^{-1} . They have estimated the dynamical masses in the case these structures are virialised, and found ~ 9 and $\sim 3 \times 10^{13} M_{\odot}$ respectively, implying a total mass for the structure of more than $10^{14} M_{\odot}$.

More recently, Kurk et al. (2004) have performed infrared spectroscopy and established the presence of nine line emitters within 0.6 Mpc of the radio-galaxy. They have found three emitters showing an additional line which confirms the identification with H_{α} at $z = 2.15$, while four more have spectra consistent with H_{α} at this redshift, one being a QSO as indicated by the broadness of its emission line. One emitter shows only a single strong line, which is possibly H_{α} and one emitter exhibits two lines which probably originate from two emission line regions within one galaxy at $z = 2.16$. Additional evidence for identification of all observed lines with H_{α} is the small velocity dispersion (360 km s^{-1}) as compared with the width of the selection filter. This dispersion is also smaller than the dispersion of the Ly_{α} emitters found by Pentericci et al. (2000).

Carilli et al. (2002) performed a high resolution X-ray observations of the Spiderweb galaxy with the ACIS-S detector on the Chandra observatory. They showed that the X-ray emission from the radio-galaxy is dominated by emission from the active galactic nucleus (AGN) with a 2 to 10 keV luminosity of $4 \times 10^{45} \text{ erg s}^{-1}$. Moreover they found that the relative X-ray and radio properties of the AGN in the Spiderweb galaxy are similar to those seen for the AGN in the archetype powerful radio galaxy Cygnus A. Carilli et al. (2002) estimated that between 10% and 25% of the X-ray emission from the Spiderweb complex is spatially extended on scales of $10''$ to $20''$. The extended X-ray emission is elongated, with a major axis aligned with that of the radio source. While the X-ray and radio emissions are elongated on similar scales and position angles, there is no one-to-one correspondence between the radio and X-ray features in the source. They concluded that most likely origin for the extended X-ray emission in the observed region is thermal emission from shocked gas, although they could not rule-out a contribution from inverse Compton emission. If the emission is from hot gas, the estimated gas density is 0.05 cm^{-3} and the estimated gas mass is $2.5 \times 10^{12} M_{\odot}$. Thus, pressure in this hot gas is adequate to confine the radio emitting plasma and the optical line emitting gas. Carilli et al. (2002) set an upper limit of $1.5 \times 10^{44} \text{ erg s}^{-1}$ to the (rest frame) 2 to 10 keV luminosity of any normal cluster atmosphere associated with the Spiderweb complex.

They did not detect any emission associated to any of the Ly_{α} emitting galaxies in the putative proto-cluster, outside of the Ly_{α} halo of the Spiderweb galaxy itself, to a (rest frame) 2 to 10 keV luminosity limit of $1.2 \times 10^{43} \text{ erg s}^{-1}$. Carilli et al. (2002) also detected emission from a $z = 2.183$ QSO located $2'$ west of the Spiderweb system, with a luminosity of $1.8 \times 10^{44} \text{ erg s}^{-1}$.

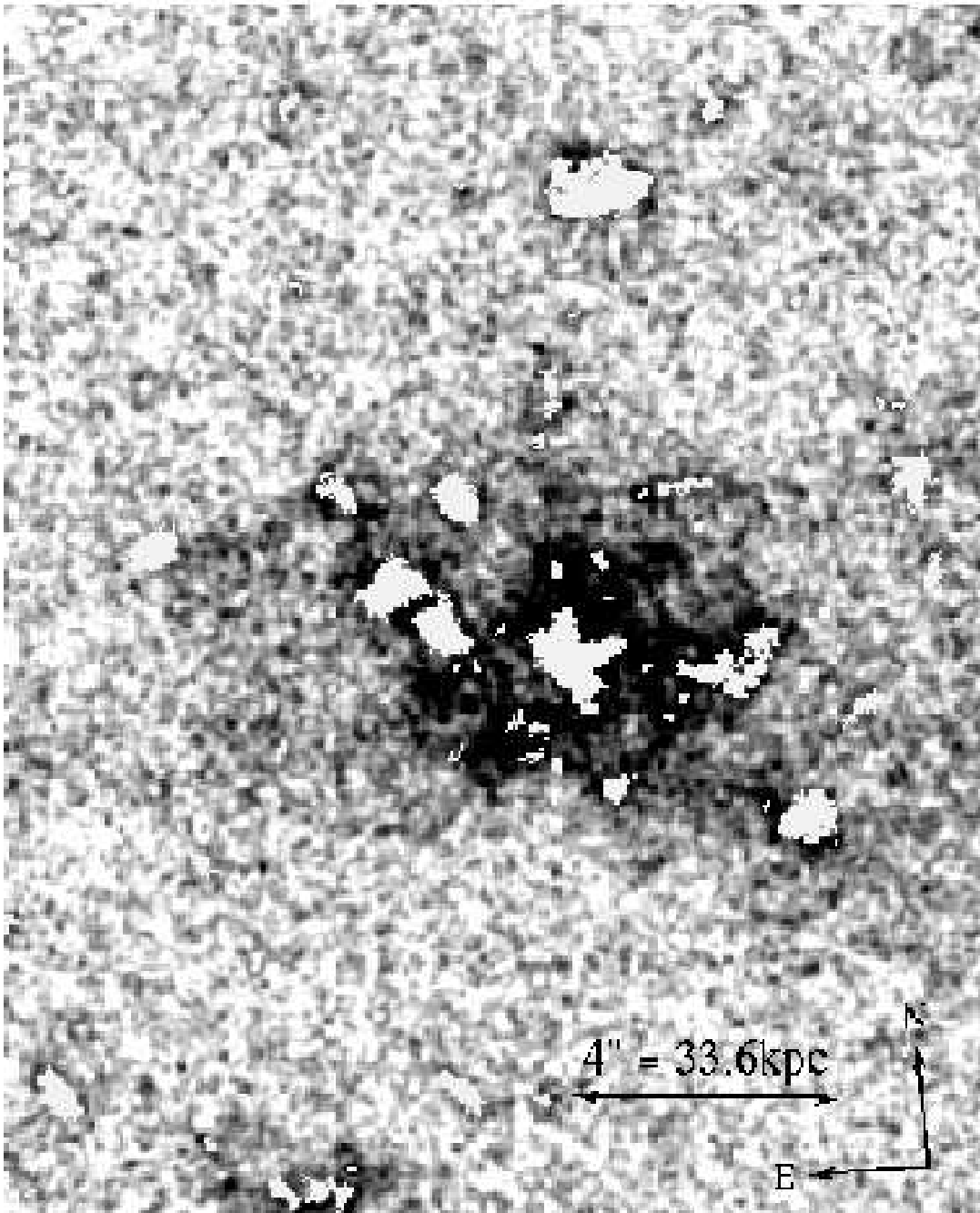


Figure 2.14: g_{475} image of MRC 1138-262 and surrounding 15×18.5 region, smoothed with a Gaussian of $s = 0.05$ arcsec. All regions identified as galaxies have been removed and are coloured white. The intergalactic light is clearly visible between the radio and satellite galaxies (from Hatch et al. 2008).

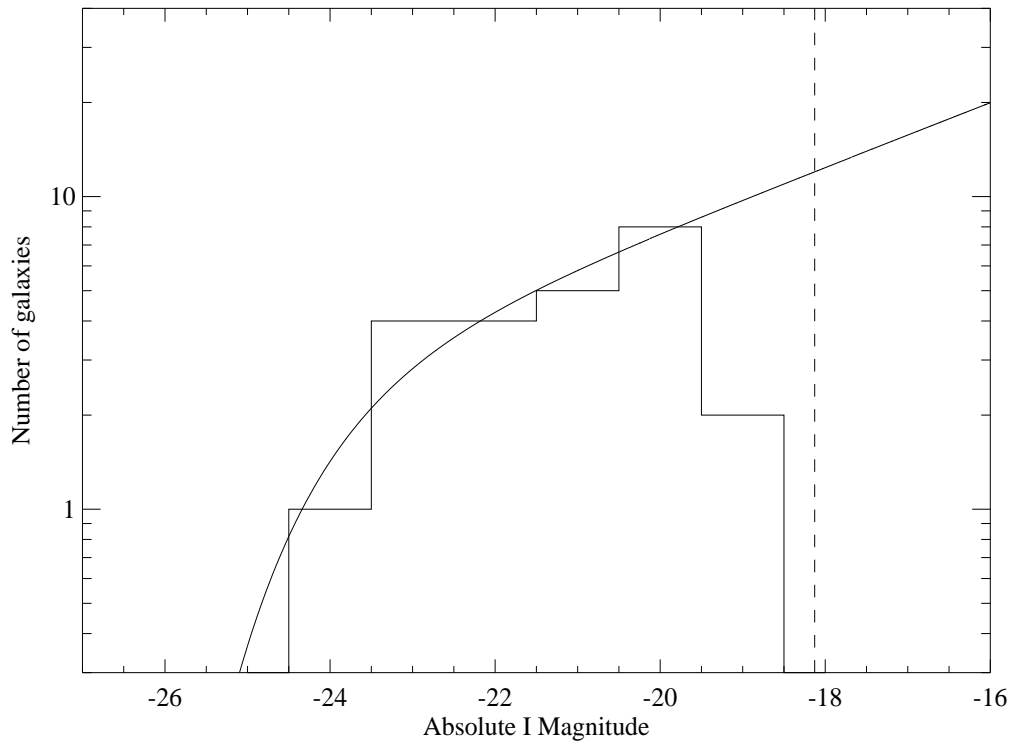


Figure 2.15: The luminosity function of the galaxies within the Spiderweb complex. The solid line is a Schechter function fit to the data. The dotted line indicates how much of the luminosity function is missing if the intergalactic light results from a population of fainter galaxies; approximately 15 galaxies with absolute I_{814} magnitude (rest frame NUV) between $19.5 < \text{mag} < 18.1$ would provide the necessary light (from Hatch et al. 2008).

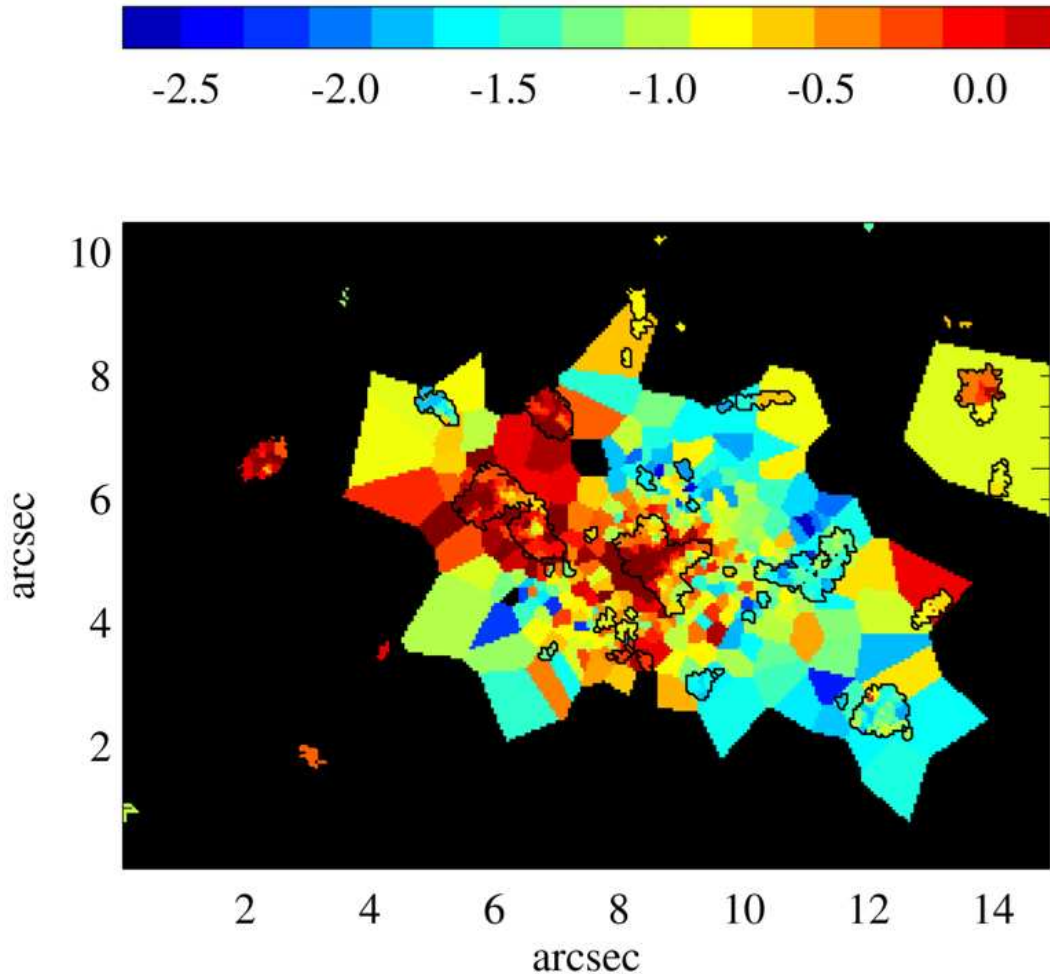


Figure 2.16: Slope β of UV spectrum of galaxies and intergalactic light of the Spiderweb system. Data has been binned in 2D as described in the text. Galaxies are outlined in black. The L_{y_α} flux peaks on the galaxy that lies ~ 3 arcsec West of the radio galaxy which has the bluest colour compared to the other satellite galaxies. Image is rotated 5 degrees East from North, with North Up and East left (from Hatch et al. 2008).

CHAPTER 3

NUMERICAL COSMOLOGY AND GALAXY FORMATION

In this Chapter we will present an overview of the numerical techniques developed for cosmological purposes. We address the reader to more comprehensive reviews for a detailed treatment of the topics discussed in next Sections (e.g. Hockney & Eastwood 1988; Bagla 2005; Dolag et al. 2008b).

This Chapter is structured as follow. Section 3.1 we will provide an overview of the numerical methods that have been developed for solving the N-body problem, with particular emphasis to the TREE algorithm implemented in the GADGET-2 code¹ (Springel et al., 2001; Springel, 2005). In Section 3.2 we will describe picture the technique aimed at generating the initial conditions (ICs) used in our cosmological simulations. In Section 3.3 we will present hydrodynamical methods which are used to follow cosmic structure formation. In particular, we will focus on the SPH algorithm implemented in the GADGET-2 code (Springel et al., 2001; Springel, 2005) applied to obtain the results of the following Chapters. In Section 3.4 we will shortly describe the main characteristics and features of the GADGET-2 code. In Section 3.5 we will present the basic principles of spectro-photometric codes, with particular emphasis on the GALAXEV code by Bruzual & Charlot (2003). We will then present two algorithms [SKID² by Stadel 2001 and SUBFIND by Springel et al. 2001] for the identification of gravitationally bound substructures in cosmological hydrodynamical simulations in Section 3.6. Finally, in Section 3.7, we will briefly review about a widely used technique in galaxy formation's models complementary to direct hydrodynamical cosmological simulations: the semi-analytic approach.

¹<http://www.MPA-Garching.MPG.DE/gadget/>

²See <http://www-hpcc.astro.washington.edu/tools/skid.html>

3.1 GRAVITATIONAL DYNAMICS: THE N-BODY TREE CODE

The study of the N-body problem was topic of interest since already the XVIII century. It consists in finding the solutions of the equation of motion for a number N of point-like particles with mass m_i whose dynamics is purely gravitational. From the Keplerian theory it is possible to show that an analytical solution to this problem exists for $N = 2$. Already Poincaré (1891) highlighted that for $N \geq 3$ it does not exist a general analytical solution to the N-body problem, and the only way to face the problem is numerically. N-body numerical simulations were used for the first time in the sixties for the study of cosmic structure formation. They become a fundamental part of the study of cosmology only in the eighties, thanks to the development of fast computers and efficient computing algorithms. Now, a large part of our knowledge on the formation and evolution of cosmic structures is based on the results from numerical simulations. For reviews of this topics, see e.g. Hockney & Eastwood (1988); Bagla (2005); Dolag et al. (2008b).

A typical simulation which aims at describing a portion of the Universe and the gravitational evolution of the dark matter component uses a large number N of collisionless particles in a cubic box. This box, has to be sufficiently large to reach scales within which the Universe is nearly homogeneous. However, simulations are limited by the total number of particles, since the computational cost increases rapidly with it. Each simulation essentially represents a compromise between its mass resolution and its dimension, given the available computing resources.

Given the initial conditions (see Section below), one essentially needs to compute, for each particle, the resulting force due to the gravitational attraction of all the other particles. We first consider the simplest case of two particles i and j . The two particles attract each other with force:

$$\vec{F}_{ij} = \frac{Gm_i m_j (\vec{x}_i - \vec{x}_j)}{(|\vec{x}_i - \vec{x}_j|^2 + \epsilon^2)^{3/2}}, \quad (3.1)$$

where G is the gravitational constant, m_i and m_j are the masses of the particles, x_i and x_j are the coordinates of the particles and ϵ is the softening parameter. Since nothing prevents two particles to be very close, the gravitational force could in principle diverge, thus requiring an infinite accuracy in the integration of the orbits. To prevent this, the ϵ term is added to the denominator. This term essentially represents the spatial resolution of the particle dynamics. At each time-step it is necessary to compute the global gravitational force acting on each particle, due to the distribution of all the other particles. The simplest way to do so is to compute \vec{F}_{ij} for all pairs of particles. This method was adopted by early simulations and is called *Particle-Particle method (PP)*. It provides a very accurate estimate of the gravitational force, but its computational cost rapidly increases with the number of particles, since the number of operations required at each time-step is $N(N - 1)/2$. In order to treat more complex systems, it is necessary to reduce the number of operations.

3.1. Gravitational dynamics: the N-body TREE code

The solution adopted by a large part of N-body codes called *Particle-Mesh codes (PM)*, is to compute the large-scale gravitational field over a grid. In this case the Poisson's equation:

$$\vec{\nabla}^2 \Phi(\vec{x}, t) = 4\pi G a^2 [\rho(\vec{x}, t) - \bar{\rho}(t)], \quad (3.2)$$

where Φ is the gravitational potential and $\bar{\rho}(t)$ is the background density, is solved in the Fourier space. The computational cost is sensitively reduced ($O(N \log N)$, where N is the number of grid points), but the resolution is limited by the grid spacing. To solve this problem, modern versions of these codes supplement the force computation on scales below the mesh size with a direct summation. Codes implemented with this philosophy are called *Particle-Particle-Particle-Mesh codes (P³M)*. Another possibility is to place mesh refinements on highly clustered regions. These family of codes are thus called *Adaptive Mesh Refinements (AMR) codes*.

The TREE algorithm follows a completely different approach; the idea is to treat distant particles as one single particle by adopting a hierarchical partitioning system, which has been developed by Barnes & Hut (1986). The structure may be thought as an ideal tree. The smallest elements are cells containing one single particle, which can be thought as the leaves of the tree. These particle-bearing cells are grouped into larger cells, the nodes, which are in turn grouped into larger nodes down to the root, i.e. the whole simulation box. Each small and large cell will be characterised by the total mass and centre-of-mass of the particle(s) it contains. The construction of the tree follows a partitioning procedure, which is sketched in Fig. 3.1 for the case of a two-dimensional simulation.

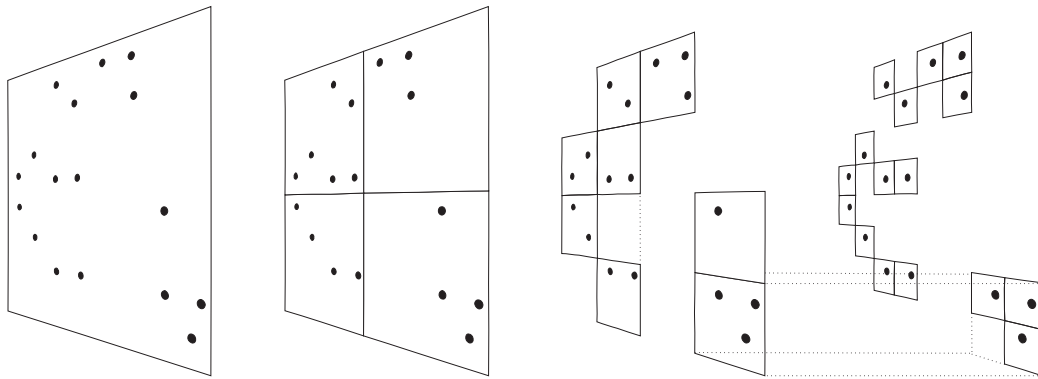


Figure 3.1: Schematic illustration of the TREE code scheme in two dimensions (Springel et al. 2001). The particles on the left are enclosed in a first level cell (main node) that is iteratively split into 4 squares (8 cubes for the three-dimensional case) until one particle remains (the leaf of the tree).

The process starts by considering the largest cell, which contains the whole simulation box. It is divided into 2^3 sub-cells, each having side equal to one half of the side of the parent cell. If a cell contains two or more particles, it is in turn divided into sub-cells and

the division process continues until each cell contains no more than one particle. When the partitioning process is finished, the space is divided into a number of cells of different size, which either contain exactly one particle or are progenitors to further cells, in which case each cell carries the monopole and quadrupole moments of all the particles that lie inside its volume. The force computation proceeds by an iterative process, which walks up the tree, summing the appropriate contribution from each node, which is determined by the accuracy parameter θ (typically $\theta \sim 1$) in the following way. Let l be the length of a cell and D the distance from the cells centre-of-mass and the particle. Then if $l/D < \theta$ the contribution of the cell content to the total force acting on the particle P is computed by treating it a single particle, otherwise its sub-cells are considered. This process is repeated iteratively until the resolution criterion is satisfied or a one-particle cell is reached. Recent numerical simulations achieved very high resolution within very large simulated volumes. For examples the so-called Millennium Run (Springel et al. 2005a) based on the GADGET-2 code traced more than 10 billion particles within a simulated cube box of $500 h^{-1}\text{Mpc}$. Figure 3.2 shows the complex topology of the “cosmic web” in a ΛCDM universe. The zoomed out panel at the bottom of the figure reveals a tight network of cold dark matter clusters and filaments of characteristic size $\sim 100 h^{-1}\text{Mpc}$. On larger scales, there is little discernible structure and the distribution appears homogeneous and isotropic. Subsequent images zoom in by factors of four onto the region surrounding one of the many rich galaxy clusters in the simulation. The final image reveals several hundred dark matter substructures, resolved as independent, gravitationally bound objects orbiting within the cluster halo. These substructures are the remnants of dark matter halos that fell into the cluster at earlier times.

More recently Kim et al. (2008) presented The Horizon Run N-body simulation, using $4120^3 \simeq 69.9$ billion particles, and covering a volume of $(6.592 h^{-1}\text{Gpc})^3$ which corner-to-corner stretches all the way to the horizon of the visible Universe. Figure 3.3 shows a $64h^{-1}\text{Mpc}$ -thick slice through the Horizon simulation showing the matter density field in the past light cone all the way to horizon. The thickness of the wedge is constant and the opening angle is 45 degrees. The Earth (the observation point) is at the vertex and the upper boundary is the Big Bang surface at $z = \infty$. The distribution of the CDM particles is converted to a density field using the Triangular Shaped Cloud binning method (Hockney & Eastwood 1981), and the density field before $z = 23$ was obtained by linearly evolving the initial density field backward in time. The radial scale of the slice is the look-back time, so the upper edge corresponds to the age of the universe, 13.6 billion years located at the comoving distance of $500 h^{-1}\text{Mpc}$.

We just mention that on small scales, other two recent projects have tried to reproduce a Milky Way-sized dark matter halo with extremely high-resolution: The Aquarius Project (Springel et al. 2008) and the Via Lactea Projects (Diemand et al. 2008, and references therein). The first group have simulated 6 different halos, each at several different numerical resolutions, finding in the largest simulation, nearly 300,000 gravitationally bound sub-halos within the virialised region of the halo. The latest simulation of the Via Lactea Project took one million CPU hours to finish and has over one billion particles with a mass of only 4.1

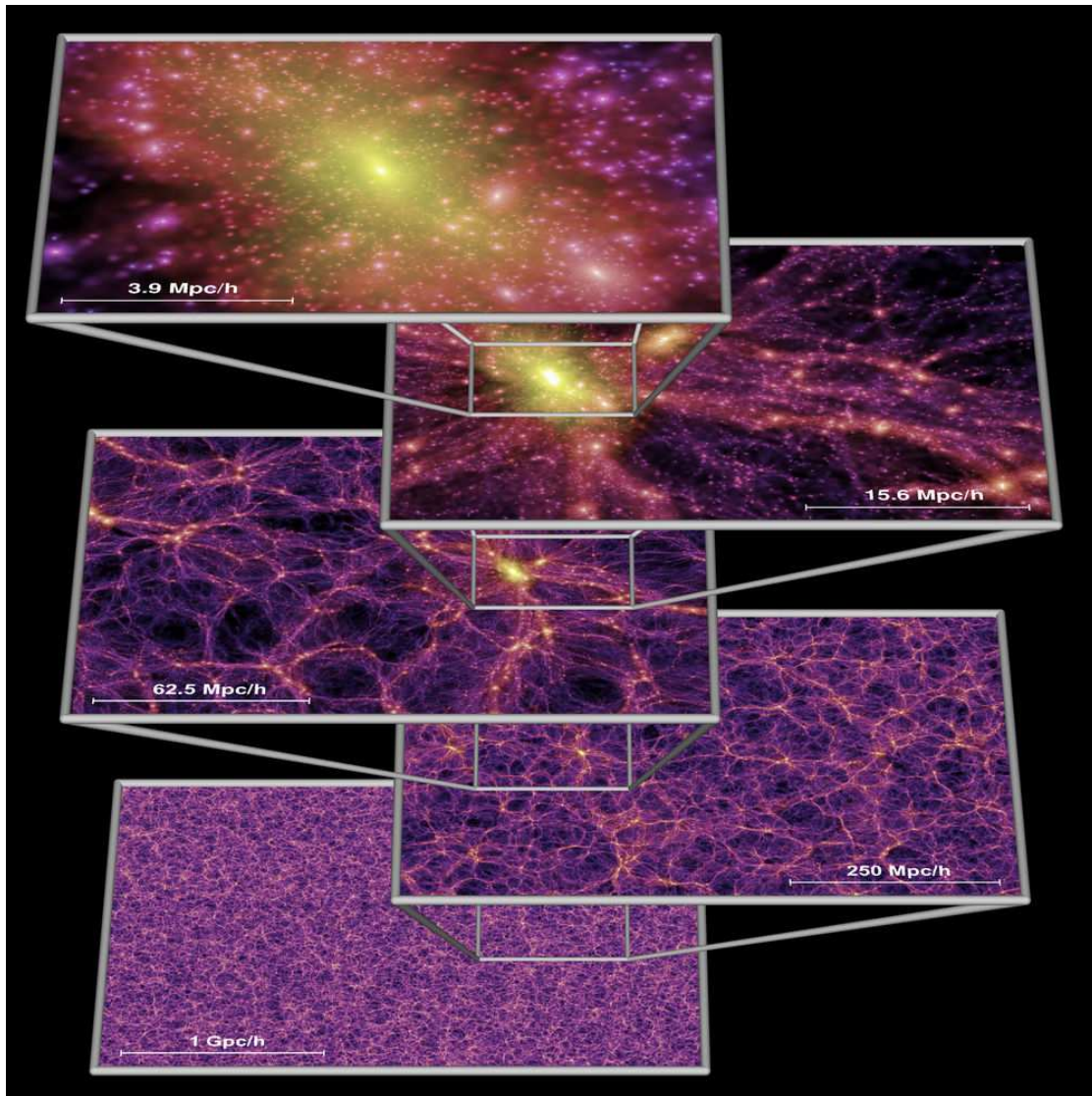


Figure 3.2: The dark matter density field on various scales from the Millennium simulation. Each individual image shows the projected dark matter density field in a slab of thickness $15 h^{-1}\text{Mpc}$ (sliced from the periodic simulation volume at an angle chosen to avoid replicating structures in the lower two images), colour-coded by density and local dark matter velocity dispersion. The zoom sequence displays consecutive enlargements by factors of four, centred on one of the many galaxy cluster halos present in the simulation (from Springel et al. 2005).

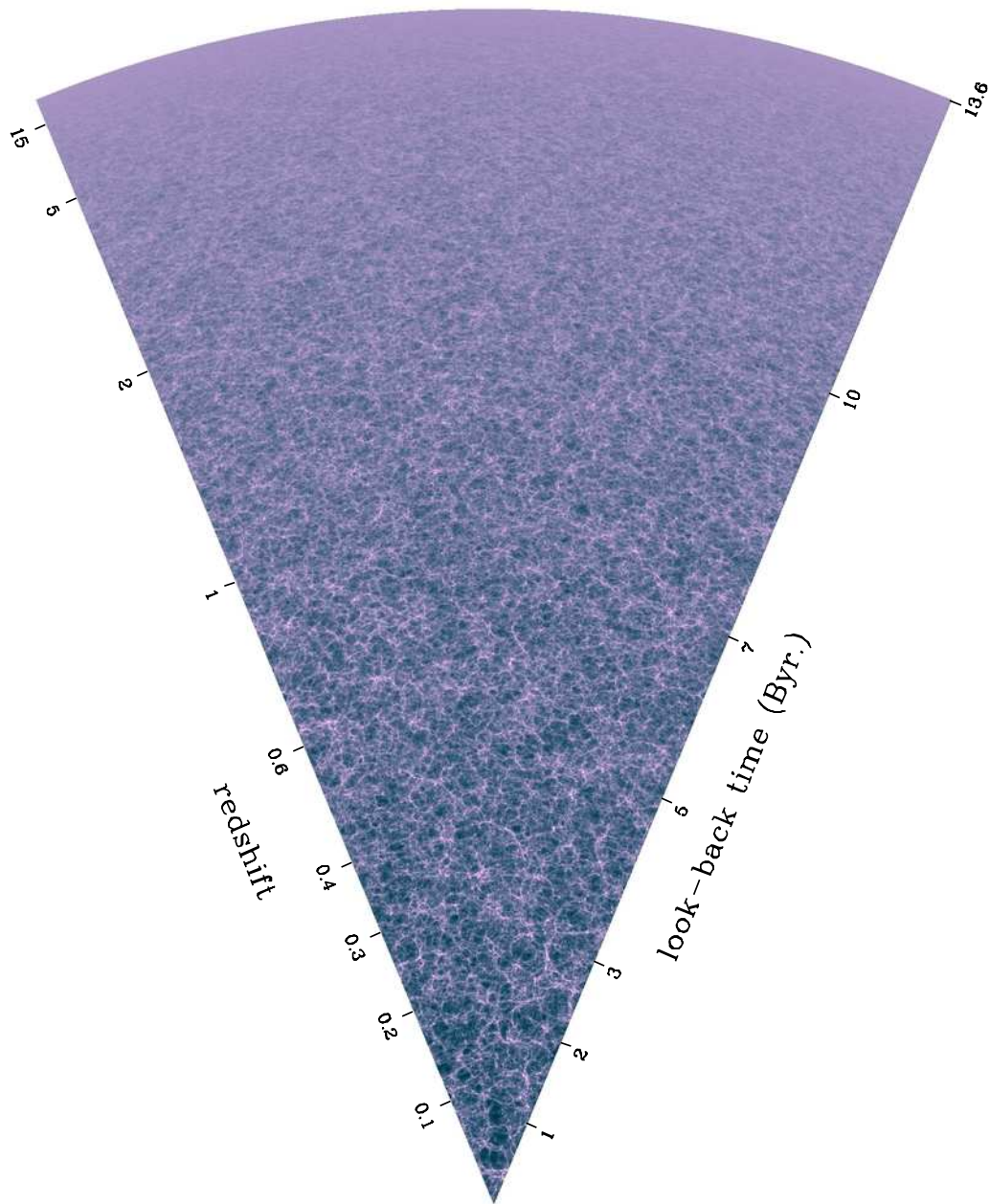


Figure 3.3: A $64h^{-1}$ Mpc-thick slice through this simulation showing the matter density field in the past light cone as a function of look-back time all the way to the horizon from the Horizon simulation. The thickness of the wedge is constant and the opening angle is 45 degrees. The Earth is at the vertex and the upper boundary is the Big Bang surface at a look-back time of 13.6 billion years (from Kim et al. 2008).

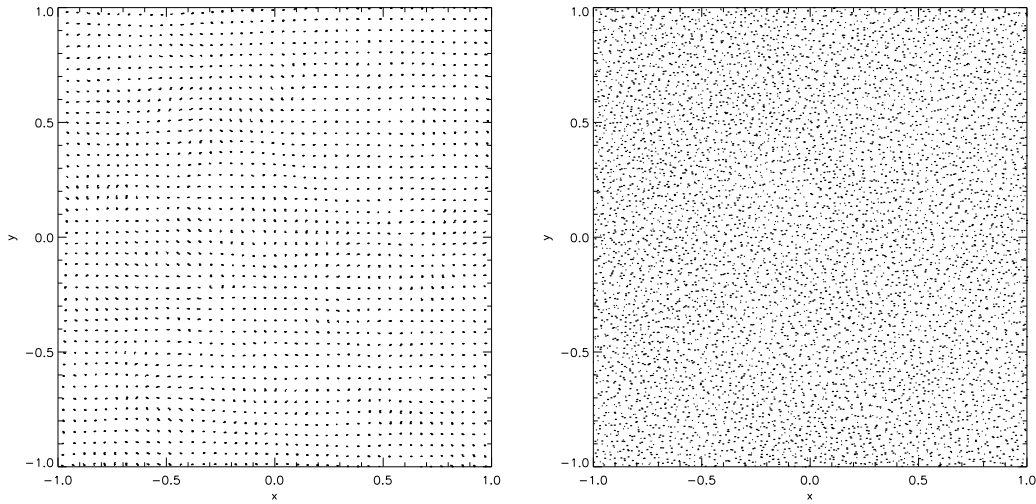


Figure 3.4: The particle distribution with the imposed displacements, taken from the same cosmological initial conditions, once based on an originally regular grid (left panel) and once based on a glass like particle distribution (right panel). Credits: Dolag et al. (2008).

thousand solar masses.

3.2

 INITIAL CONDITIONS

Having robust and well justified initial conditions is one of the key points of any numerical simulation. For cosmological purposes, observations of the large-scale distribution of galaxies and of the CMB agree to good precision with the theoretical expectation that the growth of structures starts from a Gaussian random field of initial density fluctuations (see also Appendix A.); this field is thus completely described by the power spectrum $P(|\vec{k}|)$ whose shape is theoretically well motivated and depends on the cosmological parameters and on the nature of Dark Matter.

To generate the initial conditions, one has to generate a set of complex numbers with a randomly distributed phase ϕ and with amplitude normally distributed with a variance given by the desired spectrum (e.g. Bardeen et al., 1986). This can be obtained by drawing two random numbers ϕ in $]0, 1[$ and A in $]0, 1[$ for every point in k -space

$$\hat{\delta}_{\vec{k}} = \sqrt{-2P(|\vec{k}|)\ln(A)}e^{i2\pi\phi}. \quad (3.3)$$

To obtain the perturbation field generated from this distribution, one needs to generate the

potential $\Phi(\vec{q})$ on a grid \vec{q} in real space via a Fourier transform, e.g.

$$\Phi(\vec{q}) = \sum_k \frac{\hat{\delta}_k}{k^2} e^{i\vec{k}\vec{q}}. \quad (3.4)$$

The subsequent application of the Zel'dovich approximation (Zel'Dovich, 1970) enables one to assign the initial positions

$$\vec{x} = \vec{q} - D^+(z)\Phi(\vec{q}) \quad (3.5)$$

and velocities

$$\vec{v} = \dot{D}^+(z)\vec{\nabla}\Phi(\vec{q}) \quad (3.6)$$

of the particles, where $D^+(z)$ and $\dot{D}^+(z)$ indicate the cosmological linear growth factor and its derivative at the initial redshift z (see Appendix A). A more detailed description can be found in e.g. Efstathiou et al. (1985).

There are two further complications which should be mentioned. The first is that one can try to reduce the discreteness effect that is induced on the density power spectrum by the regularity of the underlying grid of the particle positions \vec{q} that one has at the start. This can be done by constructing an amorphous, fully relaxed particle distribution to be used, instead of a regular grid. Such a particle distribution can be constructed by applying negative gravity to a system and evolving it for a long time, including a damping of the velocities, until it reaches a relaxed state, as suggested by White (1996). Fig. (3.4) gives a visual impression on the resulting particle distributions.

A second complication is that, even for studying individual objects like galaxy clusters, large-scale tidal forces can be important. A common approach used to deal with this problem is the so-called ‘‘zoom’’ technique: a high resolution region is self-consistently embedded in a larger scale cosmological volume at low resolution (see e.g. Tormen et al., 1997). This approach usually allows an increase of the dynamical range of one to two orders of magnitude while keeping the full cosmological context. For galaxy simulations it is even possible to apply this technique on several levels of refinements to further improve the dynamical range of the simulation (e.g. Stoehr et al., 2003).

3.3 HYDRODYNAMICAL METHODS: THE SMOOTHED PARTICLE HYDRODYNAMICS (SPH) TECHNIQUE

With all the methods described in the previous Sections, it is possible to find numerical solutions to the N-body gravitational problem. Nevertheless, baryonic matter has a much more complicated physics and behaviour. Therefore to have a complete and coherent description of cosmology, we need to implement models which describe the behaviour of gas and stars, besides the dark matter. Related to the physical processes of the baryonic component are the majority of all the astrophysical observable.

Thus, our models should be able to treat:

3.3. Hydrodynamical methods: The Smoothed Particle Hydrodynamics (SPH) technique

- Thermodynamics
- Radiative processes and absorption
- Influence of star formation
- Feedback effect, metal enrichment from stellar population and Active Galactic Nuclei (AGN).

The basic ingredient of these models is fluidodynamics, therefore numerical methods with the aim of describe these processes are called hydrodynamical methods.

The description of hydrodynamical processes through numerical methods can be basically classified in two general categories (see Dolag et al. 2008 for a more comprehensive description of the topics treated in this Section):

- **Eulerian techniques**

In Eulerian techniques the evolution of the physical quantities is followed at fixed spatial points. From a practical point of view, space is subdivided into a grid of points (fixed or adaptive) and in each resulting cell the evolution of variables associated to the physical quantities of interest is followed in time.

- **Lagrangian techniques**

In Lagrangian techniques instead physical quantities are associated to each particle representing the fluid element and their evolution is followed as a function of time and space along the particles trajectory. These techniques, therefore, need a discretisation of the fluid in particles, which generally will occupy different positions at different times. To each particle will be then associated the physical quantities of interest.

We will focus the rest of this Section on the description of a Lagrangian technique to solve hydrodynamics called Smoothed Particle Hydrodynamics (SPH), originally introduced by Lucy (1977) and Gingold & Monaghan (1977) (for recent reviews, see Springel 2005; Monaghan 2006). The simulations analysed in this Thesis are indeed based on the SPH technique. SPH avoids the main limitation due to the use of a grid on the dynamic range in spatial resolution or on the global geometry. Its main limitations are the treatment of the shocks, which is done by introducing an artificial viscosity, and the fact that it is not possible to represent an arbitrarily large density gradient with a finite number of particles. The SPH is particularly well suited to be used in association with a TREE N-body code, since their underlying principles are similar. Both techniques are fully Lagrangian and neither use a grid. The resulting code naturally allows to follow the evolution of a large number of particles within a Lagrangian framework (Hernquist & Katz 1989). In the SPH, the fluid is modelled as composed by a number of elements which are represented by particles. Thus, if the system is

evolved according to the laws of hydrodynamics, the density field ρ can be estimated from the local density of particles. Since the computational model consists of a finite number of fluid elements, local averages must be performed over volumes of nonzero extent. This is conveniently accomplished by introducing a systematic procedure for smoothing out local statistical fluctuations in the particle number. The mean value of a physical field, $f(\vec{r})$, within a given interval can be determined through kernel estimation according to

$$\langle f(\vec{r}) \rangle = \int W(|\vec{r} - \vec{r}'|, h) f(\vec{r}') d^3\vec{r}'. \quad (3.7)$$

where $W(\vec{r})$ is known as the smoothing kernel, h is the smoothing length, which specifies the extent of the averaging volume, and the integration is over all space. The smoothing kernel is normalised to unity. It is also required that $\langle f(\vec{r}) \rangle \rightarrow f(\vec{r})$ for $h \rightarrow 0$. Within reasonable assumptions on the kernel function $W(\vec{r})$, Hernquist & Katz (1989) show that the error made in approximating $f(\vec{r})$ by its smoothed estimate $\langle f(\vec{r}) \rangle$ is $O(h^2)$. If the values of $f(\vec{r})$ are known only at a finite number of discrete points, distributed with number density $n(\vec{r}) = \sum_{j=1}^N \delta(\vec{r} - \vec{r}_j)$, then the smoothed equivalent can be written as (Hernquist & Katz 1989):

$$\langle f(\vec{r}) \rangle = \sum_{j=1}^N \frac{f(\vec{r}_j)}{\langle n(\vec{r}) \rangle} W(|\vec{r} - \vec{r}_j|, h). \quad (3.8)$$

In particular, if a mass m_j is associated with each fluid element of density ρ_j then:

$$\langle \rho(\vec{r}) \rangle = \sum_{j=1}^N m_j W(|\vec{r} - \vec{r}_j|, h). \quad (3.9)$$

In every time-step the SPH code must solve the fluid equations: the mass conservation is assured by the fact that the kernel function is normalised to unity ($\int W(\vec{r}) d\vec{r} = 1$), while in the adiabatic regime the Euler and the energy conservation equations become:

$$\left(\frac{d\vec{v}}{dt} \right) = - \sum_{j=1}^N m_j \left[\frac{P}{\rho^2} + \frac{P_j}{\rho_j^2} \right] \vec{\nabla} W(|\vec{r} - \vec{r}_j|, h) \quad (3.10)$$

and

$$\left(\frac{d\epsilon}{dt} \right) = \frac{P}{\rho^2} \sum_{j=1}^N m_j (\vec{v} - \vec{v}_j) \cdot \vec{\nabla} W(|\vec{r} - \vec{r}_j|, h). \quad (3.11)$$

respectively. The description of a non-conservative physical system can be implemented by modifying Eq. 3.11. For example a radiative gas is obtained by adding a cooling term. On the contrary the description of phenomena like shock-heating requires the addition of artificial viscosity terms in Eq. 3.10. An important advantage of the SPH formalism is that it provides a natural means for estimating gradients of the local fluid properties. Gradients

of the physical variables are replaced by derivatives of the smoothing kernel, thereby constraining $W(\vec{r})$ to be differentiable or at least the same order as that of the terms present in the dynamical equations. In addition, the kernel should be sharply peaked and approach a delta function as $h \rightarrow 0$, in order that the smoothing estimates retain a local character. A kernel with compact support is generally preferred for reasons of computational cost, so as to perform the integration over a finite portion of volume. The GADGET-2 code on which our simulations are based, adopts the following kernel:

$$W(r, h) = \frac{8}{\pi h^3} \begin{cases} 1 - 6(r/h)^2 + 6(r/h)^3 & 0 \leq r \leq h/2 \\ 2(1 - r/h)^3 & h/2 \leq r \leq h \\ 0 & r \geq h \end{cases} \quad (3.12)$$

where r is the distance from the particle position. Note that both the first and the second derivatives of the above kernel are continuous. The local spatial resolution is determined by the smoothing length h . A more traditional approach adopts the same h for all particles. However, a constant h would yield relatively more accurate estimates in regions with a high density of particles than in lower density regions. Furthermore, all the structures smaller than h would not be resolved, thus not taking full advantage of the adaptive Lagrangian nature of the SPH method. An adaptive h instead allows at the same time to achieve the necessary resolution in denser regions and to maintain the same level of accuracy at all points on the fluid, thus improving consistency and efficiency of the code. The value of h is then determined from the local particle density, by keeping the number of neighbourhoods either exactly, or at least roughly, constant.

3.4 THE GADGET-2 CODE

The simulations analysed for our work have been realised with the GADGET-2 code (Springel et al. 2001; Springel 2005). GADGET-2 (**G**alaxies with **D**ark matter and **G**as int**E**rac**T**) is a TREE-SPH algorithm with a fully adaptive step refinement integration scheme. It is also possible to choose between a full TREE algorithm or a combined PM -TREE algorithm for the gravitational treatment.

Figure 3.5 is an example of the evolution at redshift $z=9, 5$ and 0 of the gas density within a cosmological hydrodynamical simulation that has been realised with the GADGET-2 code within a cosmological box of $192 \text{ h}^{-1} \text{ Mpc}$ side and containing 2×480^3 DM and gas particles for a Λ CDM cosmology (Borgani et al. 2004). This sequence shows the hierarchical growth of structure along filaments and groups and clusters placed at the intersection of filaments.

We show in Figure 3.6 (Borgani & Kravtsov 2009) how the distributions of DM (upper panels), gas (central panels) and star (lower panels) evolve across cosmic time inside the region forming a cluster, as predicted by a cosmological hydrodynamical simulation based on the GADGET-2 code. The gas distribution generally traces the DM distribution, with its pressure support making it smoother below the Jeans length scale. Furthermore, stars form

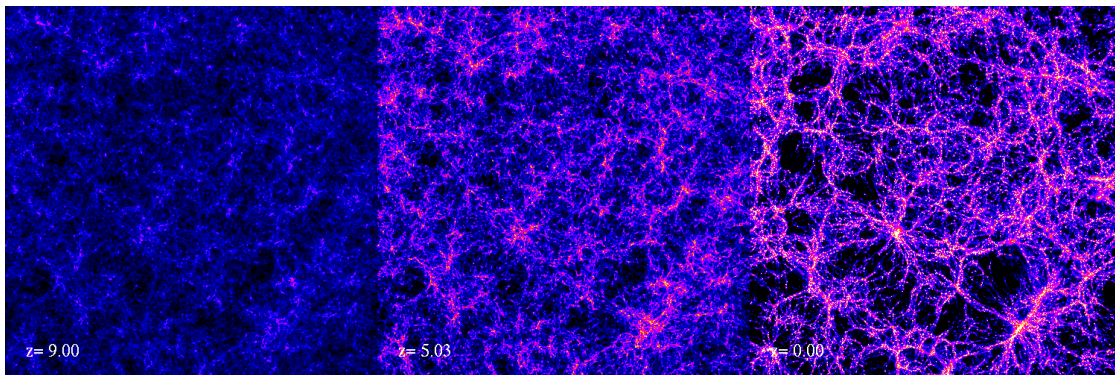


Figure 3.5: Evolution at $z = 9, 5$ and 0 of a TREE-SPH simulation realised with the GADGET-2 code for a Λ CDM within a cosmological box of $192 \text{ h}^{-1} \text{ Mpc}$ (from Borgani et al. 2004).

since early epochs within high density halos, where gas can efficiently cool over a short time scale, thus making their distribution quite clumpy. These density maps highlight the hierarchical fashion in which the formation of cosmic structures proceeds. At early epochs a large number of small DM halos are already in place and their distribution traces the nodes of a complex filamentary structure, the so-called cosmic web. As time goes on, these filaments keep accreting matter, while small halos flows along them, finally merging onto larger halos, placed at the intersection of filaments, where galaxy clusters form (see also Chapter 5). By the present time (left panels) a rather massive galaxy cluster has formed at the intersection of quite large filamentary structures.

More in detail the following astrophysical processes were implemented in the SPH scheme of the GADGET-2 code:

3.4.1. Radiative cooling

In a simple view, radiative cooling is computed assuming an optically thin gas of primordial composition (mass-fractions of $X = 0.76$ for hydrogen and $1 - X = 0.24$ for helium) in collisional ionisation equilibrium, following Katz et al. (1996). The code also includes a photo-ionising, time-dependent, uniform ultraviolet (UV) background expected from a population of quasars (e.g. Haardt & Madau 1996), which reionises the Universe at $z \simeq 6$. The effect of a photo-ionising background is that of inhibiting gas collapse and subsequent star formation within the haloes of sub- L_* galaxies (e.g. Benson et al. 2002), thus having a secondary impact at the resolution of our simulations. Additionally, one should take into account the effect of metal species. The presence of metals will drastically increase the possible processes by which the gas can cool. As it becomes computationally very demanding to calculate the cooling function in this case, one usually resorts to a pre-computed, tabu-

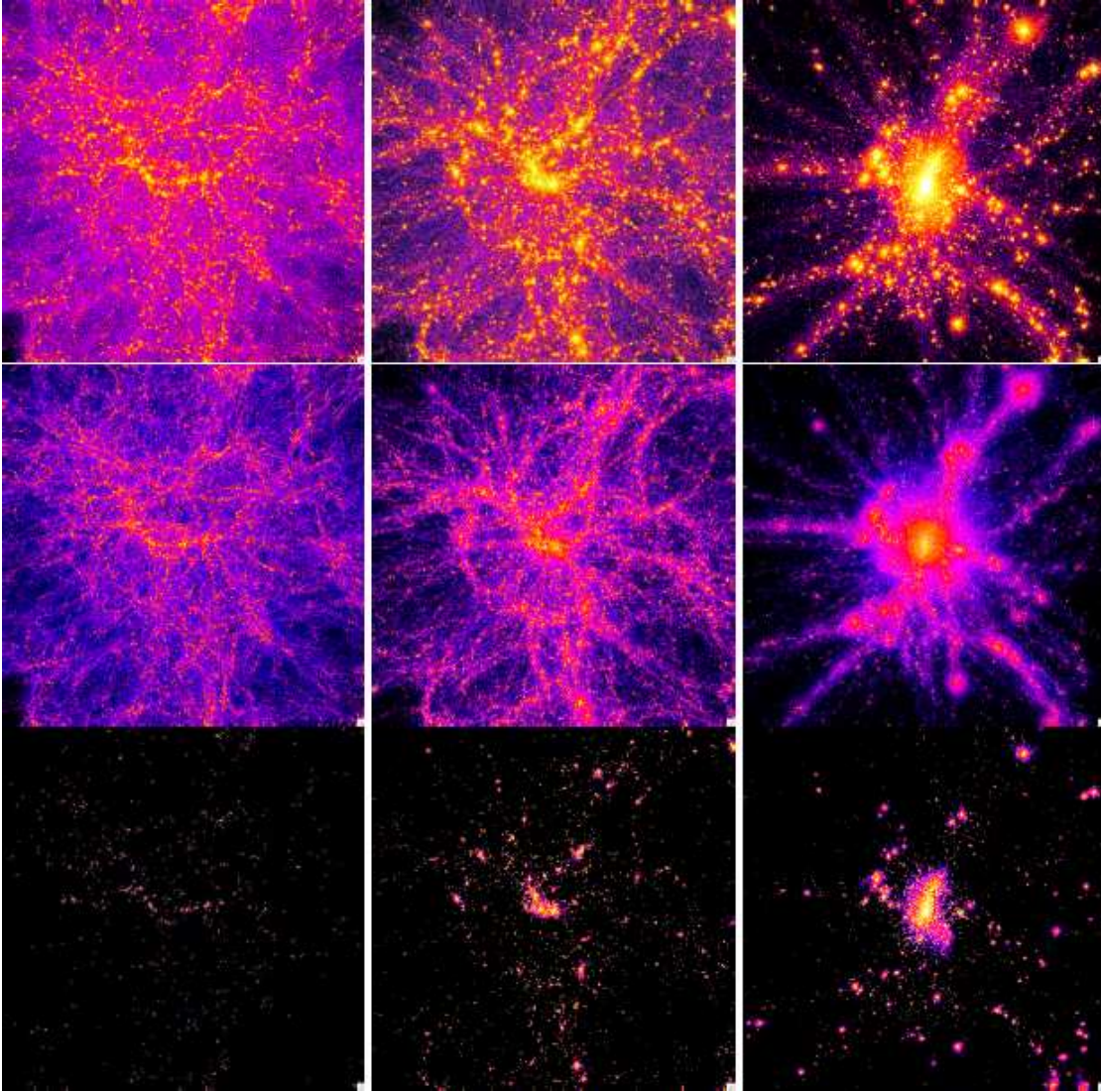


Figure 3.6: The formation of a galaxy cluster in a cosmological context, as described by a hydrodynamical simulation carried out with the Tree-SPH GADGET-2 code Springel (2005). Upper, central and bottom panels refer to the density maps of dark matter, gas and star distributions, respectively. From left to right we show the snapshots at $z = 4$, where putative proto-cluster regions are traced by the observed concentrations of Lyman-break galaxies and Lyman- α emitters Overzier et al. (2008), at $z = 2$, where highly star-forming radio-galaxies should trace the early stage of cluster formation Miley et al. (2006); Saro et al. (2009); see Chapter 5, and at $z = 0$. This cluster has a total virial mass $M_{vir} \simeq 10^{15} h^{-1} M_{\odot}$ at $z = 0$ (Dolag et al. 2008). Each panel covers a comoving scale of about $24 h^{-1} \text{Mpc}$, while the cluster virialised region at $z = 0$ is nearly spherical with a radius of about $3 h^{-1} \text{Mpc}$ (from Borgani & Kravtsov 2009, in preparation).

lated cooling function. Note that almost all implementations solve the cooling of the gas as a “sub time step” problem, decoupled from the hydrodynamical treatment. In practice this means that one assumes that the density is fixed across the time step. Furthermore, the time step of the underlying hydrodynamical simulation are in general, for practical reasons, not controlled by or related to the cooling time-scale. The resulting uncertainties introduced by these approximations have not yet been deeply explored and clearly leave room for future investigations. For the formation of the first objects in haloes with virial temperatures below 10^4 K, the assumption of ionisation equilibrium no longer holds. In this case, one has to follow the non-equilibrium reactions, solving the balance equations for the individual levels of each species during the cosmological evolution. In the absence of metals, the main coolants are H_2 and H_2^+ molecules (see Abel et al., 1997). HD molecules can also play a significant role. When metals are present, many more reactions are available and some of these can contribute significantly to the cooling function below 10^4 K. For more details see Galli & Palla (1998), Maio et al. (2007), Tornatore et al. (2007a) and references therein.

3.4.2. Star formation

Star formation is treated using the hybrid multiphase model for the interstellar medium introduced by Springel & Hernquist (2003a). We refer to this paper for a detailed description of the method, providing here only a short summary of the model. The ISM is pictured as a two-phase fluid consisting of cold clouds that are embedded at pressure equilibrium in an ambient hot medium. The clouds form from the cooling of high-density gas, and represent the reservoir of baryons available for star formation. For a gas particle to be eligible to form stars, it must have a convergent flow, and have density in excess of some threshold value, e.g.

$$\rho_i > 0.1 \text{ atoms cm}^{-3}. \quad (3.13)$$

These criteria are complemented by requiring the gas to be Jeans unstable, that is

$$\frac{h_i}{c_i} > \frac{1}{\sqrt{4\pi G \rho_i}}, \quad (3.14)$$

where h_i is either the *SPH* smoothing length and c_i is the local sound speed. This indicates that the individual resolution element gets gravitationally unstable. At high redshift, the physical density can easily exceed the threshold given in Eq. 3.13, even for particles not belonging to virialised halos. Therefore one usually applies a further condition on the gas over-density,

$$\frac{\rho_i}{\rho_{\text{mean}}} > 55.7, \quad (3.15)$$

which restricts star formation to collapsed, virialised regions. Note that the density criterion is the most important one. Particles fulfilling it in almost all cases also fulfil the other two criteria.

Once a gas particle is eligible to form stars, its star formation rate can be written as

$$\frac{d\rho_*}{dt} = -\frac{d\rho_i}{dt} = \frac{c_*\rho_i}{t_*}, \quad (3.16)$$

where c_* is a dimensionless star formation rate parameter and t_* the characteristic timescale for star formation. The value of this timescale is usually taken to be the maximum of the dynamical time $t_{\text{dyn}} = (4\pi G\rho_i)^{-0.5}$ and the cooling time $t_{\text{cool}} = u_i/(du_i/dt)$. In principle, to follow star formation, one would like to produce continuously collisionless star particles. However, for computational and numerical reasons, one approximates this process by waiting for a significant fraction of the gas particle mass to have formed stars according to the above rate; when this is accomplished, a new, collisionless “star” particle is created from the parent star-forming gas particle, whose mass is reduced accordingly. This process takes place until the gas particle is entirely transformed into stars. In order to avoid spurious numerical effects, which arise from the gravitational interaction of particles with widely differing masses, one usually restricts the number of star particles (so called *generations*) spawned by a gas particle to be relatively small, typically 2 – 3. Note that it is also common to restrict the described star-formation algorithm to only convert a gas particle into a star particle, which correspond to the choice of only one *generation*. In this case star and gas particles have always the same mass.

To get a more continuous distribution of star particle masses, the probability of forming a star can be written as

$$p = 1 - \exp\left(-c_*\frac{\Delta t}{t_*}\right) \quad (3.17)$$

and a random number is used to decide when to form a star particle.

According to this scheme of star formation, each star particle can be identified with a Simple Stellar Population (SSP), i.e. a coeval population of stars characterised by a given assumed initial mass function (IMF) and same metallicity. Further, assuming that all stars with masses larger than $8 M_\odot$ will end as type-II supernovae (SN II), one can calculate the total amount of energy (typically 10^{51} erg per supernova) that each star particle can release to the surrounding gas. Under the approximation that the typical lifetime of massive stars which explode as SN II does not exceed the typical time step of the simulation, this is done in the so-called “instantaneous recycling approximation”, with the feedback energy deposited in the surrounding gas in the same step. In addition, clouds in supernova remnants are evaporated. These effects establish a tightly self-regulated regime for star formation in the ISM.

3.4.3. The chemical evolution model

In this section we provide a basic description of the key ingredients required by a model of chemical evolution. For a more detailed description we refer to Tornatore et al. (2007a), Borgani et al. (2008) and Matteucci (2003).

As we described in the previous Section, each star particle must be treated as a simple stellar population (SSP), i.e. as an ensemble of coeval stars having the same initial metallicity. Every star particle carries all the physical information (e.g. birth time t_b , initial metallicity and mass) that is needed to calculate the evolution of the stellar populations that they represent, once the lifetime function, the IMF and the yields for SNe and intermediate and low mass stars (ILMS hereafter) have been specified. Therefore, we can compute for every star particle at any given time $t > t_b$ how many stars are dying as SN II and SN Ia, and how many stars undergo the AGB phase. An important parameter entering in the model of chemical evolution is the fraction A of stars, in the mass range $0.8\text{--}8 M_\odot$, belonging to binary systems which explodes as SN-Ia in the single-degenerate scenario (Greggio & Renzini 1983; Matteucci & Greggio 1986).

It is generally assumed that the stars having mass above $8 M_\odot$ at the end of the hydrostatic core burning undergo an electron capture process, leading to a core collapse. A large amount of energy can be transferred to the outer layers during this phase due to a substantial production of neutrinos that easily escape from the central core. Although theoretical work has not yet been able to reproduce a sufficient energy deposition, it is currently supposed that this process leads to an explosive ejection of the outer layers, giving rise to a SN II. We remind the reader that $8 M_\odot$ is a commonly adopted fiducial value, although the limiting mass for the onset of explosive evolution is still debated (e.g., Portinari et al. 1998).

A different ejection channel is provided by the SNIa that are believed to arise from thermonuclear explosions of white dwarfs (WD hereafter) in binary stellar systems as a consequence of the matter accretion from the companion (e.g., Nomoto & et al. 2000). However, there are still a number of uncertainties about the nature of both the WD and the companion and about the mass reached at the onset of the explosion (e.g., Matteucci & Recchi 2001, Yungelson & Livio 2000). Finally, a third way to eject heavy elements in the interstellar medium is the mass loss of ILMS by stellar winds.

In summary, the main ingredients that define a model of chemical evolution are the following: (a) the adopted lifetime function, (b) the adopted yields and (c) the IMF which fixes the number of stars of a given mass. We describe each of these ingredients in the following.

As for the mass-dependent lifetime function, different choices have been proposed in the literature, assuming them either to be independent of metallicity (Padovani & Matteucci 1993; Maeder & Meynet 1989; Chiappini et al. 1997), or by explicitly including the dependence on the metallicity (Raitieri et al. 1996; Portinari et al. 1998).

As for the stellar yields, they specify the amount of different metal species which are released during the evolution of a SSP. A number of different sets of yields have been proposed in the literature for the ILMS (Renzini & Voli 1981a; Marigo 2001) and for SN-Ia (Nomoto et al. 1997a; Iwamoto et al. 1999; Thielemann et al. 2003). As for SN-II, there are many proposed sets of metallicity-dependent yields (Woosley & Weaver 1995a; Portinari et al. 1998; Chieffi & Limongi 2004), which are based on different assumptions of the underlying model of stellar structure and evolution.

As for the initial mass function (IMF), $\Phi(m)$, it is defined as the number of stars of a

given mass per unit logarithmic mass interval. It directly determines the relative ratio between SN-II and SN-Ia and, therefore, the relative abundance of α -elements and Fe-peak elements. The shape of the IMF also determines how many long-living stars will form with respect to massive short-living stars. In turn, this ratio affects the amount of energy released by SNe and the present luminosity of galaxies, which is dominated by low mass stars, and the (metal) mass-locking in the stellar phase. As of today, no general consensus has been reached on whether the IMF at a given time is universal or strongly dependent on the environment, or whether it is time- dependent, i.e. whether local variations of the values of temperature, pressure and metallicity in star-forming regions affect the mass distribution of stars. The most famous and widely used single power-law IMF is the Salpeter one (Salpeter 1955), while Arimoto & Yoshii (1987) proposed a flatter IMF, which predicts a relatively larger number of massive stars. In general, IMFs providing a large number of massive stars are usually called top-heavy. More recently, different expressions of the IMF have been proposed in order to model a flattening in the low-mass regime that is currently favoured by a number of observations. Kroupa (2001) introduced a multi-slope IMF, while Chabrier (2003) proposed another expression, with a smoothly varying slope, which is quite similar to that one proposed by Kroupa. Theoretical arguments (Larson 1989) suggest that the present-day characteristic mass scale, where the IMF changes its slope, $\sim 1 M_{\odot}$ should have been larger in the past, so that the IMF at higher redshift was top-heavier than at present. While the shape of the IMF is determined by the local conditions of the inter-stellar medium, direct hydrodynamical simulations of star formation in molecular clouds are only now approaching the required resolution and sophistication level to make credible predictions on the IMF (Bonelli et al. 2006; Padoan et al. 2007).

Clearly, a delicate point in hydrodynamical simulations is deciding how metals are distributed to the gas surrounding the star particles. The physical mechanisms actually responsible for enriching the inter-stellar medium (ISM; e.g., stellar winds, blast waves from SN explosions, etc.) take place on scales which are generally well below the resolution of current cosmological simulations. For this reason, the usually adopted procedure is that of distributing metals according to the same kernel which is used for the computation of the hydrodynamical forces, a choice which is anyway quite arbitrary.

3.4.4. Feedback from galactic winds

If not counteracted by some sort of feedback process, cooling is well known to overproduce the amount of stars both in the average environment and in the group/cluster over-dense environment (e.g. Balogh et al. 2001; Borgani et al. 2004, and references therein). As discussed by Springel & Hernquist (2003a), their multiphase ISM model alone does, however, not fully resolve this problem, despite its ability to regulate the consumption of cold gas into stars within the ISM. This is because the cooling rates within haloes remain essentially unaffected in the model, i.e. the supply of gas to the dense star-forming ISM is largely un-

changed, while by construction the phases of the ISM remain coupled to each other, preventing baryons to leave the ISM (except for dynamical effects such as gas stripping in mergers). However, galactic outflows are observed and expected to play a key role in transporting energy and metals produced by the stellar population into the IGM/ICM. To account for them, Springel & Hernquist (2003a) suggested a phenomenological description of galactic winds as an extension of their model, which has been included in the simulation. According to their implementation, the wind velocity, v_w , scales with the fraction η of the SN-II feedback energy that contributes to the winds, as $v_w \propto \eta^{1/2}$ [see equation (28) in Springel & Hernquist 2003]. The total energy provided by SN-II is computed by assuming that they originate from stars with mass $> 8 M_\odot$ for a Salpeter (1955) initial mass function, with each SN releasing 10^{51} erg. For example, assuming $\eta = 0.5$ and 1, yield to $v_w \simeq 340$ and 480 km s^{-1} , respectively.

In summary, the version of GADGET-2 that has been used to realise the analysed cosmological simulations has the following characteristics:

- TREE algorithm for the computation of the gravitational forces;
- SPH algorithm for the computation of the hydrodynamical forces;
- Cooling processes with a UV background and star formation;
- A detailed treatment of stellar evolution and chemical enrichment;
- A phenomenological treatment of feedback based on galactic winds fed by supernovae explosions.

As a result, our simulations will predict a population of stellar particles. For each of them we will be able know its age, mass and a chemical composition. With the use of spectrophotometric codes we are therefore able to compute the resulting optical/near-IR luminosities of our star particles, within suitable chosen bands.

3.5 SPECTRO-PHOTOMETRIC CODES

In this section we will discuss the basic characteristics of spectro-photometric codes, in particular the GALAXEV code by Bruzual & Charlot (2003) which has been used to assign luminosities to our simulated galaxy population.

Integrated light from galaxies is a unique source of informations to understand the evolution of the Star Formation Rate (SFR) and the Initial Mass Function (IMF). Observable properties of galaxies such as magnitudes, colours, metallicities of stars and gas, intensity

of emission and absorption lines, will generally be a function of both galaxy's age and cosmological evolution. Thus, it is very important to disentangle these two effects. In this framework, synthetic stellar population models are a powerful tool to compute the separate contribution of intrinsic and apparent (due to cosmology) galaxy evolution.

In literature exists a number of different models of spectro-photometric evolution (e.g. Arimoto & Yoshii 1987b, Buzzoni 1989, Brocato et al. 1990, Bruzual A. & Charlot 1993, Bruzual & Charlot 2003). Each of these models has the following free-parameters:

- The Initial Mass Function (IMF) $\phi(m)$;
- The Star Formation Rate (SFR) $\psi(t)$;
- The evolution of metallicity $Z(t)$.

The basic ingredients of these models are the stellar evolutionary tracks and the spectral libraries, which can be both empirical or based on stellar atmosphere models. For a star of mass m and metallicity Z it is thus possible to compute the effective temperature $T_{eff}(m, Z, t)$ and luminosity $L(m, Z, t)$ at any given time t . We can therefore describe parametrically the evolution of every star in the Hertzsprung-Russel diagram both in the main sequence and post main sequence phases.

3.5.1. Basic principles

The fundamental brick in synthetic stellar population models is represented by the *simple stellar population (SSP)*. By SSP we mean population of coheve stars born all at the same time with an instantaneous burst of star formation (e.g. Renzini & Voli 1981b). After their formation, the evolution of a SSP will be purely passive. SSPs are computed from the stellar evolutionary tracks, for a given IMF and metallicity Z .

Let us call $l_\lambda(Z, M, t - \tau)$ the luminosity emitted at the time t at the wavelength λ from a star of mass M , metallicity Z and age τ . The luminosity at the wavelength λ of a SSP characterised by an IMF $\phi(m)$ can be computed as:

$$L_{SSP,\lambda}(Z, t - \tau) = \int_{M_{min}}^{M_{max}} \phi(m) l_\lambda(Z, M, t - \tau) dM, \quad (3.18)$$

where M_{min} and M_{max} are the minimum and maximum mass of stars in the stellar population.

At this point we define the *Composite Stellar Population (CSP)* as the sum of different SSP, which will be in general characterised by different ages, metallicities and masses. Luminosity of a CSP at the time t at a given wavelength λ can be thus computed as:

$$L_\lambda(t) = \int_0^t \int_{Z_i}^{Z_f} \psi(t - \tau) L_{SSP,\lambda}(Z, t - \tau) dZ d\tau, \quad (3.19)$$

where Z_i and Z_f are respectively the initial and final metallicities, $\psi(t - \tau)$ is the SFR at the time $(t - \tau)$ and τ is the age of each SSP.

3.5.2. The GALAXEV code

GALAXEV is a library of evolutionary synthetic stellar population models computed with the code by Bruzual & Charlot (2003). This code allows us to compute spectral evolution of stellar populations in a wide range of metallicities with a resolution of 3 \AA in the band between 3200 \AA and 9500 \AA and with a lower resolution in the other bands. The stellar evolution tracks are based on the Padova library (1994) (Alongi et al. 1993; Bressan et al. 1993; Fagotto et al. 1994a; Fagotto et al. 1994b; Fagotto et al. 1994c; Girardi et al. 1996). This library includes tracks for initial metallicities $Z = 0.0001, 0.0004, 0.004, 0.008, 0.02$ (solar) and $Z = 0.05$ and ages between 10^5 and 2×10^{10} years, for different IMFs. A dust attenuation model based on the two simple components by Charlot & Fall (2000) is also implemented. As a result, the code gives at each time-step:

- Magnitudes of the CSP computed in different bands;
- Intensity of spectral indexes;
- Supernova rates per year per luminosity;
- Planetary nebula formation rate;
- Number of white dwarf, neutron stars and black holes;
- Total mass in stars and in gas;
- Star Formation Rates.

We report in Fig. 3.7 an example of the evolution of the mass-to-luminosity ratio in B , V and K band computed with the GALAXEV libraries for a single SSP with a Salpeter IMF with solar metallicity. As long as the SSP is *young*, blue stars dominate, thus the mass to light ratio is lower in the B and V bands, rather than the K band. While the SSP is becoming older, stars which dominate are the redder ones, therefore the M/L ratio is lower in the K band than in the B and V bands.

3.6 IDENTIFYING GALAXIES

In this section we briefly discuss two codes which we have used in our work to identify gravitationally bound structures in simulations. For our purposes, we focused on the identification methods of gravitationally bound star particles which we identify as *bona fide* galaxies

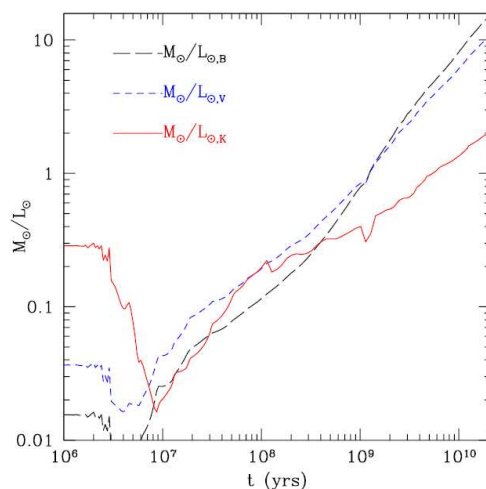


Figure 3.7: This picture shows the evolution of the M/L ratio in B , V and K band for a Salpeter IMF with solar metallicity computed with the GALAXEV code.

within our simulations. More in detail we will briefly describe the SKID algorithm³ (Stadel, 2001) and the SUBFIND algorithm (Springel et al. 2001).

3.6.1. The SKID algorithm

We provide a short description of how we applied this algorithm, while a more detailed discussion and presentation of tests is provided elsewhere (e.g. Murante et al. 2007; Saro et al. 2006 and Borgani et al. 2006). An overall density field is computed by using the distribution of all the particle species, by using a SPH spline-kernel. The star particles are then moved along the gradient of the density field in steps of $\tau/2$, where we assume $\tau \simeq 3\epsilon_{\text{Pl}}$ as the typical SKID length scale comparable to the simulation force resolution. When a particle begins to oscillate inside a sphere of radius $\tau/2$, it is stopped. Once all particles have been moved, they are grouped using a friends-of-friends (FOF) algorithm, with linking length $\tau/2$, applied to the new particle positions. The binding energy of each group identified in this way is then used to remove from the group all star particles which are recognised as unbound. All particles in a sphere of radius τ , centred on the centre of mass of the group, are used to compute such a gravitational binding energy. Finally, we identify as “bona fide” galaxies only those SKID-groups containing at least 32 star particles after the removal of unbound stars.

³See <http://www-hpcc.astro.washington.edu/tools/skid.html>

3.6.2. The SUBFIND algorithm

Similar to the SKID algorithm, also the starting point of the SUBFIND algorithm is the computation of an overall density field by using the distribution of all the particle species, based on a SPH spline-kernel. At this point, SUBFIND descend the potential gradient until a saddle point is found. This saddle point allows one to distinguish between substructure candidates and the main halo, which is the structure containing the largest number of particles of a friend-of-friend (FOF) group. Up to this point, the construction of sub-halo candidates has been based on the spatial distribution of particles alone. A more physical definition of substructure is obtained by adding the requirement of self-boundedness. The SUBFIND code therefore subject each sub-halo candidate to an un-binding procedure to obtain the true substructure. To this end, it successively eliminates particles with positive total energy, until only bound particles remain. We note that the algorithm is in principle fully capable of detecting arbitrary levels of sub-haloes within sub-haloes. Finally only structures with minimum number of particles larger than a certain value N_{ngb} ($N_{ngb} = 20$, typically) are considered as *bona fide* structures. In Figure 3.8 from Springel et al. (2001), we show a typical example of substructure identified using SUBFIND. By eye, one can clearly spot substructure embedded in the FOF-group. The algorithm SUBFIND finds 56 sub-haloes in this case. The largest one is the ‘background’ main halo, shown in the top right panel of Fig. 3.8. It represents the backbone of the group, with all its small substructure removed. This substructure is made up of 55 sub-haloes, which are plotted in a common panel on the lower left. Particles not bound to any of the sub-haloes form “fuzz”, and are displayed on the lower right. These particles primarily lie close to the outer edge of the group.

The main difference between the SKID and the SUBFIND algorithms is that SUBFIND, by construction, assigns all the bound particles of a FOF group which are not assigned to any substructure to the main halo. This choice mostly affects the identification of the central galaxy of a cluster halo. As shown by Murante et al. (2007), simulations predict the formation of a significant amount of Intra-Cluster light associated to the build-up of the BCG by repeated mergers. These star particles are still gravitationally bound to the main halo (which is the cluster itself), therefore SUBFIND is not able to separate the diffuse component from the true BCG stellar population, contrary to the SKID algorithm. Figure 3.9 shows the comparison between the galaxy population of a simulated massive ($M_{200} \sim 10^{15} h^{-1} M_{\odot}$) cluster at $z = 0$ as it is identified by the SKID and by the SUBFIND algorithms. The simulation is based on the GADGET-2 code and includes radiative cooling, star formation but no feedback, in a similar way as the simulation described in Chapter 7. Left panel shows the cumulative stellar mass functions of galaxies identified within r_{200} by both the SKID and the SUBFIND codes. We note that the stellar mass of galaxies identified by SKID and by SUBFIND are in excellent agreement, apart from the most massive galaxy in the cluster, the BCG. The difference in the first bin is due to the diffuse stellar component which the SUBFIND algorithm assigns to the BCG’s stellar mass, while it is considered as a separate component in

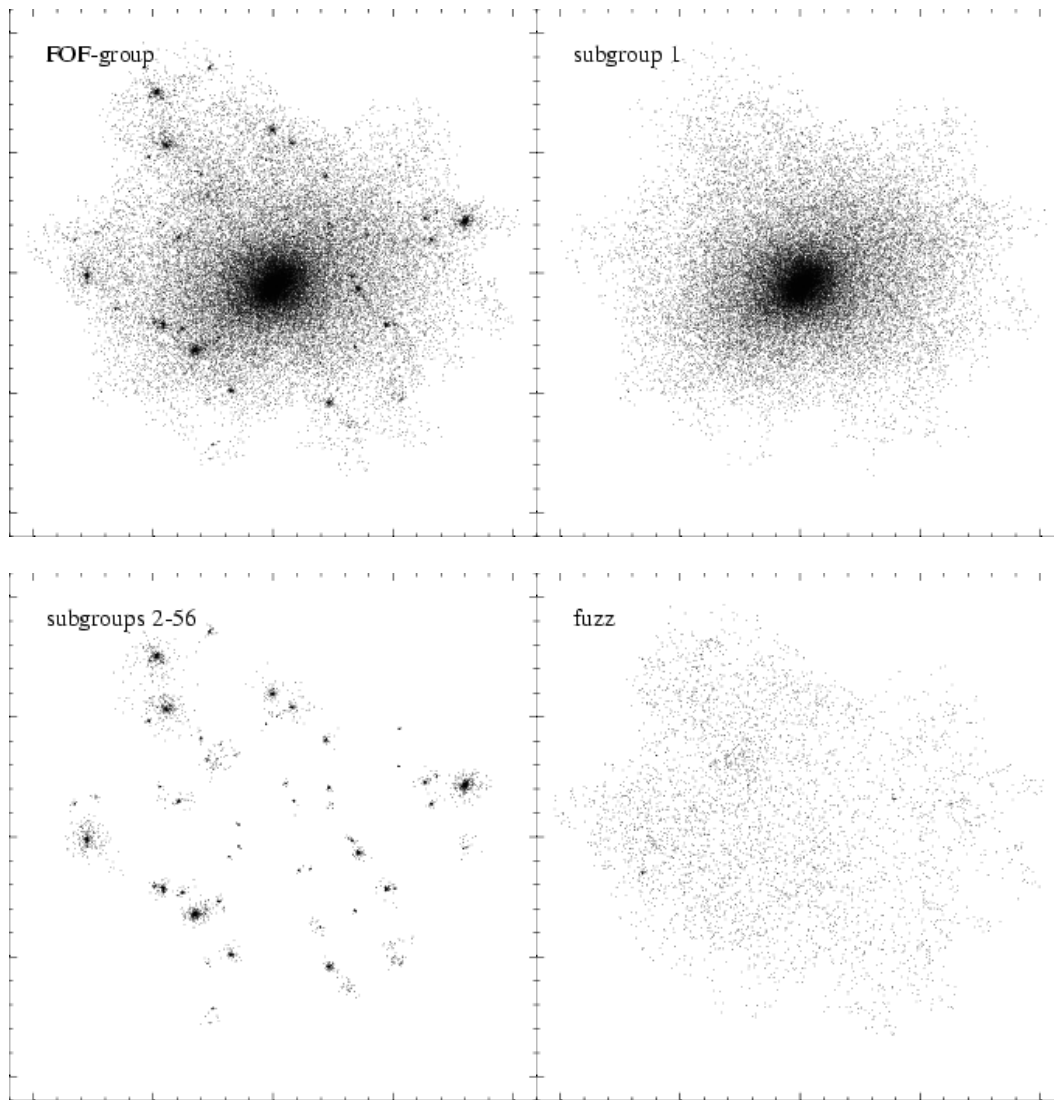


Figure 3.8: Example for a sub-halo identification with SUBFIND. The top left panel shows a small FOF-group (44800 particles). SUBFIND identifies 56 sub-haloes within this group, the largest one forms the background halo and is shown on the top right, while the other 55 sub-haloes are plotted on a common panel on the lower left. Particles not bound to any of the sub-haloes form “fuzz”, and are displayed on the lower right (from Springel et al. 2001).

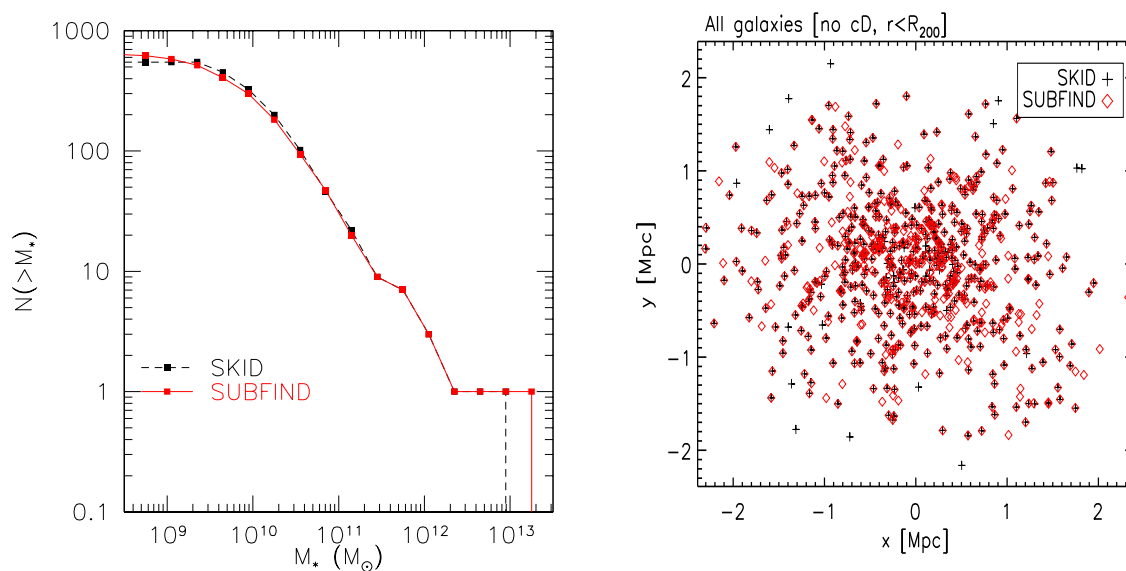


Figure 3.9: A comparison between the galaxy population of a simulated massive ($M_{200} \sim 10^{15} h^{-1} M_\odot$) cluster at $z = 0$ as it is identified by the SKID and by the SUBFIND algorithms. The simulation is based on the GADGET-2 code and includes radiative cooling, star formation but no feedback, in a similar way as described in Chapter 7. Left panel shows the cumulative stellar mass functions of galaxies identified within r_{200} by both the SKID and the SUBFIND codes. Right panel shows a map in the plane x-y of the position of the identified galaxies in cluster-centric coordinates.

the SKID code. Right panel shows a map in the x-y plane of the position of the identified galaxies in cluster-centric coordinates. We note that the positions of identified galaxies are in remarkably good agreement and that galaxies which have no counterparts are preferentially placed in the outer region of the cluster and have stellar masses close to the resolution limit of the simulation.

3.7 SEMI-ANALYTIC MODELS: AN OVERVIEW

We briefly present in this Section the basic principles behind a widely used family of techniques to study galaxy formation within the cosmological hierarchical framework, which is complementary to direct hydrodynamical cosmological simulations: the semi-analytic approach. These models assume that baryons follow the dynamics of Dark Matter (computed either via numerical simulations or analytically). Then, within the DM haloes of galaxies, physics of baryons is followed with “physical motivated recipes”. We refer to the review by Baugh (2006) for more detailed descriptions.

3.7.1. Dark matter haloes

Dark matter haloes are the cradles of galaxy formation. Hierarchical galaxy formation models require three basic pieces of information about dark matter haloes:

- The abundance of haloes of different masses.
- The formation history of each halo, commonly called the merger tree.
- The internal structure of the halo, in terms of the radial density profile and their angular momentum.

These fundamental properties of the dark matter distribution are now well established, thanks mainly to the tremendous advances made possible by N-body simulations.

The merger histories of dark matter haloes can be extracted from N-body simulations which have sufficiently frequent outputs. SAMs which compute the merging history of dark matter haloes in this way (e.g. De Lucia & Blaizot 2007) are commonly known as hybrid N-body semi-analytic models. Alternatively, merger trees can also be generated using a Monte-Carlo approach by sampling the distribution of progenitor masses predicted using extended Press-Schechter theory (Lacey & Cole 1993; Somerville & Kolatt 1999; Cole et al. 2000a; Menci 2002). Left panel of Figure 3.10 by Baugh (2006) shows a schematic merger tree for a dark matter halo. The horizontal lines represent snapshots in the evolution of the history of the halo, corresponding to time-steps in an N-body simulation or Monte-Carlo realisation of the merger tree ($t_1 < t_2$). The size of the circle indicates the mass of the halo. The haloes grow through merger events between haloes and by accretion of objects below the (halo)

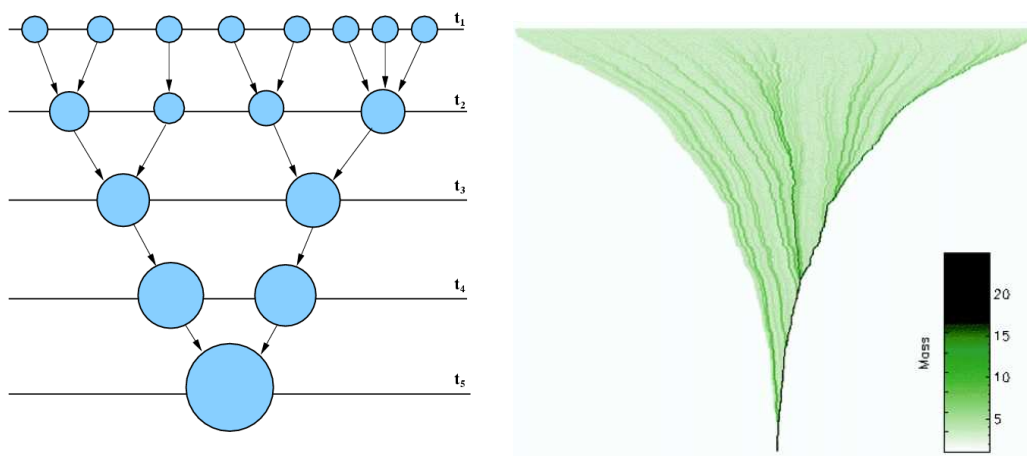


Figure 3.10: Left panel: A schematic merger tree for a dark matter halo. The horizontal lines represent snapshots in the evolution of the history of the halo, corresponding to time-steps in an N-body simulation or Monte-Carlo realisation of the merger tree ($t_1 < t_2$). The size of the circle indicates the mass of the halo. The haloes grow through merger events between haloes and by accretion of objects below the (halo) mass resolution (e.g. as depicted between steps t_3 and t_4). The final halo is shown at t_5 (from Baugh 2006). Right panel: A merging tree from a Monte Carlo simulation, showing the formation history of a central dominant galaxy in a large DM halo with present mass $10^{13} M_{\odot}$. Time runs from top to bottom, from $z = 10$ to the present. Each branch represents a progenitor of the final galaxy, and the colour code (shown on the right in units of $5 \times 10^{11} M_{\odot}$) quantifies the mass of the corresponding progenitor. A total of some 10^3 progenitors are involved, with the main one being represented on the rightmost branch (from Cavaliere & Menci 2007).

mass resolution (e.g. as depicted between steps t_3 and t_4). The final halo is shown at t_5 . In the right panel of Fig. 3.10 by Cavaliere & Menci (2007) it is shown instead a merging tree from a Monte Carlo simulation, showing the formation history of a central dominant galaxy in a large DM halo with present mass $10^{13} M_{\odot}$. Each branch represents a progenitor of the final galaxy, and the colour code (shown on the right in units of $5 \times 10^{11} M_{\odot}$) quantifies the mass of the corresponding progenitor. A total of more than 10^3 progenitors are involved, with the main one being represented on the rightmost branch. The internal structure of dark matter haloes is important for determining the rate at which gas can cool and the size and dynamics of galaxies (see next subsection).

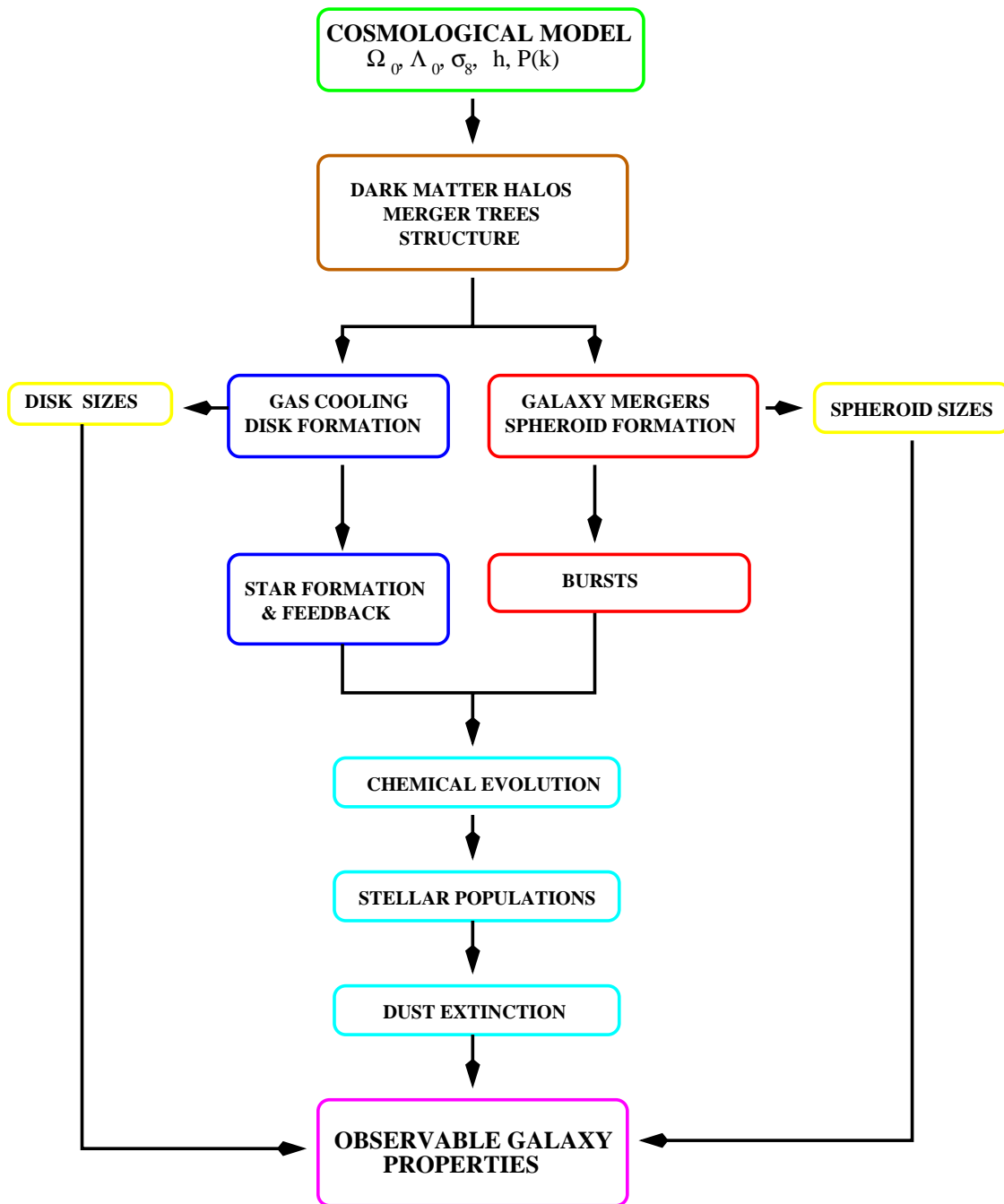


Figure 3.11: A schematic overview of the ingredients of a hierarchical galaxy formation model (from Baugh 2006).

3.7.2. Astrophysical gas processes

In this section, we describe the more complicated elements entering in a hierarchical galaxy formation. These processes are far more difficult to deal with than gravitational instability, and are often dissipative and nonlinear. The physics behind the phenomena that are described in this section are in general poorly understood. To counter this, recipes or prescriptions which contain parameters are employed. The values of the parameters are set by requiring that the model reproduces a subset of the available observations, both at low and high redshift. In general, the form of the rule adopted to describe a given process is motivated by a result from a more detailed numerical simulation or from observations. An overview of the processes typically incorporated in semi-analytical models and the interplay among them is shown in Fig. 3.11. More in detail semi-analytic models should take into account the astrophysical processes described here below.

3.7.3. The cooling of gas

Gas cooling is central to the process of galaxy formation, as it sets the rate at which the raw material for star formation becomes available. The basic model of how gas cools inside dark matter haloes was set out in detail by White & Frenk (1991). Figure 3.12 shows a schematic of the basic cooling models used in SAMs. Each line represents a stage in the cooling process. In the first step (t_1), baryons fall into the gravitational potential well of the dark matter halo. The presence of a photo-ionising background may reduce the fraction of baryons that fall into low mass haloes. This gas is assumed to be heated by shocks as it falls into the potential well, attaining the virial temperature associated with the halo (t_2). In the third step (t_3), the inner parts of the hot gas halo cool, forming a rotationally supported disc. At a later stage (t_4), the radius within which gas has had time to cool advances outwards towards the virial radius of the halo and the cold gas disc grows in size. More in detail the system is assumed to be in hydrostatic equilibrium at the time $t = 0$. For each mass shell at radius r a cooling time can be defined as:

$$t_{\text{cool}}(r) := \left| \frac{d \ln T}{dt} \right|^{-1} = \frac{3k_B T_g(r) \mu m_p}{2\rho_g(r) \Lambda(T_g(r))}, \quad (3.20)$$

where Λ is the cooling function. The left-hand-side of the above equation follows from the assumption that dT is computed for an isobaric transformation. The cooling radius at the time t for the classical model, $r_C(t)$, is defined through the relation

$$r_C(t) : t_{\text{cool}}(r_C) = t. \quad (3.21)$$

In other words, the function $r_C(t)$ is the inverse of the function $t_{\text{cool}}(r)$. It is then assumed that each shell cools after one cooling time. The resulting mass deposition rate reads

$$\dot{M}_{\text{cool}} = 4\pi r^2 \rho_g(r_C) \frac{dr_C}{dt}. \quad (3.22)$$

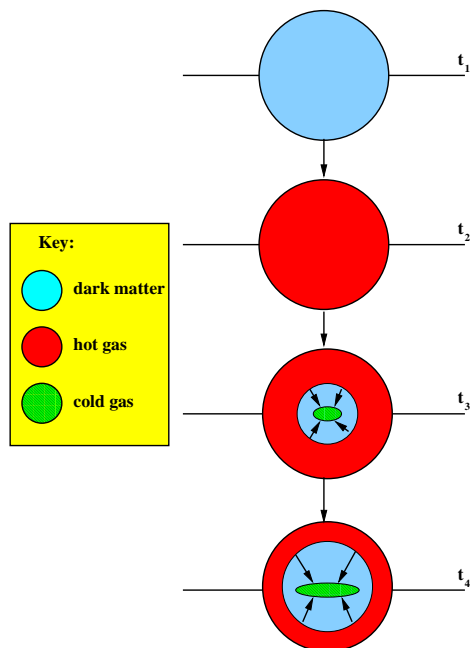


Figure 3.12: A schematic of the basic cooling model used in semi-analytical models (from Baugh 2006).

where a dot denotes a time derivative. Recently, Viola et al. (2008) compared the resulting evolution of the cooled mass with the predictions of the classical cooling model of White & Frenk with the numerical results of a set of radiative SPH hydrodynamical simulations of isolated halos, with gas sitting initially in hydrostatic equilibrium within NFW potential wells. They concluded that the classical cooling model of White & Frenk systematically underestimates the cooling rate. This disagreement is ascribed to the lack of validity of the assumption that each mass shell takes one cooling time, computed on the initial conditions, to cool to low temperature.s

3.7.4. Star formation

The lack of a theory of star formation, may, at first sight, appear to thwart any attempt to produce a theory of galaxy formation. Semi-analytical modellers have instead be forced to take a more pragmatic, top-down approach. A simple estimate of the global rate of star formation in a model galaxy can be made on dimensional grounds:

$$\dot{M}_* \propto \frac{M_{\text{cold}}}{\tau}, \quad (3.23)$$

where the star formation rate, \dot{M}_* , depends upon the amount of cold gas available, M_{cold} , and a characteristic timescale τ . The timescale could be chosen to be proportional to the dynamical time within the galaxy, $\tau_{\text{dyn}} = r_{\text{gal}}/v_{\text{gal}}$, or to be some fixed value. Typically, some additional dependence on the circular velocity is incorporated into the definition of τ , which is important when attempting to reproduce the observed gas fractions in spirals as a function of luminosity (e.g. Cole et al. 1994; Cole et al. 2000b). The *effective* star formation timescale is in practice a modified version of τ , due to feedback processes, which deplete the reservoir of cold gas, and the replenishment of the cold gas supply by material that is recycled by stars.

Schmidt (1959) proposed a model in which the star formation rate per unit area of a galaxy ($\dot{\Sigma}_*$) scales with a power of the surface density of the cold gas, Σ_g : $\dot{\Sigma}_* \propto \Sigma_g^n$. Kennicutt (1998) verified this form for a large sample of spiral and star-burst galaxies, finding $n \sim 1.4$. The Schmidt law can be rewritten in the form of Eq. 3.23, with τ replaced by the dynamical time of the galaxy. A process closely correlated with the description of the star formation is the chemical evolution of the gas and stellar component. A good description of the chemical evolution is indeed strongly affecting the cooling function and the cooling rate, thus the whole star formation history (see also Section 3.4.3).

3.7.5. Feedback processes

The need for physical mechanisms that are able to modulate the efficiency of galaxy formation as a function of halo mass, over and above the variation in the cooling time of the hot gas with halo mass, was recognised from the first calculations of the galaxy luminosity function in hierarchical clustering cosmologies. White & Rees (1978) found that their prediction for the faint end of the luminosity function was steeper than the observational estimates available at the time, leading them to speculate that this discrepancy could be resolved if there was a process that would make low-mass galaxies relatively more vulnerable to disruption. Such processes are included in modern models under the blanket heading of ‘feedback’. The most common form of feedback used in hierarchical models is the ejection of cold gas from a galactic disk by a supernova driven wind (e.g. Larson 1974; Dekel & Silk 1986). The reheated cold gas could be blown out to the hot gas halo, from which it may subsequently recool, or it may even be ejected from the halo altogether and left unable to cool until it is incorporated into a more massive halo at a later stage in the merger hierarchy. There is now convincing observational evidence for the existence of supernova driven winds in dwarf galaxies (Martin 1999; Ott et al. 2005). Other forms of feedback act to modify the rate at which gas cools, either by altering the density profile or entropy of the hot gas halo (following the injection of energy into the hot gas halo) or by reducing the fraction of baryons that fall into dark matter haloes and changing the cooling rate (i.e. photo-ionisation suppression of cooling in low mass haloes) or by stifling the cooling flow by injecting energy. Initially, as remarked upon above, the motivation for invoking feedback was to reduce the efficiency

of star formation in low mass haloes, in order to flatten the slope of the faint end of the predicted galaxy luminosity function, thus bringing it in line with the extant observations (Cole 1991; White & Frenk 1991).

In recent years, the focus has shifted to reproducing the break at the bright end of the luminosity function. The overproduction of bright galaxies is a problem that has dogged hierarchical galaxy formation models for more than a decade. It turns out that, in order to produce a good match to the exponential break in the luminosity function, the super-wind is required to be extremely efficient (perhaps implausibly so) at coupling the energy released by supernovae into driving cold gas from the disk. Benson et al. (2003) remarked that such a super-wind may be feasible if it is driven by the energy released by the accretion of material onto a black hole at the centre of the galaxy.

Building upon previous work which examined the impact of AGN on aspects of galaxy formation (e.g. Granato et al. 2004; Monaco & Fontanot 2005; Cattaneo et al. 2005; Di Matteo et al. 2005), a lot of groups have also developed semi-analytical models in which AGN act to suppress cooling (Croton et al. 2006; Bower et al. 2006; Cattaneo et al. 2006; Fontanot et al. 2006; Menci et al. 2006; De Lucia & Blaizot 2007; Fontanot et al. 2007), even if with different implementations. They have successfully represented both the Magorrian relation (Magorrian et al. 1998) which correlates the black hole mass and bulge mass and the break at the bright end of the luminosity function. Figure 3.13 (Benson et al. 2003) shows how the observed mass function of galaxies (points) compares with the halo mass function derived from simulations (dashed line). In this model, the mass function of dark matter halos (Jenkins et al., 2001) has been converted into a luminosity function simply by assuming a fixed mass-to-light ratio ($M/L_K = 11M_\odot/L_{K,\odot}$), chosen so as to match the knee of the observed luminosity function. As is well known, this produces a luminosity function which is much steeper at the faint end than is observed, and also fails to cut off at bright magnitudes. The majority of current models of galaxy formation explain the lack of galaxies in the low-mass end compare to the mass function of DM haloes in terms of efficient feedback from galactic winds due to SNe explosions. The few cut-off of galaxies at the high-mass end is instead usually interpreted as an effect of efficient feedback from AGN.

3.7.6. Galaxy mergers

In the two-stage model of galaxy formation proposed by White & Rees (1978) dark haloes are assumed to grow through mergers and accretion, with dynamical relaxation effects erasing any trace of the progenitor haloes at each stage of the merging hierarchy (see Press & Schechter 1974). The halo resulting from a merger or accretion event is assumed to be smooth and devoid of any substructure. White & Rees argued that galaxies survive the merger of their parent haloes as a result of them being more concentrated than the dark matter, due to the dissipative cooling of gas.

The White & Rees picture of galaxy formation leads naturally to a scenario in which a

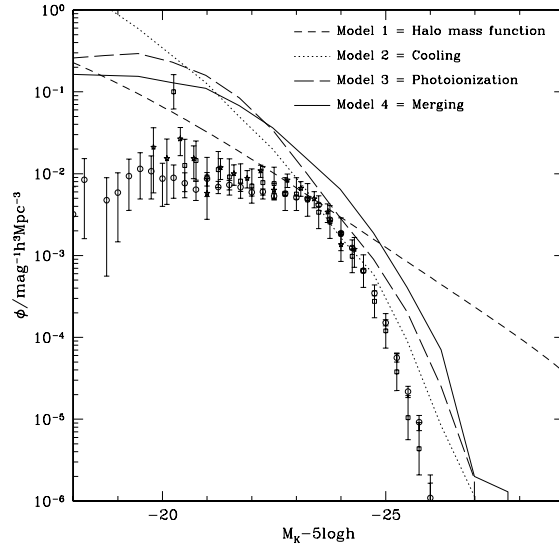


Figure 3.13: The K-band luminosity function of galaxies. The points show the observational determinations of Cole et al. (2001, circles), Kochanek et al. (2001, squares) and Huang et al. (2003, $z < 0.1$, stars). Lines show results from different GALFORM models. Model 1 (dashed line) shows the result of converting the dark matter halo mass function into a galaxy luminosity function by assuming a fixed mass-to-light ratio chosen to match the knee of the luminosity function. Model 2 (dotted line) shows the result from GALFORM when no feedback, photoionization suppression, galaxy merging or conduction are included. Models 3 and 4 (long dashed and solid lines respectively) show the effects of adding photoionization and then galaxy merging (from Benson et al. 2003).

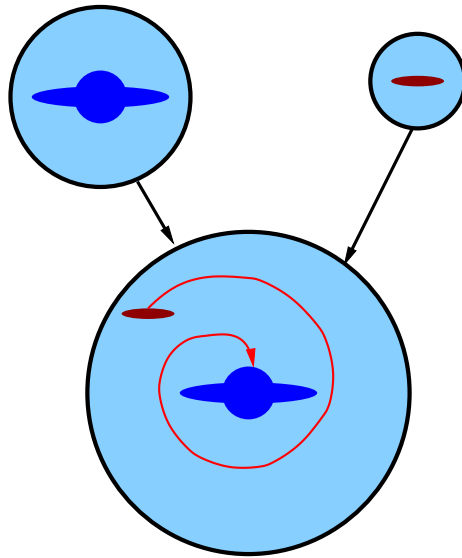


Figure 3.14: A schematic view of a merger between two dark matter haloes. The progenitors of the final halo each contain a galaxy. After the haloes merge, the more massive galaxy is placed at the centre of the newly formed halo. Any hot gas that cools would be directed onto the central galaxy (for simplicity, in this illustration, the haloes have exhausted their supply of hot gas). The smaller galaxy becomes a satellite of the central galaxy. The orbit of the satellite galaxy decays due to dynamical friction. The satellite may eventually merge with the central galaxy (from Baugh 2006).

dark halo contains a massive central galaxy surrounded by smaller satellite galaxies. These satellites were formerly central galaxies in the progenitors of the current halo which were present in the earlier stages of the merger hierarchy. The satellite galaxies retain their identity after their parent halo merges with a more massive object due to their high concentration. However, as the satellites orbit the central galaxy in their common dark halo, they gradually lose energy through dynamical friction, an effect originally calculated for star clusters by Chandrasekhar (1943). The gravitational attraction exerted by the mass of the satellite galaxy on its surroundings draws the material in the halo towards it. This produces a wake of higher density material along the path of the satellite. The satellite therefore feels a stronger gravitational pull from the region of the halo that it has just passed through compared with the region it is about to travel through, which acts as a brake on its motion. The orbital energy of the satellite decays as a result and it spirals in towards the central galaxy (Binney & Tremaine 1987). A timescale can be computed for the dynamical friction process to remove the orbital energy of the satellite completely. If this timescale is shorter than the lifetime of the dark halo, then the satellite merges with the central galaxy (see Fig. 3.14). We will show in Chapter 6 how this merging-time is affected by the presence of gas related physical processes.

We will describe in Chapters 4 and 5 how we have applied the numerical methods presented in Sections 3.4, 3.5 and 3.6 to analyse and compare our simulations with the observed properties of the galaxy population described in Chapter 2. In Chapter 6 we will apply the SAM by De Lucia & Blaizot (2007) to estimate the effect of gas-dynamics on the predicted cluster galaxy population. Finally in Chapter 7 we will compare the cluster galaxy population predicted by stripped-down versions of the same SAM and by direct simulations based on the GADGET-2 code.

CHAPTER 4

SIMULATIONS OF THE GALAXY POPULATION IN NEARBY CLUSTERS

In this Chapter we compare simulation predictions on the global properties of nearby galaxy clusters to the observational results shown in Chapter 2. The content of this Chapter largely reflects the results presented in two papers which have already been published (Saro et al. 2006 and Fabjan et al. 2008). The plan of this Chapter is as follow. In Section 4.1 we provide the general characteristics of the simulated clusters and describe the relevant features of the GADGET-2 version used for this analysis. In Section 4.2 we will describe the method of galaxy identification and how luminosities in different bands are computed. Section 4.3 contains the description of the properties of the simulated galaxy population and their comparison with observational data. In particular, we will discuss the radial distribution of galaxies, the CMR, the mass–luminosity ratio, the luminosity function, the star formation rate and the colour and age gradients and the SN-Ia rate. We will discuss in Section 4.4 the effects of numerical resolution on the stability of the results of our analysis. Our main results will be summarised and discussed in Section 4.5.

Within the general framework of the Λ CDM cosmological scenario, galaxies arise from the hierarchical assembly of dark matter (DM) halos. The gravitational dynamics of these halos is relatively simple to describe to high precision with modern large supercomputer simulations (e.g., Springel et al., 2005b) (see Chapter 3). However, the observational properties of galaxies are determined by the combined action of the assembly of DM halos and by the physical processes which define the evolution of the cosmic baryons. A complex interplay between radiative gas cooling, star formation, chemical enrichment and release of energy feedback from supernovae (SN) and active galactic nuclei (AGN) is expected to determine the properties of the stellar population in galaxies. At the same time, the cluster environment is expected to play a significant role in altering the evolution of galaxies. For instance, ram pressure exerted by the hot intra-cluster medium (ICM) can lead to the removal of a substantial fraction of the interstellar medium (ISM; Gunn & Gott 1972), thereby affecting galaxy

SIMULATIONS OF THE GALAXY POPULATION IN NEARBY CLUSTERS

morphology, star formation and luminosity (e.g., Abadi et al., 1999; Kenney et al., 2004, , and references therein).

In this context, semi-analytical models of galaxy formation have been used since several years as a flexible tool to study galaxy formation within the cosmological hierarchical framework as we discussed in Chapter 3 (e.g., Kauffmann et al., 1993; Somerville & Primack, 1999; Cole et al., 2000a; Menci et al., 2002; Monaco et al., 2007; De Lucia & Blaizot, 2007, and references therein). A powerful implementation of this method is that based on the so-called hybrid approach, which combines N-body simulations, to accurately trace the merging history of DM halos, and semi-analytic models to describe the physics of the baryons (e.g., Kauffmann et al., 1999a). Springel et al. (2001) applied this method to a DM simulation of a cluster, with high enough resolution to allow them resolving the population of dwarf galaxies. As a result, they found that several observational properties (e.g., luminosity function, mass-to-light ratio and morphological types) are rather well reproduced. Diaferio et al. (2001b) applied a semi-analytical model to a DM simulation of a large cosmological box, with the aim of performing a combined study of kinematics, colours and morphologies for both cluster and field galaxies. They concluded that a good agreement with observations holds for cluster galaxies, while colours and star formation rates of field galaxies were shown to evolve more rapidly than observed. Casagrande & Diaferio (2006) applied the same semi-analytical model to a constrained simulation of the local universe and concluded that significant differences exist between the observed and the predicted properties of the large-scale distribution of galaxy groups. De Lucia et al. (2004b) incorporated in their model also a scheme of metal production to follow the enrichment of ICM and galaxies (see also Cora 2006). Among their results, they found that the colour-magnitude relation (CMR) is mainly driven by metallicity effects, the redder galaxies on the sequence being on average the more metal rich. Lanzoni et al. (2005) applied their semi-analytical model to a set of DM cluster simulations. They also included a prescription to account for the effect of ram-pressure stripping of the ISM as the galaxies move in the hot cluster atmosphere, and found it to have only a very little effect on the galaxy population.

A complementary approach to the semi-analytical models is represented by using full hydrodynamical simulations, which include the processes of gas cooling and star formation. The clear advantage of this approach, with respect to semi-analytical models, is that galaxy formation can be now described by following in detail the evolution of the cosmic baryons while they follow the formation of the cosmic web. However, the limitation of this approach lies in its high computational cost, which prevents it to cover wide dynamic ranges and to sample in detail the parameter space describing the processes of star formation and feedback. For these reasons, describing the process of galaxy formation with a self-consistent hydrodynamic approach within the typical cosmological environment of ~ 10 Mpc, relevant for galaxy clusters, represents a challenging task for simulations of the present generation.

In a pioneering paper, Metzler & Evrard (1994) studied the effect of including galaxies for the energy feedback and chemical enrichment of the ICM. Since these simulations did not have enough resolution to identify galaxies, they have been placed by hand, identifying them

with the peaks of the initial density field. Frenk et al. (1996) used for the first time a radiative simulation of a cluster and identified galaxies as concentrations of cooled gas. The aim of their study was to compare the dynamics of member galaxies to that of DM particles. They concluded that galaxies suffer for a substantial dynamical bias, a result which has not been confirmed by more recent hydrodynamical simulations (e.g., Faltenbacher et al., 2005; Biviano et al., 2006). Thanks to the ever improving supercomputing capabilities and efficiency of simulation codes, a number of groups have recently completed hydrodynamical simulations of galaxy clusters, which have good enough resolution to trace the galaxy population with better reliability. Nagai & Kravtsov (2005) used simulations of eight groups and clusters, performed with an adaptive mesh refinement code, including star formation, feedback from supernovae and chemical enrichment, to describe the spatial distribution of galaxies inside clusters. They found that galaxies are more centrally concentrated than DM sub-halos, with their number density profile described by a NFW shape (Navarro et al., 1996), although with a smaller concentration parameter than for the DM distribution. Romeo et al. (2005) used SPH simulations of two clusters, including a similar physics, used spectrophotometric code to derive galaxy luminosities in different bands. They analysed the resulting color–magnitude relations (CMR) and luminosity functions, claiming for an overall general agreement with observations. More recently Romeo et al. (2008) analysed a set of 12 groups and 2 simulated cluster in order to follow the building-up of the the colour-magnitude relation. They have found that the evolution of the colour-magnitude properties of galaxies within the hierarchical framework is mainly driven by star formation activity during dark matter haloes assembly. Galaxies progressively quenching their star formation settle to a very sharp ‘red and dead’ sequence, which turns out to be universal, its slope and scatter being almost independent of the redshift (since at least $z \sim 1.5$) and environment.

In this Chapter will present a detailed analyses of the galaxy population for a set of 18 simulated clusters, which span the mass range from $\simeq 5 \times 10^{13} M_{\odot}$ to $\simeq 2 \times 10^{15} M_{\odot}$. The simulations have been performed with the Tree-SPH code GADGET-2 (Springel, 2005). They include the effect of radiative cooling, an effective model for star formation from a multi-phase ISM (Springel & Hernquist, 2003b), a phenomenological recipe for galactic winds, a detailed stellar evolution model, thereby accounting also for life–times and metal production from different stellar populations (Tornatore et al. 2004; Tornatore et al. 2007a).

These simulations have been carried out also by varying both the shape of the initial mass function (IMF) and the feedback strength. The inclusion of a detailed model of chemical enrichment allows us to compute luminosities and colours for galaxies of different metallicities, by using the GALAXEV spectrophotometric code (Bruzual & Charlot, 2003). In this Chapter we will concentrate on the properties of galaxy clusters at $z = 0$ and we will consider also the evolution of the SN-Ia rate in clusters. As we will discuss, several observational trends are reproduced quite well by our simulations, although a number of significant discrepancies are found. For this reason, the aim of our analysis will be more that of understanding the directions to improve simulations, rather than seeking for a best fitting between model predictions and observations.

4.1 THE SIMULATIONS

4.1.1. The simulated clusters

Our set of clusters are identified within nine Lagrangian regions, centred around as many main clusters (see also Dolag et al. 2008a for a detailed description of the simulated clusters). They were extracted from a DM-only simulation with a box size of $479 h^{-1}\text{Mpc}$ of a flat ΛCDM model with $\Omega_m = 0.3$ for the matter density parameter, $h = 0.7$ for the Hubble constant in units of $100 \text{ km s}^{-1}\text{Mpc}^{-1}$, $\sigma_8 = 0.9$ for the r.m.s. fluctuation within a top-hat sphere of $8 h^{-1}\text{Mpc}$ radius and $\Omega_b = 0.04$ for the baryon density parameter (Yoshida et al., 2001).

Thanks to the fairly large size chosen for these Lagrangian regions, several of them contain other interesting clusters, besides the main one. In this way, we end up with 18 clusters with mass M_{200} in the range¹ $5 \times 10^{13} - 1.8 \times 10^{15} M_\odot$, out of which 4 clusters have $M_{200} > 10^{15} M_\odot$ (see Table 4.1). Figures 4.1 and 4.2 show a representation of a sample of 8 analysed clusters colour coded respectively in gas density and gas temperature. They exhibit how structure formation grows preferentially along filaments of cold and dense gas which can even penetrate the shock heated diffuse atmosphere of virialised gas permeating the inner cluster regions. Mass resolution is increased inside the interesting regions by using the Zoomed Initial Condition (ZIC) technique by Tormen et al. (1997). Unperturbed particles positions were placed on a ‘glass’ (White, 1996), and initial displacements were then assigned according to the Zel’dovich approximation (e.g. Shandarin & Zeldovich, 1989). Besides the low-frequency modes, which were taken from the initial conditions of the parent simulation, the contribution of the newly sampled high-frequency modes was also added. The mass resolution was progressively degraded in more distant regions, so as to save computational resources while still correctly describing the large-scale tidal field of the cosmological environment.

Once initial conditions are created, we split particles in the high-resolution region into a DM and a gas component, whose mass ratio is set to reproduce the assumed cosmic baryon fraction. Instead of placing them on top of each other, in order to avoid spurious numerical effects, we displace gas and DM particles such that the centre of mass of each parent particle is preserved and the final gas and dark matter particle distributions are interleaved by one mean particle spacing. In the high-resolution region, the masses of the DM and gas particles are set to $m_{\text{DM}} = 1.13 \times 10^9 h^{-1} M_\odot$ and $m_{\text{gas}} = 1.7 \times 10^8 h^{-1} M_\odot$, respectively. The Plummer-equivalent softening length for the gravitational force is set to $\epsilon_{\text{P1}} = 5.0 h^{-1} \text{kpc}$, kept fixed in physical units from $z = 5$ to $z = 0$, while being $\epsilon_{\text{P1}} = 30.0 h^{-1} \text{kpc}$ in comoving units at higher redshift.

¹We define M_Δ as the mass contained within a radius encompassing a mean density equal to $\Delta\rho_c$, with ρ_c the critical cosmic density. See Appendix A.

Table 4.1: Characteristics of the clusters identified within the simulated regions at $z = 0$. Col. 1: name of the simulated region; Col. 2: name of the clusters within each region; Col. 3: value of the total mass, M_{200} , contained within the radius r_{200} encompassing an average density 200 times larger than the critical cosmic density ρ_c (units of $10^{14} M_{\odot}$); Col. 4: total number of galaxies, N_{200} , within r_{200} , having a minimum number of 32 star particles.

Region name	Cluster name	M_{200}	N_{200}
g1	g1.a	12.9	418
	g1.b	3.55	149
	g1.c	1.39	51
	g1.d	0.96	33
	g1.e	0.64	35
g8	g8.a	18.4	589
	g8.b	1.02	42
	g8.c	0.67	18
	g8.d	0.59	26
	g8.e	0.54	21
g51	g51.a	10.9	371
g72	g72.a	10.7	440
	g72.b	1.55	60
g676	g676.a	0.89	23
g914	g914.a	0.86	16
g1542	g1542.a	0.89	34
g3344	g3344.a	0.97	29
g6212	g6212.a	0.92	22

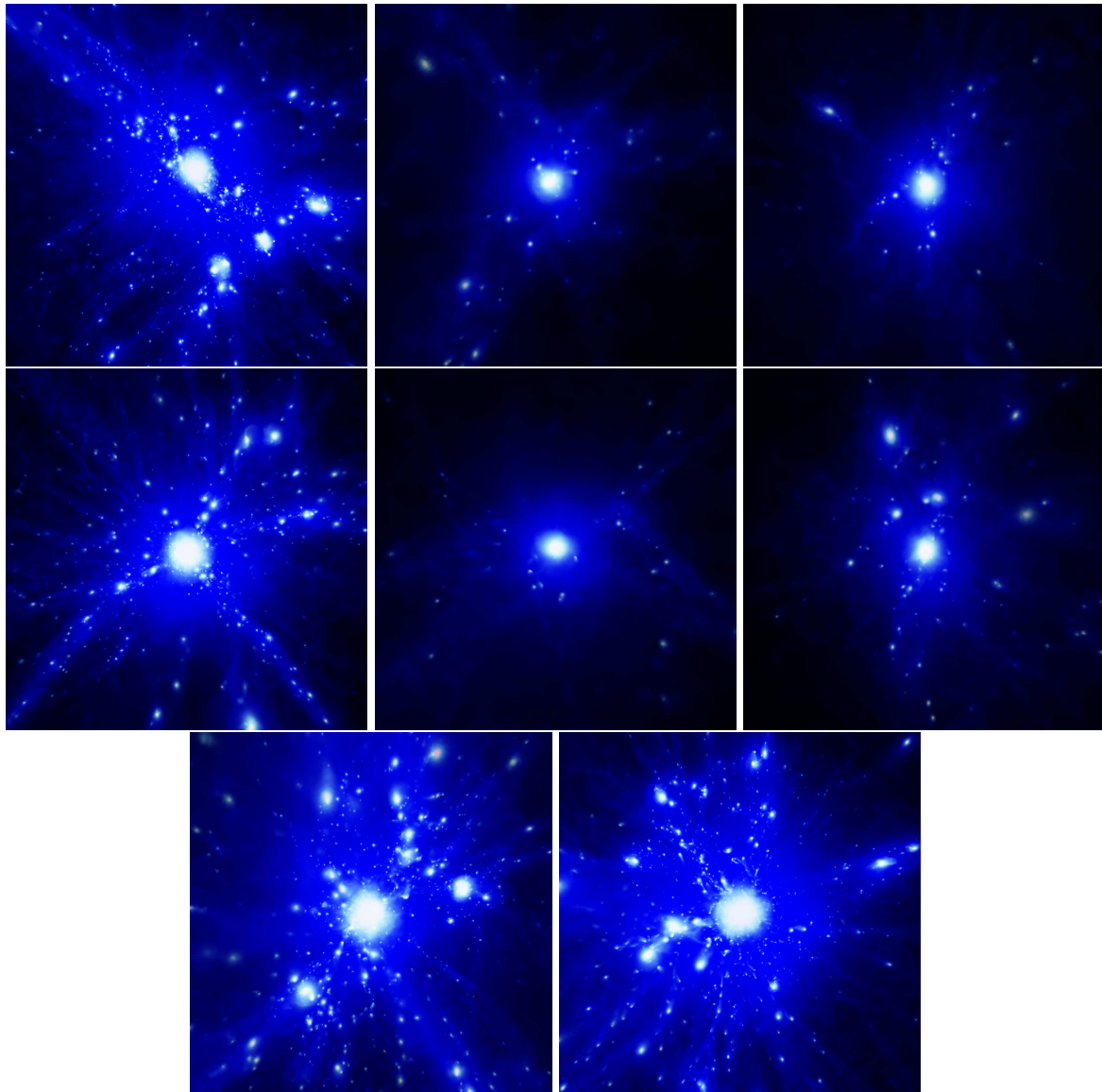


Figure 4.1: We show in these panels a representation of the gas density for a sample of 8 analysed clusters. The brighter the colours are, the larger the density is.

4.1.2. The code

Our simulations are based on an evolution of GADGET-2² (Springel et al., 2001; Springel, 2005), which includes a detailed treatment of chemical enrichment from stellar evolution (Tornatore et al. 2004; Tornatore et al. 2007a). As we discuss in Chapter 3, GADGET-2 is

²<http://www.MPA-Garching.MPG.DE/gadget/>

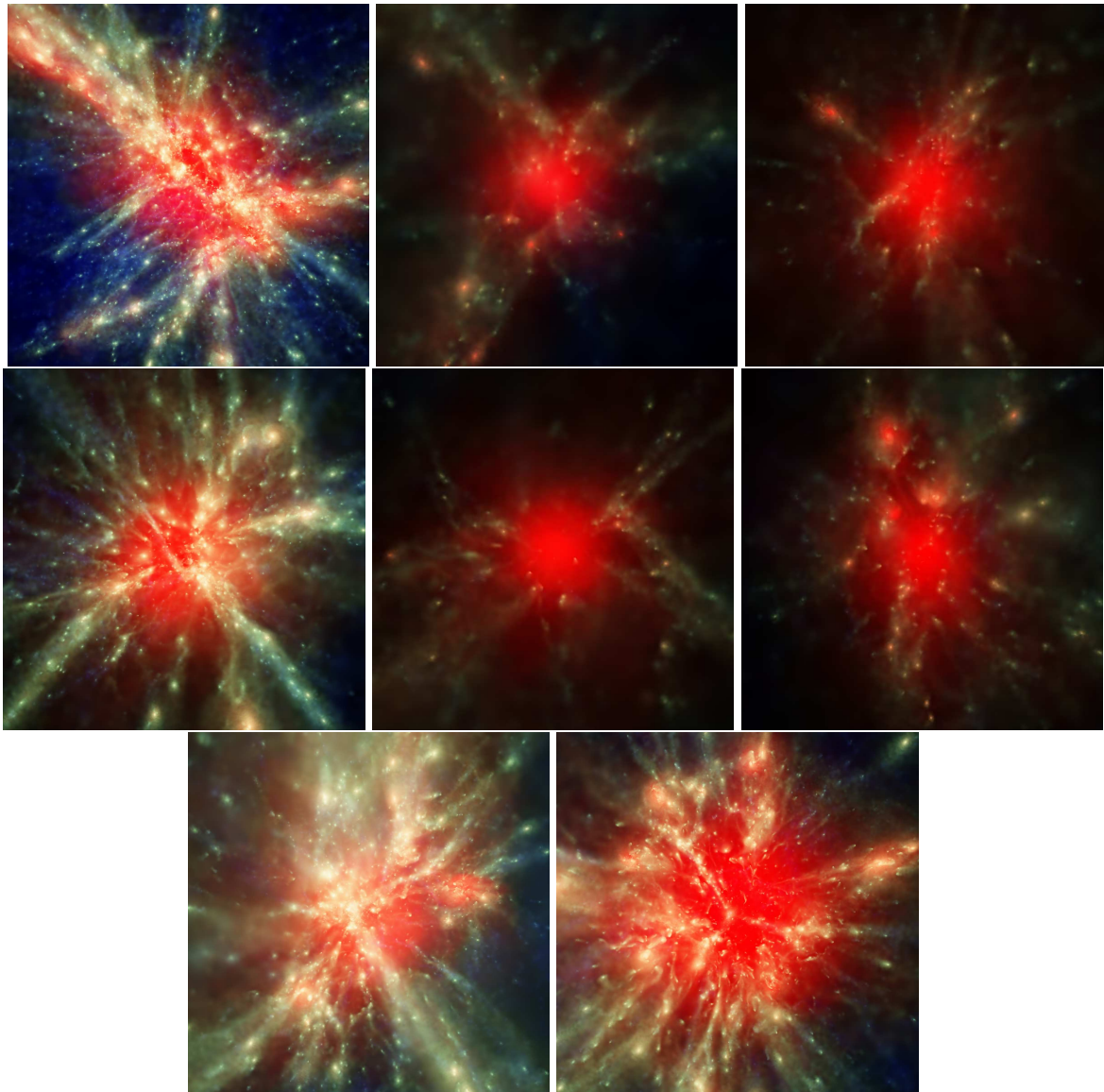


Figure 4.2: We show in these panels a representation of the gas temperature for a sample of 8 analysed clusters. Brighter colours are for colder gas and redder colours are for hotter gas.

a parallel Tree+SPH code with fully adaptive time-stepping, which includes an integration scheme which explicitly conserves energy and entropy (Springel & Hernquist, 2002), radiative cooling, the effect of a uniform and evolving UV background (Haardt & Madau, 1996), star formation from a multiphase interstellar medium and a prescription for galactic winds triggered by SN explosions (see Springel & Hernquist 2003b for a detailed description, SH03 hereafter), and a numerical scheme to suppress artificial viscosity far from the shock regions

(see Dolag et al. 2005). In the original version of the code, energy feedback and global metallicity were produced only by SN-II under the instantaneous–recycling approximation (IRA).

We have suitably modified the simulation code, so as to correctly account for the lifetimes of different stellar populations, to follow metal production from both SN-Ia and II, while self–consistently introducing the dependence of the cooling function on metallicity by using the tables by Sutherland & Dopita (1993). A detailed description of the implementation can be found in Tornatore et al. (2007a), while we provide here a short descriptions of the most relevant features of the code.

In order to maintain the general approach of the multiphase model by SH03, we assume that stars with masses $> 40 M_{\odot}$ explode into SN-II soon after their formation, thereby promptly releasing energy and metals. In contrast, we correctly account for the lifetime of stars having masses smaller than $40 M_{\odot}$. The simulations that we will discuss here use the lifetimes provided by Maeder & Meynet (1989), which have been shown to reproduce the abundance pattern in the Milky Way (Chiappini et al., 1997). Within the stochastic approach to star formation (SH03), each star particle is generated with a mass equal to one third of the mass of its parent gas particle.

Therefore, each star particle is considered as a SSP, with its own mass, metallicity and redshift of formation. For each SSP we compute both the number of stars turning into SN-II and Ia at each time-step and the number of stars ending their AGB phase. Then we calculate the amount of energy and metals produced by each star particle in a given time interval, decreasing accordingly the mass of the particle. In this way, each star particle is characterised by both its initial mass, assigned at the time of its formation, and its final mass, which is updated during the evolution. Both SN-II and SN-Ia are assumed to release 10^{51} ergs each, while no energy output is associated to the mass loss from AGB stars. The relative number of SN-II and SN-Ia depends on the choice of the stellar initial mass function (IMF). In the following, we will assume for the IMF the power–law shape $dN/d\log m \propto m^{-x}$. Simulations will be run by assuming the Salpeter IMF with $x = 1.35$ (Salpeter, 1955, Sa-IMF hereafter) and a top–heavy IMF with $x = 0.95$ (Arimoto & Yoshii 1987a, TH-IMF hereafter).

The SN-Ia are associated to binary systems whose components are in the $0.8\text{--}8 M_{\odot}$ mass range (Greggio & Renzini, 1983), while SN-II arise from stars with mass $> 8 M_{\odot}$. In the following, we will assume that 10 per cent of stars in the $0.8\text{--}8 M_{\odot}$ mass range belongs to binary systems, which then produces SN-Ia. We use the analytical fitting formulas for stellar yields of SN-Ia, SN-II and PNe provided by Recchi et al. (2001), and based on the original nucleosynthesis computations of Nomoto et al. (1997b), using their W7 model, Woosley & Weaver (1995b) and Renzini & Voli (1981a). The formulation for the SN-Ia rate has been calculated as in Matteucci & Recchi (2001). In the simulations that we present, besides H and He, we have followed Fe, O, C, Si, Mg, S. Once produced by a star particle, metals are spread over the same number of neighbours, 64, used for the SPH computations, also using the same kernel. We normalise the IMFs in the mass range $0.1\text{--}100 M_{\odot}$. Owing to the

uncertainty in modelling yields for very massive stars, we take yields to be independent of mass above $40 M_{\odot}$. While any uncertainty in the yields of such massive stars has a negligible effect for the Salpeter IMF, their accurate description (e.g., Thielemann et al., 1996; Heger & Woosley, 2002) is required when using a top–heavier IMF.

Our prescription to account for stellar evolution in the simulations implies a substantial change of the multiphase “effective model” by SH03, which we have suitably modified to account for (a) the contribution of the energy reservoir provided by the SN which are treated outside the IRA, and (b) the metal–dependence of the cooling function, that we introduce using the tables from Sutherland & Dopita (1993). The resulting density threshold for a gas particle to become multiphase, thereby being eligible to undergo star formation, is fixed to $n_H = 0.1 \text{ cm}^{-3}$ at zero metallicity. According to Eq.(23) of SH03, this threshold is inversely proportional to the cooling function. Since the latter depends on metallicity, we take self–consistently a metallicity–dependent star–formation threshold for gas having a non-zero metallicity.

SH03 also provided a phenomenological description for galactic winds, which are triggered by SN energy release and whose strength is regulated by two parameters. The first one gives the wind mass loading according to the relation, $\dot{M}_W = \eta \dot{M}_*$, where \dot{M}_* is the star formation rate. Following SH03, we assume $\eta = 3$. The second parameter is the wind velocity, v_w . For the runs based on the Salpeter IMF, we always use $v_w = 500 \text{ km s}^{-1}$. For the above values of η and v_w , all the energy from SN-II is converted in kinetic energy, as in the original SH03 paper. Springel & Hernquist (2003c) made a study of the star formation history predicted by hydrodynamical simulations which include galactic winds with a similar velocity. They concluded that the resulting star fraction at $z = 0$ and high- z star formation history are comparable to the observed ones. In order to verify the effect of galactic ejecta, the g676 and g51 regions are also simulated with the Salpeter IMF, but setting to zero the wind velocity (Sa-NW runs). As for the runs based on the top–heavy IMF, we will also use $v_w = 500 \text{ km s}^{-1}$ for all clusters, with the exception of g676 and g51 regions, for which we also use $v_w = 1000 \text{ km s}^{-1}$ (TH-SW runs). In this case, the two wind speeds correspond to an energy budget of about 0.4 and 1.4 times the energy provided by SN-II. An efficiency larger than unity can be justified on the ground of the large uncertainties on the actual energy released by SN-II explosions. In this perspective, we also take the value of the wind velocity as a confidence value. A wind velocity $v_w = 1000 \text{ km s}^{-1}$ is intended to represent an extreme feedback case, so that comparing the results with the two values of wind velocity allows us to check the effect of a stronger feedback on the final properties of the galaxy population. We summarise in Table 4.2 the IMFs and feedback used in our simulations.

SIMULATIONS OF THE GALAXY POPULATION IN NEARBY CLUSTERS

Table 4.2: Characteristics of the simulations. Col. 1: simulation name; Col. 2: IMF slope; Col 3: wind speed, v_w (units of km s^{-1}).

Name	IMF slope	v_w
Sa	1.35	500
Sa-NW	1.35	0
TH	0.95	500
TH-SW	0.95	1000

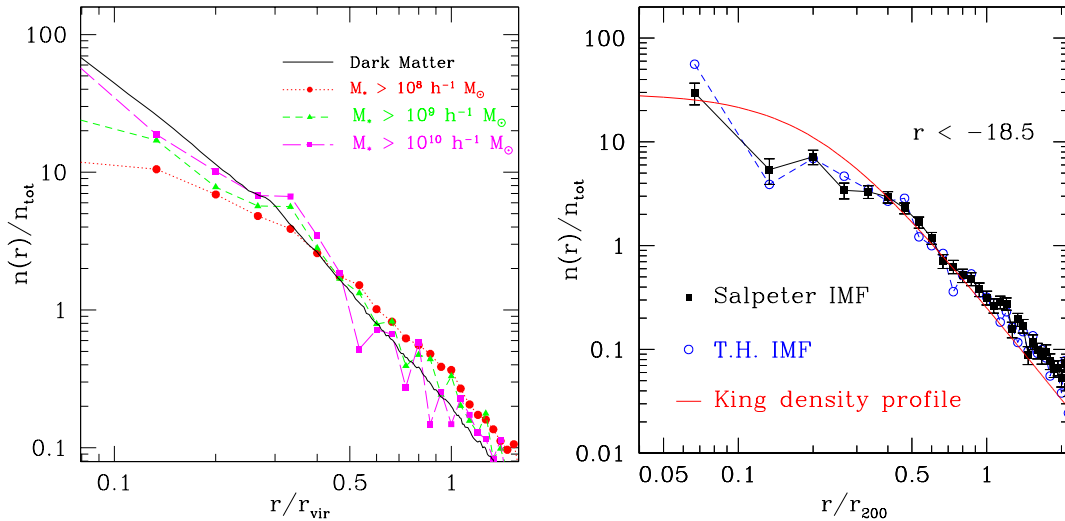


Figure 4.3: The number density profile of cluster galaxies. Left panel: the profiles of galaxies of different stellar mass, averaged over all clusters, for the runs with Salpeter IMF (filled symbols). Shown with the solid curve is the average DM profile. All profiles are normalised to the total number density within the virial radius. Right panel: The number density of galaxies, brighter than $r = -18.5$, contained within a given radius, normalised to the total number density found within the r_{200} . Filled squares and open circles are by combining all the simulated clusters, for the Salpeter and for the top-heavy IMF, respectively. The solid curve is the best-fit King model to the number density profiles of cluster galaxies from the analysis of RASS–SDSS data by Popesso et al. (2006b), here plotted with arbitrary normalisation. Error-bars in the simulation profile correspond to Poissonian uncertainties. For reasons of clarity they have been plotted only for the Salpeter runs.

4.2 ASSIGNING LUMINOSITIES TO GALAXIES

As a first step, we identify galaxies from the distribution of star particles by applying the SKID algorithm³ (Stadel, 2001) as already discussed in Chapter 3. We recall to the reader

³See <http://www-hpcc.astro.washington.edu/tools/skid.html>

that we identify as “bona fide” galaxies only those SKID–groups containing at least 32 star particles after the removal of unbound stars.

Since each star particle is treated as a SSP, with formation redshift z_f and metallicity Z , we can assign to it luminosities in different bands by resorting to a spectrophotometric code, for the appropriate IMF used in the corresponding simulation.

To this purpose, we have used the outputs of the GALAXEV code by Bruzual & Charlot (2003) (see Chapter 3) to create a grid of metallicity and age values for a SSP of $1M_\odot$. Luminosities in different bands are then assigned to each SSP of this grid. Since two different IMFs are used for our simulations, this grid is also computed for both the Salpeter (1955) and the top–heavy IMF. Note that GALAXEV assumes that contributions of different metal species to the total metallicity are in solar proportions, while this is not necessarily true for the star particles in our simulations. For this reason, we use the total metallicity of each star particle (i.e., the sum of the contributions from the different elements) as input for GALAXEV. We have verified that, using instead Iron or Oxygen as proxy for the global metallicity, our final results are left essentially unchanged. Consistent with the stellar evolution implemented in the simulation code, GALAXEV accounts for stellar mass loss. Therefore, we use the initial mass of each star particle in the simulations as input to GALAXEV to compute the corresponding luminosities. For each star particle we interpolate its age and metallicity with the appropriate entries of the grid. Finally, we evaluate the luminosity $L_{*,\nu}$ of each star particle, which is treated as a SSP of mass M_* and age t , in the ν band by:

$$L_{*,\nu}(t) = \frac{M_*(t)}{M_\odot} L_\nu(1M_\odot) \quad (4.1)$$

In this way, the luminosity in the ν band of each galaxy is given by the sum of the luminosities contributed by each member star particle. As a final result, for each galaxy our analysis provides stellar mass, mean stellar age, metallicity, star-formation rate (SFR), absolute magnitudes in the U, B, V, R, I, J, K , bolometric standard Johnson bands and in the g, u, r, i, z SLOAN bands.

We note that GALAXEV accounts for metallicity values in the range 0.005–2.6 Z_\odot . While only a negligible number of stars have a metallicity below the lower limit of this interval, a sizeable number of particles, especially for the top–heavy IMF, are found with metallicities exceeding the upper limit. Whenever the particle metallicity lies outside the above range, they are set to the value of the nearest boundary.

4.3 RESULTS

4.3.1. The number-density profile of cluster galaxies

A well established result from collisionless simulations of galaxy clusters is that the radial distribution of galaxy–sized sub-halos is less concentrated than that of DM (e.g. Ghigna

et al., 2000a; Springel et al., 2001; De Lucia et al., 2004a), and also less concentrated and more extended than the observed radial distribution of cluster galaxies (e.g. Diemand et al., 2004; Gao et al., 2004a). While some residual numerical over-merging can still be present at the high resolution achieved in DM-only simulations, it has been suggested (Diemand et al., 2004) that over-merging may be physical in origin and related to the dissipation-less dynamics. The possibility to include radiative cooling and star formation in hydrodynamical simulations allows one to verify whether the same result holds also for the galaxies identified from the star distribution. The general conclusion from these analyses is that the radial distribution of simulated galaxies is indeed more concentrated than that of DM sub-halos (e.g., Nagai & Kravtsov, 2005). An intermediate approach, based on coupling semi-analytical models of galaxy formation with high resolution collisionless simulations (e.g., Springel et al., 2001; Kravtsov et al., 2004; Gao et al., 2004a; De Lucia et al., 2004b; Lanzoni et al., 2005), confirms that the radial distribution of galaxies is more extended compared to DM. Clearly, the dynamics of halo formation in these studies is driven by the collisionless component. Therefore, suitable effective recipes should be included to prevent physical over-merging of galaxies within DM halos, so as to achieve agreement with the observed radial galaxy distribution (e.g. Springel et al., 2001; De Lucia et al., 2004b).

We show in the left panel of Figure 4.3 the number density profiles of cluster galaxies, after averaging over all the simulated clusters, compared to the corresponding average DM density profile. As discussed by Nagai & Kravtsov (2005), selecting galaxies in hydrodynamical simulations of clusters, which include star formation, produces profiles which are generally steeper than those of DM halos. We confirm here that galaxy profiles become closer to the DM profile as more massive galaxies are selected, with objects more massive than $10^{10} M_{\odot}$ tracing a distribution quite close to the DM one. This is just the consequence of the improved capability of more massive galaxies to preserve their identity within merging halos. Indeed, since galaxies are more concentrated than their hosting DM halos, they are able to better survive to disruption and merging, thereby providing a better sampling of the underlying DM distribution. While this trend is generally consistent with observations, a close comparison with data requires assigning luminosities to simulated galaxies. For this reason, we also show in the right panel of Fig.4.3 the number density profiles of galaxies brighter than $r = -18.5$ and compare it to the best fit to the observed profiles by Popesso et al. (2006b), who trace these profiles out to $\simeq 2r_{200}$. Galaxies of this luminosity have a typical stellar mass of the order of $5 \times 10^9 M_{\odot}$ in the simulations with Salpeter IMF. In general, the observed and the simulated profiles are quite similar down to $\simeq 0.4r_{200}$. At smaller radii there is a trend for simulated galaxies to have a lower number density than in real clusters. Therefore, although tracing galaxies instead of DM halos helps in the comparison with the observed galaxy profiles, still over-merging is the likely reason for the shallower profile as traced by simulated galaxies.

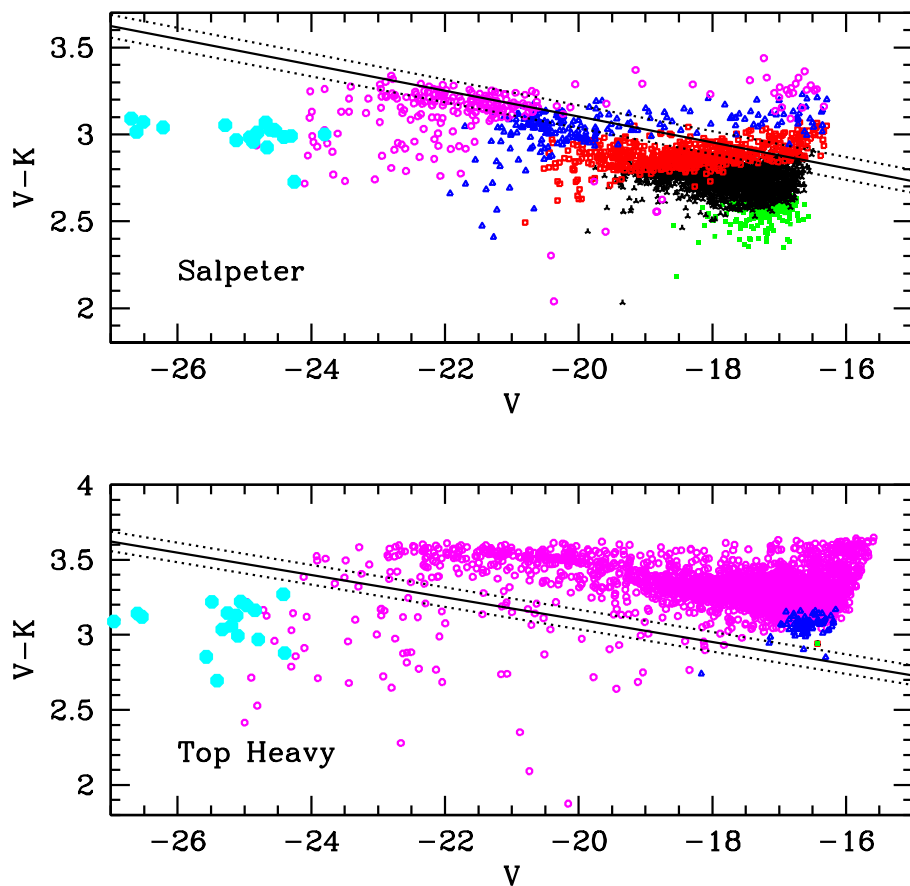


Figure 4.4: The $V-K$ vs. V colour–magnitude relation by combining all the galaxies within the virial radii of the simulated clusters, for the Salpeter IMF (top panel) and for the top–heavy IMF with normal feedback (bottom panel). Straight lines in each panel show the observed CMR relations by Bower et al. (1992), with the corresponding intrinsic standard deviations. Big filled dots mark the BCG of each cluster. Different symbols and colours are used for galaxies having different metallicities. Magenta open circles: $Z > 1.5Z_{\odot}$; blue filled triangles: $1.5 < Z/Z_{\odot} < 1$; red open squares: $1 < Z/Z_{\odot} < 0.7$; black open triangles: $0.7 < Z/Z_{\odot} < 0.4$; green filled squares: $Z < 0.4Z_{\odot}$.

4.3.2. The colour–magnitude relation

As discussed in Chapter 2, bright massive ellipticals, which dominate the population of cluster galaxies, are observed to form a tight correlation between galaxy colours and magnitudes, the so–called red sequence or colour–magnitude relation (CMR) (e.g., Bower et al., 1992; Prugniel & Simien, 1996; Andreon et al., 2004; López-Cruz et al., 2004; Gladders & Yee,

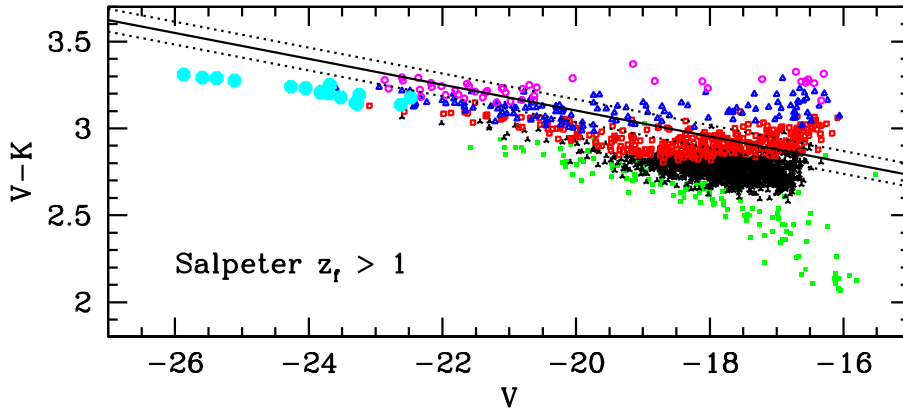


Figure 4.5: The same as the top panel of Figure 4.4, but only including in the computation of the luminosities the star particles having redshift of formation $z_f > 1$.

2005; McIntosh et al., 2005). Attempts to compare the observed CMR to that predicted by cosmological models of galaxy formation have been performing both using semi-analytical approaches (e.g., De Lucia et al., 2004b; Lanzoni et al., 2005) and full hydrodynamical simulations (Romeo et al., 2005). As a general results, model predictions reproduce the slope of the CMR reasonably well, but with a scatter which is generally larger than observed. Romeo et al. (2005) simulated one Virgo-sized and one Coma-sized cluster. They found that a top-heavy IMF reproduces the normalisation of the CMR better than a Salpeter IMF, which gives too blue colours as a consequence of the too low metallicity. This conclusion is at variance with respect to that reached by De Lucia et al. (2004a) who, instead, reproduce the correct CMR normalisation with a Salpeter IMF. Thanks to the larger number of simulated clusters, we can perform the comparison between simulated and observed CMR with much improved statistics. The results of this comparison are shown in Figure 4.4. As a term of comparison, we use the observational determinations by Bower et al. (1992) (see also Terlevich et al. 2001) for the $V - K$ vs. V CMR, which has been determined in the magnitude range $[-18, -23]$. Quite apparently, a Salpeter IMF is successful in reproducing the correct amplitude of the CMR at the bright end, $V \lesssim -20$, while it tends to produce too blue faint galaxies. The slope of the CMR appears to be driven by metallicity, the brighter galaxies being redder mainly as a consequence of their higher metal content, thus in line with the interpretation by Kodama & Arimoto (1997). At the same time, we note that a top-heavy IMF produces too metal-rich galaxies, thereby inducing too high a normalisation of the CMR.

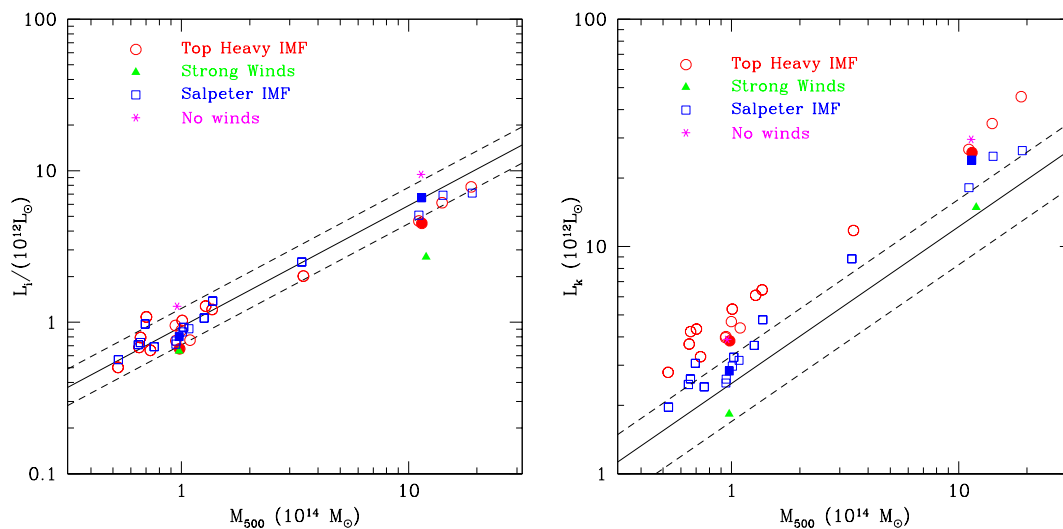


Figure 4.6: The comparison between simulated and observed relation between mass and luminosity in the i band (left panel) and in the K band (right panel). In each panel, squares are for the Salpeter IMF, circles for the top-heavy IMF with normal feedback, triangles for the top-heavy IMF with strong feedback and asterisks for the Salpeter IMF with no feedback. Filled squares and circles are for the g676 and g51 runs, so as to make clear the effect of changing the feedback strength. The straight solid lines are the best fitting results from Popesso et al. (2005) for the i band and from Lin et al. (2004) for the K band, with the dashed lines marking the corresponding observational scatter.

The metal content of galaxies is clearly determined by the combined action of stellar nucleosynthesis and other processes which bring enriched gas far from star forming regions, thus preventing all metals from being locked back in newly forming stars. Processes, such as ram pressure stripping (e.g., Domainko et al., 2006) and galactic winds (e.g., Aguirre et al., 2001) have been suggested as the possible mechanisms to enrich the diffuse intergalactic medium. Clearly, the more efficient these mechanisms, the lower the expected metallicity of stars and, therefore, the bluer their colours. In order to verify whether more efficient galactic winds may decrease the metallicity of galaxies in the runs with top-heavy IMF, we have re-simulated the g676 and g51 clusters using $v_w = 1000 \text{ km s}^{-1}$ for the galactic winds (TH-SW runs). However, while the effect of the stronger feedback is that of decreasing the number of galaxies, (see also Sect. 4.3.4 below), it leaves their metal content, and, therefore, the high CMR normalisation, almost unchanged.

Although a Salpeter IMF fares rather well as for the CMR, we note that all the BCGs (big filled circles in Fig.4.4) are much bluer, by about 0.5 magnitude, than expected from the red sequence. Such a blue excess of the colours of the BCGs, which takes place despite their high metallicity, finds its origin in the large star formation rate, associated to over-cooling,

which takes place in the central cluster regions. Typical values for the star formation rate of the BCG in our simulations are in range 600–1000 M_{\odot}/yr for the most massive clusters ($M_{200} \simeq 10^{15} M_{\odot}$) and $\sim 100 M_{\odot}/\text{yr}$ for the least massive ones ($M_{200} \simeq 10^{14} M_{\odot}$). Although observations indicate the presence of some ongoing star formation in some BCGs located at the centre of cool core clusters, they are always at a much lower level and consistent with a star formation rate of $\sim 10\text{--}100 M_{\odot}/\text{yr}$ for clusters of comparable richness (e.g., Johnstone et al., 1987; Bregman et al., 2006; McNamara et al., 2006, and references therein).

The effect of recent star formation on the CMR is explicitly shown in Figure 4.5. We show here the case in which all star particles, formed at redshift $z < 1$ are excluded from the computation of the galaxy luminosities. This is equivalent to assume that we completely quench star formation since $z = 1$. Neglecting recent star formation has the twofold effect of reducing the scatter in the CMR and of making BCG colours significantly redder, although they still fall slightly below the observed relation.

4.3.3. The mass–luminosity ratio

In Chapter 2 we presented a number of observational analyses which have established that the mass–to–light ratio in clusters generally increases with the cluster mass, $M/L \propto M^{\gamma}$ with $\gamma \simeq 0.2\text{--}0.4$, over a fairly large dynamic range, from poor groups to rich clusters (e.g., Adami et al., 1998; Girardi et al., 2000, 2002; Bahcall & Comerford, 2002; Lin et al., 2003, 2004; Rines et al., 2004b; Ramella et al., 2004; Popesso et al., 2005). A likely explanation for this trend is the reduced cooling efficiency within more massive, hotter halos (e.g., Springel & Hernquist, 2003c), which reduces star formation within richer clusters. In fact, an increasing trend of M/L with cluster mass is naturally predicted by semi–analytical models of galaxy formation (e.g., Kauffmann et al., 1999a).

In Figure 4.6 we compare the relation between mass and luminosity within r_{500} for our simulated clusters, and compare it to the i –band results by Popesso et al. (2005) and to the K –band results by Lin et al. (2004). In general, we find that the M/L from simulations is rather close to the observed one in the i band, also with a comparably small scatter. In the K band, a Salpeter IMF still agrees with observations within the statistical uncertainties, while the top–heavy IMF produces too red galaxies, thus consistent with the results of the CMR, as shown in Fig.4.4. We fit our mass–luminosity relation with a power–law

$$\frac{L}{10^{12} L_{\odot}} = \beta \left(\frac{M_{500}}{10^{14} M_{\odot}} \right)^{\alpha}, \quad (4.2)$$

we find $(\alpha, \beta)_i = (0.74, 0.92)$ and $(\alpha, \beta)_K = (0.76, 3.2)$ in the i and K band, respectively, for the runs with Salpeter IMF, while $(\alpha, \beta)_i = (0.70, 0.91)$ and $(\alpha, \beta)_K = (0.74, 4.7)$ for the top–heavy IMF. Therefore, our simulations agree with the observational trend for an increasing mass-to-light ratio with cluster mass, independent of the IMF and luminosity band. Using the stronger feedback for the top–heavy IMF turns into a sizeable suppression

of the luminosity, especially for g51.

The reasonable level of agreement between the observed and the simulated M/L may suggest that our simulations produces a realistic population of galaxies. However, as demonstrated in Figure 4.7, this is not the case. In this figure, we compare the simulated and observed number of cluster galaxies, brighter than a given luminosity limit, both in i and in the K bands. Clearly, simulations under-predict such a number, by a factor $\sim 2-3$. This result is at variance with respect to that from semi-analytical models of galaxy formation, which instead predict the correct number of cluster members (e.g., De Lucia et al., 2004b; Lanzoni et al., 2005). However, semi-analytical models are generally successful in producing the correct LF. They employ a suitable technique to track galaxies, based on the assumption that, once a "satellite" galaxy is formed inside a DM halo, it preserves its identity and survive to a possible disruption of the hosting halo (Springel et al., 2001). Accordingly, the position of a galaxy is later assigned to the position of the DM particle which was most bound within the DM halo before it was disrupted, thereby preventing an excessive merging rate between galaxies.

On the one hand, it is tempting to explain the lack of galaxies in our simulations as the result of an excessive merging. On the other hand, the inclusion of radiative cooling and star formation should produce galaxies in our simulations which, in fact, survive to the merging of DM halos, and behave as the "satellite" galaxies introduced in the semi-analytical models. Clearly, a reason of concern in our simulations is related to the force and mass resolutions adopted (see Section 4.1), which may produce fragile galaxies and/or induce spurious numerical over-merging. In Section 4.4 we present a resolution study which is aimed at verifying whether and by how much the cluster galaxy population changes when increasing the resolution. After varying the mass resolution by a factor 45, and the corresponding softening parameters by a factor $\simeq 3.6$, we find no appreciable variations of the stellar mass function of cluster galaxies. We also verified that the lack of galaxies is not related to numerical heating induced by an non optimal choice of gravitational softening (e.g., Thomas & Couchman, 1992). After running a series of simulations, using different choices for ϵ_{pl} , we find that our softening choice is very close to that maximising the low end of the galaxy stellar mass function.

As for the effect of feedback, a wind velocity of 500 km s^{-1} is large enough to devoid the gas content of galaxies with mass $M \lesssim 10^{11} M_{\odot}$ and, therefore, to suppress the number of galaxies above the luminosity limits considered in Fig. 4.7. Wind velocities this high are generally expected for star-burst galaxies (e.g., Heckman, 2003), while they may be too high for the general galaxy population. In order to test this effect, we have performed simulations of g676 and g51 with Salpeter IMF in the extreme case in which winds are excluded. In these cases, the numbers of galaxies reported in Fig.4.7 increase by more than a factor of two, thus bringing simulation results into much better agreement with observational data. However, the price to pay for this is the increased total luminosities, as a result of the larger number of stars formed, which introduces a tension between simulations and observations, as shown in Fig.4.6. The need to reconcile at the same time the number of galaxies and

the total luminosity points toward a scenario in which feedback is relatively less effective in small galaxies, while being more effective in suppressing star formation in massive rare objects. Since massive galaxies are observed to be almost passively evolving, this implies that the required feedback mechanism should not be directly linked to star formation. In this respect, AGN have been suggested to be the natural source for this kind of feedback (e.g., Croton et al., 2006; Bower et al., 2006; Menci et al., 2006; De Lucia & Blaizot, 2007).

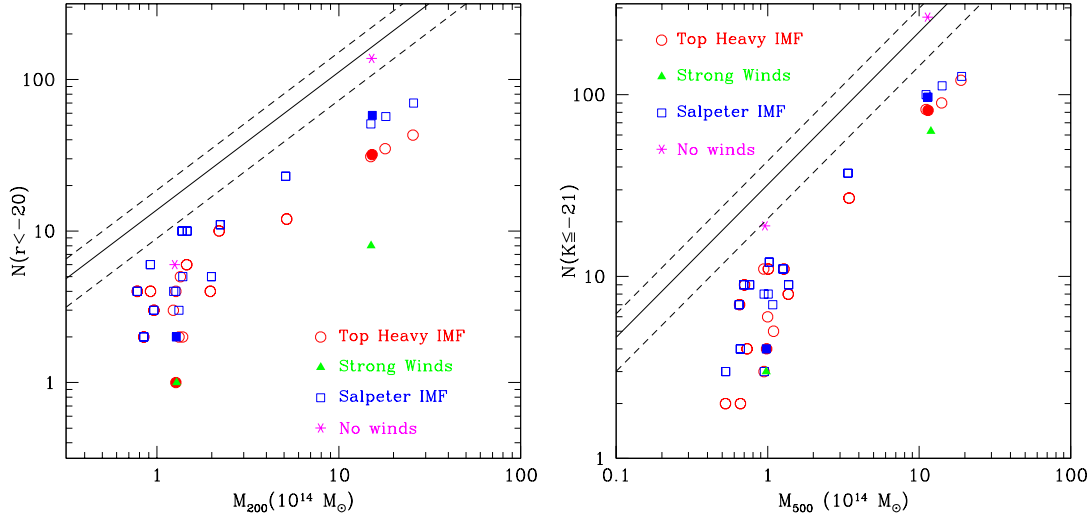


Figure 4.7: The number of galaxies within clusters above a given luminosity limit. Left panel: results in the r band, compared to the observational best-fitting result from SDSS data by Popesso et al. (2006b) (the dashed lines mark the intrinsic scatter of the observational relation). Right panel: results in the K band, compared to the observational best-fitting result from 2MASS data by Lin et al. (2004). Symbols for the simulations have the same meaning as in Figure 4.6.

4.3.4. The luminosity function

The luminosity function (LF) of cluster galaxies has been the subject of numerous studies through the years (e.g., Dressler, 1978; Colless, 1989; Biviano et al., 1995; Goto et al., 2002; De Propriis et al., 2003; Popesso et al., 2006a, and references therein). Despite this, a general consensus on a number of issues has still to be reached. Among them, we mention the LF universality among clusters and between clusters and field, and the slope of the faint end. For instance, Popesso et al. (2006a) have recently analysed SDSS data for a set of cluster selected in the X-ray band in the RASS. As a result, they found that the LF is universal, once calculated within the same physical radius, r_{200} or r_{500} . Furthermore, the LF can not be fitted by a single Schechter (1976) function, since it displays a marked upturn at faint magnitudes.

Similar, a steepening on the faint end of the LF in the Coma cluster core is also found by Milne et al. (2007). These results is at variance with other analyses. For instance, Adami et al. (2000) and Mobasher et al. (2003) performed deep spectroscopic survey of the Coma cluster and found no evidence for an upturn of the LF at faint magnitudes.

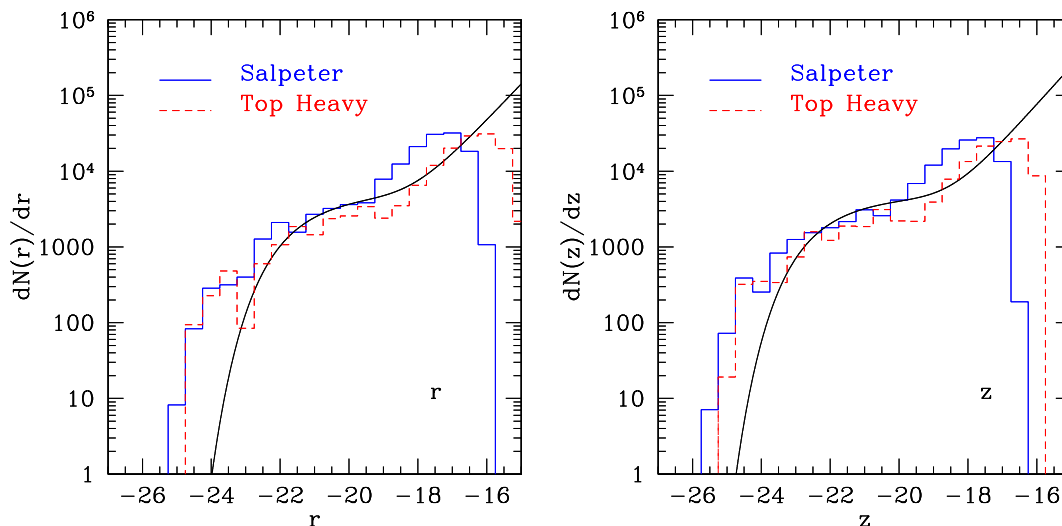


Figure 4.8: The Comparison between the simulated (histograms) and the observed (curves) luminosity functions of cluster galaxies in the Sloan- r (left panel) and z (right panel) bands. The smooth curves are the best fit to the SDSS data analysed by Popesso et al. (2006a). In each panel, the solid and the dashed histograms are for the Salpeter and for the top-heavy IMF, respectively. Normalisation of the simulated LF are chosen to match the observed one at $r = -20$ and $z = -20$ with the Salpeter LF. Consistent with the observational analysis, the brightest cluster galaxies (BCGs) are not included in the computation of the luminosity function.

In the following, we will discuss a comparison between the LF in our simulated clusters and the observational results by Popesso et al. (2006a). To this purpose, we have computed the simulated LF, within r_{200} , in the r and z bands, which are two of the four SDSS bands where the analysis by Popesso et al. (2006a) has been performed. Consistently with their approach, we have used the procedure introduced by Colless (1989) to compute a composite luminosity function from the contribution of clusters having different richness. Accordingly, the number of galaxies N_j within the j -th luminosity bin is defined as

$$N_j = \frac{N_0}{m_j} \sum_i \frac{N_{ij}}{N_{0,i}}. \quad (4.3)$$

Here m_j is the number of clusters having galaxies in the j -th luminosity bin, N_{ij} is the number of galaxies in that luminosity bin contributed by the i -th cluster, $N_{0,i}$ is the LF

normalisation for the i -th cluster and $N_0 = \sum_i N_{0,i}$. Following Popesso et al. (2006a), we compute $N_{0,i}$ as the number of galaxies in the i -th cluster which are brighter than r , $z = -19$. With this definition, each cluster is weighted inversely to its richness, in such a way to avoid the richest clusters to dominate the shape of the LF. Also, consistent with Popesso et al. (2006a), we do not include the BCGs in the estimate of the LF. Owing to the too small number of galaxies found in our simulated clusters, we already know in advance that the normalisation of the simulated LF must be lower than the simulated one. Therefore, we decide to normalise the simulated LF by hand, so that the LF for the Salpeter IMF matches the observed one at $r = -20$ and $z = -20$. The resulting rescaling factor is then used also to re-normalise the LF for the runs with the top-heavy IMF. In this way, we preserve the difference in normalisation between the two series of runs, which is induced by the different choices for the IMF.

The results of this comparison are shown in Figure 4.8. The bright end of the simulated LF is clearly shallower than that of the observed one. This is consistent with the picture that over-cooling takes place within the more massive halos, which hosts the brighter galaxies. The simulated LF shows a steepening at the faint end, which resembles that found by Popesso et al. (2006a). Looking at the combined differential stellar mass function of all the cluster galaxies (see Figure 4.9), we note an indication for a steepening of its slope at the low-mass end, $M_* \lesssim 3 \times 10^{10} M_\odot$. It is this steepening which causes the corresponding steepening of the luminosity functions. Quite interestingly, the faint end of the CMR (see Fig. 4.4) shows a population of small red galaxies, which are in fact associated to the excess of faint galaxies shown by the luminosity function. It is tempting to make a correspondence between these galaxies and the faint red galaxies which are claimed by Popesso et al. (2006a) to contribute to the steepening of their luminosity function. However, we consider it as premature to draw strong conclusions about the slope of the luminosity function in simulations until the latter will be demonstrated to roughly produce the correct total number of galaxies.

A comparison between the LFs produced by the Salpeter and the top-heavy IMF shows that the latter is shifted towards fainter magnitude, especially in the faint end. This effect is also visible in the corresponding stellar mass functions of the cluster galaxies (see Fig.4.9). While both IMFs produces indistinguishable mass functions at the high end, galaxy masses for the top-heavy IMF tend to have lower values. This difference is induced by the larger metal content associated to the top-heavy IMF, which makes cooling more efficient within halos near the resolution limit. Finally, we show in Figure 4.10 the effect of increasing the feedback efficiency on the LF. In this case, we use the same normalisation for the two IMFs, in order to directly see the effect of changing the feedback strength. Quite interestingly, the effect is that of suppressing the bright end of the LF, while leaving the faint end almost unaffected.

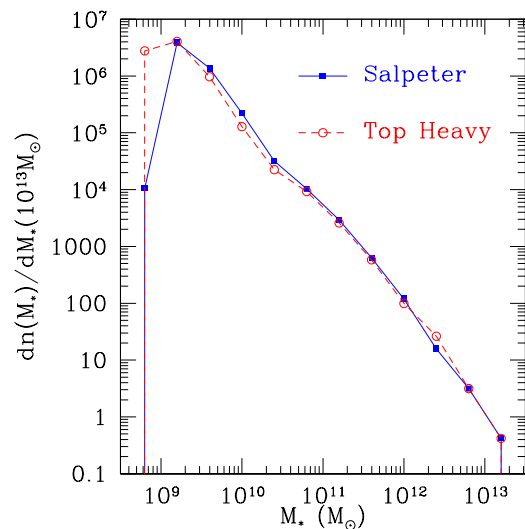


Figure 4.9: The combined stellar mass function for the galaxies identified within r_{200} of all clusters. The solid and the dashed histograms correspond to the Salpeter and to the top-heavy IMF, respectively.

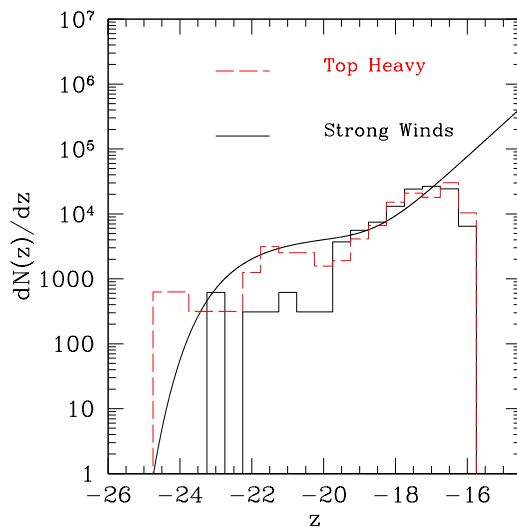


Figure 4.10: The effect of a stronger feedback on the z -band luminosity function. The histograms show the combined luminosity function for the g51 and g676 clusters in the case of standard feedback ($v_w = 500 \text{ km s}^{-1}$, dashed line) and of strong feedback ($v_w = 1000 \text{ km s}^{-1}$, solid line). The smooth curve is the best-fit to the SDSS data by Popesso et al. (2006a).

4.3.5. Radial dependence of the galaxy population

A number of observations have established that the galaxy population in clusters is characterised by the presence of colour gradients, with bluer galaxies preferentially avoiding to reside in the innermost cluster regions (Butcher & Oemler, 1984). For instance, Pimblet et al. (2006) found a decreasing trend of the $B - R$ colour with cluster-centric distance for the galaxies lying on the CMR of nearby optically selected clusters. Similar results have also been found by Abraham et al. (1996), Carlberg et al. (1997) and Wake et al. (2005) for moderately distant X-ray selected clusters. Quite consistently, outer cluster regions are populated by a larger fraction of blue galaxies (e.g., De Propris et al., 2004), thus confirming that more external galaxies are generally characterised by a relatively younger stellar population. This effect may result both as a consequence of the cluster environment, which excises star formation in infalling galaxies, and/or due to an earlier formation epoch of galaxies residing in the cluster centre (e.g., Ellingson et al., 2001). In general, the presence of a gradient in the galaxy colours is naturally predicted by semi-analytical models of galaxy formation (e.g., Diaferio et al., 2001b).

In the left panel of Figure 4.11 we show the radial variation of the $B - V$ colour for all galaxies found in our set of simulated clusters. Consistent with observational results, the mean galaxy colours become bluer as we move towards the outer cluster regions. Quite remarkably, this effect extends well beyond the virial radius, thus implying that galaxies feel the cluster environment already at fairly large distances. While the trend exists for both a Salpeter and a top-heavy IMF, the latter generally predicts much redder colours, consistent with the CMR results shown in Fig. 4.4. Our results for the Salpeter IMF are consistent with those reported by Diaferio et al. (2001b) for the low-redshift bin ($0.18 < z < 0.3$) of the CNOC1 cluster sample.

We note a sudden inversion of the colour gradients in the innermost regions, where galaxies are characterised by much bluer colours. These galaxies generally correspond to the cluster BCGs, which, as already discussed are much bluer than expected from the CMR red sequence (see Fig. 4.4). In fact, the galaxies identified in this region correspond to the BCG, which, as we have already discussed, are characterised by a strong excess of star formation. The effect is more pronounced for the top-heavy IMF, which produces more metals and, therefore, makes over-cooling even stronger. This highlights once again the presence of too high a cooling rate at the centre of the simulated clusters, which is not prevented by the model of SN feedback adopted in our simulations. The presence of colour gradients corresponds to the presence of age gradients. We show in the right panel of Fig. 4.11 the radial dependence of the fraction of galaxies younger than 8.5 Gyrs. Quite apparently, there is a continuous trend for galaxies to be younger in the outer cluster regions. The trend extends out to $2r_{vir}$, with no evidence for convergence for a stable mean age in the field. This result further confirms that the presence of a cluster induces environmental effects in the galaxy population already at quite large distances. Much like for the colours, we note an inversion of the trend in the innermost regions, which is due to the excess star formation taking place

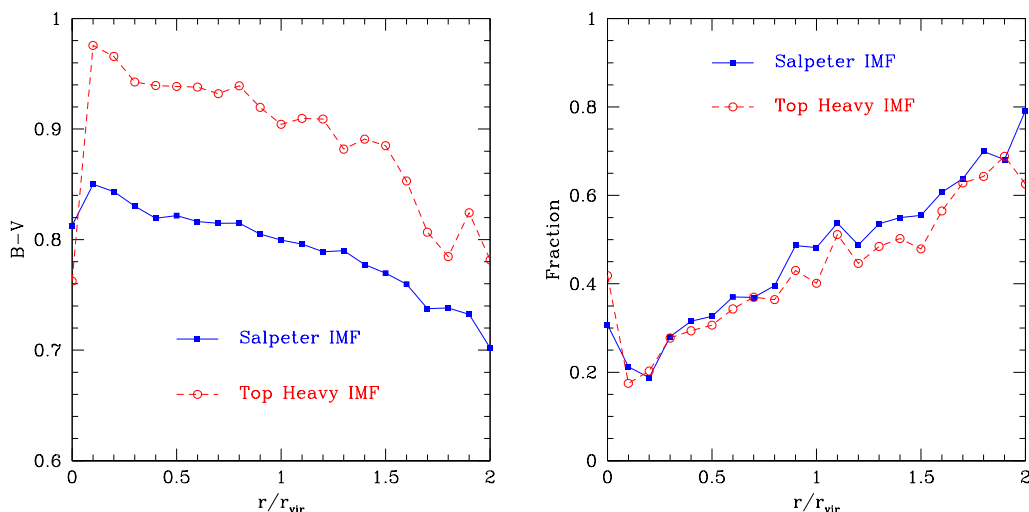


Figure 4.11: Left panel: The radial dependence of galaxy colours, averaged over all simulated clusters. In each panel, solid lines with filled squares are for the Salpeter IMF, while dashed line with open circles are for the top-heavy IMF. The reported results are the average over all the simulated clusters. Right panel: The fraction of galaxies younger than 8.5 Gyr, as a function of cluster-centric distance, in units of r_{vir} . Symbols and line types have the same meaning as in the left panel.

in the central BCGs. The fact that the inversion is more pronounced for the top-heavy IMF is in line with its higher enrichment, which makes gas cooling more efficient.

A consistent result also holds for the radial dependence of the star formation rate (SFR). In Figure 4.12 we show the specific SFR (i.e., the SFR per unit stellar mass) as a function of the cluster-centric distance. Once we exclude the contribution of the BCG in the central bin, we observe a steady increase of the SFR toward external cluster regions. In general, these results are in line with observational evidences for a younger, more star forming galaxy population in the cluster outskirts. For instance, Biviano et al. (1997) analysed the galaxy population in the ESO Nearby Abell Cluster Survey (ENACS) and found that emission-line galaxies tends to under populate the central regions of clusters. Balogh et al. (1997) analysed data from the CNOC1 survey of medium-distant galaxy clusters ($z \simeq 0.2-0.6$) and found evidences for a continuous increase of the SFR out to $2r_{200}$. In a similar way, Moran et al. (2005) analysed a large sample of spectroscopic data, covering a ~ 10 Mpc regions around a Cl0024 at $z \simeq 0.4$. Again, they found that galaxies appear to be younger at large radii. However, differently from our results, they detect evidences for an increase of star formation around r_{vir} , possibly triggered by the interaction with the dense environment of the ICM.

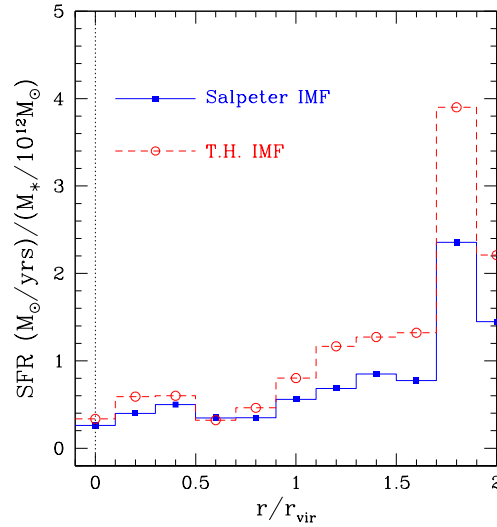


Figure 4.12: The specific mean star formation rate, averaged over all the simulated clusters, as a function of the cluster–centric distance. Symbols and line types have the same meaning as in Figure 4.11. In the central bin we have excluded the contribution from the BCGs.

4.3.6. The SN-Ia rate

The supernova rate represents a useful diagnostic to link the observed evolution of the ICM metallicity to the past history of star formation and to shed light on the relative contribution of SN-Ia and SN-II in releasing metals. In particular the ratio between the SN rate and the B-band luminosity, the so-called SNU_B , can be used to distinguish the relative contribution of SN-Ia, which form in binary systems of stars with masses in the range $(0.8-8) M_\odot$ and the short-living massive stars that contribute substantially to the B-band luminosity of galaxies. In this section we present a comparison between the results of our four most massive simulated clusters and observational data of SNU_B in galaxy clusters from Gal-Yam et al. (2002), Mannucci et al. (2008) and Sharon et al. (2007). For each of the simulated clusters we adopted three different shapes for the stellar initial mass function. Besides the Salpeter (1955) IMF, we used also the IMF proposed by Kroupa (2001) and the top–heavier IMF by Arimoto & Yoshii (1987). In the following, we label the runs that use the Salpeter, Arimoto–Yoshii and Kroupa IMFs with *Sal*, *AY* and *Kr* respectively. As for the set of simulated clusters discussed in the previous Sections, for our reference runs we will use $A = 0.1^4$, as suggested by Matteucci & Gibson (1995) to reproduce the observed ICM metallicity (see also Portinari et al. 2004). As we shall discuss in the following, the simulation with the *AY* IMF tends to overproduce Iron (see also Section 4.3.2). In the attempt to overcome this problem, we also

⁴We recall that A is the fraction of stars, in the mass range $0.8-8 M_\odot$, belonging to binary systems which explodes as SN-Ia in the single–degenerate scenario, see Chapter 3

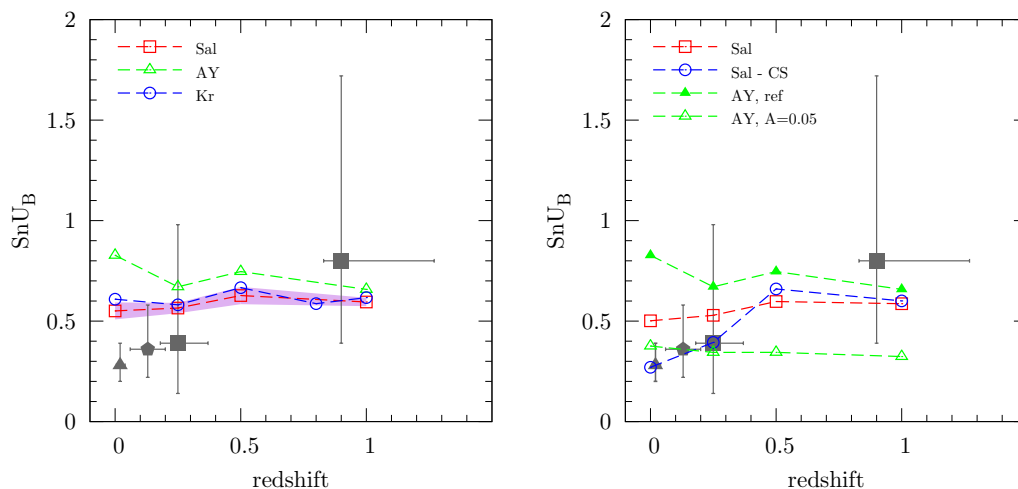


Figure 4.13: Comparison between the observed and the simulated evolution of the SN-Ia rate per unit B-band luminosity (SNU_B). In both panels, filled symbols with error-bars refer to observational data from Mannucci et al. (2008) (triangle), Gal-Yam et al. (2002) (squares) and Sharon et al. (2007) (pentagon). Left panel: the effect of changing the IMF. The open squares are for the Salpeter (1955) IMF, the open triangles are for the top-heavy IMF by Arimoto & Yoshii (1987a) and the open circles for the IMF by Kroupa (2001). For the Salpeter IMF, the shaded area show the r.m.s. scatter evaluated over the four simulated clusters, while for the other two IMFs only the result for the g51 cluster is shown. Right panel: the effect of suppressing low-redshift star formation and of changing the binary fraction on the SNU_B evolution of the g51 cluster. The open squares and the open circles are for the reference run with Salpeter (1955) IMF and for the same run with cooling and star formation stopped at $z = 1$ (CS run), respectively. The filled and the open triangles are for the runs with Arimoto & Yoshii (1987a) IMF, using $A = 0.1$ and $A = 0.05$ for the fraction of binary stars, respectively.

carried out a run with the AY IMF using also $A = 0.05$. The simulation analysis finalised to compute the SNU_B proceeds as follows. We compute the SNU_B values by also including the contribution of the SN-Ia arising from diffuse stars, while the B-band luminosity is computed by including only the contribution of the identified galaxies, as explained in Section 4.2.

In the left panel of Figure 4.13 we compare the SNU_B values from the simulations with different IMFs with observational data. In performing this comparison one potential ambiguity arises from the definition of the extraction radius, within which luminosities and SN-Ia rates are measured in observations, since different authors use different aperture radii. To address this issue we computed SNU_B in the simulations within R_{vir} and verified that the

results are left unchanged when using instead R_{500} .

Observational data show a declining trend at low redshift. This is generally interpreted as due to the quenching of recent star formation, which causes the number of SN-Ia per unit B-band luminosity to decrease after the typical lifetime of the SN-Ia progenitor has elapsed. On the other hand, our simulations predict a rather flat evolution of the SNU_B , independently of the choice for the IMF, which is the consequence of the excess of low-redshift star formation. The runs based on the Salpeter and on the Kroupa IMF produce very similar results. Although the Kroupa IMF produces a higher rate of SN-Ia, due to its higher amplitude in the $(1-8) M_\odot$ stellar mass range, this is compensated by the higher values of L_B . These two IMFs both agree with the observational data at $z \gtrsim 0.3$ within the large observational uncertainties, while they over-predict the rates measured for local clusters. Although the excess of recent star formation in the central regions of our simulated clusters produces too blue BCGs (see previous Sections), the large number of SN-Ia associated to this star-formation overcompensate the excess of blue light.

As for the simulation with the Arimoto–Yoshii IMF, it predicts an even higher SNU_B at low redshift. As shown in the right panel of Fig.4.13, decreasing the binary fraction to $A = 0.05$ decreases the value of the SNU_B by more than a factor 2. While this helps in reconciling the simulation results with the low-redshift data, it introduces a tension with the data at $z \sim 1$.

Truncating star formation at $z = 1$ (right panel of Fig.4.13) has the desired effect of decreasing the value of SNU_B below $z = 0.5$. Quite interesting, for $0.5 \lesssim z \lesssim 1$ the decreasing trend of the SN-Ia rate is compensated by the corresponding decrease of the B-band luminosity, while it is only at $z > 0.5$ that the decrease of the SN-Ia rate takes over and causes the decrease of the SNU_B values.

4.4 TESTING NUMERICAL EFFECTS ON THE GALAXY STELLAR MASS FUNCTION

In this Section we discuss the stability, against possible numerical effects, of the stellar mass function of the galaxies identified inside simulated clusters. In particular, we will focus the analysis on (a) the effect of changing the softening of the gravitational force, to control the possible presence of spurious numerical heating (e.g., Thomas & Couchman, 1992); (b) the effect of mass and force resolution. As for the softening choice, it is known that using too small values may induce spurious heating of the gas particles by two-body collisions, thereby inhibiting gas cooling inside small halos. On the other hand, increasing it to too large a value also reduces the number of galaxies as a consequence of the lower number of resolved small halos (Borgani et al., 2006). As for the resolution, increasing it has the effect to better resolve the low end of the mass function and, in general, is expected to produce a more reliable galaxy population.

4.4. Testing numerical effects on the galaxy stellar mass function

The tests described in this Section are based on three cluster sized halos, which have been re-simulated by varying mass and force resolution. These clusters have virial masses in the range $(1.6\text{--}2.9) \times 10^{14} M_{\odot}$ and are described in detail by Borgani et al. (2006). They have been simulated for the same cosmological model of the clusters described in the previous sections, but with a lower normalisation of the power spectrum, $\sigma_8 = 0.8$. At the lowest resolution, the mass of the gas particle is $m_{\text{gas}} \simeq 6.9 \times 10^8 M_{\odot}$ and the Plummer–equivalent softening for gravitational forces is set to $\epsilon = 7.5h^{-1}\text{kpc}$ at $z = 0$. We point out that the simulations analysed and described in Section 4.1.1 have a mass resolution which is better than the above one by about a factor of four. Runs at increasingly higher resolution have been performed by decreasing the particle masses by a factor 3, 10 and 45, with the softening correspondingly decreased according to the $m^{1/3}$ scaling. Therefore, at the highest resolution, it is $m_{\text{gas}} \simeq 1.5 \times 10^7 M_{\odot}$ and $\epsilon = 2.1h^{-1}\text{kpc}$. This mass resolution is $\simeq 11$ times higher than used for the set of simulations described in Section 4.1.1. For the most massive of these three clusters, we have also repeated the simulation at 10 times the basic mass resolution with four different choices of the gravitational softening. In particular, we have decreased it by a factor two, with respect to the standard choice, and increased it by a factor two and four. As such, this set of simulations allows us to verify the stability of the galaxy stellar mass function against changing mass resolution and the choice for the gravitational softening.

The simulations have been performed with the original prescription for star formation and feedback presented by Springel & Hernquist (2003b), with a wind speed $v_w \simeq 480 \text{ km s}^{-1}$, therefore comparable to that assumed in previous analysis as standard feedback. However, those runs did not include the prescription for stellar evolution and chemical enrichment, which we used for the simulations analysed in this Chapter. Since each gas particle is allowed to spawn two star particles, the latter have a mass which is half of that of the parent gas particle. As discussed by Borgani et al. (2006), this series of runs produces an amount of stars within the virial radius of the clusters, which is almost independent of the resolution, thereby preventing the runaway of cooling with increasing resolution. We show in Figure 4.14 the effect of varying the softening on the cumulative stellar mass function of the galaxies identified inside the virial radius. As expected, decreasing the softening to half the standard value has the effect of suppressing the low end of the mass function, $M \lesssim 2 \times 10^{10} h^{-1} M_{\odot}$, as a consequence of spurious numerical heating of gas. On the other hand, increasing the softening by a factor four also induces a suppression of low–mass galaxies, as a consequence of the lack of resolution. At larger masses, using a too small softening has the effect of increasing the mass function, although the rather small number of galaxies in the high mass end prevents from detecting systematic trends. These results demonstrate that our lack of galaxies can not be explained by a non–optimal choice of the gravitational force softening. As for the effect of resolution, we plot in Figure 4.15 the combined cumulative stellar mass function for all the galaxies identified within the virial radii of the three clusters, simulated at four different resolutions. The first apparent effect of increasing resolution is that of steepening the mass function in the low mass end. In the mass range where galaxies are identified with at least

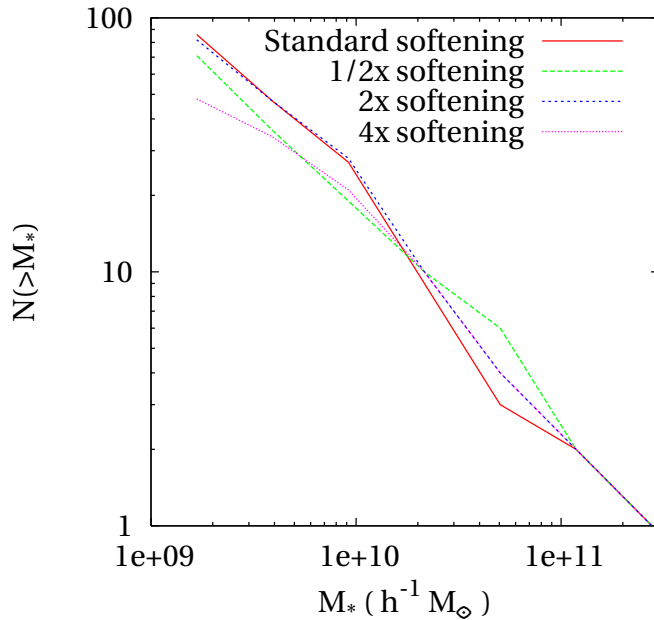


Figure 4.14: The cumulative stellar mass function of the galaxies identified within the virial radii of the most massive among the three simulated clusters described in this Section (see also Borgani et al. 2006). All the simulations have been done at fixed mass resolution, which correspond to an increase by a factor 10 with respect to the basic resolution (i.e., $m_{\text{gas}} \simeq 6.9 \times 10^7 M_{\odot}$; see text). The four curves correspond to the different choices for the gravitational softening. The labels indicate the factor by which the softening has been changed, with respect to the standard choice of $3.5h^{-1}\text{kpc}$.

64 star particles at the different resolutions, which correspond to $M_* \simeq 2.2 \times 10^{10} h^{-1} M_{\odot}$ for the lowest resolution run, the mass functions have a weaker dependence on resolution, with a decreasing trend of the high end of the mass function. This steepening of the high end of the mass function at increasing resolution is the consequence of the reduction of overmerging, which makes small halos surviving more efficiently and, therefore, prevents their disruption and accretion inside massive halos. This result demonstrates that, at least at the highest resolution reached in this test, also resolution is not the reason for the too low number of galaxies found in the simulated clusters, when compared to observations (see discussion in Sect. 4.3.3).

4.5 SUMMARY AND DISCUSSION

In this Chapter we have presented an analysis of the galaxy population in cosmological hydrodynamical simulations of galaxy clusters at $z = 0$. The inclusion of a detailed treatment

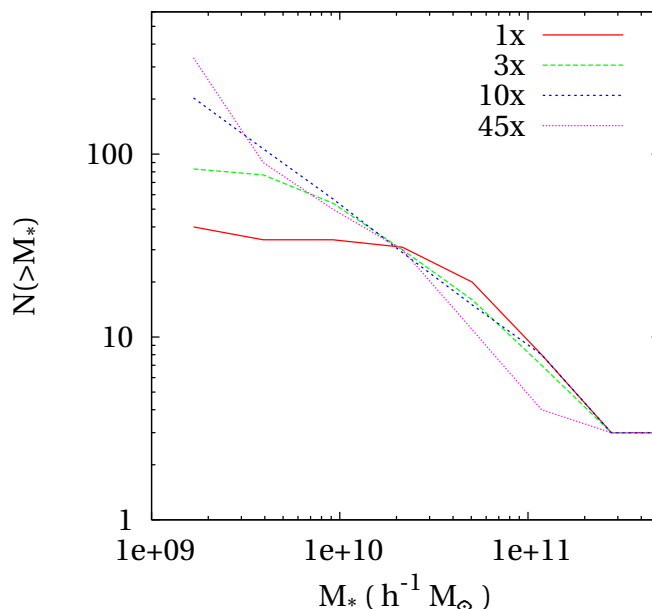


Figure 4.15: The combined cumulative stellar mass function of the galaxies identified within the virial radii of the three clusters. The four curves correspond to the different resolutions at which the clusters have been simulated. Continuous, long-dashed, short-dashed and dotted curves are for the simulations at progressively increasing resolution. The labels indicate the factor by which mass resolution is increased, with respect to the lowest resolution run (1x).

of stellar evolution and chemical enrichment (Tornatore et al. 2004; Tornatore et al. 2007a) in the GADGET-2 code (Springel, 2005) has allowed us to derive the properties of galaxies in the optical/near-IR bands. In our simulations each star particle is treated as a single stellar population (SSP) characterised by a formation time and a metallicity. Based on this, we apply the GALAXEV spectro-photometric code (Bruzual & Charlot, 2003) to compute luminosities in different bands. Simulations have been carried out for a representative set of galaxy clusters, containing 19 objects with mass M_{200} ranging from $5 \times 10^{13} M_{\odot}$ to $1.8 \times 10^{15} M_{\odot}$. All clusters have been simulated assuming both a standard Salpeter IMF (Salpeter, 1955) and a power-law top-heavier IMF with exponent $x = 0.95$ (Arimoto & Yoshii, 1987a). The main results of our analysis can be summarised as follows.

1. Both the colour-magnitude relation (CMR) and the M/L ratio are in reasonable agreement with observational data for a Salpeter IMF. In contrast, using a top-heavy IMF provides too high a metallicity of galaxies, which turns into too red colours. This spoils the agreement with the CMR and with the M/L ratio in the K band. The CMR is confirmed to be a metallicity sequence, in the sense that more enriched galaxies systematically populate the brighter redder part of the sequence.

SIMULATIONS OF THE GALAXY POPULATION IN NEARBY CLUSTERS

2. Galaxies are systematically older and redder in central cluster regions, thus in keeping with observational results. This trend extends at least out to $2r_{vir}$, thus showing that the galaxy population feels the presence of a cluster well beyond its virial region.
3. Due to the over-cooling occurring in the central cluster regions, BCGs are always much bluer and more massive than observed, and characterised by too high a recent star formation. Indeed, neglecting the contribution of stars formed at $z < 1$ produces significantly redder BCGs, thus in better agreement with observational data.
4. The number density profile of galaxies is confirmed to steepen with the galaxy stellar mass, approaching the DM profile for the galaxies with $M_* > 10^{10} M_\odot$. However, when compared to the observations (e.g., Popesso et al., 2006b), the simulation profiles are flatter than the observed ones inside $0.4r_{200}$.
5. Simulated clusters have about three times fewer galaxies above a given luminosity limit than real clusters. We have verified that this disagreement is directly related neither to lack of mass and force resolution, nor to numerical gas heating due to a non optimal choice of the softening parameter. This leaves as further possibilities more subtle numerical effects or a better suited implementation of energy feedback.
6. The luminosity function (LF) is shallower than the observed one in the bright end, thus confirming that feedback is not strong enough to suppress cooling in the most massive halos. In the faint end, the LF steepens and indicates the presence of an excess of small red galaxies. Although this result resembles that found in observational data by Popesso et al. (2006a), we warn against its over-interpretation, in the light of the deficit of the overall number of galaxies found in the simulated clusters.
7. A comparison of the SN-Ia rate per unit B–band luminosity, $\text{Sn}U_B$, show that our simulations are generally not able to reproduce the observed declining trend at low redshift. This result is explained by the excess of recent star formation taking place in the central regions of galaxy clusters. Indeed, excising star formation at $z < 1$ produces an evolution of $\text{Sn}U_B$ which is consistent with the observed one.

The results of our analysis support the capability of hydrodynamical simulations of galaxy clusters to reproduce the general trends characterising their galaxy population. Therefore, simulations in which the properties of the stellar population are self-consistently predicted from the gas dynamics, can provide an alternative and complementary approach to semi-analytical methods. However, at present, our simulations have two main limitations in accounting for the observed properties of the cluster galaxy population.

First of all, the deficit of galaxies produced in our simulations suggests that they are not able to produce galaxies which are resistant enough to survive the tidal field of the cluster environment. Indeed, the shallow galaxy number density profile in central cluster regions shows that the problem is more apparent where effects of galaxy disruption are expected to

be stronger. This result on the lack of galaxies is at variance with respect to the predictions of semi-analytical models (SAM) of galaxy formation, which produce roughly the correct number of cluster galaxies (e.g., De Lucia et al., 2004b; Lanzoni et al., 2005). Comparisons between the galaxy populations predicted by hydrodynamical simulations and by SAM have shown a reasonable level of agreement. However, these comparisons have been always performed by excluding the effect of energy feedback (e.g., Helly et al., 2003a; Cattaneo et al., 2007) or explicit conversion of cooled gas particles into collisionless stars (e.g., Yoshida et al., 2002).

Furthermore, we always find that the brightest cluster galaxies (BCGs) are much bluer and star forming than observed. While the adopted feedback scheme, based on galactic winds, is efficient in regulating star formation for the bulk of the galaxy population, it is not able to quench low-redshift star formation in the central cluster regions, to a level consistent with observations. Clearly, the required feedback mechanism should be such to leave the bulk of the galaxy population unaffected while acting only on the very high end of the galaxy mass distribution. Feedback from central AGN represents the natural solution and provides in principle a large enough energy budget (e.g., Rafferty et al., 2006). Its detailed implementation in cosmological hydrodynamical simulations requires understanding in detail the mechanisms for the thermalisation of this energy in the diffuse medium (e.g., Zanni et al., 2005; Sijacki & Springel, 2006).

An ambitious goal for hydrodynamical simulations of the next generation will be that of describing in detail the complex interplay between the history of star formation and the thermodynamical and chemical evolution of the diffuse cosmic baryons. For this to be reached, it is mandatory that simulations are able to produce a realistic population of galaxies, both in terms of colour and of luminosity and mass distribution. Therefore, simulation codes will be required on the one hand to have numerical effects under exquisite control and, on the other hand, to include physically motivated schemes of energy and metal feedback.

CHAPTER 5

SIMULATING THE CORE OF A PROTO-CLUSTER REGION AT $z \simeq 2$

In this Chapter we address the question of how simulations compare with observations at high redshift. We will present results from high-resolution simulations of two proto-cluster regions at $z \sim 2$ that we compare to observational results of the Spiderweb galaxy presented in Chapter 2. In Section 5.1 we will present the main characteristics of the simulated proto-clusters. The aim of this analysis is to verify to what extent simulations of proto-cluster regions in a standard cosmological scenario resemble the observed properties of the Spiderweb complex. We will discuss these points from Section 5.2 to Section 5.4. Furthermore, we provide predictions on the properties of the proto intra-cluster medium (ICM), in view of future deep X-ray observations of high-redshift proto-cluster regions in Section 5.5. We will present our conclusions in Section 5.6.

The content of this Chapter largely reflects the results presented in a paper which has already been published (Saro et al. 2009).

As already discussed in the Introduction, within the standard cosmological model of structure formation, galaxy clusters trace regions where the hierarchical build up of galaxies and their interaction with the inter-galactic medium (IGM) proceed at a somewhat faster rate compared to regions of the Universe with ‘average’ density. Finding and observing high-redshift progenitors of galaxy clusters can provide invaluable information on the processes which led to their formation and evolution. The most distant clusters to date have been identified out to $z \lesssim 1.5$ from deep X-ray and infra-red observations (e.g. Mullis et al., 2005; Eisenhardt et al., 2008b; Stanford et al., 2005, and references therein). A powerful technique, that extends these studies to higher redshift, is to search for over-densities of emission line galaxies in the neighbourhood of luminous high-redshift radio galaxies (e.g. Pentericci et al., 1998). Although these regions are expected not to trace virialised clusters, they likely identify the progenitors of present day clusters, offering a unique opportunity to study the evolutionary processes which determine their observational properties. Recently, a number

of observations of distant putative proto-clusters, like the one associated with the so-called “Spiderweb Galaxy” at $z = 2.16$ (Miley et al. 2006), have demonstrated that these regions are characterised by intense dynamical and star formation activity (e.g. Pentericci et al. 2000, M06, Venemans et al. 2007; Overzier et al. 2008, and references therein).

On the theoretical side, modern cosmological hydrodynamical simulations are now reaching good enough resolution, and include detailed treatments of a number of astrophysical processes, to provide an accurate description of the assembly of galaxy clusters. As shown in the previous Chapter, these simulations are now able to reproduce the basic properties observed for the bulk of the cluster galaxy population at low redshift, while generally predicting too massive and too blue BGCs, due to the absence on an efficient feedback mechanism that suppresses the star formation activity in these galaxies at late times (e.g., Saro et al., 2006; Romeo et al., 2008).

5.1 THE SIMULATED PROTO-CLUSTERS

We analyse simulations of two proto-cluster regions, both selected at redshift $z \simeq 2.1$, which by $z = 0$ will form a relatively poor cluster (C1) and a rich cluster (C2). These two regions have been extracted from two different lower resolution parent cosmological boxes, and re-simulated at higher force and mass resolution using the Zoomed Initial Condition (ZIC) technique by Tormen et al. (1997). The parent simulations correspond to two renditions of the Λ CDM cosmological model, with the same values for the parameters $\Omega_m = 0.3$, $h_{100} = 0.7$ and $\Omega_b = 0.04$, and different values for the normalisation of the power spectrum ($\sigma_8 = 0.8$ for C1 - Borgani et al. 2004, and $\sigma_8 = 0.9$ for C2 - Yoshida et al. 2001, see also cluster g8 high resolution from Dolag et al. 2008a, also described in the previous Chapter).

The Lagrangian regions where mass and force resolutions were increased extend out to ~ 10 virial radii of the clusters at $z = 0$. The total number of high resolution DM particles in these regions is about 7.8×10^6 for C1 and 2.4×10^7 for C2, with an initially similar number of gas particles. The basic characteristics of the simulated clusters at $z = 2.1$ are summarised in Table 5.1. At $z = 0$, the masses of these clusters are $M_{200} \simeq 1.6 \times 10^{14} M_\odot$ and $1.8 \times 10^{15} M_\odot$ for C1 and C2 respectively. The mass of each gas particle is $m_{gas} \simeq 1.5 \times 10^7 M_\odot$ for C1, and $2.8 \times 10^7 M_\odot$ for C2. The Plummer-equivalent softening scale for the gravitational force is $\epsilon_{pl} = 2.1 h^{-1}$ kpc for C1 and $2.75 h^{-1}$ kpc for C2, in physical units (e.g. Borgani et al., 2006). We verified that, by suitably rescaling particle velocities in the initial conditions of the C2 cluster so as to decrease σ_8 to 0.8, the virial mass of this system decreases by about 30 per cent, both at $z = 0$ and at $z = 2.1$.

The simulations were carried out using the TreePM-SPH GADGET-2 code (Springel, 2005), including the effective star formation model by Springel & Hernquist (2003b) and the chemical enrichment model by Tornatore et al. (2007b) (see Chapter 3). The effective model of star formation assumes that dense star-forming gas particles have a cold neutral and a hot ionised component, in pressure equilibrium. The cold component represents the reservoir

5.2. Mass and luminosity of proto-cluster galaxies

Table 5.1: Characteristics of the two simulated proto-clusters at $z \simeq 2$. Col. 2: mass contained within r_{200} (in units of $10^{13} M_{\odot}$). Col. 3: r_{200} (in physical $h^{-1}\text{kpc}$). Col. 3 and 4: total stellar mass (in units of $10^{12} M_{\odot}$), and number of identified galaxies within r_{200} . Col. 5: X-ray luminosity in the [0.5–2.0] keV observer-frame energy band (units of $10^{43} \text{erg s}^{-1} \text{cm}^{-2}$). Col. 6: spectroscopic-like temperature. Col. 7: emission weighted Iron metallicity within r_{200} .

Cluster	M_{200}	r_{200}	M_*	N_{gal}	L_X	T_{sl}	Z_{Fe}
C1	2.9	234.7	1.2	491	3.6	1.7	0.37
C2	21.9	452.6	6.6	1571	41.3	4.7	0.46

for star forming material.

Within the adopted stochastic scheme of star formation, each gas particle can spawn three star particles, with mass $m_* \simeq 0.5 \times 10^7 M_{\odot}$ for C1, and $0.9 \times 10^7 M_{\odot}$ for C2. The chemical enrichment model assumes a Salpeter shape (Salpeter, 1955) for the stellar initial mass function (IMF), and uses the same yields and stellar lifetimes adopted in Fabjan et al. (2008). The simulations also include the kinetic feedback from galactic outflows introduced by Springel & Hernquist (2003b). We assume $v_w = 500 \text{ km s}^{-1}$ for the wind velocity, and a mass upload rate equal to two times the local star formation rate. With these choices, the kinetic energy of the outflows is roughly equal to all the energy available from SN-II for the adopted IMF.

Galaxies are identified by applying the SKID algorithm (Stadel, 2001) (see Section 3.6) to the distribution of star particles, using the procedure described in Murante et al. (2007). We identify as “bona fide” galaxies only those SKID-groups containing at least 32 star particles after the removal of unbound stars.

5.2

MASS AND LUMINOSITY OF PROTO-CLUSTER GALAXIES

Figure 5.1 shows the projected stellar mass density maps for C1 (left panel) and C2 (right panel). Simulated maps extend in projection along the whole high-resolution region and are $150 h^{-1}\text{kpc}$ on a side, covering an area which roughly corresponds to the physical size of the ACS images for the assumed cosmology. The maps in Figure 5.1 are qualitatively similar to observations of the Spiderweb complex (Miley et al. 2006), in particular for the C1 cluster, where the most massive galaxy is surrounded by several galaxies of comparable mass in the process of merging to form a dominant central object. The C2 cluster shows evidence of ongoing merging processes onto the BCG, which exhibits a double peaked stellar mass density. In both clusters, a dominant central galaxy is already in place.

Both clusters have a conspicuous population of inter-galactic stars. The presence of a

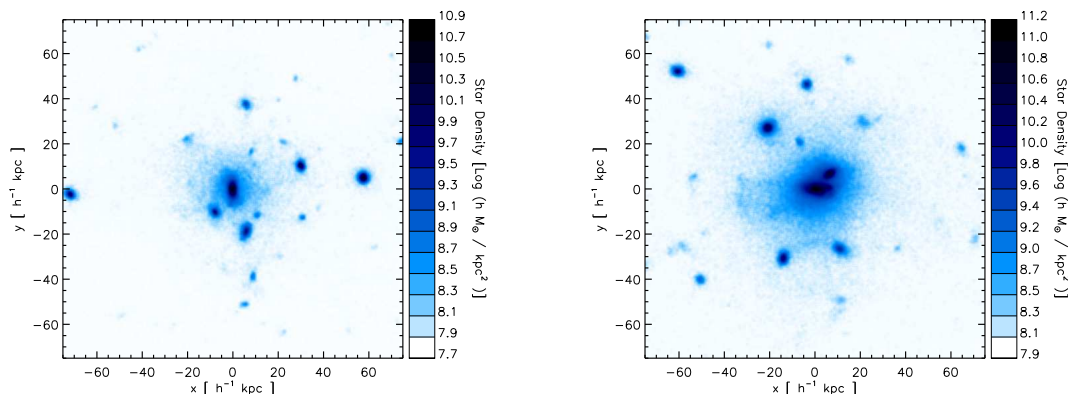


Figure 5.1: The projected stellar mass density for the C1 (left panel) and C2 (right panel) clusters at $z \simeq 2.1$, within a region of $150 h^{-1} \text{kpc}$ on a side, centred on the most massive galaxy.

massive BCG and the visual impression of a significant ongoing merging activity suggest that the merging processes associated to the BCG assembly might be responsible (at least in part) for the generation of the intra-cluster light (e.g. Zibetti et al., 2005; Murante et al., 2007; Pierini et al., 2008). Within the region shown, the diffuse stellar component contributes 16 and 30 per cent of the total stellar mass for C1 and C2 respectively. We also note the presence of several elongated galaxies, similar to the tadpole galaxies observed in the Spiderweb complex (Miley et al. 2006).

The BCG of the C2 cluster has a stellar mass of $4.8 \times 10^{12} M_{\odot}$, about 6 times more massive than the BCG of C1, which is $7.9 \times 10^{11} M_{\odot}$. The second most massive galaxy in the cluster C1 is about a factor four less massive than the BCG, while the second most massive galaxy in the cluster C2 is about a factor ten less massive than the corresponding BCG. Pentericci et al. (1998) estimated the stellar mass of the radio-galaxy in the Spiderweb complex from its K -band luminosity. They found a value of $\sim 10^{12} M_{\odot}$, comparable to the mass of the C1 BCG, but much less massive than the C2 BCG.

As we discussed in the previous Chapter, each star particle is treated as a single stellar population, with formation redshift z_f , metallicity Z , and appropriate IMF. Luminosities in different bands are computed using the spectro-photometric code GALAXEV (Bruzual & Charlot, 2003), as explained in Chapter 4. We have computed luminosities of galaxies in the two HST ACS camera (observer frame) filters F475W (g_{475}) and F814W (I_{814}). All magnitudes given in the following are AB magnitudes. The effect of dust attenuation is included by adopting the two-component model by Charlot & Fall (2000), in a similar way as described in De Lucia & Blaizot (2007) (see also Fontanot et al. 2008). We have divided

5.2. Mass and luminosity of proto-cluster galaxies

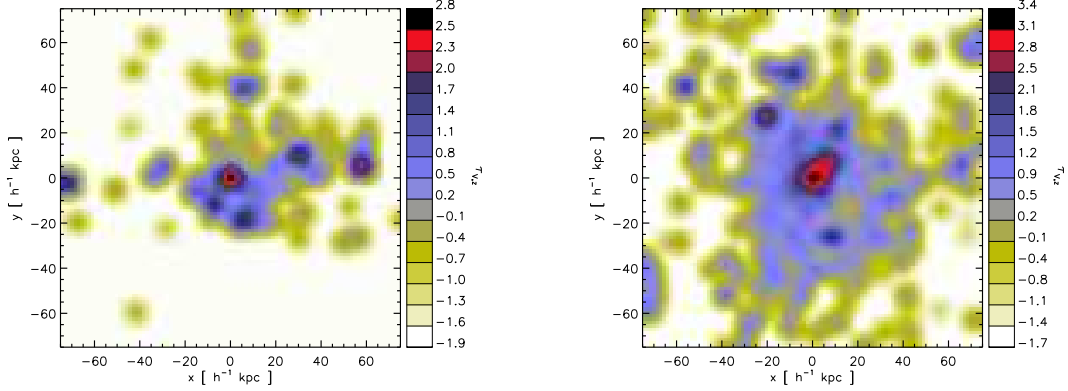


Figure 5.2: The computed optical depth τ_V map in logarithmic scale for the C1 (left panel) and C2 (right panel) clusters at $z \simeq 2.1$, within a region of $150 h^{-1} \text{kpc}$ on a side, centred on the most massive galaxy.

our analysed box into a grid of cubic cells of linear size A . In each cell we have computed the resulting optical depth τ_V as:

$$\tau_V = \left(\frac{Z_{gas}}{Z_{\odot}} \right)^{1.6} \left(\frac{M_{gas}}{2.1 \times 10^{21} \times 1.4 \times m_p \times A^2} \right), \quad (5.1)$$

where m_p is the proton mass and the factor 1.4 scales to the average number of H atoms for a typical chemical composition of gas. M_{gas} and Z_{gas} are the mass and the mean metallicity of cold gas in each cell. Finally the factor 2.1×10^{21} is a normalising factor to typical H column density of galaxies. The resulting optical depth is much less than unity for the majority of the lines of sight, while it is $\tau_V \gg 1$ in the regions of most intense star formation, where τ_V reaches values of about a thousand. Figure 5.2 shows the resulting optical depth τ_V for the two clusters C1 (left panel) and C2 (right panel).

The dust-attenuated luminosity contributed by a star particle, having age t and coordinates (x_i, y_i, z_i) at the position (x_i, y_i, z_f) can be computed as:

$$L_{\lambda, z_f} = L_{\lambda, z_i} \exp \left(- \sum_{j=i}^f \tau_{\lambda}(x_i, y_i, z_j) \right), \quad (5.2)$$

where τ_{λ} is the optical depth at the wavelength λ and is related to τ_V by the relation

$$\tau_{\lambda} = \begin{cases} \tau_V (\lambda / 550 \text{ nm})^{-0.7} & \text{if } t \leq 10^7 \text{ yrs} \\ \mu \tau_V (\lambda / 550 \text{ nm})^{-0.7} & \text{if } t > 10^7 \text{ yrs} \end{cases} \quad (5.3)$$

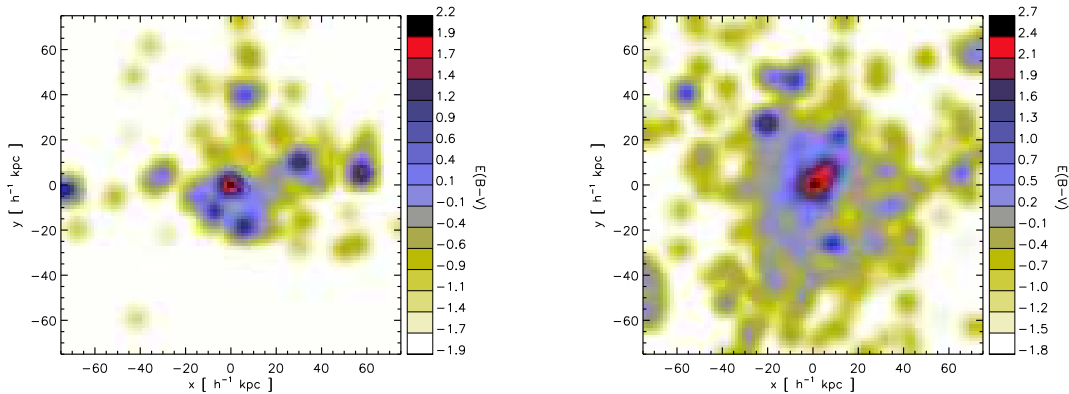


Figure 5.3: The computed reddening $E(B - V)$ map in logarithmic scale for the the C1 (left panel) and C2 (right panel) clusters at $z \simeq 2.1$, within a region of $150 h^{-1} \text{kpc}$ on a side, centred on the most massive galaxy.

where μ is drawn randomly from a Gaussian distribution with mean 0.3 and width 0.2, truncated at 0.1 and 1 (De Lucia & Blaizot 2007, see also Kong et al. 2004).

The resulting $E(B - V)$ computed from the optical depth shown in Figure 5.2 for the two simulated proto-clusters is presented in Figure 5.3. Similar to the optical depth τ_V , also the reddening $E(B - V)$ has a wide range of values and correlates with the cold gas reservoir. In Chapter 2 we have shown that Hatch et al. (2008) have estimate a dust correction of $E(B - V) \sim 0.1 \div 0.25$ associated to the majority of line of sight corresponding to the intergalactic light. We note in Figure 5.3 that the predicted values of $E(B - V)$ in our simulations are of the same order of magnitude in correspondence of the diffuse stellar component, while much higher values characterise star forming regions.

Figure 5.4 shows the luminosity functions (LFs) of the galaxies identified in the two regions shown in Figure 5.1, in the F814W(I_{814}) ACS filter band, including the dust correction described in the previous section. Observational determination by Hatch et al. (2008)¹, are also shown as a dotted histogram. With the adopted dust correction, the luminosity of the C1 BCG is comparable to the observed one, while that of the C2 BCG is about one magnitude brighter than observed. Interestingly, the brightest galaxy in the C2 cluster is not the central galaxy, but a massive galaxy at the edge of the analysed box (it corresponds to the galaxy at the position $x \simeq -60$ and $y \simeq 50$ in the right panel of Figure 5.1). This particular galaxy appears to be quite massive but not star forming (see Figure 5.7). It does not have a signifi-

¹The luminosity function published by Hatch et al. (2008) did not include the correction factor $2.5 \times \log_{10}(1 + z)$ (R.A. Overzier, private communication). We have included this correction in the observed luminosity function plotted in Figure 5.4

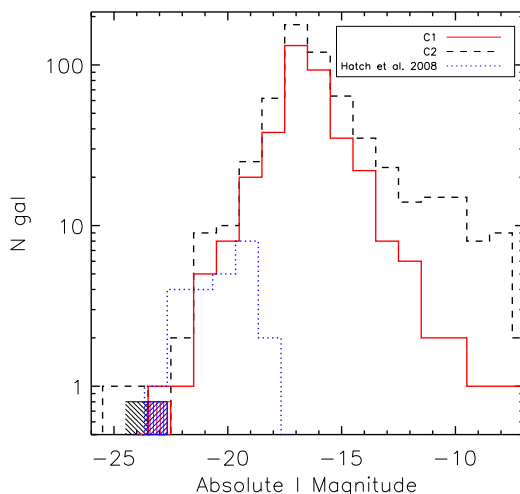


Figure 5.4: Galaxy luminosity function within the region shown in Figure 5.1, in the F814W(I_{814}) ACS filter band. Results for the C1 and for the C2 simulated clusters are shown as solid and dashed histograms respectively. The dotted blue histogram shows the observed luminosity function by Hatch et al. (2008) within the same region. The shaded regions show the luminosity of the observed and of the simulated BCGs, with the same colour code described above.

cant cold gas reservoir and therefore is only weakly attenuated. The BCGs are indicated by shaded regions in Figure 5.4, and appear to be in reasonable agreement with observational measurements. This is in apparent contradiction with the above mentioned evidence for a too large mass of the C2 BCG. This can be explained by the very large star formation rates that are associated to the C2 BCG (see below), which can turn into an excessively large dust extinction. Therefore, having reproduced the UV luminosity does not guarantee that we have correctly described the star formation history of the BCG.

We note that the luminosity functions in our simulations rise steadily at magnitudes fainter than the completeness limit of the observational data. These fainter galaxies are expected to contribute to the budget of diffuse light by an amount which depends of their surface brightness. Summing up the stellar masses of galaxies fainter than $I_{814} = -19$, our simulations predict that the fraction of diffuse stellar component increases by 8 and 5 per cent for the C1 and C2 cluster respectively.

Figures 5.5 and 5.6 show the resulting surface brightness maps projected in the x-y plane in the I_{814} and g_{475} band respectively for the C1 (left) and C2 (right) simulated clusters. We remind the reader that to have a better and more coherent match between observations and simulations, one should convolve a map like those of Figures 5.5 and 5.6 with the PSF of the telescope, add the noise, cut at a limiting magnitude and apply the same criteria used in observations to identify galaxies in the mock images, rather than using dynamical and kinematical informations to identify simulated galaxies. Quite interestingly, even if maps like

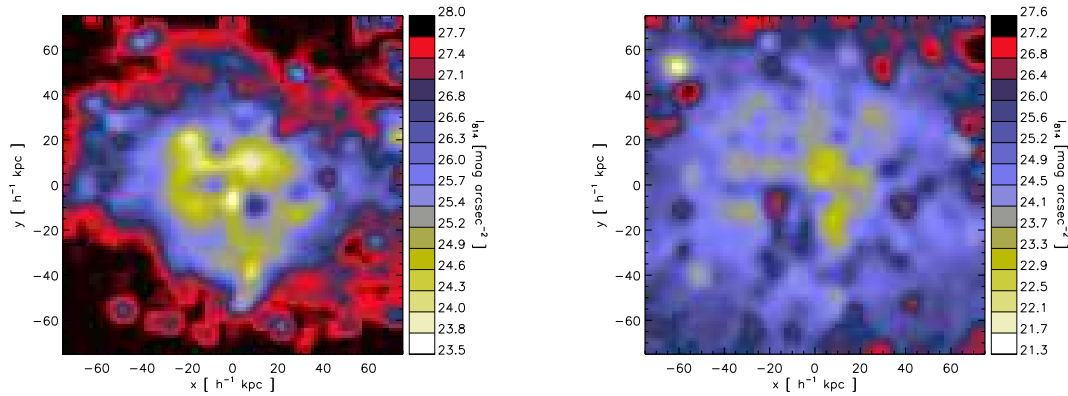


Figure 5.5: The projected surface brightness map in the I_{814} band for the C1 (left panel) and C2 (right panel) clusters at $z \simeq 2.1$, within a region of $150 h^{-1} \text{kpc}$ on a side, centred on the most massive galaxy.

those in Figures 5.5 and 5.6 represent a picture at quite high frequency rest-frame bands as UV and NUV (which are generally associated to star forming regions), they seem to qualitatively reflect better the stellar density map shown in Figure 5.1 rather than map of SFR of Figure 5.7 (see next section).

5.3 STAR FORMATION

Using the observed UV continuum, Hatch et al. (2008) traced the star formation pattern in the Spiderweb complex, finding evidence of diffuse star formation not associated to galaxies. In order to compare the observational results to predictions from our simulations, we show in Figure 5.7 the star formation rate (SFR hereafter) density map for the C1 (left panel) and C2 (right panel) cluster. Red crosses mark the positions of the half most massive galaxies identified within the region shown. The star formation in the simulations is computed for each star-forming gas particle (Springel & Hernquist, 2003b), so Figure 5.7 gives a snapshot of the instantaneous SFR. The total SFR in the region considered is $\sim 600 M_{\odot}/\text{yrs}$ for the C1 cluster and $\sim 1750 M_{\odot}/\text{yrs}$ for the C2 cluster. Hatch et al. (2008) suggest a total SFR for the Spiderweb system of $\simeq 130 M_{\odot}/\text{yrs}$ within an area of 65kpc^2 without any dust correction. Assuming a minimum dust correction of $E(B - V) \simeq 0.1$, they estimate a lower limit of $\simeq 325 M_{\odot}/\text{yrs}$. While this number is reasonably close to that found for C1, bringing it into agreement with the SFR measured for C2 would require a rather unrealistic dust extinction.

Comparing the positions of the galaxies with the distribution of the star formation, it is apparent that they do not always coincide. With the exclusion of the BCGs, which domi-

5.4. Are the proto-clusters in virial equilibrium?

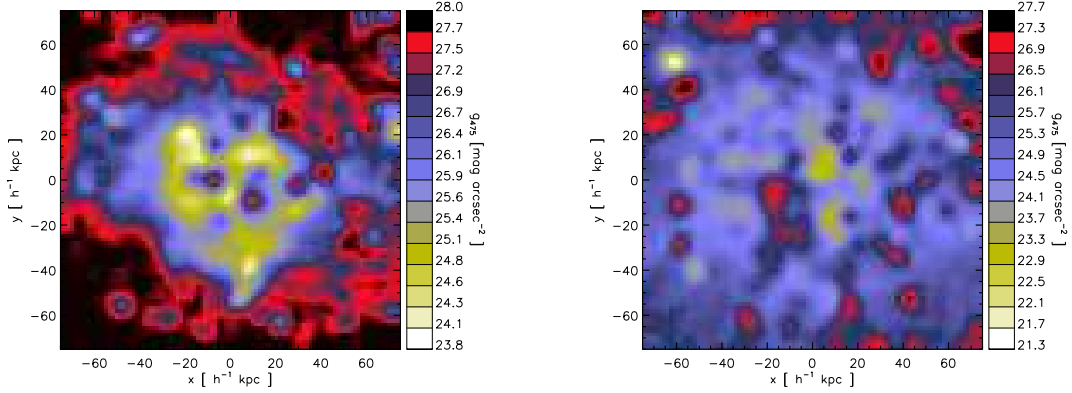


Figure 5.6: The projected surface brightness map in the g_{475} band for the C1 (left panel) and C2 (right panel) clusters at $z \simeq 2.1$, within a region of $150 h^{-1} \text{kpc}$ on a side, centred on the most massive galaxy.

nate the total SFR in both clusters contributing from 55 (C1) to 67 (C2) per cent of the total SFR, most of the massive galaxies are not strongly star forming. The total SFR of identified galaxies accounts for 90 per cent and 81 per cent of the total SFR for the clusters C1 and C2 respectively. The remaining ‘diffuse’ star formation appears to take place both in extended structures and in ‘clumps’. While the former likely trace genuine distributions of diffuse star-forming gas, the clumps often correspond to galaxies which fall below the SKID galaxy identification threshold.

5.4 ARE THE PROTO-CLUSTERS IN VIRIAL EQUILIBRIUM?

Miley et al. (2006) measured line-of-sight velocities for a small number of galaxies and found fairly large values relative to the Spiderweb galaxy, up to almost 2000 km s^{-1} for one galaxy. Although the rather limited statistics prevent an accurate virial analysis of the system, these values hint at a rather large virialised mass. By computing the one-dimensional velocity dispersion (σ_v) for the fifty most massive galaxies contained within r_{200} (i.e. those which more likely will have a redshift measurement in the Spiderweb complex), we find $\sigma_v = 481 \text{ km s}^{-1}$ for C1 and 916 km s^{-1} for C2. These velocities are found to be only 6–8 per cent lower than those estimated from the DM particles, suggesting the presence of a small velocity bias. Using the best-fit $\sigma_v - M_{200}$ relation obtained by Evrard et al. (2008) from a

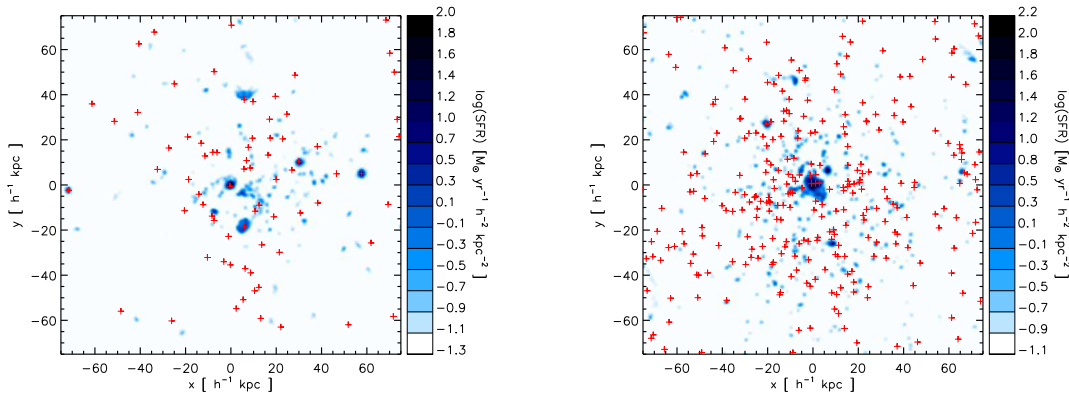


Figure 5.7: The map of star formation rate density for the C1 (left) and C2 (right) cluster, within the same region shown in Figure 5.1. Red crosses mark the positions of the 50 per cent most massive galaxies identified in projection within this region.

variety of N-body simulations, we obtain $M_{200} \simeq 2.7 \times 10^{13} h^{-1} \text{Mpc}$ for C1, and $M_{200} \simeq 1.9 \times 10^{14} h^{-1} \text{Mpc}$ for C2. These values are similar to the true M_{200} values (see Table 1), thus demonstrating that virial equilibrium holds within r_{200} in these proto-cluster regions. We plot in Figure 5.8 the velocity distribution of all galaxies found in projection within the same area shown in Figure 5.1. The effect of line-of-sight contamination from fore/background galaxies is evident for C1, whose distribution shows an excess of galaxies with velocities $\gtrsim 1000 \text{ km s}^{-1}$. For the C2 cluster, we have a non-negligible probability of measuring a relative velocity as large as 2000 km s^{-1} , while this represents a very unlikely event for the C1 cluster. Therefore, even within the limited statistics of available observations, the measured velocities for the flies of the Spiderweb system are preferentially expected in a proto-cluster as massive as C2.

Pentericci et al. (2000) measured redshifts for 15 Ly- α emitters in the Spiderweb region and found a velocity dispersion $\sigma_v = 900 \pm 240 \text{ km s}^{-1}$ (see also Venemans et al. 2007). However, the region sampled by these Ly- α observations has a physical size of about $3 h^{-1} \text{Mpc}$, much larger than the expected virialised region. In order to compare with these observational data, we have computed σ_v for the 50 most massive galaxies within $3 h^{-1} \text{Mpc}$ from the BCGs of our simulated clusters. We find $\sigma_v = 331 \text{ km s}^{-1}$ for C1 and $\sigma_v = 683 \text{ km s}^{-1}$ for C2. This result indicates again that a proto-cluster as massive as C2 is preferred with respect to the poorer C1 cluster. We notice, however, that the resulting velocity dispersion of the poorer C1 cluster is in close agreement with the inferred velocity dispersion of H α emitters around the Spiderweb galaxy by Kurk et al. (2004). Indeed, as discussed in Chapter 2, Kurk et al. (2004) found values of $\sigma_v \sim 360 \text{ km s}^{-1}$, much lower

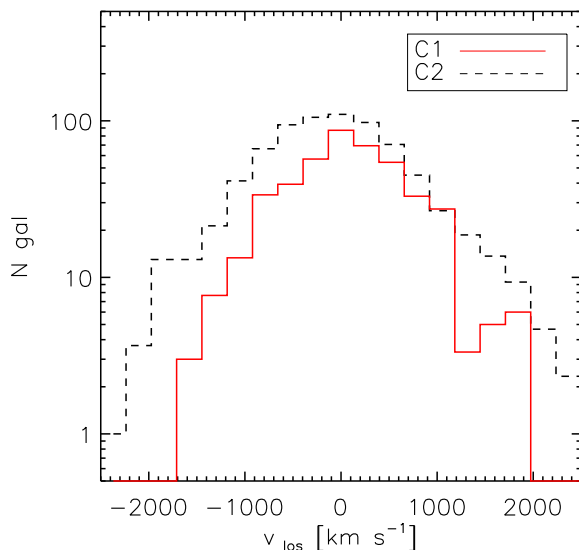


Figure 5.8: Histogram of line-of-sight galaxy velocities the C1 (solid line) and C2 (dashed line) clusters. Each histogram shows the average over three independent projections of a square region of $150 h^{-1} \text{kpc}$ on a side.

than the one of the C2 richer cluster.

The too intense (with respect to observational estimates) star formation that takes place in the C2 BCG suggests that AGN feedback may have already partially quenched star formation in the Spiderweb galaxy. Indeed, the Spiderweb galaxy has been originally identified as a radio-galaxy with extended and distorted radio lobes (Pentericci et al., 1998), consistent with the presence of a “radio-mode” AGN. Furthermore, Nesvadba et al. (2006) carried out an integral-field spectroscopic study of the Spiderweb complex and found evidences for massive outflows of gas which are interpreted as due to the action of AGN feedback.

5.5 PREDICTED X-RAY PROPERTIES

Deep follow-up observations in the X-ray band of a handful of clusters at $z > 1$ are now pushing the study of the thermo- and chemo-dynamical properties of the ICM to large look-back times. Although we have probably to wait for the next generation of X-ray satellites to push these studies to $z \gtrsim 2$, it is interesting to make predictions for the X-ray luminosity, temperature and level of metal enrichment of proto-cluster regions, like the one traced by the Spiderweb galaxy.

Our simulations unambiguously predict that already at $z \simeq 2.1$, the gravitational potential of proto-cluster regions are permeated by a hot ICM. Indeed, for the C1 and C2 clusters we measure a temperature of about 2 and 5 keV, respectively (see Table 1). The X-ray luminosity of C1 is typical of a nearby group, while that of C2 is comparable to the luminosity

of a typical bright nearby cluster. At the redshift of the Spiderweb galaxy, these luminosities correspond to fluxes in the [0.5–2] keV (observer frame) band of about 1.0×10^{-15} for C1 and $1.5 \times 10^{-14} \text{ erg s}^{-1} \text{ cm}^{-2}$ for C2, for the cosmological model assumed in our simulations. A fairly high level of enrichment is predicted already at $z \gtrsim 2$, extending to higher redshift the results obtained out to $z \simeq 1.3$ with Chandra and XMM observations (Balestra et al., 2007; Maughan et al., 2008).

A relatively shallow Chandra observation, with an exposure of 40 ks, has been used by Carilli et al. (2002) to look for an extended X-ray emission around the Spiderweb galaxy. These authors measured a luminosity of $L \simeq 3.5 \times 10^{44} \text{ erg s}^{-1}$ (rescaled to our cosmology) in the [2–10] keV band. They also placed an upper limit of $1.7 \times 10^{44} \text{ erg s}^{-1}$ for a relaxed cluster atmosphere. For C2, we find a luminosity in the same band of about $6.8 \times 10^{44} \text{ erg s}^{-1}$. A luminosity of the hot gas surrounding the Spiderweb galaxy lower than predicted for C2 can be interpreted as due to a significant heating from the radio galaxy. Clearly, the relatively short exposure time of this observation makes a precise determination of the X-ray from a diffuse hot gas rather uncertain.

The flux predicted for C1 can in principle be reached with a sufficient long exposure with the Chandra and XMM satellites. However, surface brightness dimming and the limited extension of the emission likely prevents it from being detectable as an extended source using available X-ray telescopes. For C2, the predicted flux is comparable to (or brighter than) that of clusters at $z > 1$ observed with Chandra and XMM to study the thermal and chemical properties of the ICM. A potential complication for the detection of an extended thermal free-free emission from the hot gas permeating the Spiderweb complex could come from non-thermal X-ray emission associated to star formation and/or generated by the inverse-Compton scattering of a population of relativistic electrons, associated to the radio galaxy, off the CMB photons (Fabian et al., 2003).

Although making a quantitative assessment of the observability of the hot ICM surrounding the Spiderweb galaxy goes beyond the aims of this Chapter, we point out that such a target can be well suited to push the capabilities of the present generation of X-ray satellites, while being optimal for large collecting area telescopes of the next generation.

We note that our analysis is based on only two simulations. Clearly, for a better assessment of the capability of current numerical models in reproducing observations of proto-cluster structures it would be ideal to carry out a statistical comparison by enlarging both the set of simulated clusters and the number of observed proto-cluster regions.

5.6 CONCLUSIONS

We have carried out an analysis of high-resolution hydrodynamical simulations of two proto-cluster regions at $z \simeq 2.1$, with the main purpose of comparing them with the observed properties of the Spiderweb galaxy complex (Miley et al. 2006, Hatch et al. 2008). These proto-clusters will form at $z = 0$ a relatively poor and a rich cluster of galaxies (C1

and C2 respectively; see Table 1). The comparison is aimed at demonstrating to what extent predictions from simulations of proto–cluster regions within a Λ CDM framework are able to reproduce the observational properties of the Spiderweb complex, and to shed light on the processes regulating star formation within the deepest potential wells at $z \sim 2$. The main results of our analysis can be summarised as follows.

- Both simulated proto–clusters are characterised by the presence of a dominant massive central galaxy, surrounded by less massive galaxies in the process of merging, qualitatively resembling the observed Spiderweb galaxy.
- The star formation rate within the C1 proto–cluster ($\sim 600 M_{\odot} \text{yr}^{-1}$) is consistent with the observed one, while the corresponding value for C2 ($\simeq 1750 M_{\odot} \text{yr}^{-1}$) is in excess with respect to observational measurements.
- The BCG of C1 has an UV luminosity comparable to that of the Spiderweb galaxy, while the BCG of the C2 cluster is about one magnitude brighter.
- The velocity dispersions of our simulated clusters within r_{200} are consistent with virial equilibrium expectations. In addition, the velocities measured for the galaxies surrounding the Spiderweb system (Miley et al. (2006), Venemans et al. 2007) are generally consistent with those of the C2 cluster, while being much larger than those measured for C1.
- The inter-galactic medium permeating the C1 and C2 proto–cluster regions has temperatures of about 2 keV and 5 keV respectively, and both clusters exhibit an enrichment level comparable to that observed in nearby clusters. The predicted X–ray fluxes from thermal bremsstrahlung make these objects potentially detectable as extended sources, and make them ideal targets to study the enrichment of the intra–cluster medium at unprecedented redshift, with X–ray telescopes of the next generation.

The emerging scenario is that the Spiderweb complex likely traces the formation of a rich galaxy cluster, whose virial mass at $z = 0$ is $\sim 10^{15} h^{-1} \text{Mpc}$. The excess of star formation found in our simulations suggests that an AGN feedback might be necessary already at $z \sim 2$ to quench star formation and regulate the structure of the “cool core” (see also Nesvadba et al., 2006). The search for proto-cluster regions at $z \gtrsim 2$ and their follow–up observations with X–ray telescopes of the next generation will contribute to fill the gap between $z \lesssim 1$ studies of the thermo- and chemo-dynamics of the ICM and the study of the IGM at $z > 2$.

CHAPTER 6

THE EFFECT OF GAS-DYNAMICS ON SEMI-ANALYTIC MODELING OF CLUSTER GALAXIES

In the previous two Chapters we presented results on the properties of the galaxy population in clusters by using direct high-resolution hydrodynamical cosmological simulations. Besides this method, a complementary tool to study galaxy formation within a cosmological framework is provided by semi-analytic models (SAMs). In hybrid SAM (see Section 3.7) the merging history of haloes is usually traced by DM N-body simulations, while the physics of baryons is followed with simplified prescriptions. The use of DM only simulations to predict the merging history of haloes could in principle provide non fully correct description of the gravitational dynamics of merging when also a gas component is present. In this Chapter we have used a hybrid SAM (De Lucia & Blaizot, 2007) to address this point, by comparing SAM prediction of four clusters simulated with only DM particles and with both DM and gas particles. The plan of the Chapter is as follows. In Sec. 6.1 we describe the cluster simulations used in this study, and describe the method used for the construction of the galaxy merger trees. In Sec. 6.2 we provide a brief description of the SAM adopted, and in Sec. 6.3 we present the results of our analysis. Finally, in Sec. 6.4, we summarise our findings and give our conclusions. The content of this Chapter largely reflects the results presented in one paper which has already been published (Saro et al. 2008). During the last

decade, a number of observational tests of the standard cosmological model have ushered in a new era of ‘precision cosmology’. Precise measurements of angular structure in the Cosmic Microwave Background (CMB), combined with other geometrical and dynamical cosmological tests have constrained cosmological parameters tightly (Komatsu et al., 2008, and references therein) confirming the hierarchical cold dark matter model (CDM) as the ‘standard’ model for structure formation. While the cosmological paradigm is well established, our understanding of the physical processes regulating the interplay between different

THE EFFECT OF GAS-DYNAMICS ON SEMI-ANALYTIC MODELING OF CLUSTER GALAXIES

baryonic components is still far from complete, and galaxy formation and evolution remains one of the most outstanding questions of modern astrophysics.

Different approaches have been developed in order to link the observed properties of luminous galaxies to those of the dark matter haloes in which they reside. Among these, semi-analytic models (SAMs) of galaxy formation have developed into a flexible and widely used tool that allows a fast exploration of the parameter space, and an efficient investigation of the influence of different physical assumptions. Computational costs are therefore reduced with respect to hydrodynamical simulations, but this is done at the expense of an explicit description of the gas dynamics (for a recent review on SAMs, see Baugh, 2006). Although recent work has started analysing the properties of the galaxy populations in hydrodynamical simulations (e.g. Frenk et al., 1996; Pearce et al., 1999; Nagamine et al., 2005; Nagai & Kravtsov, 2005; Saro et al., 2006; Oppenheimer & Davé, 2006), the computational time is still prohibitive for simulations of galaxies in large cosmological volumes. In addition, the uncertainties inherent in the physical processes at play obviously place strong limits on the accuracy with which galaxies can be simulated. As a consequence, these numerical studies also require an adequate handling of ‘sub-grid’ physics either because the resolution of the simulation becomes inadequate to resolve the scale of the physical process considered, or because we do not have a “complete theory” of that particular physical process (which is almost always true). It is therefore to be expected that SAMs will remain a valid method to study galaxy formation for the foreseeable future.

In their first renditions, SAMs took advantage of Monte Carlo techniques coupled to merging probabilities derived from the extended Press-Schechter theory to construct merging history trees of dark matter haloes (Kauffmann et al., 1993; Cole et al., 1994). An important advance of later years has been the coupling of semi-analytic techniques with direct N -body simulations (Kauffmann et al., 1999b; Benson et al., 2000). Since dark matter only simulations can handle large numbers of particles, such ‘hybrid’ models can access a very large dynamic range of mass and spatial resolution offering, at the same time, the possibility to model the spatial distribution of galaxies within dark matter haloes. It is also interesting to note that there have been a number of recent studies showing that the extended Press-Schechter formalism does not provide a faithful description of the merger trees extracted directly from N -body simulations (Benson et al., 2005; Li et al., 2007; Cole et al., 2008). This might have important consequences on the predicted properties of model galaxies, although a detailed investigation of the influence of analytical versus numerical merger trees on the predicted properties of model galaxies has not been carried out yet.

A related question is whether the inclusion of the baryonic component alters the halo dynamics with respect to a purely dark matter (DM) simulation. Processes like ram-pressure stripping and gas viscosity are expected to produce a significant segregation between the collisional and collisionless components (Vollmer et al., 2001). These effects are likely more important in environments characterised by high densities and large velocity dispersions (like galaxy clusters), and are expected to change the dynamics and the timing of halo mergers. As the merger history of model galaxies in a SAM is essentially driven by the merger his-

tory of its parent halo, any physical process that affects halo mergers will influence model predictions in some measure. We note that recent work has used merger trees from non-radiative hydrodynamic simulations (e.g. Cora et al., 2008) to study the chemical enrichment of the intra-cluster medium (ICM). This approach offers the advantage of providing a three-dimensional picture of the ICM, while keeping the advantage of exploring different physical choices with sensibly reduced computational times with respect to hydrodynamical simulations. The question of how SAM predictions are affected by using merger trees from different types of simulations (e.g. DM and hydrodynamical simulations) has, however, not been addressed.

The purpose of this Chapter is to quantify the effects of the presence of gas on the merger histories of haloes, and on predictions from a galaxy formation model. To this aim, we have used a sample of DM-only and non-radiative hydrodynamical simulations of four massive galaxy clusters (see Sec. 6.1). The merger trees constructed from these simulations have been used as input for a SAM (see Sec. 6.2), and results have been used to carry out a careful comparison of the statistical properties of the galaxy populations and of the formation history of the brightest cluster galaxies (BCGs) from the two sets of simulations.

The use of non-radiative hydrodynamics is only a first step towards a detailed comparison between SAMs and hydrodynamic simulations. A more realistic comparison should include also gas cooling and processes related to compact object physics, such as star formation, supernovae feedback and super-massive black holes production and evolution. We will present this analysis in a future work. We note that previous work has already compared results of smooth particle hydrodynamics (SPH) simulations and SAMs to calculate the evolution of cooling gas during galaxy formation (Benson et al. 2001; Yoshida et al. 2002; Helly et al. 2003b; see also Cattaneo et al. 2007), but a detailed comparison is still lacking.

6.1 THE SIMULATIONS

In this study, we use a set of four simulations of massive isolated galaxy clusters. More in detail the analysed simulated clusters are the four most massive clusters already presented in Chapter 4. For each halo, both a DM run and a non radiative gas run were carried out. We refer to the first ones with the label DM and for the second ones with the label GAS. For the DM runs, the masses of the high-resolution DM particles is $m_{\text{DM}} \simeq 1.3 \times 10^9 M_{\odot}$. In the GAS runs, the value of m_{DM} is suitably decreased so as to match the assumed cosmic baryon fraction. The resulting mass of the gas particles is $m_{\text{gas}} = 1.7 \times 10^8 M_{\odot}$. In Table 6.1, we list the value of M_{200} , r_{200} , and the total number of sub-haloes within r_{200} .

The simulations were carried out using the TreePM-SPH code GADGET-2 (Springel, 2005). All GAS runs used in this study include only non-radiative processes. The Plummer-equivalent softening length for the gravitational force is set to $\epsilon = 5 h^{-1} \text{kpc}$ in physical units from $z = 5$ to $z = 0$, while at higher redshifts it is set to $\epsilon = 30 h^{-1} \text{kpc}$ in comoving units. The smallest value assumed for the smoothing length of the SPH kernel is half the

THE EFFECT OF GAS-DYNAMICS ON SEMI-ANALYTIC MODELING OF CLUSTER GALAXIES

Table 6.1: Some numerical information about the four clusters used in this study. Column 1: name of the run; Column 2: M_{200} , in units of $10^{14} M_{\odot}$; Column 3: r_{200} , in units of $h^{-1} \text{Mpc}$; Column 4: total number of sub-haloes within r_{200} .

Cluster name	M_{200}	r_{200}	N_{200}
g1 DM	13.2	1.78	276
g1 GAS	12.2	1.74	228
g51 DM	10.8	1.67	229
g51 GAS	10.6	1.66	200
g72 DM	10.9	1.68	250
g72 GAS	10.7	1.66	238
g8 DM	18.6	2.00	355
g8 GAS	19.4	2.03	219

gravitational softening. Simulation data were stored in 93 outputs that are approximately logarithmically equispaced in time down to $z \sim 1$, and approximately linearly equispaced in time thereafter. Each simulation output was analysed in order to construct merger trees of all identified sub-haloes using the software originally developed for the Millennium Simulation project¹. We refer to Springel et al. (2001) and to Springel et al. (2005a) for a detailed description of the substructure finder and of the merger tree construction algorithm. In the following, we briefly summarise the main steps of the procedure, and the changes we implemented to adapt the available software to our simulations.

For each simulation snapshot, we constructed group catalogues using a standard friends-of-friends (FOF) algorithm with a linking length of 0.16 in units of the mean inter-particle separation. Each group was then decomposed into a set of disjoint substructures identified as locally over-dense regions in the density field of the background main halo. The substructure identification was performed using the algorithm SUBFIND (Springel et al., 2001). For the Millennium Simulation, all sub-haloes with at least 20 bound particles were considered to be genuine substructures. In our work, we raise this limit to at least 32 particles. We have checked that, with this choice, ‘evanescent’ substructures (i.e. objects close to the resolution limit that occasionally appear and then disappear) are avoided. This turns out to be important particularly for our GAS runs. We remind that SUBFIND classifies all particle inside a FOF group either as belonging to a bound substructure or as being unbound (see Section 3.6). The self-bound part of the FOF group itself will also appear in the substructure list and represents what we will refer to as the ‘main halo’. This particular halo typically contains 90 per cent of the mass of the FOF group (Springel et al., 2001).

The sub-halo catalogues have then been used to construct merging histories of all self-bound structures in our simulations, using the same procedure outlined in Springel et al. (2005a), as updated in De Lucia & Blaizot (2007). This procedure is based on the identifica-

¹<http://www.mpa-garching.mpg.de/galform/virgo/millennium/>

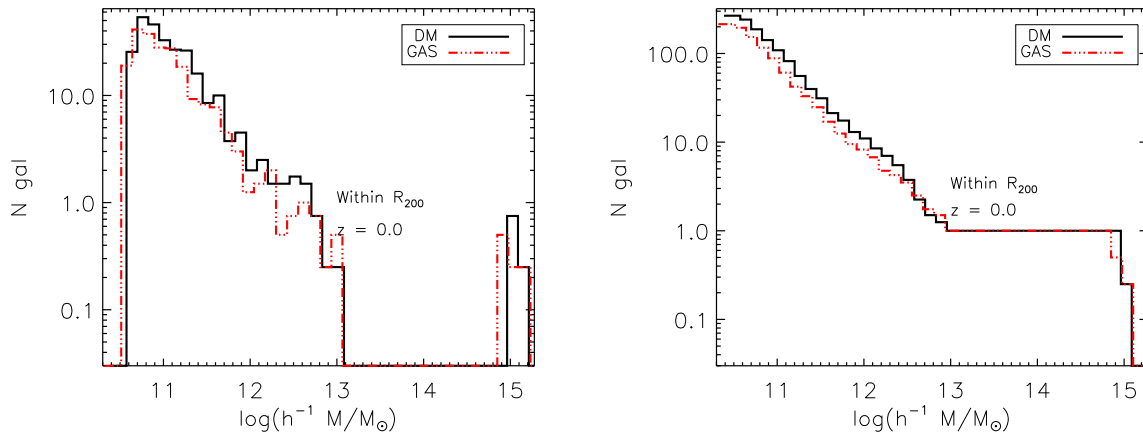


Figure 6.1: Mean differential (left) and cumulative (right) mass functions of all sub-haloes identified within r_{200} and at $z = 0$, averaged over the four simulated clusters used in this study. Solid black lines are for the DM runs, while dot-dashed red lines are for GAS runs. For each cluster, we also show the main halo, using the corresponding value of M_{200} . For all other substructures, masses are given by the sum of the masses of all their bound particles.

tion of a unique descendant for each self-bound structure. In order to identify the descendant of a given halo, all sub-haloes in the following snapshot that contain its particles are identified. Particles are then counted by giving higher weight to those that are more tightly bound in the halo under consideration. The halo that contains the largest fraction of the most bound particles is chosen as descendant of the halo under consideration. In our GAS runs, the original weighting scheme used in Springel et al. (2005a) leads to a number of premature mergers for small structures. In order to avoid this problem, we increased by a factor of one third the weight of the most bound particles with respect to the original choice (see also Dolag et al., 2008a). Our choice results in a better tracing of bound structures in our GAS runs, while leaving the results of the DM runs unaffected. The merger trees constructed as described above represent the basic input needed for the semi-analytic model described in Sec. 6.2.

Figure 6.1 shows differential (left panel) and cumulative (right panel) mass functions of the sub-haloes identified at $z = 0$ within r_{200} , averaged over the four simulated clusters. We have included in these distributions the four main haloes of the simulations, using the corresponding value of M_{200} for the mass. These correspond to the mass bins around $\sim 10^{15} h^{-1} \text{Mpc}$ in the differential mass function. For all other sub-haloes, the mass used in Figure 6.1 is the sum of the masses of all their bound particles. We will adopt this definition, as well as within the semi-analytic model, whenever an estimate of the substructure mass is needed. The left panel of Figure 6.1 shows that the DM mass function lies slightly but systematically above that measured from the GAS runs. This difference is larger than that corresponding to the shift in mass by the baryon fraction, and it cannot be accounted for by

assuming that all gas is stripped from all sub-haloes. It seems that in the non–radiative runs, sub-haloes that are stripped of their gas become both less massive more and weakly bound (Dolag et al., 2008a). This is probably also the reason of the systematic difference between M_{200} in DM and GAS runs shown in Table 6.1. The g8 cluster is an exception: for this cluster, M_{200} in the GAS run is larger than the corresponding value from the DM run, and the number of sub-haloes within r_{200} in the GAS run is much lower than the corresponding number in the DM run. The peculiar behaviour of this cluster can be explained by taking into account its accretion history. This is the most massive cluster in our sample, and it did not undergo any major merger event after $z \sim 1$. As a consequence, sub-haloes in the GAS run spent a long time in a hot, high–pressure atmosphere that can efficiently remove their gas through ram–pressure stripping. Turning back to Figure 6.1, the drop at masses $\lesssim 10^{10.5}h^{-1}M_{\odot}$ is due to our choice of considering only substructures with at least 32 bound particles. In the GAS runs, the drop occurs at slightly lower masses because of the reduced value of the gas particle mass with respect to the DM particle mass.

Although the difference is small, Figure 6.1 shows that our GAS runs contain less substructures than the corresponding DM runs. In the following sections, we will analyse the impact of these differences on prediction from a semi-analytic model of galaxy formation.

6.2 THE SEMI-ANALYTIC MODEL

In this work, we use the semi-analytic model described in De Lucia & Blaizot (2007). We recall that the semi-analytic model we employ builds upon the methodology originally introduced by Kauffmann et al. (1999b), Springel et al. (2001) and De Lucia et al. (2004b). The modelling of various physical processes has been recently updated as described in Croton et al. (2006) who also included a model for the suppression of cooling flows by ‘radio-mode’ AGN feedback. We refer to the original papers for details. In this study, we have assumed a Salpeter Initial Mass Function, and a recycled gas fraction equal to 0.3.

The semi-analytic model adopted here includes explicitly dark matter substructures. This means that the haloes within which galaxies form are still followed even when accreted onto larger systems. As explained in Springel et al. (2001) and De Lucia et al. (2004b), the adoption of this particular scheme leads to the definition of three different ‘types’ of galaxies. Each FOF group hosts a ‘Type 0’ galaxy. This galaxy is located at the position of the most bound particle of the main halo, and it is the only galaxy fed by radiative cooling from the surrounding hot halo medium. All galaxies attached to dark matter substructures are referred to as ‘Type 1’. These galaxies were previously central galaxies of haloes that merged to form the larger system in which they currently reside. The positions and velocities of these galaxies are followed by tracing the surviving core of the parent halo. The hot reservoir originally associated with the galaxy is assumed to be kinematically stripped at the time of accretion and is added to the hot component of the new main halo. Tidal truncation and stripping rapidly reduce the mass of dark matter substructures below the resolution limit of

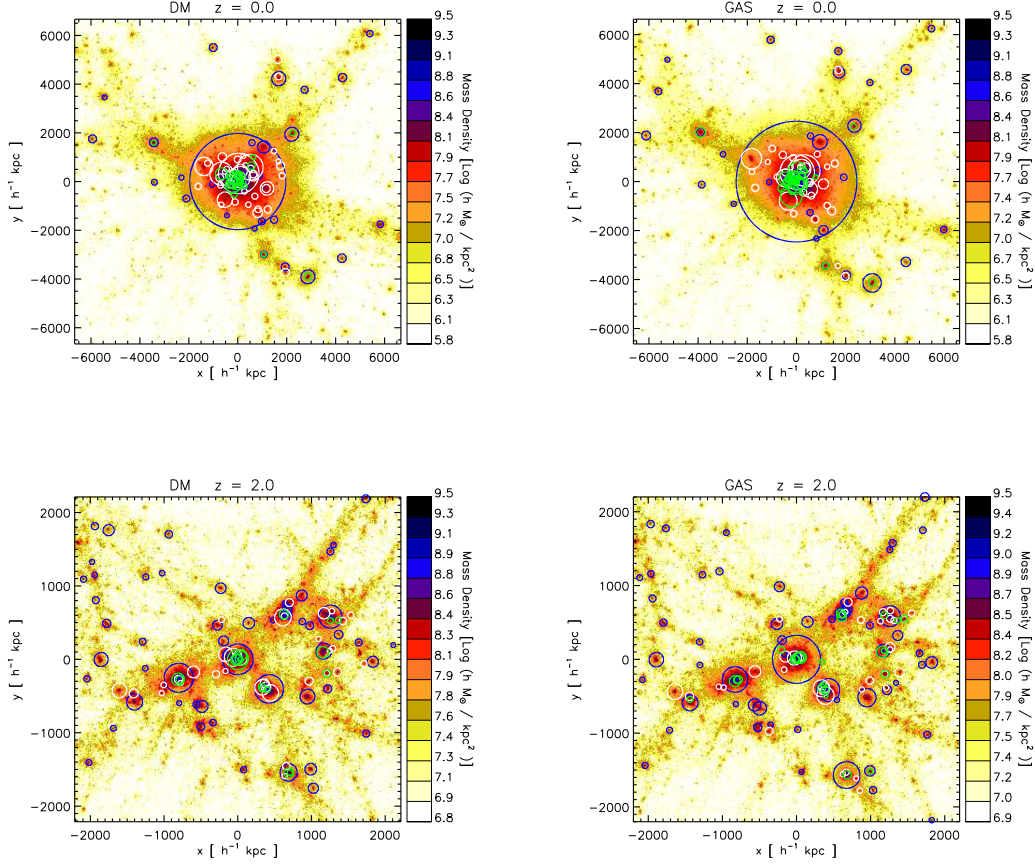


Figure 6.2: Density map of the g51 cluster for the DM run (left panels) and for the GAS run (right panels), at $z = 0$ (upper panels) and at $z = 2$ (lower panels). Positions are in comoving units. In the upper panels, the positions of all galaxies with stellar mass larger than $10^{11}h^{-1}M_{\odot}$ are marked by circles whose radii are proportional to the galaxy stellar mass. Different colours are used for different galaxy types: blue for Type-0, white for Type-1, and green for Type-2 galaxies. In the lower panels, we have marked by circles all galaxies more massive than $5 \times 10^{10}h^{-1}M_{\odot}$, and used the same colour-coding.

the simulation (De Lucia et al., 2004a; Gao et al., 2004c). When this happens, we estimate a residual surviving time for the satellite galaxies using the classical dynamical friction formula (see Sec. 6.3.3), and we follow the positions and velocities of the galaxies by tracing the most bound particles of the destroyed substructures. Galaxies no longer associated with distinct dark matter substructures are referred to as ‘Type 2’ galaxies, and their stellar mass is assumed not to be affected by the tidal stripping that reduces the mass of their parent haloes.

Figure 6.2 shows the density map of the cluster g51 from the DM run (left panels) and from the GAS run (right panels). The projections are colour-coded by mass density, computed within a box of 13 Mpc comoving for the maps at $z = 0$ (upper panels) and 4.4 Mpc comoving for the maps corresponding to $z = 2$ (lower panels). The boxes corresponding to $z = 0$ are centred on the most bound particle of the main halo, while those corresponding to $z = 2$ are centred on the position of the most bound particle of the main progenitor of the cluster halo (i.e. the progenitor with the largest mass) at the corresponding redshift. The positions of all galaxies more massive than $10^{11}h^{-1}M_{\odot}$ at $z = 0$ and $5 \times 10^{10}h^{-1}M_{\odot}$ at $z = 2$ are shown in projection and marked by circles whose radii are proportional to the galaxy stellar mass. Different colours are used for different galaxy types (blue for Type-0, white for Type-1, and green for Type-2 galaxies). The top panels of Figure 6.2 show that the massive end of the stellar mass function at $z = 0$ is dominated by Type-0 and Type-1 galaxies (blue and white circles) located within ~ 2 Mpc from the cluster centre. Type-2 galaxies (green circles) appear to be more concentrated towards the centre than Type-1 galaxies (see Sec. 6.3.2). The brightest cluster galaxy (BCG hereafter) in the GAS run is more massive than its counterpart in the DM run. At $z = 2$ (lower panels), the cluster is still in the process of being assembled. In the DM run, there is no single dominant galaxy, and the region within ~ 2 Mpc from the main progenitor of the BCG is characterised by the presence of other three galaxies of similar mass. In the GAS run, the stellar mass of the main progenitor of the BCG is already about a factor 2 larger than other massive central galaxies in the same region. The proto-cluster regions shown in the lower panels of Figure 6.2 exhibit a complex dynamics, which witnesses the ongoing assembly of the BCG, and a rather intense star formation activity (see also Chapter 5).

6.3 RESULTS

We will compare now the mass distributions and the spatial distributions of the galaxies identified in the DM and GAS runs. We will show that, while such distributions agree quite well, there are differences in the final masses of the BCGs. We argue that these differences are due to the effects of gas dynamics on sub-halo merging times and orbital distribution.

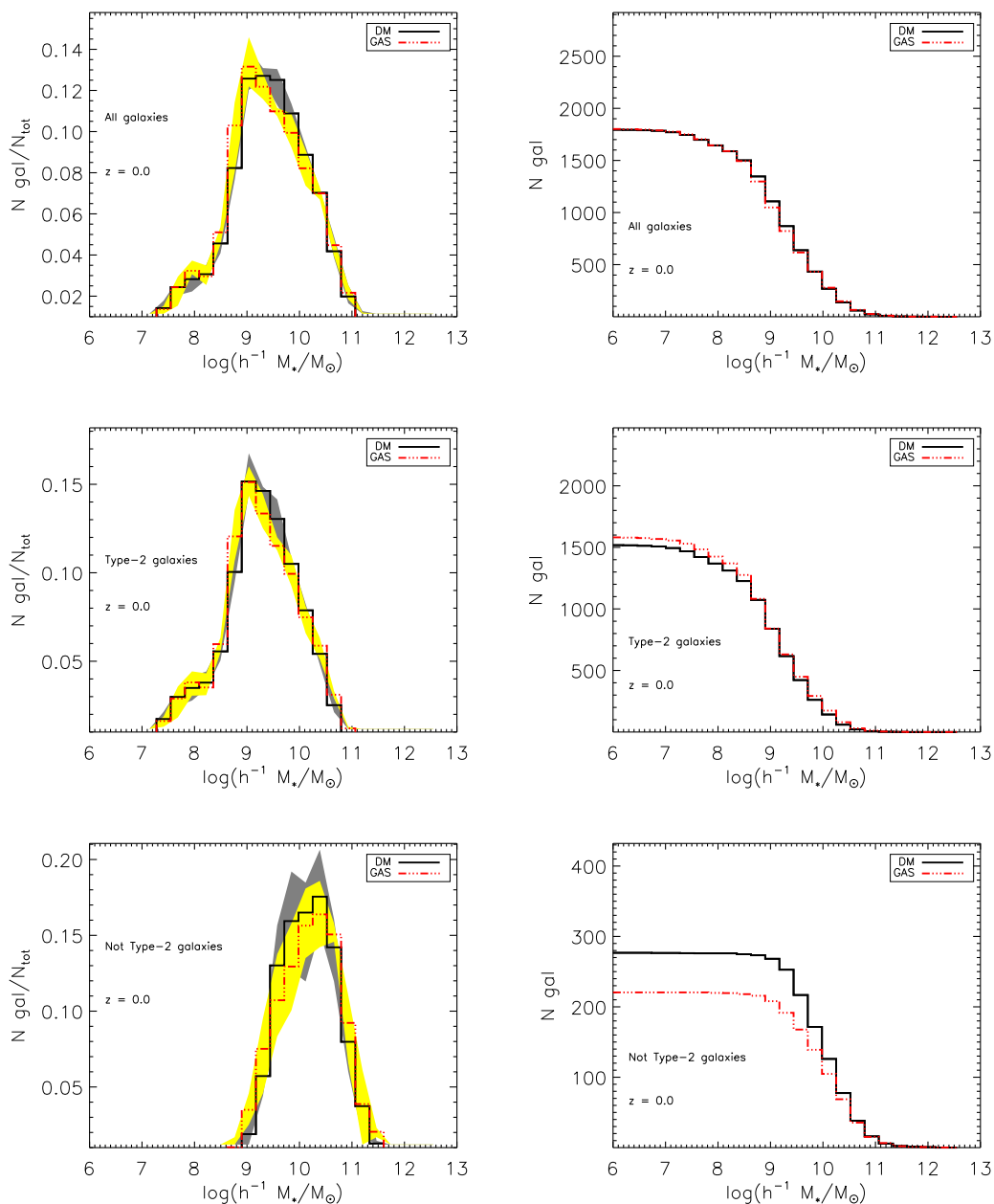


Figure 6.3: Differential (left panels) and cumulative (right panels) stellar mass functions for all galaxies within r_{200} at $z = 0$, in the four simulated clusters used in this study. The differential mass functions have been normalised to the total number of galaxies within r_{200} in each cluster. The solid histograms show the mean of the distributions from the four clusters, while the shaded region indicate, for each value of the stellar mass, the minimum and maximum number of galaxies. Solid black lines are for the DM runs, while dot-dashed red lines are for GAS runs. We show separately the stellar mass functions of the whole galaxy population (upper panels), of the Type-2 satellite galaxy population (central panels) and the Type-0 and Type-1 galaxies (lower panels).

6.3.1. The stellar mass function

In Sect. 6.1, we have shown that the number of sub-haloes in the GAS runs is slightly lower than the corresponding number from the DM-only run (see Figure 6.1). The naive expectation is to have a total number of galaxies in the GAS runs which is lower than the corresponding number in the DM runs (at least Type-0 and Type-1 galaxies). Figure 6.3 shows that this is indeed the case, but it also shows a number of other interesting points.

The left panels of Figure 6.3 show the differential (upper panel) and cumulative (lower panel) stellar mass function for the whole galaxy population within r_{200} , averaged over the four clusters used in this study. The shaded regions indicate, for each value of the stellar mass, the minimum and maximum number of galaxies in the simulated clusters. The agreement between the two set of runs is quite good, but for a slight shift towards lower stellar masses for galaxies with mass $\sim 3 \times 10^9 M_{\odot}$. This agreement is mainly due to the dominant contribution of the Type-2 galaxy population, whose stellar mass function is shown in the central panels of Figure 6.3. The corresponding mass function for Type-0 and Type-1 galaxies is shown in the right panels. In order to separate differences in the total number of galaxies from differences in their mass distributions, the differential mass functions shown in the upper panels of Figure 6.3 have been normalised to the total number of galaxies, while the cumulative mass functions in the lower panels indicate the un-normalised number of galaxies within r_{200} . We recall that in this region, there is only one Type-0 galaxy for each cluster (its BCG). Therefore all galaxies (but the four BCGs) shown in the right panels are Type-1 galaxies.

The difference found in Figure 6.1 reflects into a different distribution and total number of Type-0 and Type-1 galaxies. This difference is, however, compensated by the distribution and number of Type-2 galaxies, which dominate the stellar mass function in number and represent the dominant galaxy population at lower masses. The number of Type-2 galaxies in the GAS runs is slightly larger, in relative terms, than in the DM runs. This small difference is however enough to compensate the deficit of Type-1 galaxies in the GAS runs. As explained in Sec. 6.1, we have considered as genuine substructures all those with at least 32 bound particles. Our resolution limit for the galaxy stellar mass is therefore $M_{\text{star}} \simeq 32 \times M_{\text{part}} \times f_{\text{bar}} \simeq 7 \times 10^9 h^{-1} M_{\odot}$ (with $f_{\text{bar}} = 0.17$). This value is close to the peak of the differential mass functions shown in the upper panels of Figure 6.3. All galaxies below this mass limit were born in fully resolved haloes, but were not able to transform all their baryons into stars (e.g. because their parent halo was accreted onto a bigger system, their gas reservoir was stripped and their star formation activity suppressed, or because they are young gas-rich galaxies in haloes that formed relatively late).

6.3.2. The number density profiles

Figure 6.4 shows the density profile of all galaxies within r_{200} from the DM (black solid lines) and the GAS (red dot-dashed lines) runs. Solid lines show the average obtained by stacking

the profiles of the four clusters used in this study, while shaded regions show the minimum and maximum value obtained for the simulated clusters. As for Figure 6.3, we show the density profile corresponding to the whole galaxy population in the upper left panel, and the contributions from Type-2 and non-Type-2 galaxies in the upper right and lower panels respectively. All profiles have been normalised to the mean galaxy density within r_{200} , and correspond to the galaxies identified at $z = 0$. In all panels, the dashed green line shows the average DM profile of the simulated clusters, normalised to match the density profile of the galaxies in the inner bin.

The galaxy density profile is dominated by the Type-2 galaxy population at all radii, and follows very nicely the underlying DM profile, in agreement with what found by Gao et al. (2004b). By definition, the central Type-0 galaxies populate the innermost bin in Figure 6.4. The lower panel of this figure shows that Type-1 galaxies tend to avoid the central cluster regions, where they are efficiently destroyed by the intense tidal field of the parent halo. The radial profile of Type-1 galaxies is ‘anti-biased’ relative to the dark matter profile in the inner regions, as expected from studies of dark matter substructures (Ghigna et al., 2000b; De Lucia et al., 2004b).

The agreement between the DM and GAS runs is quite good. The only notable difference is a small shift towards the centre for the positions of Type-1 galaxies in the GAS runs. We have verified, however, that this difference is due to a single galaxy which is found closer to the centre in the GAS run of the cluster g72. The shift is due to the influence of the gas on the orbit of substructures, as we will discuss in the following.

The good agreement for the radial distribution of Type-2 galaxies in the two sets of runs used in this study is not obvious. We recall that the positions of Type-2 galaxies are given by the updated positions of the particles that were the most bound particles of the parent substructure, before their masses were reduced below the resolution limit of the simulation. The agreement between the DM and GAS runs therefore implies that the presence of gas in the simulation does not significantly alter the distribution of those particles, which trace the spatial distribution of DM particles.

6.3.3. Merging times

In the previous section, we have shown that the cluster galaxy population resulting from the model employed in this study is dominated in number by Type-2 galaxies. Model predictions for this galaxy population are very sensitive to the residual merging times that are assigned to Type-2 galaxies when their parent dark matter sub-haloes are stripped below the resolution limit of the simulation.

These merging times, which regulate for how long a Type-2 galaxy keeps its identity before merging with the central galaxy of its own halo, are computed using the following

THE EFFECT OF GAS-DYNAMICS ON SEMI-ANALYTIC MODELING OF CLUSTER GALAXIES

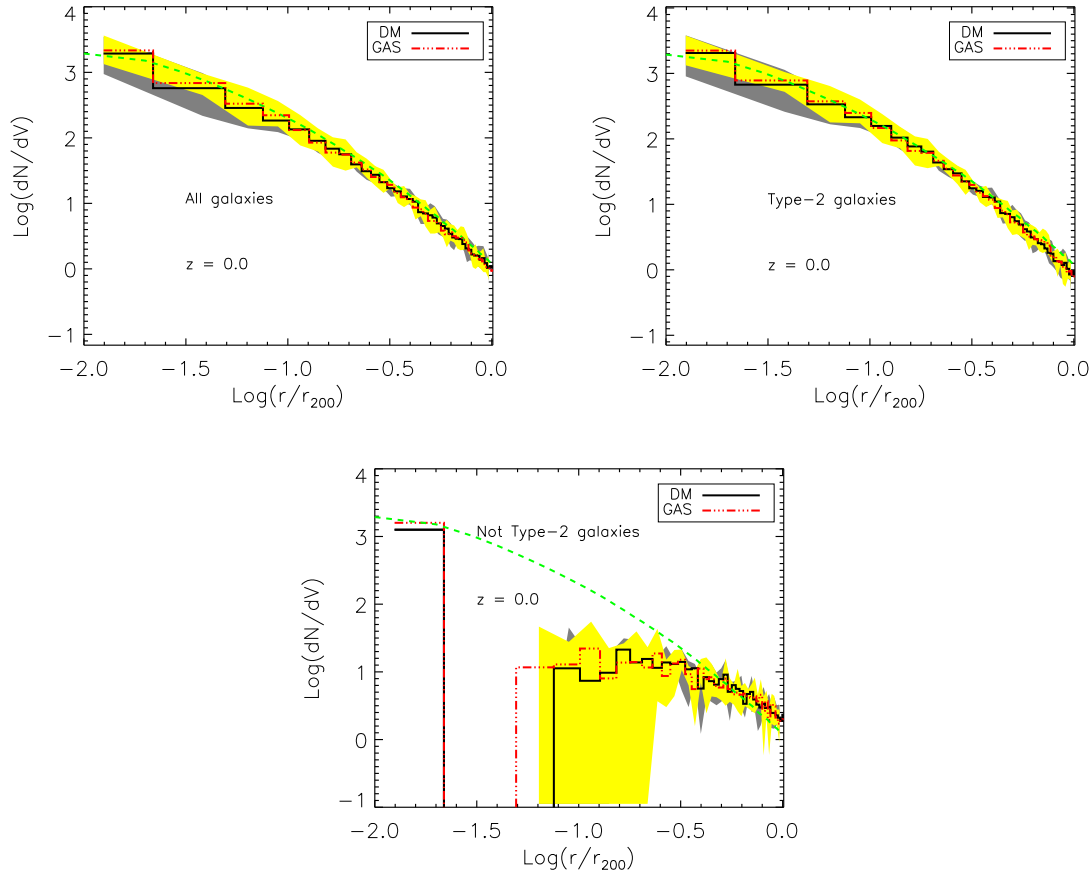


Figure 6.4: Averaged radial density of galaxies identified $z = 0$ and within r_{200} for the four clusters used in our study. The distribution is normalised to the mean density of galaxies within r_{200} . Histograms show the mean of the four clusters, while their dispersion is indicated by the shaded regions. Solid black lines are for DM runs, while dashed-dotted red lines are for GAS runs. The dashed green line in each panel shows the mean density profile of dark matter. The three panels show separately the radial density of the whole galaxy population (upper left panel), of the Type-2 satellite galaxy population (upper right panel), and of the Type-0 and Type-1 satellite galaxies (lower panel).

implementation of the Chandrasekhar (1943) dynamical friction formula:

$$T_{\text{merge}} = 1.17 \times \frac{D^2 \times V_{\text{virial}}}{\log\left(\frac{M_{\text{main}}}{M_{\text{sat}}} + 1\right) \times G \times M_{\text{sat}}} . \quad (6.1)$$

In the above equation, D is the distance between the merging halo and the centre of the structure on which it is accreted, V_{virial} is the circular velocity of the accreting halo at the

virial radius, M_{sat} is the mass associated with the merging satellite, and M_{main} is the mass of the accreting halo. All quantities entering in Eq. (6.1) are computed at the last time the merging satellite can be associated with a resolved dark matter substructure. We note that satellite galaxies can merge either with Type-0 or with Type-1 galaxies, but the majority of the mergers occur between Type-2 and Type-0 galaxies. In this case, M_{main} is M_{200} of the accreting halo, while in the case of a merger between a Type-2 and a Type-1 galaxy, M_{main} is given by the sum of the masses of all bound particles associated with the accreting halo.

We note that Eq. (6.1) is adapted from the original formulation derived by Chandrasekhar in the approximation of an orbiting point mass satellite in a uniform background mass distribution. It is also worth reminding the reader that our formulation of dynamical friction does not include any dependence on the orbital distribution. Furthermore, M_{sat} in our SAM formulation does not include the mass associated with the stars and to the cold inter-stellar medium of the galaxy in the merging substructure. We have verified, however, that by taking into account this baryonic component does not alter significantly our results.

Two recent papers (Boylan-Kolchin et al., 2008; Jiang et al., 2008) have studied merging time-scales using N-body and hydro/N-body simulations. Both studies have pointed out that a formulation similar to that given in Eq. (6.1) systematically underestimates merging time-scales, although they derived new fitting formulae which differ in a number of details. In this work, we are only concerned with differences due to the application of the same formula to different runs, while we plan to come back to the validity of the Chandrasekhar formula in a future work. We also note that, in the standard application of the dynamical friction formula, quantities related to the merging satellite are computed at the time at which the satellite crosses the virial radius of the accreting halo, while in our case satellites are traced until their mass is reduced below the resolution limit of the simulation by tidal stripping. Merging times are computed at this time, so that D is the distance of the merging satellite (the position of its most bound particles) to the centre of the accreting halo, and it can be larger or smaller than the virial radius of this halo.

In Sec. 6.1, we have shown that the number of haloes in the GAS runs is approximately equal or slightly lower than the number of haloes in the DM runs. Given this difference in the number of haloes, an excess of Type-2 galaxies in the GAS runs can have two possible explanations: a shorter lifetime of substructures or longer merging times assigned to Type-2 galaxies. In order to test which of these two alternative explanations applies, we turn to our simulation results.

Figure 6.5 shows the distribution of the lifetimes of sub-haloes in the DM (solid black line) and in the GAS simulations (dashed red line). For each sub-halo, its lifetime is computed as the time elapsed between the last time it was identified as a main halo (i.e. hosting a Type-0 galaxy at its centre) and the time it merged (i.e. its mass dropped below the resolution limit of the simulation). For this figure and for those in the remainder of this section, we have stacked the results from the four clusters used in this study. Figure 6.5 shows that the distribution of lifetimes of Type-1 galaxies does not differ significantly in the DM and in the GAS runs. The excess of Type-2 galaxies must therefore be ascribed to different merging

THE EFFECT OF GAS-DYNAMICS ON SEMI-ANALYTIC MODELING OF CLUSTER GALAXIES

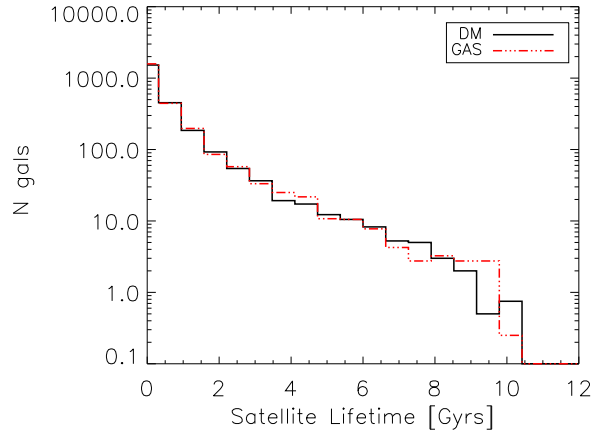


Figure 6.5: Distribution of lifetimes of Type-1 galaxies. The lifetime is defined here as the time elapsed between the last time the galaxy was a Type-0 galaxy and the time the substructure mass was reduced below the resolution limit of the simulation (the galaxy becomes a Type-2). Results from the four simulated clusters have been stacked together. The solid black line is for the DM runs, and the red dashed line corresponds to the GAS runs.

times associated with them in the two runs, with merging times expected to be systematically longer in the GAS runs. In order to verify our expectation, we show in the upper left panel of Figure 6.6 the distribution of the merging times which were assigned to Type-2 galaxies identified at $z = 1$. The figure shows that there is an excess of Type-2 galaxies with merging times shorter than ~ 3 Gyr in the DM runs, and a corresponding excess of galaxies with merging times larger than the same value in the GAS runs. The upper right panel of Figure 6.6 shows the formation times of the Type-2 galaxies identified at $z = 1$, i.e. the lookback times when the galaxies become Type-2 for the first time. The distributions are very similar, confirming that these Type-2 galaxies form on average at the same time in the GAS and in the DM runs. The lower panel of Figure 6.6 shows the distribution of T_{delay} , which is defined as the difference between the formation times of the Type-2 galaxies identified at $z = 1$ and the merging times they get assigned. According to this definition, the integral of this distribution between a given T_{delay} and infinity gives the total number of Type-2 galaxies at $z = 1$ that have merged since lookback time T_{delay} . The fact that the distribution for the GAS runs lies above that of the DM runs for negative values of T_{delay} indicates that the excess of Type-2 galaxies in the GAS runs will continue at least in the next five Gyrs after the present time.

Figure 6.6 therefore proves that the excess of Type-2 galaxies in the GAS runs (shown in the central panels of Figure 6.3) is due to the fact that these galaxies get assigned longer merging times in the GAS runs with respect to the corresponding merging times assigned to Type-2 galaxies in the DM runs. It is interesting to ask what is the origin of these differences. This can be done by considering all quantities entering Eq. (6.1).

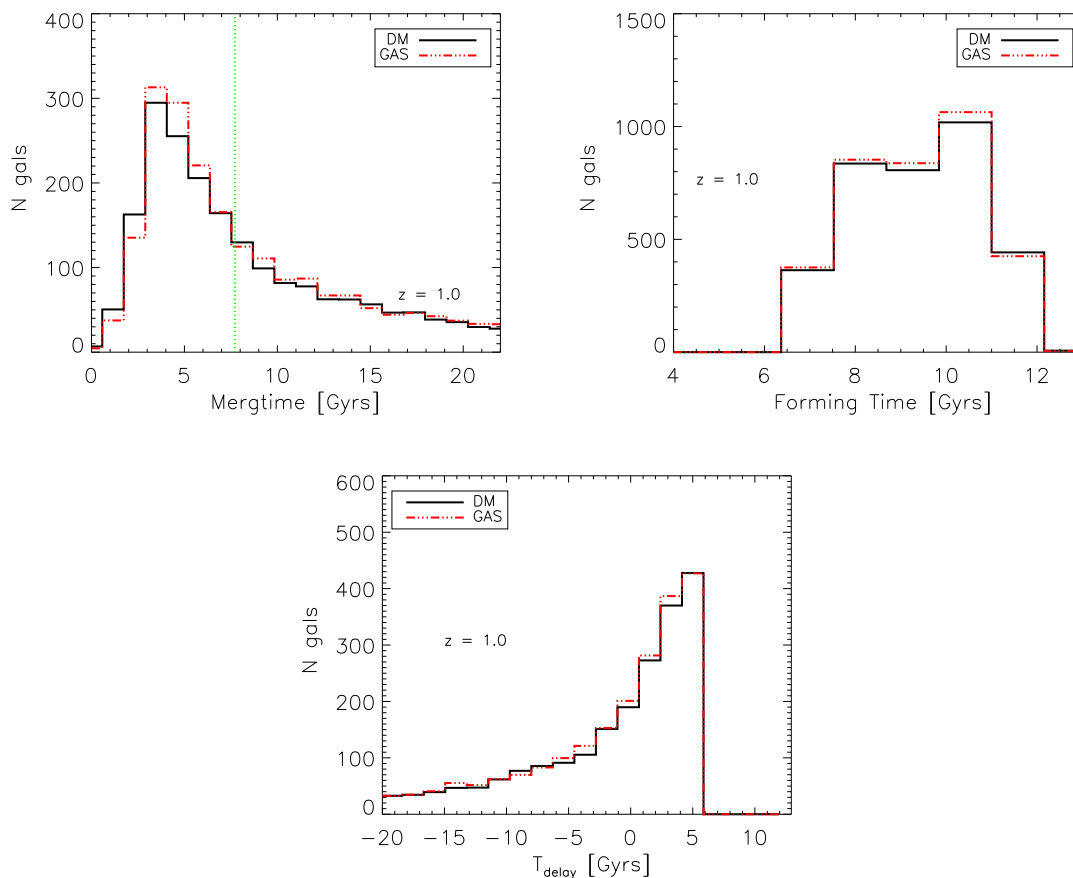


Figure 6.6: Upper left panel: distributions of the merging times assigned to the Type-2 galaxies identified at $z = 1$ in the four simulated clusters. The solid black line shows the result from the DM runs, while the dot-dashed red line is for the GAS runs. The vertical green dotted line marks the value of the lookback time at $z = 1$. All galaxies whose merging time is smaller than this value will merge by $z = 0$. Upper right panel: distribution of the formation times of the Type-2 galaxies, i.e. the lookback times when the galaxies first become Type-2. Lower panel: distribution of the differences between the formation and the merging times (T_{delay}) of the Type-2 galaxies identified $z = 1$ (see text).

The upper left panel of Figure 6.7 shows the dependence of the satellite mass on T_{delay} , for all Type-2 galaxies identified at $z = 1$. The solid lines show the median of the distributions, while dot-dashed lines mark the 25th and 75th percentiles. Black and red lines are used for the DM and the GAS runs respectively. The figure indicates that, for a fixed value of T_{delay} , Type-2 galaxies in the GAS runs are created in substructures whose mass is systematically lower than the corresponding quantity in the DM runs. This difference is of the order

THE EFFECT OF GAS-DYNAMICS ON SEMI-ANALYTIC MODELING OF CLUSTER GALAXIES

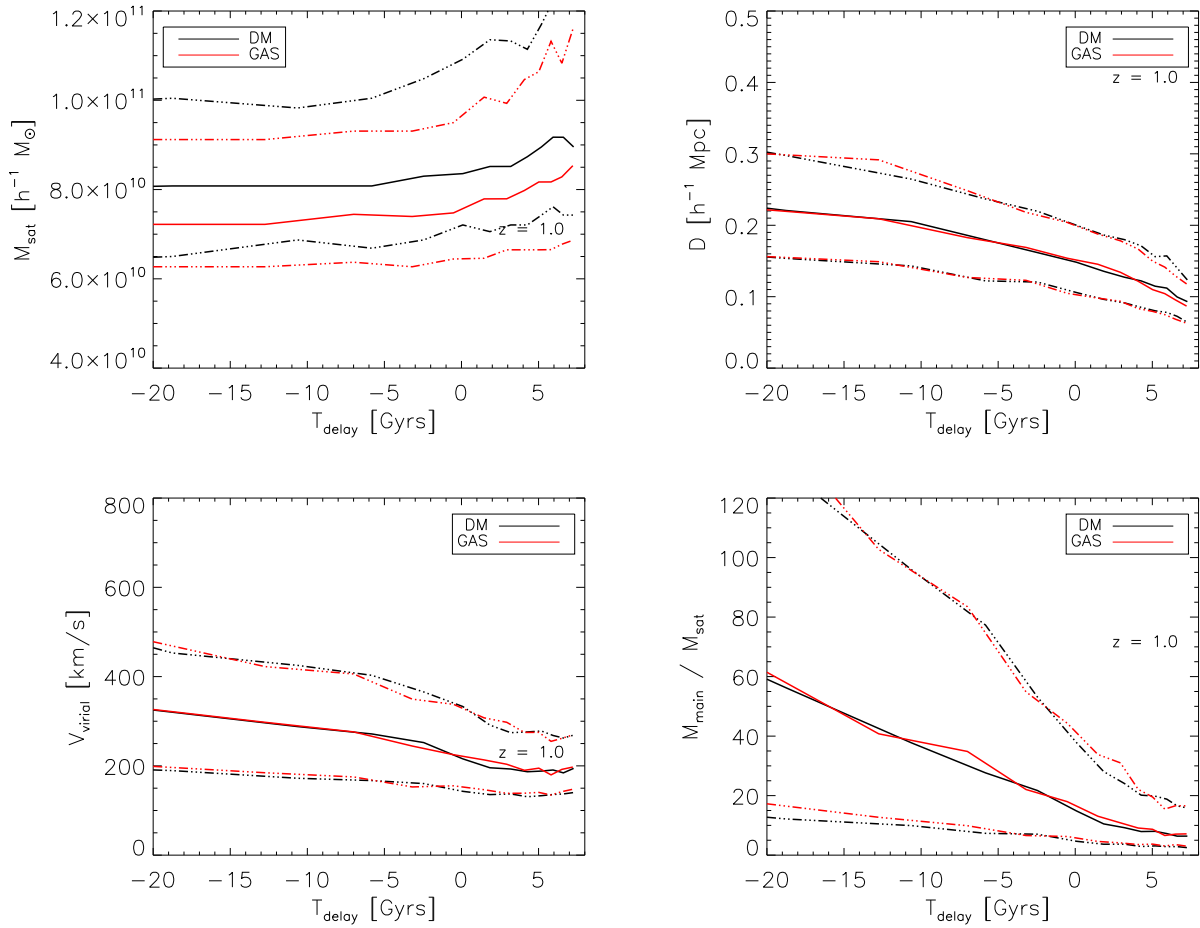


Figure 6.7: Dependence of satellite mass (upper left panel), distance from the centre of the accreting halo (upper right panel), circular velocity of the accreting halo at the virial radius (lower left panel), and ratio between the mass of the accreting halo and the satellite mass (lower right panel) on T_{delay} . In all panels, solid lines show the median of the distributions, while dot-dashed lines show the 25th and 75th percentile of the distributions. Black lines are used for the DM runs and red lines for the GAS runs. Quantities refer to Type-2 galaxies identified at $z = 1$.

of the baryonic fraction, and is due to the fact that when sub-haloes lose their identity in the GAS runs, their baryonic component has been stripped by ram–pressure. A systematically lower mass for substructures in the GAS runs provides indeed longer merging times for the Type-2 galaxies (see Eq. 6.1).

No significant difference between the GAS and the DM runs can be noticed for quantities like the distance between the merging halo and the centre of the accreting halo (top right panel of Figure 6.7) and the circular velocity of the accreting halo (bottom left panel of Figure 6.7). Finally, the bottom right panel of Figure 6.7 shows the ratio between the mass of the accreting halo and the satellite mass, which enters in the Coulomb logarithm at the denominator of Eq. (6.1). If the effect of ram–pressure was that of stripping gas only from the satellite and not from the accreting halo, we would expect a difference between the GAS and the DM runs, in the opposite sense of that shown in the top left panel of Figure 6.7. The figure shows a very slight tendency for larger mass ratios in the GAS runs. This suggests that also the accreting haloes tend to have a deficit of gas, with respect to the DM runs, although the difference is less significant than that found for the satellite mass. In addition, the merging times have a logarithmic dependence on the mass ratio.

Results shown in Figure 6.7 show then that longer merging times for Type-2 galaxies in the GAS runs are essentially due to a systematic decrease of the satellite mass, caused by ram–pressure stripping. Figure 6.8 shows again the satellite mass as a function of T_{delay} , but this time for all Type-2 galaxies identified at $z \simeq 3.4$. At this earlier epoch, the cluster is not fully assembled yet, and the proto-cluster region contains gas with lower pressure. It is to be expected then that the effect of ram–pressure stripping is less significant. This expectation is confirmed by the results shown in the figure, which suggests no significant difference between the GAS and DM runs at this epoch.

It is worth noticing at this point that the effect of ram–pressure stripping is likely to be over-estimated in non–radiative simulations. In a more realistic case, we expect a significant fraction of baryons to be converted into stars before the effect of ram–pressure stripping becomes significant. This expectation, however, needs to be verified with hydrodynamical simulations which also include star formation and feedback processes.

6.3.4. The brightest cluster galaxies

In the previous sections, we have carried out a statistical comparison between the galaxy populations from the DM and GAS runs. The general level of agreement is quite good, although our analysis points out a number of interesting differences. In particular, we have shown that the presence of the gas affects the dynamics of sub-haloes, so as to make an object-by-object comparison difficult. This difficulty does not hold for the brightest cluster galaxies (BCGs) which, due to their special location at the centre of the biggest halo in the simulation, can be unambiguously identified both in the DM and in the GAS runs. In this section, we will compare the BCG formation history in the two sets of runs used for our

THE EFFECT OF GAS-DYNAMICS ON SEMI-ANALYTIC MODELING OF CLUSTER GALAXIES

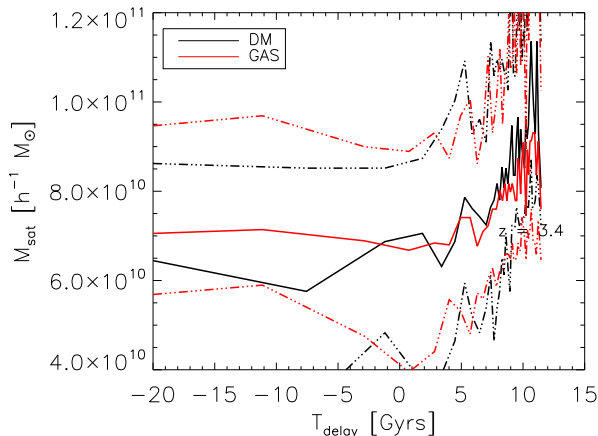


Figure 6.8: Satellite mass as a function of T_{delay} (as in the upper left panel of Figure 6.7), for all Type-2 galaxies identified at $z = 3.4$.

study.

For each of the simulated clusters used in our study, we constructed the full merger tree of the final BCG tracing back in time all its progenitors and their histories. In Figure 6.9, we show as dotted lines the total stellar mass contained in the Type-0 progenitors of the BCG. This mass traces, for most of the time, the stellar mass of the main progenitor of the BCG. At very early times, it also includes the stellar mass of other central galaxies that belong to the tree of the BCG and that are accreted onto the cluster halo at later times (see Figure 1 of De Lucia & Blaizot 2007). We also show the integral of the star formation rate (SFR) in all the Type-0 progenitors for the DM runs (solid black lines) and for the GAS runs (dot-dashed red lines). The difference between the final stellar mass and the integral of the SFR is due to stellar mass losses². In all the simulations used in this study, the integral of the SFR is constant over the last 10 Gyrs, suggesting that all stars that end up in the final BCGs were already formed at $z \simeq 2$, in agreement with findings by De Lucia & Blaizot (2007). Figure 6.9 also shows that the BCGs in the GAS runs are systematically more massive than their counter-parts in the DM runs, confirming the visual impression from Figure 6.2. This difference amounts to a few per cent in the g72 simulation (lower left panel), but it reaches values larger than 25 per cent of the final stellar mass for the g51 simulation (upper right panel). The difference is established at high redshift, during the formation of the bulk of the stars that end up in the final BCGs (i.e. the rising part of the curves showing the integral of the SFR).

We have verified that this difference is sometimes due to one massive satellite galaxy

²We recall that we adopt an instantaneous recycling approximation and that, for the adopted IMF, the recycled fraction is 0.3

which merges with the main progenitor of the BCG within $z = 0$ in the GAS run, while it gets a longer time-scale for merging in the DM run. This can be clearly seen in the case of the g51 cluster (upper right panel of Figure 6.9), where the red dotted line shows an increase of about $5 \times 10^{11} h^{-1} M_{\odot}$ in stellar mass due to a single merging event at a lookback time of ~ 1.5 Gyr. Note that this behaviour is opposite to the statistical trend that we have observed in section 6.3.3, where Type-2 galaxies in the GAS runs were found to have longer merging times.

In order to understand in detail this difference, we show in the left panel of Figure 6.10 the orbit of the sub-halo originating this Type-2 galaxy, before its merging with the g51 cluster. Black diamonds show the orbit from the DM run, while red filled circles correspond to the orbit from the GAS run. The positions of the sub-halo are initially very similar in the two runs. As it approaches the high-density environment of the cluster, it is slowed down by ram-pressure. The right panel of Figure 6.10 shows the evolution of the cluster-centric distance of the sub-halo. The figure shows that the pericentric and apocentric passages in the GAS runs take place at a larger distance in the GAS run with respect to the DM run at a lookback time of about 9.3 Gyr, and at a smaller distance at a lookback time of about 8.9 Gyr. The sub-halo has then a more circular orbit in the GAS run (see also Puchwein et al., 2005). Besides modifying the shape of the orbit and the timing of the merging, ram-pressure also makes the substructure more fragile. Indeed, this sub-halo loses its identity 8.6 Gyr ago in the GAS run, at a cluster-centric distance of about $0.3 h^{-1} \text{Mpc}$. In the DM run, the same sub-halo loses its identity about 8.3 Gyr ago, at a cluster-centric distance of about $0.4 h^{-1} \text{Mpc}$. Since the residual merging time assigned to the galaxy at its centre is proportional to the square of this distance (see Eq. 6.1), the resulting merging time in the GAS run is more than 40 per cent shorter than in the DM run, and the sub-halo disappears about 0.3 Gyr earlier. The merging occurs before $z = 0$ in the GAS run, and causes the sudden increase of the stellar mass of the BCG visible in the top right panel of Figure 6.9.

We recall that the upper right panel of Figure 6.7 shows that there is no significant difference, in terms of distance from the accreting halo, between the DM and GAS runs. This is in apparent contradiction with the above example. That figure was, however, obtained for all the Type-2 galaxies identified at $z = 1$, irrespective of their mass. In Figure 6.11, we repeat the same plot but considering only Type-2 galaxies with stellar masses larger than $10^{11} M_{\odot}$. These massive satellites belong to sub-haloes that lose their identity at systematically smaller distances in the GAS runs, like in the example illustrated in Figure 6.10. This example is then not just a statistical fluctuation, but rather the result of a more general trend for massive Type-2 satellites whose number is, however, quite low.

Finally, we note that the difference between the mass of the BCGs in the DM and GAS runs is due mainly to a different number of progenitors, rather than to a difference in their intrinsic star formation rate. This is illustrated in Figure 6.12 which shows the amount of stars formed ‘in situ’ in the main progenitor of the BCG (solid black and dot-dashed red lines), and the total stellar mass in the main progenitor at each time (dotted lines). The stars formed in the main progenitor make up only a small fraction (about one tenth) of the final

THE EFFECT OF GAS-DYNAMICS ON SEMI-ANALYTIC MODELING OF CLUSTER GALAXIES

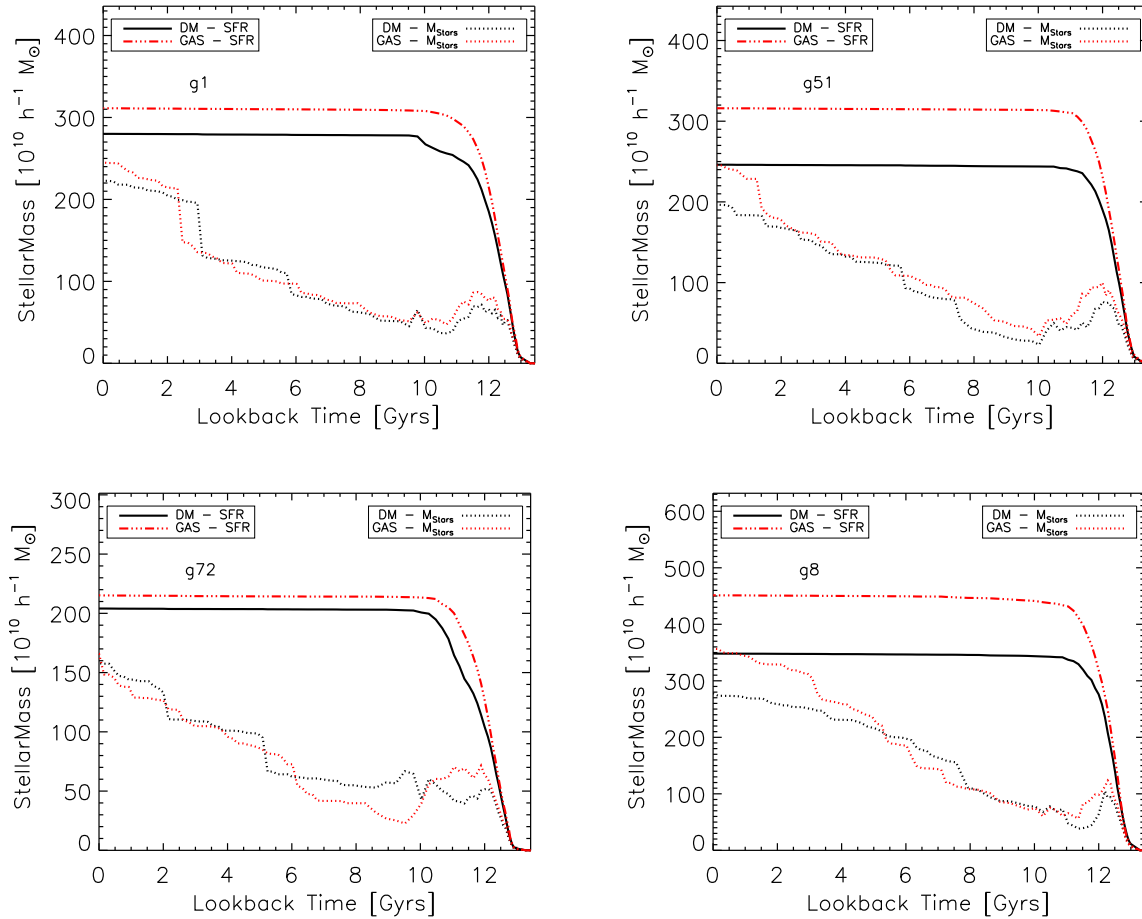


Figure 6.9: Evolution of the Type-0 progenitors of the BCG for the four simulated clusters used in this study. In each panel, the solid black lines and the dashed red lines show the integral of the SFR associated with the progenitors of the BCG for the DM runs and for the GAS runs respectively. The black and the red dotted lines show the total stellar mass of all Type-0 progenitors of the BCGs.

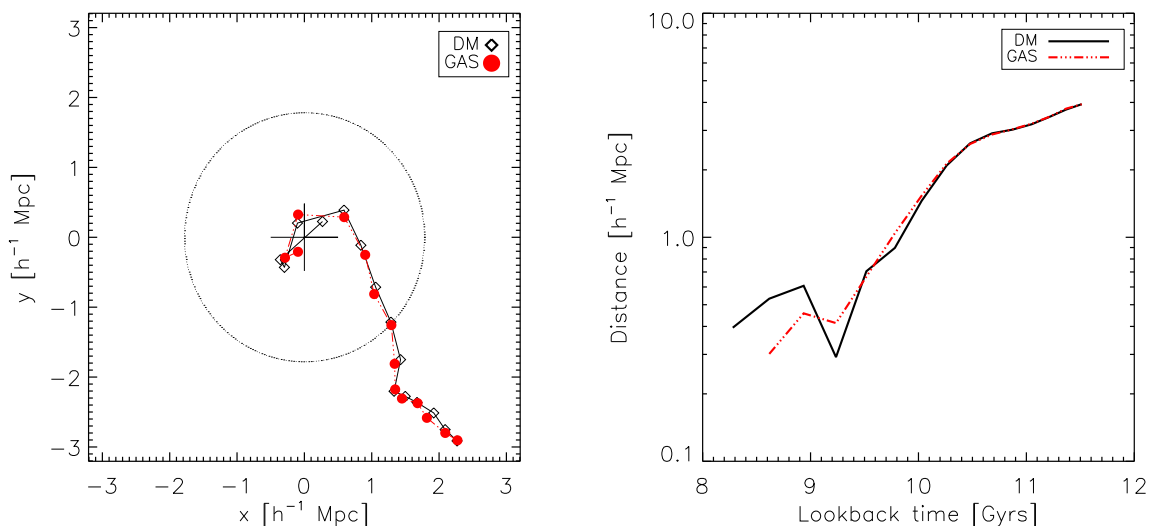


Figure 6.10: Left panel: comparison between the trajectories of a sub-halo merging with the g51 cluster, projected on the x - y plane. Open black diamonds are for the DM run, while filled red circles are for the GAS run. At each redshift, the coordinates of the merging sub-halo are computed with respect to the cluster centre at the corresponding redshift. The big black circle shows the centre of the cluster at each snapshot, and its radius is equal to the corresponding value of r_{200} at the last snapshot in which the sub-halo was identified in the DM run. Right panel: evolution of the cluster-centric distance of the same sub-halo in the DM (black solid line) and GAS (red dot-dashed line) run.

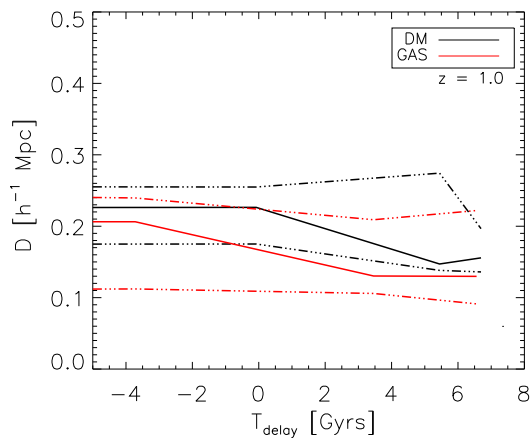


Figure 6.11: Same as for the upper right panel of Figure 6.7, but only for Type-2 galaxies with stellar masses larger than $10^{11} M_{\odot}$.

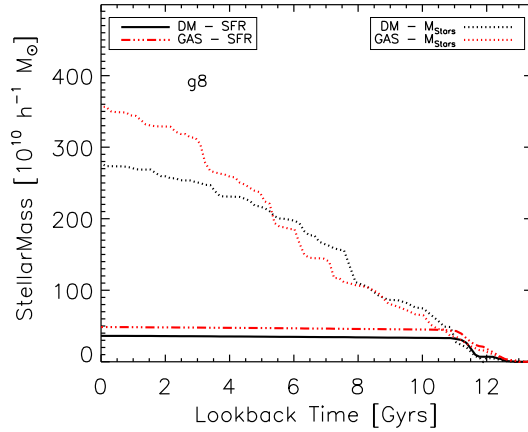


Figure 6.12: Total mass in the main progenitor of the BCG of the cluster g8 (dotted lines) for the DM (black) and GAS (red) runs. The black solid line and the red dot-dashed line show the integral of the SFR in the main progenitor of the BCG.

stellar mass in the BCG, and most of these stars are formed relatively early (more than 10 Gyrs ago). This is in agreement with results by De Lucia & Blaizot (2007, see their Figure 4). The figure shows that the amount of stars formed ‘in situ’ is comparable in the DM and GAS runs while the total mass in the main progenitor of the BCG in the GAS run increases more steeply than in the DM run, and reaches a final value that is about 1.3 times larger.

6.4 SUMMARY AND DISCUSSION

In this Chapter we have used numerical simulations to analyse how the presence of non-radiative gas dynamics affects the predictions of semi-analytic models of galaxy formation for the properties of cluster galaxies. The main results of our work can be summarised as follows.

- [1] The stellar mass function of galaxies from DM-only runs is in quite good agreement with that obtained from non-radiative hydrodynamical runs. This result is a combination of two different and opposite effects.
 - Due to a reduced number of sub-haloes in the GAS runs (see Figure 6.1), these simulations result in a galaxy population with a reduced number of Type-0 and Type-1 galaxies (i.e. central galaxies of a halo, either the main halo or a proper substructure).
 - Due to a systematic increase of the residual merging times assigned to Type-2 galaxies (those associated with haloes disrupted below the resolution limit of

the simulation), the cluster galaxy population in the GAS runs contains a larger number of Type-2 galaxies than the DM runs.

- [2] The longer merging times assigned on average to Type-2 galaxies in the GAS runs are due to ram–pressure stripping, which removes gas from the merging sub-haloes and makes them more fragile. The effect of ram–pressure is more important at lower redshift, when the cluster has already assembled in a dominant structure with a high–pressure atmosphere that can efficiently remove gas from substructures. When considering the entire satellite population, we find a systematic difference between the DM and GAS runs in the sense that merging substructures are less massive in the runs with gas. This trend, however, is reversed when concentrating on the most massive satellites (see item 4 below).
- [3] Type-2 galaxies dominate the radial density profile of cluster galaxies particularly in the inner regions, in agreement with results by Gao et al. (2004b). Galaxies associated with distinct dark matter substructures (Type-1 galaxies) exhibit a flatter distribution and their contribution to the inner regions of galaxy clusters is negligible. We did not find any significant difference, in terms of spatial distribution, between the DM and the GAS runs.
- [4] Although a statistical comparison between galaxy populations from the two sets of runs results in a quite nice agreement, a one-to-one comparison for the brightest central galaxies shows that these galaxies tend to have larger stellar masses in runs with gas. The difference varies from cluster to cluster and it is generally due to single merging events of relatively massive satellites which get assigned lower merging times in the GAS runs (see the example shown in Figure 6.10). The final difference in stellar mass is then due primarily to a different accretion history of satellite galaxies in the two sets of runs, and not to intrinsic differences in the star formation rates in the main progenitor.

Our results demonstrate that predictions of semi-analytic models of galaxy formation are not significantly affected when non-radiative hydrodynamic simulations are used to construct the halo merger trees which provide the skeleton of the model. This statement is, however, correct only in a statistical sense. The presence of the gas induces significant differences in the timing of the halo mergers, and affects significantly the halo orbits making them more circular, on average. Although these effects might be over-estimated in our non–radiative runs, our results suggest that an accurate treatment of merging times is crucial for predicted quantities like the mass accretion history of model brightest cluster galaxies. As sub-haloes are fragile systems that are rapidly reduced below the resolution limit of the simulation (De Lucia et al., 2004a; Gao et al., 2004c), the treatment of satellite mergers in semi-analytic models requires the use of analytic formulations (e.g. the Chandrasekhar formula). Recent

THE EFFECT OF GAS-DYNAMICS ON SEMI-ANALYTIC MODELING OF CLUSTER GALAXIES

work (Boylan-Kolchin et al., 2008; Jiang et al., 2008) has shown the limits of the formulation usually adopted in semi-analytic models. This recent work, however, does not provide consistent alternative formulations. Additional work is therefore needed in order to obtain a more realistic and detailed description of the merging process, which represents a crucial ingredient of semi-analytic models of galaxy formation.

CHAPTER 7

SPH AND SEMI-ANALYTIC MODELING OF CLUSTER GALAXIES

In this Chapter we compare predictions on the cluster galaxy population from simplified version of the semi-analytic code used also in the previous Chapter and of a Tree-SPH simulation based on the GADGET-2 code. Both techniques include only gravitational dynamics, gas cooling and star formation. No other physical process (e.g. stellar evolution, chemical enrichment or any energy feedback source) has been taken into account. Following a similar approach, Helly et al. (2003) have compared predictions of a stripped-down version of a semi-analytic model with an SPH simulation which included only cooling (see also Benson et al., 2001), with the only difference that they have set an evolving metallicity for the gas particles in the simulation. In the semi-analytic model they have artificially increased the cooling time in haloes with less than 32 particles to mimic the underestimate of the gas density, and therefore of the cooling efficiency, in these haloes. Galaxies in the SAM were matched to simulated galaxies selecting the SPH galaxies that contain the majority of the gas particles of the original halo in which the SAM galaxy formed. They found a quite good agreement, with SAM galaxies having a larger stellar mass with respect to their simulation counterpart by about 25%, excluding the most massive galaxies. For the satellite galaxies they found a similar trend, but a larger scatter. Yoshida et al. (2002) analysed a GADGET-2 simulation of a galaxy cluster and compared it with predictions of a stripped-down version of a semi-analytic model. They concluded that the predicted mass of galaxies are in good agreement, even if the scatter in the relation is large, in particular for satellite galaxies. They also found an excess of SAM galaxies which did not have a counterpart in the SPH simulation. Cattaneo et al. (2007) included in their comparison also star formation. A minimal feedback due to thermal heating of SN explosions was also included in the simulation. They analysed a cosmological box containing a most massive halo of $\sim 3 \times 10^{14} h^{-1} M_{\odot}$ and found a general good agreement, especially on the prediction of the baryonic (stellar plus gas) component. Similar to other authors they found an excess of galaxies in the stripped-down version of the

semi-analytic model compared to the simulation. None of the above mentioned studies has taken into account substructures within the SAM adopted. In this work we want to further investigate the predictions of semi-analytic models and SPH simulations on the cluster galaxy population. The simulated cluster used here is a version of the g51 cluster already described in Chapters 4 and 6, which included only gas cooling and a simple star formation scheme (Section 7.1). We run the stripped-down version of a semi-analytic model using the merger trees based on the simulation itself. In this way we can compare numerical predictions of the same galactic population, as we will describe later in the text. The plan of the Chapter is as follows. In Sec. 7.1 we describe the cluster simulation used in this study, while in Sec. 7.2 we provide a brief description of the adopted SAM. In Sec. 7.3 we present the results of our analysis regarding the comparison on the whole cluster galaxy population, while in Sec. 7.4 we focus on a detailed comparison on a sample of galaxies which have been matched in the SAM and SPH simulation. We will discuss our conclusions in Section 7.5.

7.1 THE SIMULATION

The simulation was carried out using the TreePM-SPH code GADGET-2 (Springel, 2005) and includes only gravitational dynamics, gas cooling and a simple scheme of star formation. All the gas particles colder than 10^5 K and denser than 4×10^{-27} g cm $^{-3}$ (corresponding to $n_H = 0.1$ cm $^{-3}$ for a gas of primordial composition) are immediately turned into star particles, which undergo only gravitational dynamics and are not affecting the hydrodynamical part of the computation. The Plummer-equivalent softening length for the gravitational force was set to $\epsilon = 5 h^{-1}$ kpc in physical units from $z = 5$ to $z = 0$, while at higher redshifts it was set to $\epsilon = 30 h^{-1}$ kpc in comoving units. The smallest value assumed for the smoothing length of the SPH kernel was half the gravitational softening. Simulation data were stored in 93 outputs that are approximately logarithmically equispaced in time down to $z \sim 1$, and approximately linearly equispaced in time thereafter. Each simulation output was analysed in order to construct merger trees of all identified sub-haloes as described in Chapter 6. In this Chapter, we will refer to all quantities related to the simulation with the label SPH. We identify as “bona fide” galaxies only those SUBFIND-groups containing at least 20 DM particles.

7.2 THE SEMI-ANALYTIC MODEL

We have used a stripped-down modification of the semi-analytic model described by De Lucia & Blaizot (2007) and which has been used and described in the previous Chapter. We recall that the semi-analytic model we employ builds upon the methodology originally introduced by Kauffmann et al. (1999b), Springel et al. (2001) and De Lucia et al. (2004b). We have turned off all the physical processes with the exception of the gas cooling and of the

Table 7.1: Characteristics of the analysed cluster used in this study within r_{200} at $z = 0$. Column 1: name of the run; Column 2: number of identified galaxies; Column 3: total stellar mass M_* in units of $10^{13} h^{-1} M_\odot$; Column 4: total gas mass M_{gas} in units of $10^{13} h^{-1} M_\odot$; Column 5: total star formation rate (SFR) in units of $10^3 M_\odot \text{ yr}^{-1}$. In the last row we show values for the Type-0 and Type-1 SAM galaxy population only.

Run name	N_{gal}	M_*	M_{gas}	SFR
SPH	442	5.3	9.2	0.5
SAM	2497	6.1	8.4	2.2
SAM (Types 0-1)	299	4.3	8.3	2.1

star formation, in order to have a fair comparison between the direct simulation predictions and the semi-analytic model predictions.

In this Chapter we will refer to all predictions from the semi-analytic model with the label SAM.

In Table 7.1, we list the number of identified galaxies N_{gal} , the total stellar mass M_* , the total gas mass M_{gas} and the total star formation rate SFR within r_{200} of the cluster as predicted by the SPH simulation and by the SAM. Moreover, in the last row of Table 7.1, we list the same quantities for the SAM Type-0 and Type-1 galaxy population only.

As an example of the different predictions of SPH and SAM for the build-up of galaxies, we show in Figure 7.1 a typical merger tree of a synthetic galaxy. More in detail it represent the merger tree of the fourth most massive galaxy in the SPH simulation at $z = 0$ within r_{200} . We show the merger tree of the SAM galaxy in the upper panel and the merger tree of the SPH galaxy in the lower panel. The size of the symbols is proportional to the square root of the galaxy stellar mass, and colours are a representation of the galaxy Type. We recall that by definition, in the SPH simulation a Type-2 galaxy population does not exist. Final stellar mass of the SAM galaxy is $M_* \sim 1.5 \times 10^{12} h^{-1} M_\odot$, which is about three times larger than the final stellar mass of the corresponding SPH galaxy. SPH merger trees of haloes are computed as described in the previous Chapter. Accordingly, all galaxies which lie in a merger tree are progenitors of the resulting galaxy at redshift $z = 0$. This is not the case for SAM galaxies. We recall the reader that whenever a substructure merge at a lookback time T_{init} , the associated SAM galaxy will survive and keep its identity for a time T_{merge} computed following Eq. (6.1). Therefore, in the case that T_{merge} is larger than T_{init} , the resulting Type-2 galaxy will not appear as a progenitor of the main galaxy of the tree. The net result is that merger trees of SPH galaxies have a much larger number of *branches*, corresponding to a larger number of progenitors, than SAM galaxies.

We note that in the SAM merger tree, galaxies increase their stellar mass mostly while they are Type-0 central galaxies and the gas is allowed to radiative cools toward their centre to form stars. Satellite Type-1 and Type-2 galaxies can increase their stellar mass basically only

via merging, and do not decrease their stellar mass. This is not the case for SPH galaxies. When a Type-0 galaxy enters the FoF group of another larger substructure and become a Type-1 satellite galaxy, it starts to lose its stellar mass due to tidal interactions with the main galaxy and deposits part of its stellar mass in the form of the diffuse stellar component of the Type-0 central galaxy. Therefore, by the time that the satellite galaxy merges, its stellar mass is significantly lower than before entering in the main halo. We will discuss more in detail this effect in Sections 7.3 and 7.4..

Figure 7.2 shows the stellar mass density of the cluster in the SPH simulation within a box of side $10r_{200}$ (upper panels) and in a zoomed region of side $2r_{200}$ (lower panels). Superposed on these maps we show the position of the identified galaxies in the SPH run (left panels) and in the SAM run (right panel) with stellar mass larger than $10^{11} h^{-1} M_{\odot}$ with larger radii corresponding to larger masses. Different colours are used for different galaxy types: red for Type-0, black for Type-1, and green for Type-2 galaxies. Upper panels highlight the higher stellar mass of the BCG in the SPH simulation compared to the SAM BCG. Furthermore the fraction of massive Type-0 galaxies at larger radii from the cluster centre is higher in the SPH simulation. A Type-2 galaxy population with significantly large mass is present in the central cluster region in the SAM run. Lower panels show how more massive galaxies tend to populate central regions of the cluster, with a higher number of Type-1 massive galaxies in the SAM run than in the SPH simulation, as a result of the loss of stellar mass due to tidal interaction affecting SPH satellite galaxies.

7.3 COMPARING PREDICTIONS ON THE GALAXY POPULATION

In this Section we will compare the properties of the galaxy population directly predicted by the SPH simulation with those predicted by the SAM. More in detail we will statistically compare the radial density distribution and the mass function of the synthetic galaxy populations, while we will also present a one-to-one comparison of *same galaxies* in the next Section.

7.3.1. Radial distribution of galaxies

We show in Figure 7.3 the computed radial density of galaxies identified at $z = 0$ within $5r_{200}$ of the analysed cluster used in our study. Solid black lines show the radial density of galaxies directly identified in the SPH simulation, while dashed-dotted red lines show the SAM predictions. The dashed green line in each panel shows the matter density profile normalised to match the radial density of SAM galaxies in the inner regions of the cluster. The three panels show separately the radial density of the whole galaxy population (upper panel), of the Type-2 satellite galaxy population (lower left panel), and of the Type-0 and Type-1 satel-

7.3. Comparing predictions on the galaxy population

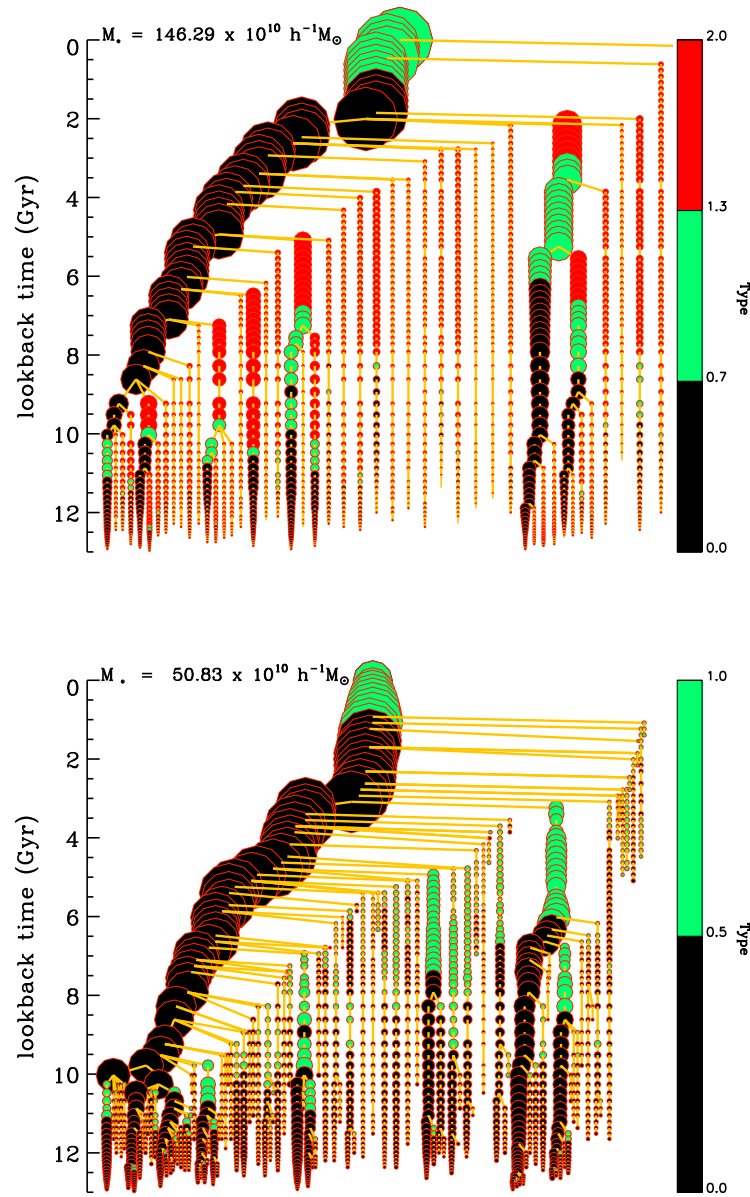


Figure 7.1: Example of a merger tree of the fourth most massive in stellar mass galaxy found in the simulation within r_{200} . Upper panel shows the merger tree of the synthetic galaxy as computed in the SAM. Lower panel shows the merger tree of the same galaxy as results directly from the simulation. Size of circles are proportional to square root of the galaxy stellar mass. Different colours are used for different galaxy types. Black is for Type-0 central galaxies, green for Type-1 satellite galaxies and red for Type-2 satellite galaxies. Final stellar mass of this galaxy is shown in the upper left corner of each panel.

SPH AND SEMI-ANALYTIC MODELING OF CLUSTER GALAXIES

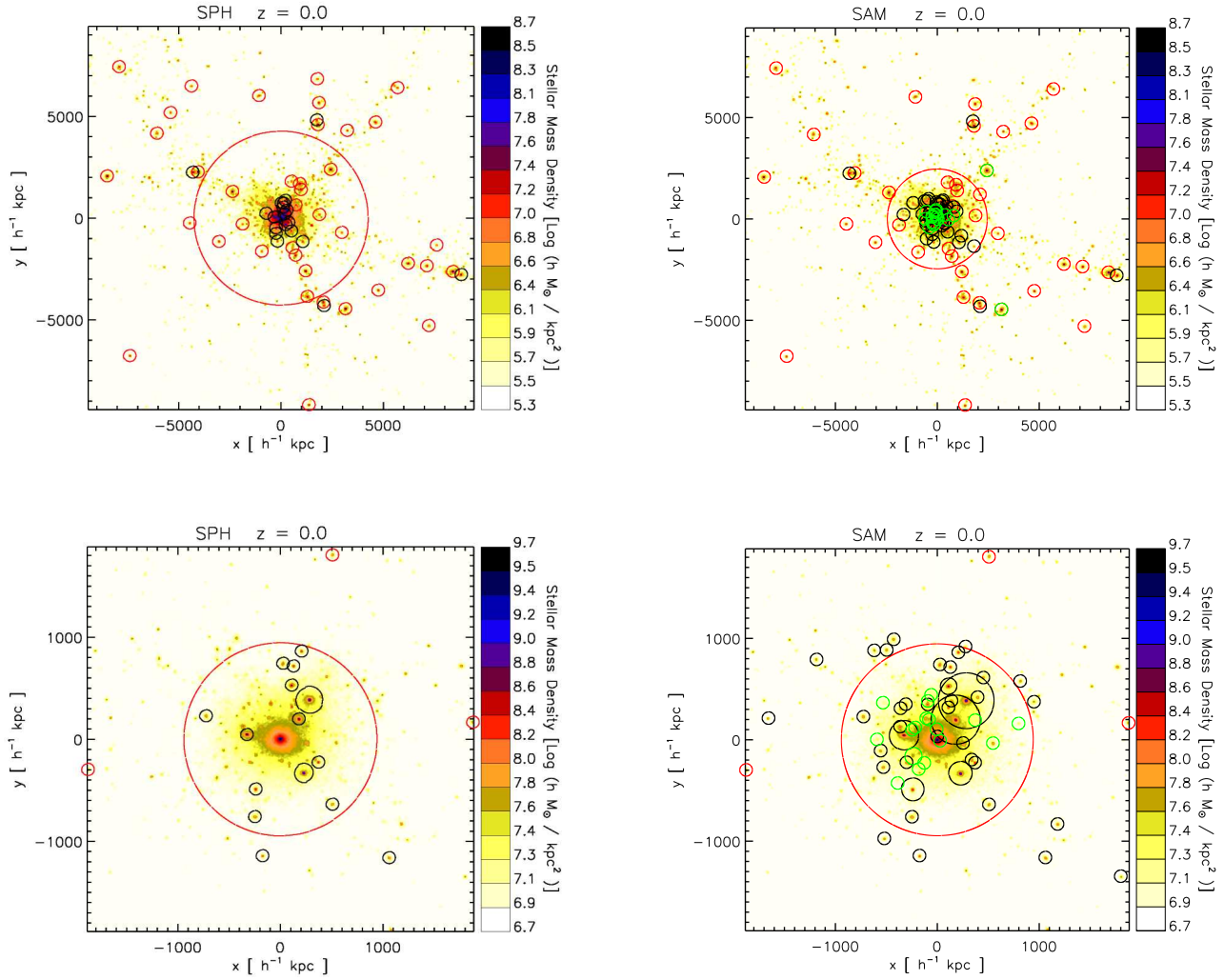


Figure 7.2: Stellar density map of a box placed at the centre of the analysed cluster and of size $10r_{200}$ (upper panels) and $2r_{200}$ (lower panels). Positions are in comoving units. The positions of all galaxies with stellar mass larger than $10^{11} h^{-1} \text{ M}_\odot$ are marked by circles with larger radii corresponding to larger stellar mass as computed in the simulation (left panels) and in the SAM (right panels). Different colours are used for different galaxy types: red for Type-0, black for Type-1, and green for Type-2 galaxies.

7.3. Comparing predictions on the galaxy population

lite galaxies (lower right panel). We note that the SPH and SAM predicted distribution of the global galaxy population differ significantly in the inner regions of the clusters where the Type-2 galaxy population becomes dominant in the SAM. The distribution of SAM galaxies closely follows the matter profile. Quite interestingly we note that in the inner regions of the cluster the number of Type-1 SPH satellite galaxies is higher than the number of Type-1 satellite galaxies in the SAM run, as reported in Table 7.1. This is quite surprising, as the dynamics of these galaxies in the SAM run is the same as in the SPH run. We have checked that these SPH galaxies which do not have a counterpart in the SAM run are galaxies for which the code used to build the merger trees has "failed" to reconstruct the correct history of galaxies. In practice, to minimise errors due to numerical noise, whenever the code does not find the descendent of a halo between two contiguous snapshots, it is allowed to find the descendent (if it exists) at a maximum "distance" of two snapshots. This population of SPH galaxies which do not have a SAM counterpart is formed by galaxies which lie in haloes that during their history have not been identified for a number of contiguous snapshots, larger or equal than three. As a result, these galaxies "disappear" at some point in the merger tree and "appear" as new ones later on. The adopted SAM assumes that all the radiative cooling is feeding the central Type-0 galaxy. This implies that in the case that these galaxies appear directly as new Type-1 satellite galaxies, the SAM predicts a null cold gas reservoir and therefore a null stellar mass. However, placed at the same position of this SPH Type-1 galaxy population which does not have a SAM counterpart, we find Type-2 galaxies in the SAM run, which are the orphan galaxies of the erroneously disappeared galaxies in the SPH simulation.

7.3.2. Mass function of galaxies

We show in Figure 7.4 the stellar mass function of galaxies identified at $z = 0$ within $1.5r_{200}$. We have plotted separately the mass functions of the whole galaxy population (upper panels), of the Type-2 satellite galaxy population (central panels), and of the Type-0 and Type-1 satellite galaxies (lower panels). Differential and cumulative mass functions are shown in left and right panels respectively. Upper panels of Fig. 7.4 emphasise the larger stellar mass associated to the SPH BCG compare to the SAM BCG. Number of galaxies in the SAM run are about a factor of five larger than SPH simulation predictions (see Table 7.1). The drop in the SPH mass function at a mass of $M_* \sim 10^9 h^{-1} M_\odot$ is due the resolution limit of our simulation. The majority of galaxies in the SAM predictions within $1.5r_{200}$ are Type-2 galaxies. Lower panels show that the total number of Type-1 satellite galaxies is larger in the SPH run than in the SAM run as described in the previous subsection. We note that the high mass end of the stellar mass function of galaxies predicted is higher in the SAM run than in the SPH run. This is, as already mentioned, not true for the BCGs. Indeed the BCG in the SPH run has a stellar mass which is almost double than the SAM BCG. We will show in the next subsections how these differences can be explained at least partially in terms of

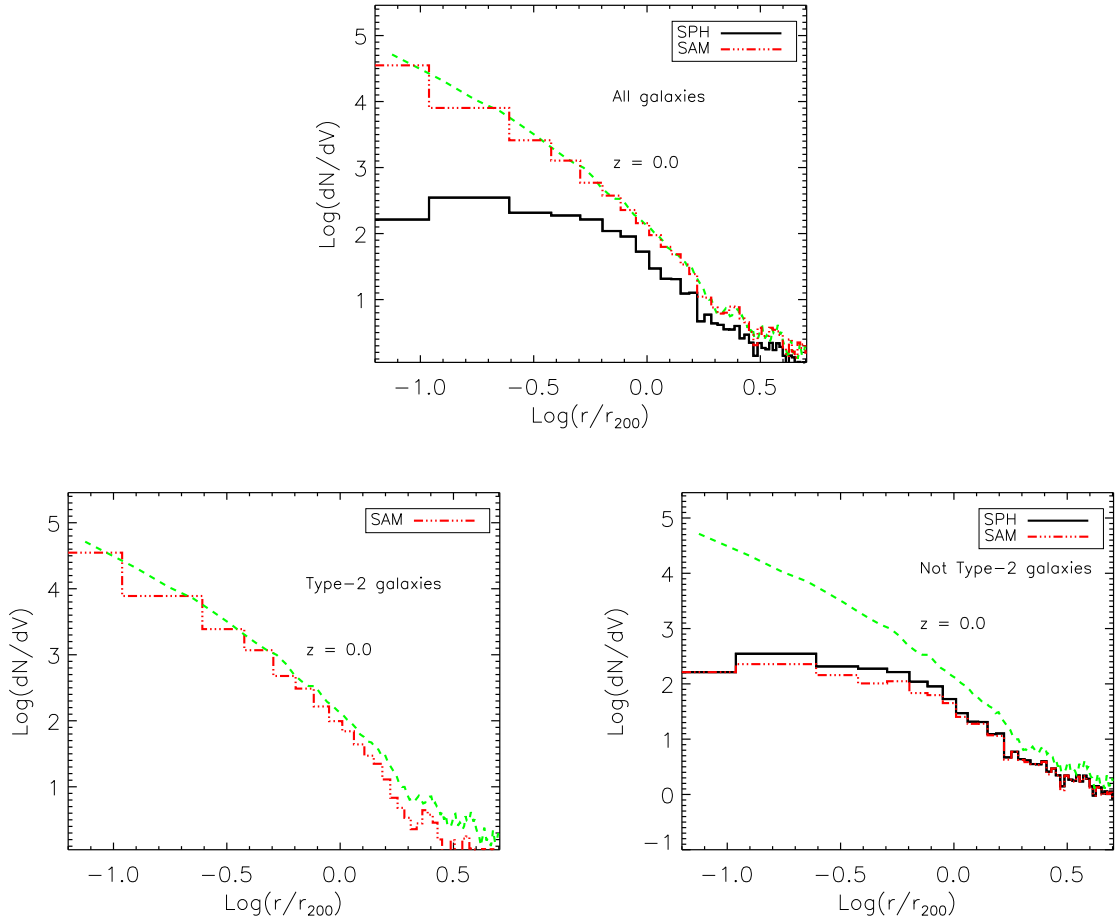


Figure 7.3: Radial density of galaxies identified at $z = 0$ and within $5r_{200}$ of the analysed cluster used in our study. Solid black lines show the radial density of galaxies directly identified in the simulation, while dashed-dotted red lines show the SAM predictions. The dashed green line in each panel shows the density profile of matter, normalised to match the radial density of SAM galaxies in the inner regions of the cluster. The three panels show separately the radial density of the whole galaxy population (upper panel), of the Type-2 satellite galaxy population (lower left panel), and of the Type-0 and Type-1 satellite galaxies (lower right panel).

tidal stripping of stellar mass from the SPH Type-1 satellite galaxies which increase the SPH BCG stellar mass in the form of diffuse stellar component and in terms of star formation in sub-resolved haloes.

7.4

COMPARING PREDICTIONS ON SINGLE GALAXIES

The dynamics of central galaxies and satellite Type-1 galaxies in the semi-analytic model are based on the merger trees computed directly from the SPH run. As a result, we can identify *same galaxies* in the two runs as the galaxies which have the same positions in both SAM and SPH galaxy catalogues. In this Section we will compare the properties of same galaxies as predicted by the SAM and the SPH simulations.

7.4.1. General behaviour

As already mentioned, we define a sample of galaxies from the two models which includes all the galaxies at $z = 0$ which have the same coordinates in the two runs. This sample includes all the central Type-0 galaxies and all the satellite Type-1 galaxies, with the exception of those Type-1 satellite galaxies in the SPH run which do not have a counterpart in the SAM run, as described in Section 7.3. In Figure 7.5 we show the stellar mass of these galaxies at $z = 0$ as predicted by the SAM (y axis) and by the direct SPH simulation (x axis). Type-0 central galaxies are shown as black crosses, while Type-1 satellite galaxies are shown as red diamonds. The cyan continuous line represents the one-to-one correspondence. Different panels show different radial bins, with the cluster-centric distance of galaxies increasing from the left top panel to the right bottom panel. We note that in the innermost part of the cluster (upper left panel), corresponding to galaxies at a distance smaller than $0.25r_{200}$, there is only one Type-0 central galaxy, which is the BCG itself, and 15 Type-1 satellite galaxies. The only galaxy lying below the cyan line and thus having a larger stellar mass predicted by the SPH simulation is the BCG. For all the Type-1 satellite galaxies, the stellar mass predicted by the SAM is larger than the one predicted by the SPH simulation even by more than one order of magnitude. In the upper right panel we show all the galaxies which have a cluster-centric distance in the range $0.25 < r/r_{200} < 0.5$. In this bin there are no Type-0 central galaxies. We note that Type-1 satellite galaxies tend to have a larger mass in the SAM run than in the SPH run. As the cluster-centric distance increase we start to find other central Type-0 galaxy. We note that, generally, Type-0 central galaxies tend to have a larger stellar mass than predicted by the SPH simulation, while Type-1 satellite galaxies tend to have a larger stellar mass predicted by the SAM. The disagreement between final stellar masses of *same galaxies* as predicted by the SAM and by the SPH simulation can be larger than an order of magnitude and the scatter around the one-to-one relationship is increasing at lower stellar masses. We further note that the disagreement between stellar masses of SAM and SPH Type-1 satellite galaxies is lower at larger radii, where the effect of tidal stripping becomes

SPH AND SEMI-ANALYTIC MODELING OF CLUSTER GALAXIES

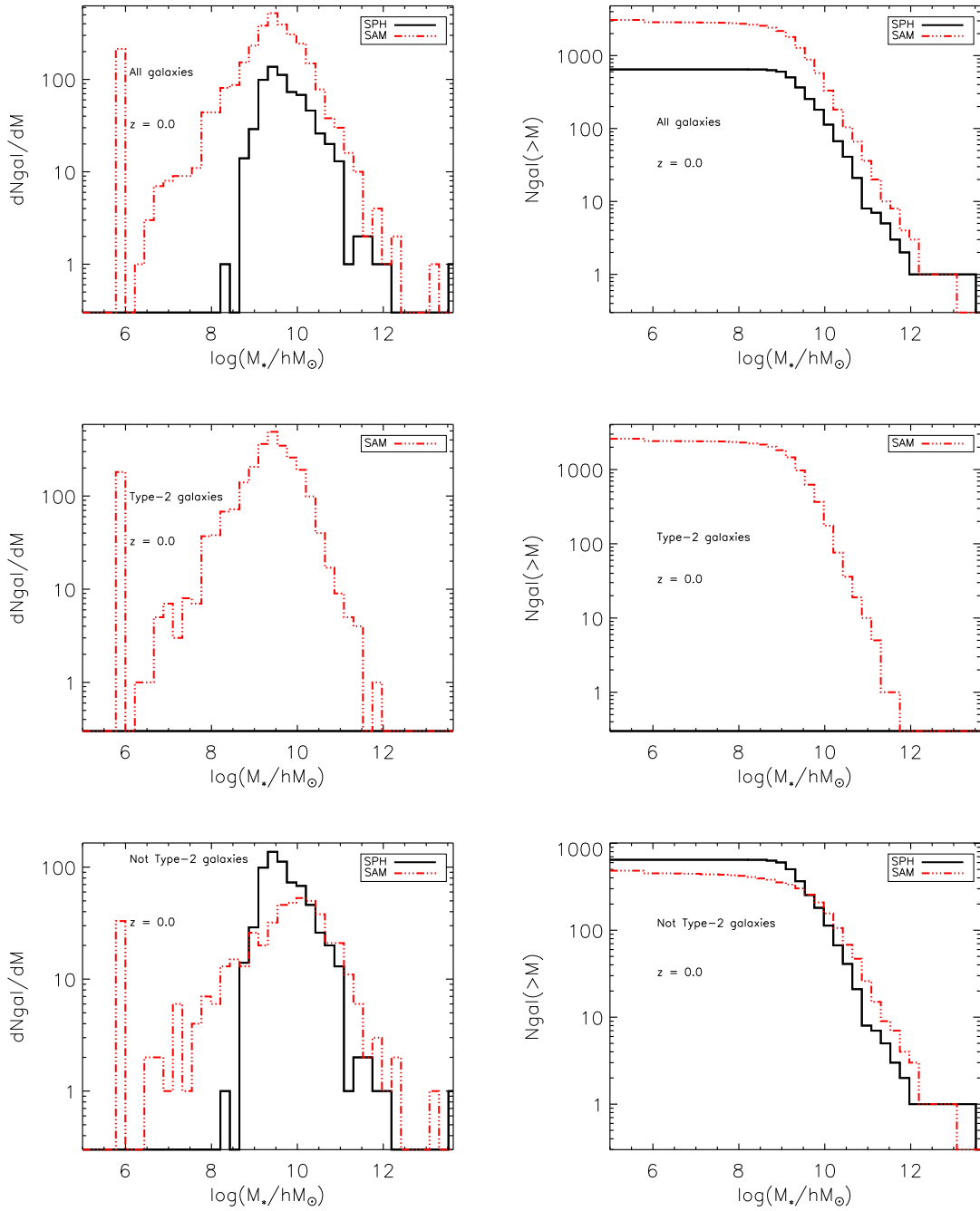


Figure 7.4: Differential (left panels) and cumulative (right panels) stellar mass functions for all galaxies within $1.5r_{200}$ at $z = 0$ in the analysed simulated cluster as predicted by the SPH simulation (black continuous lines) and by the SAM (red dashed lines). We show separately the stellar mass functions of the whole galaxy population (upper panels), of the Type-2 satellite galaxy population (central panels) and the Type-0 and Type-1 galaxies (lower panels). SAM galaxies with a stellar mass lower than $10^6 h^{-1} M_\odot$ are shown in the $10^6 h^{-1} M_\odot$ bin

less important. We recall that, however, tidal stripping of star particles from satellite galaxies is not the main process of formation of the diffuse stellar component. Indeed, Murante et al. (2007), showed that the main contribution to the diffuse stellar component is due to violent relaxation processes related to mergers in the formation of BCGs.

7.4.2. Evolution of galaxies

In the previous subsection we have shown that the direct SPH simulation generally predicts a larger stellar mass for the central Type-0 galaxies than for their counterparts in the SAM run. We now discuss more in detail this effect. In Figure 7.6 we show the evolution of the BCG as predicted by the direct SPH simulation (black lines) and by the SAM (red lines). More in detail in the upper left panel we show the number of progenitors as a function of the lookback time for the two techniques. As explained also in Section 7.2, the number of progenitors per galaxy in the SPH run is larger than in the SAM run. This difference is due to the Type-2 galaxy population, which maintain its identity in the SAM run. This population of galaxies instead does not exist in the simulations. Whenever a substructure merge in the simulation, the associated galaxy will merge as well. Thus the number of progenitors is higher in simulated galaxies. Furthermore the merging rate (the derivative of the curve) predicted by in the SAM and SPH runs looks quite different. Indeed, the merging rate is almost linear along the whole galaxy history in the SAM run, while in the SPH simulation presents a phase of fast merging activity before a lookback time of ~ 7 Gyrs, followed by a plateau which lasts between roughly 7 and 2 Gyrs ago, and then another phase of high merging rate in the last 2 Gyrs. The upper right panel shows the star formation history of the BCG progenitors as a function of the lookback time. Clearly, the predicted star formation history in the SPH and in the SAM simulated galaxies differs a lot. The SPH BCG has an initial burst of star formation placed at a lookback time of ~ 12 Gyrs followed by a sharp decline which creates most of its stellar mass. After a lookback time of ~ 7 Gyrs the star formation rate associated to the BCG progenitors is roughly constant at a value of $\sim 400 M_{\odot} \text{ yr}^{-1}$ until $z = 0$. The predicted star formation history of the SAM BCG looks quite different. It remains roughly constant along the whole history of the galaxy at a mean value of $2000 \div 3000 M_{\odot} \text{ yr}^{-1}$. Our explanation of this striking difference resides in the treatment of the cooling assumed in the semi-analytic model. In the SAM the adopted cooling model used is based on White & Frenk (1991), as described in subsection 3.4.1. The gas that falls into the potential well of a dark matter halo is all assumed to be heated by shocks, attaining the halo virial temperature, and then cools toward the centre of the main halo. A model of the cold accretion mode have been also implemented in the adopted SAM. Whenever the computed cooling radius of a halo is larger than its r_{200} , the SAM assumes that all the gas instantaneously cools toward the centre of the galaxy. This implementation is not able to describe the cold accretion mode occurring in the SPH simulated BCG at early ages. Filaments of cold gas penetrate the virial radius and directly fed the central galaxy without

SPH AND SEMI-ANALYTIC MODELING OF CLUSTER GALAXIES

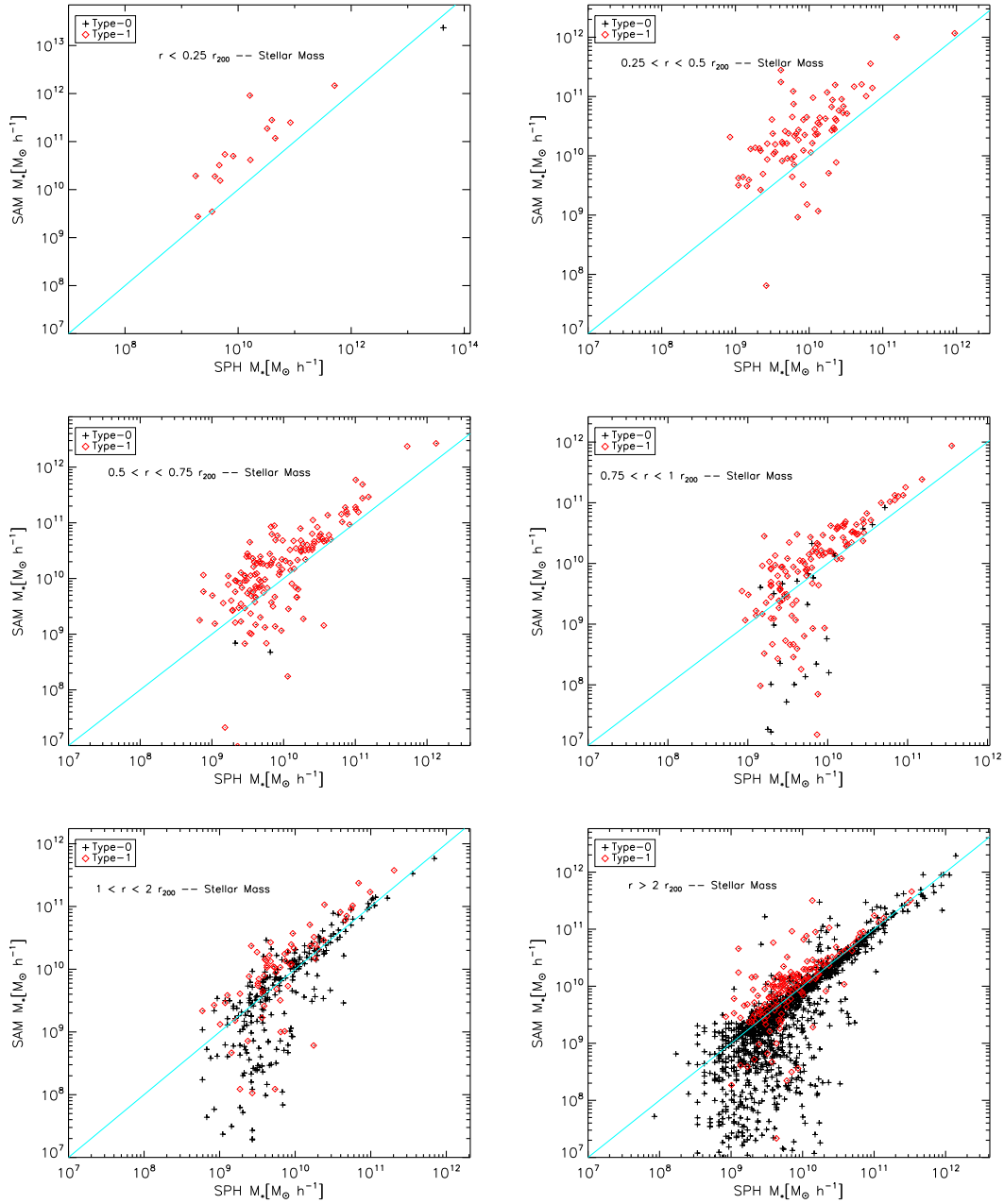


Figure 7.5: Comparison between the galaxy stellar masses as predicted by the SPH simulations (x axis) and by the SAM (y axis) at redshift $z = 0$ in different radial bins. Each symbol represent a galaxy which has the same position in both analysis, thus it is considered as *same galaxy*. The cyan continuous line represent the one to one correspondence. Black crosses are Type-0 central galaxies and red diamonds are Type-1 satellite galaxies.

7.4. Comparing predictions on single galaxies

being heated to the virial temperature (Dekel et al. 2008 and references therein). In the adopted star formation scheme of the simulation, this cold gas reservoir is instantaneously turned into stars. As a result, all the low entropy gas is converted into stars in a very efficient way, and the burst of star formation rate last for a short time. Quite interestingly, even if the predicted star formation histories of BCG galaxies differ systematically, the integral of the star formation rates along the history of the two simulated galaxies is almost identical. In other words the final stellar mass predicted by this two star formation histories is roughly the same. This can be seen by comparing the dashed-dotted black line (SPH) and the continuous red line (SAM) of the lower right panel of Fig. 7.6 which show the integral of the star formation history shown in the lower left panel of the same figure. We note that by $z = 0$ both lines converge to a value of $\sim 2.2 \div 2.310^{13} h^{-1} M_{\odot}$. A naive expectation would therefore be that the final stellar mass of BCGs agree in the two numerical predictions. This instead is not the case, as already shown in Fig. 7.4 and 7.5. Lower left panel of Fig. 7.6 shows the accretion history of the BCG progenitors. Stellar mass of the SAM BCG linearly increase, consistently with a constant star formation rate. Accretion history of the SPH BCG can be divided in two different phases. There is first regime with a sharp increase of the stellar mass at lookback times greater than 8 Gyrs, consistent with the initial burst of star formation. Then a second regime takes place for lookback times lower than roughly 6 Gyrs in which the stellar mass restart to increase almost linearly, almost doubling the final BCG stellar mass. We show again in the lower right panel the accretion history of the progenitors of the BCGs superimposed with the integral of the star formation rate plotted in the upper right panel. We note the the stellar mass of the SAM BCG agrees very well with the integral of the star formation rate, meaning the all the stellar mass associated to the BCG at $z = 0$ was formed in the BCG progenitors. This is not the case in the SPH BCG, where the integral of the star formation rate of the BCG progenitors is responsible for about only half of the final stellar mass. In other words, only about half of the final stellar mass of the BCG was formed in its progenitors. A possible contribution to the amount of this stellar component could arise from *diffuse* star formation occurring inside unresolved galaxies, which will eventually merge with the BCG by redshift $z = 0$ (as described in Chapter 5). The associated SFR of each SPH galaxy at each snapshot was computed as the total amount of stellar particles belonging to the galaxy with a formation time lower than the previous snapshot and divided by the time interval of the snapshots. As these galaxies are formally unresolved, they do not appear in the BCG merger tree, in the case that their formation is outside the FoF group of the main halo. Thus their contribution was not taken into account in the computation of the star formation history. Nevertheless their stellar mass is present and considered once merged with a resolved galaxy.

Another more likely explanation for the origin of a stellar component which is associated to the central BCG and has not been formed into its progenitors can resides in stellar particles which have been formed into other satellite galaxies and then tidally stripped to form the diffuse intra-cluster light. We know that a diffuse stellar component, which SUBFIND is not able to separate from the truly BCG stellar mass (see Chapter 3), is associated to the

formation of central cluster galaxies (see Murante et al. 2007 and references therein).

Figure 7.7 shows the evolution of the fourth most massive galaxy found in the SPH simulation at $z = 0$ within r_{200} as predicted by the direct SPH simulation and by the SAM. Merger trees of these galaxies were shown in Fig. 7.1. As this galaxy retains its dark matter halo until $z = 0$, its dynamics is described in the same way in the two models. Upper left panel shows the distance between the main progenitor of the galaxy and the centre of the cluster as a function of the lookback time. It shows how the satellite galaxy is crossing r_{200} (computed at each time) of the cluster around 1.5 Gyrs ago and reaches a minimum cluster-centric distance of $\sim 0.2r_{200}$ by $z = 0$. Dashed blue vertical line is placed at the lookback time corresponding to the transition between Type-0 and Type-1 galaxy of the galaxy main progenitor. This is the time at which the galaxy is entering in the cluster FoF group, and is roughly placed at the crossing time of the virial radius. Upper right panel shows again the difference in number of progenitors predicted by the SPH simulation and by the SAM, as explained in previous sections. The dip in the number of progenitors which is visible for example at a lookback time of ~ 9 Gyrs in the SAM run is due to numerical noise. Indeed, if a structure is not identified in a snapshot but appears back in the following one, the code used for building the merger trees is able to link the two structures and skip the snapshot where the halo is missing. The merging rate of galaxies predicted by the two techniques is more similar here than the one found for the BCG shown in Fig. 7.6. Indeed both predictions exhibit an almost constant merging rate over the last 11 Gyrs. Star formation histories for the two simulated galaxies are shown in the lower right panel. Similarly to the BCG, the SPH galaxy shows a high redshift burst of star formation rate followed by a plateau, while its SAM counterpart shows a more constant star formation history. Quite interestingly the SPH simulated galaxy shows an increase in the SFR after roughly the time in which the galaxy has crossed r_{200} . Overall, star formation histories predicted by SPH and SAM disagree less for this galaxy than for the BCG. Lower right panel shows again the integral of the star formation history (continuous red line for the SAM run and dashed-dotted black line for the SPH run) superimposed with the accretion history of stellar mass (dotted red for the SAM run and dotted black for the SPH run) of the galaxy progenitors. The sharp and narrow changes in the accretion history curves are due to numerical noise as described for the upper right panel. As for the BCG, the accretion history of the SAM galaxy closely follows the integral of the star formation history, meaning that all the stellar mass of the galaxy at $z = 0$ has been formed in the galaxy's progenitors. The behaviour of the SPH galaxy is instead more complicated, and can be divided in two different regimes:

- As long as the main progenitor of the galaxy is a central Type-0, its stellar mass is larger than the integral of the star formation history by about 15%. Indeed the galaxy is a Type-0 central galaxy. Thus it will have its own satellite galaxies, which will deposit their stellar mass as its own diffuse stellar component due to tidal stripping of star particles leading to a larger mass in stars.

7.4. Comparing predictions on single galaxies

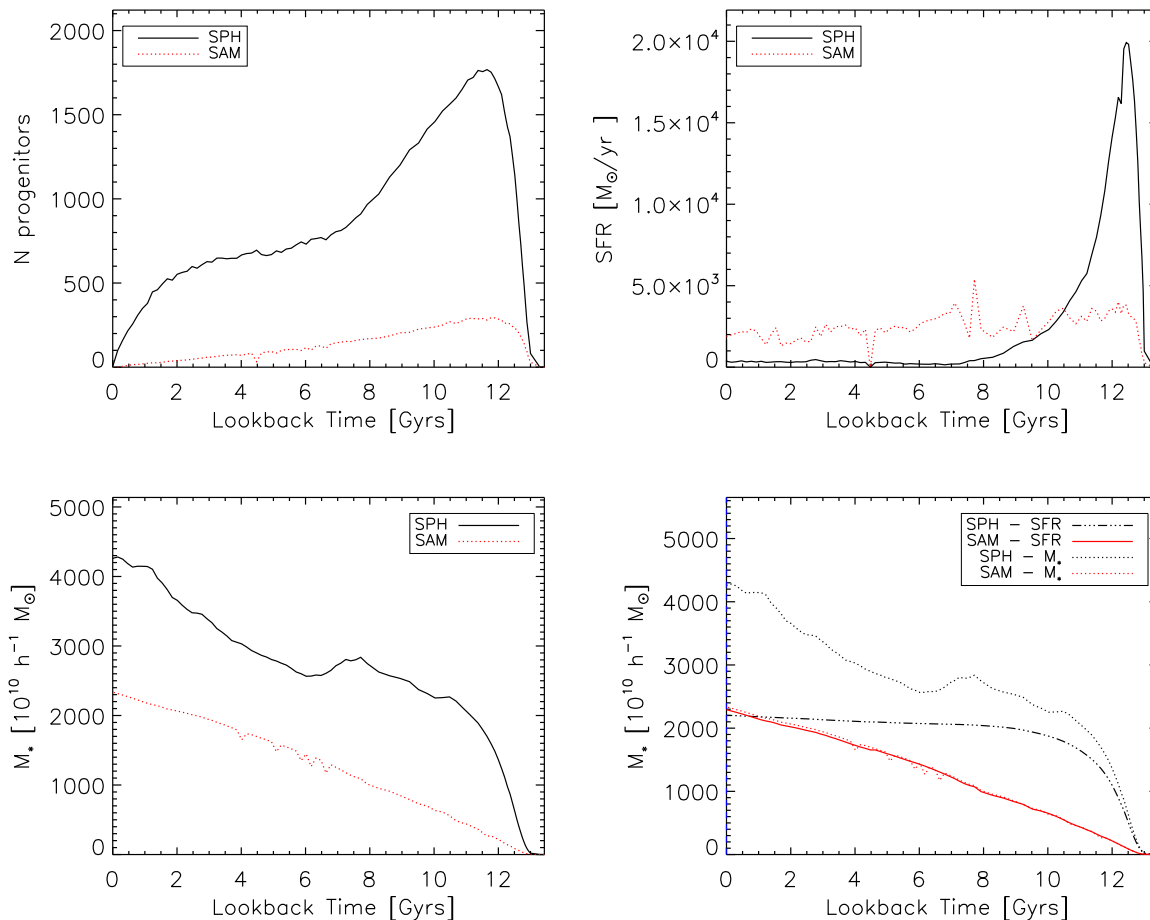


Figure 7.6: We show in this Figure the evolution of the BCG of the analysed cluster as predicted by the SPH simulation (continuous black lines) and by the SAM (dashed red lines). *Upper right panel:* The number of identified galaxies which will eventually merge with the BCG by redshift $z = 0$ as a function of the lookback time. *Upper left panel:* The total star formation rate in the identified progenitors of the BCG at redshift $z = 0$ as a function of the lookback time. *Lower right panel:* The total stellar mass in the identified progenitors of the BCG at redshift $z = 0$ as a function of the lookback time. *Lower left panel:* A comparison between the total stellar mass (dashed-dotted (SPH) and continuous (SAM) lines) and the integral of the star formation rate (dotted lines) in the identified progenitors of the BCG at redshift $z = 0$ as a function of the lookback time.

- As the galaxy crosses the virial radius and becomes a satellite Type-1 galaxy which approaches the centre of the cluster, it starts to loose stellar mass. We have checked that the loss of stellar mass in the second regime is consistent with tidal stripping of star particles due to the cluster potential well, which go into the diffuse intra-cluster component.

7.4.3. Effect of the environment

In this subsection we study the effect of the environment on the numerical prediction of the direct SPH simulation and of the SAM on two different galaxies: a Type-0 central galaxy and a Type-1 satellite galaxy. We choose two galaxies with an almost identical stellar mass predicted by the SAM at $z = 0$ of about $610^{11} h^{-1} M_{\odot}$. The evolution of the central Type-0 galaxies is shown in the left panels of Figure 7.8 and 7.9, while on the right panels is shown the evolution of the satellite Type-1 galaxy. Similarly to Figure 7.7, dashed blue vertical line is placed at the lookback time corresponding to the transition between Type-0 and Type-1 galaxy of the galaxy main progenitor. More in detail Fig. 7.8 shows the cluster-centric distance of the galaxy main progenitor as a function of the lookback time. The central galaxy is found at redshift $z = 0$ at a distance of $\sim 2.5r_{200}$ from the cluster centre, while the satellite galaxy is crossing the cluster virial radius roughly at a lookback time of ~ 9 Gyrs and by $z = 0$ have done already 6 orbits around the centre of the cluster with a period of ~ 2 Gyrs per orbit. We note that the pericentre and the apocentre, as well as the orbital period, tend to decrease with the number of orbits as a result of the momentum loss due to dynamical friction. The galaxy roughly reached its apocentre by $z = 0$ at a distance of $\sim 0.5r_{200}$. Upper panels of Fig. 7.9 show the SPH simulation and SAM prediction of the star formation histories of the two analysed galaxies. We note that the agreement between SPH and SAM predictions on the star formation history of these two galaxies is much better than in the cases shown in Fig. 7.6 and 7.7, even if the star formation history predicted by the SPH simulation still exhibits a earlier, sharper and more intense burst of star formation for both galaxies than for their SAM counterparts. A possible explanation for the earlier burst of star formation associated to SPH galaxies can also reside in the different treatment of star formation implemented in these two techniques. While the SPH simulation assumes that all the gas colder and denser than a certain threshold is immediately turned into stars, star formation in the SAM occurs with a characteriscs time-scale computed as the dynamical time of the galaxy disk. Both SPH and SAM runs predict a more intense and sharper episode of star formation at early times for the satellite galaxy than for the central galaxy. Both SPH and SAM Type-1 satellite galaxies do not predict any significant star formation activity after entering in the cluster environment. On the contrary, a mildly declining star formation rate is predicted for the Type-0 central galaxy until $z = 0$. These two behaviours are closely related: as we have chosen two galaxies with the same predicted stellar mass at $z = 0$ in the SAM run, a longer star formation in the central galaxy naturally implies a more intense burst

7.4. Comparing predictions on single galaxies

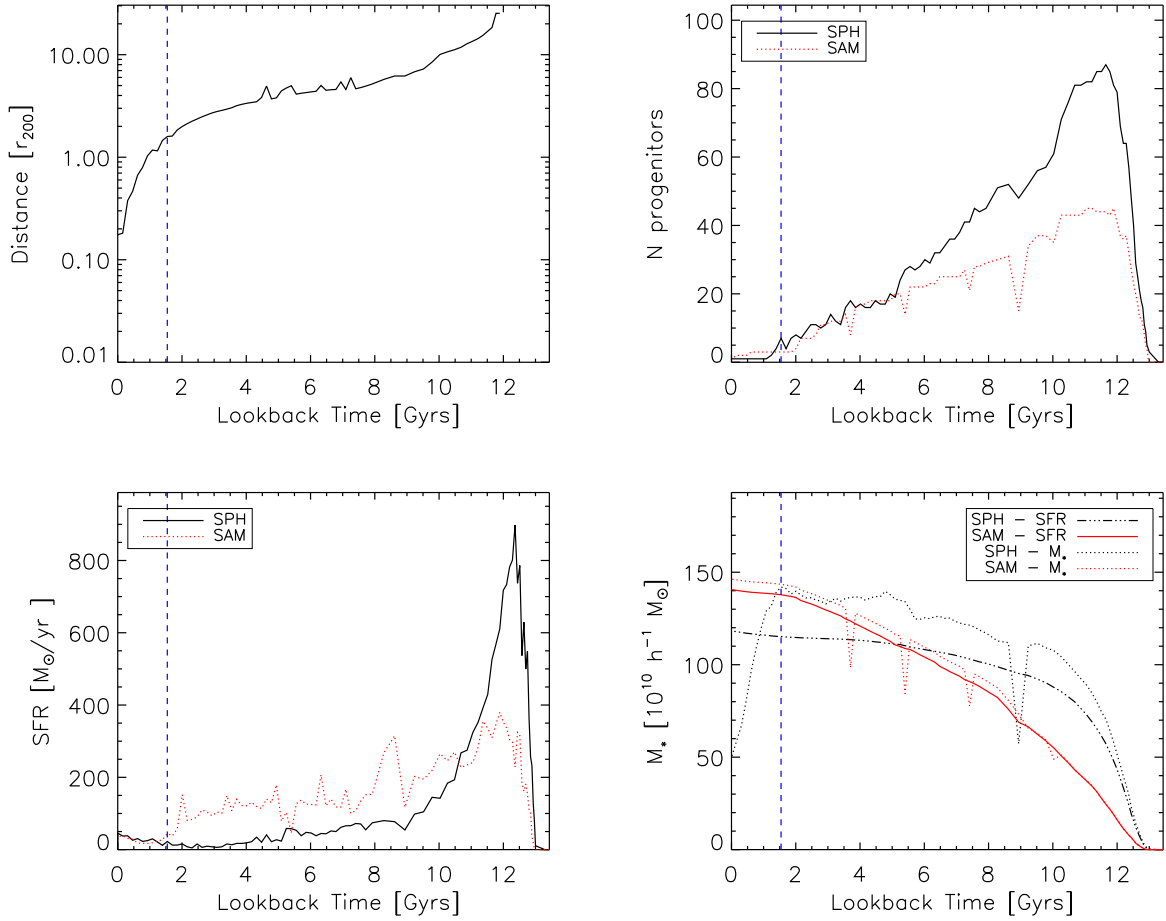


Figure 7.7: We show in this Figure the evolution of the fourth most massive galaxy within r_{200} at $z = 0$ as predicted by the SPH simulation (continuous black lines) and by the SAM (dashed red lines). Merger trees of this galaxy were shown in Fig. 7.1. *Upper right panel:* Distance between the main progenitor of the studied galaxy and the centre of the cluster as a function of the lookback time in units of the corresponding r_{200} of the cluster at that time. *Upper left panel:* The number of identified progenitors of the galaxy as a function of the lookback time. *Lower left panel:* The total star formation rate in the identified progenitors of the galaxy as a function of the lookback time. *Lower right panel:* A comparison between the total stellar mass (dashed-dotted (SPH) and continuous (SAM) lines) and the integral of the star formation rate (dotted lines) in the identified progenitors of the galaxy as a function of the lookback time. Dashed blue vertical line is placed at the lookback time corresponding to the transition between Type-0 and Type-1 galaxy of the galaxy main progenitor.

of star formation in the satellite galaxy. Lower panels of Fig. 7.9 show the accretion history of stellar mass of the two galaxies superimposed with the integral of star formation history, as explained in Fig. 7.6 and 7.7. We note that the integral of the star formation histories as predicted by the SPH simulation and by the SAM are in reasonably good agreement, with the exception of the first ~ 2 Gyrs. Stellar mass accretion for the SPH central Type-0 galaxy follows quite well the integral of the star formation history until a lookback time of 2 Gyrs. Later the galaxy starts to increment its stellar mass almost linearly due to accretion of a stellar diffuse component via tidal stripping of star particles from its satellites. As a result, the final stellar mass in the SAM run has a lower mass than its counterpart in the SPH run by $\sim 30\%$. As in Fig. 7.7, also the SPH Type-1 satellite galaxy has two different regimes. In the first ~ 3 Gyrs its stellar mass is larger than the integral of its star formation history. Later there is sharp drop in the stellar mass associated with the transition between central Type-0 and satellite Type-1 galaxy, highlighted by the dashed blue vertical line. A part for some numerical noise, the accretion history of the satellite galaxy clearly exhibits a first faster decrease of stellar mass associated to the first orbits and a smoother decrease of stellar mass associated with the later orbits. Eventually, by $z = 0$ the galaxy has lost $\sim 85\%$ of its stellar mass. Furthermore the amount of "extra" stellar mass in the form of diffuse component associated to the SPH galaxy while it is a Type-0 central galaxy, is larger for the satellite galaxy shown in the right panels than for the central galaxy shown in the left panels. This fact, as well as the more intense and earlier burst of star formation occurring into the satellite galaxy, are consistent with a scenario in which this galaxy forms in a denser environment with a higher merging rate at higher redshifts than the central galaxy shown in the left panels.

7.5 SUMMARY AND DISCUSSION

In this Chapter we have compared the cluster galaxy population predicted by an hydrodynamical cosmological simulation with the one predicted by a semi-analytic code. Both numerical predictions are based on stripped-down versions of the codes which include only gas cooling and star formation. The main results of our work can be summarised as follows.

- [1] The overall number of galaxies predicted by the SAM is much higher than the number of galaxies predicted by the SPH-simulation. This is due to presence of a Type-2 galaxy population in the SAM which is not produced by the SPH simulation and which dominate mainly the inner regions of the cluster. Quite surprisingly a larger number of Type-1 satellite galaxies is predicted in the SPH run compared to the SAM run in the central regions of the cluster. These satellite galaxies are a young population of galaxies which spend all their life as satellite galaxies. As such, radiative gas cooling does not take place at the centre of these galaxies and no star formation is predicted by the SAM.

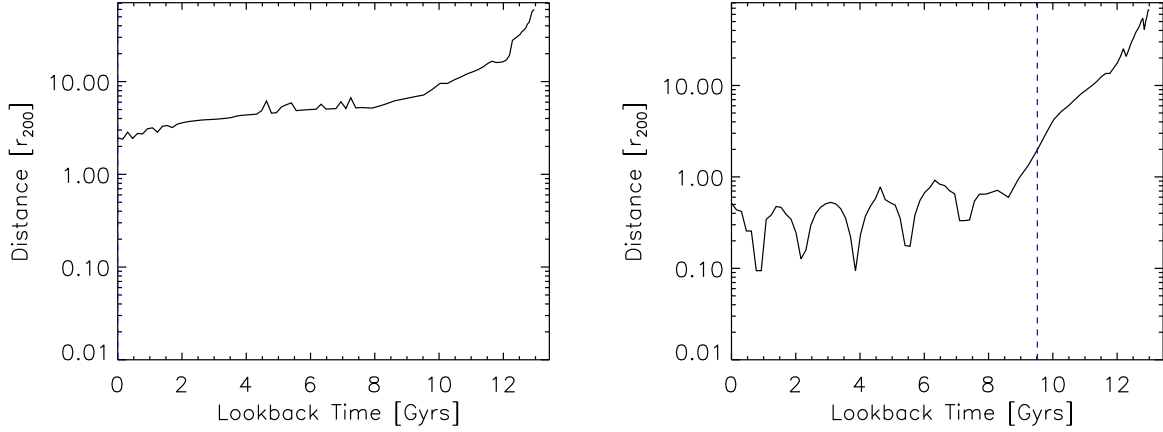


Figure 7.8: We show in this Figure the evolution of the cluster-centric distance between the main progenitor a central Type-0 galaxy (right panel) and of a satellite Type-1 galaxy (left panel) as a function of the lookback time in units of the corresponding r_{200} of the cluster at that time. Both galaxies have a predicted stellar mass at $z = 0$ of $\sim 6 \times 10^{11} h^{-1} M_{\odot}$ in the SAM run. The dashed vertical blue line is placed at the position of transition between central Type-0 and satellite Type-1 of the main progenitor of the galaxy.

- [2] We have found a general trend in the SPH central Type-0 galaxies to be more massive than their counterpart in the SAM run. On the contrary, SAM satellite Type-1 galaxies have associated a larger stellar mass than their SPH counterpart. As a result the stellar mass of the BCG is larger in the SPH simulation than in the SAM run by about a factor of two. A possible explanation for this behaviour can be found in the diffuse stellar component lost by the satellite galaxies in favour of the central Type-0 galaxy associated to tidal stripping of stellar material when the satellite galaxy approaches the centre of the main halo. These two regimes of increasing stellar mass during the phase of central galaxy and loss of stellar mass in the phase of satellite galaxy are present in all the analysed galaxies. While this mechanism arises in the SPH simulation, it is not included in the SAM description.
- [3] Star formation history of galaxies predicted by SPH and SAM models are in good agreement in lower dense environment, while the discrepancy increases in galaxies lying in deeper potential wells. We argue that the different treatment of cooling is responsible for this behaviour. In particular the cold accretion mode implemented in the SAM is not able to reproduce the very intense initial burst of star formation predicted for the BCG by the SPH simulation.
- [4] Both SPH and SAM models predict a faster and more intense burst of star formation associated to satellite galaxies compared with central galaxies of similar integrated star

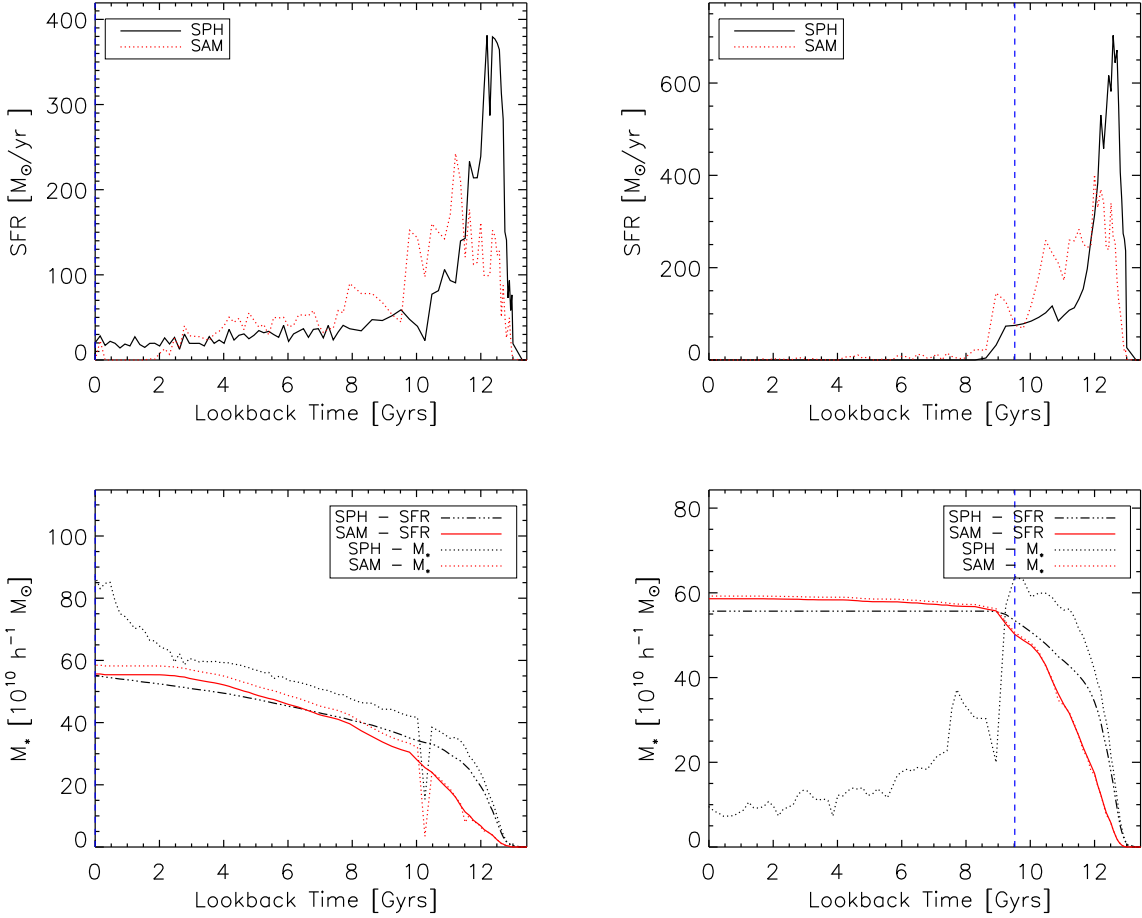


Figure 7.9: We show in this Figure the evolution of a central Type-0 galaxy (right panels) and of a satellite Type-1 galaxy (left panels) as predicted by the SPH simulation (continuous black lines) and by the SAM (dashed red lines). Both galaxies have a predicted stellar mass at $z = 0$ of $\sim 60 \times 10^{10} h^{-1} M_{\odot}$ in the SAM run. *Upper panels:* The total star formation rate in the identified progenitors of the galaxy as a function of the lookback time. *Lower panels:* A comparison between the total stellar mass (dashed-dotted (SPH) and continuous (SAM) lines) and the integral of the star formation rate (dotted lines) in the identified progenitors of the galaxy as a function of the lookback time. Dashed blue vertical line is placed at the lookback time corresponding to the transition between Type-0 and Type-1 galaxy of the satellite galaxy main progenitor.

formation history. Again, while SPH and SAM predictions on the star formation history are in reasonable agreement, the accretion history of galaxies differ substantially as a function of the environment.

Our results demonstrate that predictions of stripped-down versions of semi-analytic models and SPH simulations are in reasonable agreement in lower dense environment, while significant differences are found in overdense environments. In particular predictions on the star formation history of the BCG substantially disagree, even if the integral of the star formation history are in a close agreement. Furthermore a detailed description of the formation of a diffuse stellar component has to be included in the semi-analytic models of galaxy formation in order to give results comparable with the SPH simulations.

The results of this Chapter will be published in a forthcoming paper (Saro et al. 2009 in preparation). In order to further refine the analyses presented here, we plan undertake the two following steps:

- We need to disentangle the effects of the different treatments of gas cooling and star formation implemented in the SPH and SAM models. The large discrepancy found in the star formation histories of the SAM and SPH BCGs should be partially contributed by the inefficient treatment of the cold accretion mode implemented in the SAM. However, the time-scale of star formation associated to SAM galaxies may also play a role. In order to separate the two contributions we plan to analyse the cluster galaxy population predicted by the SAM by setting the time-scale of star formation to zero.
- The merging time associated to the Type-2 galaxy population in the SAM is responsible for the different merger trees of SPH and SAM galaxies. Indeed, to obtain a more comprehensive and coherent comparison between the SAM and SPH predictions, we need to eliminate the presence of a Type-2 galaxy population in the SAM by artificially setting to zero the merging time associated to Type-2 galaxies in the SAM run.

CHAPTER 8

CONCLUSIONS

This Section is devoted to draw the conclusions of the work presented in the previous Chapters. We discuss them in the Section 8.1, whereas in Section 8.2 we outline future prospects and developments.

8.1 DISCUSSION AND CONCLUSIONS

In this Thesis we resorted to advanced numerical methods presented in Chapter 3 to study the formation and evolution of the cluster galaxy population within the hierarchical cosmological framework. In particular in the first part of the Thesis (Chapters 4 and 5) we explored the potentiality of direct hydrodynamical cosmological simulations to study the formation and evolution of the cluster galaxies. Then, in the second half of this Thesis (Chapters 6 and 7), we studied the complementarity of the two techniques used to study galaxy formation within the hierarchical cosmological framework, semi-analytic models and direct hydrodynamical simulations. While traditionally SAMs were widely used to study galaxy formation in the last decade and earlier, only recently direct hydrodynamical simulations achieved a sufficient numerical resolution and detailed description of the physical processes to provide predictions on the statistical properties of galaxy populations in a cosmological context.

More in detail we studied the following aspects of the cluster galaxy population:

■ Properties of galaxies in nearby clusters

In Chapter 4 we presented a study of the galaxy population predicted by hydro-dynamical simulations of galaxy clusters. These simulations, which are based on the GADGET-2 Tree+SPH code, include gas cooling, star formation, a detailed treatment of stellar evolution and chemical enrichment, as well as SN energy feedback in the form of galactic winds. As such, we

CONCLUSIONS

used them to extract the spectro–photometric properties of the simulated galaxies, which are identified as clumps in the distribution of star particles. Simulations have been carried out for a representative set of 18 cluster–sized halos, having mass M_{200} in the range 5×10^{13} – $1.8 \times 10^{15} M_{\odot}$. All simulations have been performed for two choices of the stellar initial mass function (IMF), namely using a standard Salpeter IMF with power–law index $x = 1.35$, and a top–heavy IMF with $x = 0.95$. We highlight that at the moment this is the most comprehensive study on a large number of simulated galaxy clusters with different IMFs and feedback schemes presented in the literature (Saro et al. 2006, Fabjan et al. 2008).

We found that several of the observational properties of the galaxy population in nearby clusters are reproduced fairly well by simulations. A Salpeter IMF is successful in accounting for the slope and the normalisation of the colour–magnitude relation for the bulk of the galaxy population. In contrast, the top–heavy IMF produces too red galaxies, as a consequence of their exceedingly large metallicity. Simulated clusters have a relation between mass and optical luminosity which generally agrees with observations, both in normalisation and slope. Also in keeping with observational results, galaxies are generally bluer, younger and more star forming in the cluster outskirts. However, we found that our simulated clusters have a total number of galaxies which is significantly smaller than the observed one, falling short by about a factor 2–3. We have verified that this problem does not have an obvious numerical origin, such as lack of mass and force resolution. Finally, the brightest cluster galaxies are always predicted to be too massive and too blue, when compared to observations. This is due to gas over–cooling, which takes place in the core regions of simulated clusters, even in the presence of the rather efficient supernova feedback used in our simulations.

■ Simulating the core of a proto-cluster region at $z \simeq 2$

In Chapter 5 we presented results from two high–resolution hydro–dynamical simulations of proto–cluster regions at $z \simeq 2.1$ (Saro et al. 2009). The simulations have been compared to observational results for the so-called Spiderweb galaxy system, the core of a putative proto–cluster region at $z = 2.16$ described in Chapter 2, found around a radio galaxy. The simulated regions have been chosen so as to form a poor cluster with $M_{200} \simeq 10^{14} M_{\odot}$ and a rich cluster with $M_{200} \simeq 2 \times 10^{15} M_{\odot}$ at $z = 0$. The simulated proto-clusters show evidence of ongoing assembly of a dominating central galaxy. The stellar mass of the brightest cluster galaxy (BCG) of the richer system is in excess with respect to observational estimates for the Spiderweb galaxy, with a total star formation rate which is also larger than indicated by observations. We found that the projected velocities of galaxies in the richer cluster are consistent with observations, while those measured for the poorer cluster are too low compared to the observed velocities. We argued that the Spiderweb complex resemble the high–redshift progenitor of a rich galaxy cluster. Our results indicate that the included supernovae feedback is not enough to suppress star formation in these systems, supporting the need of introducing AGN feedback. According to our simulations, a diffuse atmosphere of hot gas in hydrostatic equilibrium should already be present at this redshift, and enriched

at a level comparable to that of nearby galaxy clusters. We predicted that the presence of this gas should be detectable with future deep X-ray observations.

■ The effect of gas-dynamics on semi-analytic modelling of cluster galaxies

In Chapter 6 we studied the degree to which non-radiative gas dynamics affects the merger histories of haloes along with subsequent predictions from a semi-analytic model (SAM) of galaxy formation (Saro et al. 2008). To this aim, we used a sample of dark matter only and non-radiative SPH simulations of four massive clusters. We investigated how the presence of gas-dynamical processes (e.g. ram-pressure from the hot intra-cluster atmosphere) makes haloes more fragile in the runs which include gas. This results in a 25 per cent decrease in the total number of sub-haloes at $z = 0$. The impact on the galaxy population predicted by SAMs is complicated by the presence of ‘orphan’ Type-2 galaxies, i.e. galaxies whose parent substructures are reduced below the resolution limit of the simulation. In the model employed in our study, these galaxies survive (unaffected by the tidal stripping process) for a residual merging time that is computed using a variation of the Chandrasekhar formula. Due to ram-pressure stripping, haloes in gas simulations tend to be less massive than their counterparts in the dark matter simulations. The resulting merging times for satellite galaxies are then longer in these simulations. On the other hand, we showed how the presence of gas influences the orbits of haloes making them on average more circular and therefore reducing the estimated merging times with respect to the dark matter only simulation. We found that this effect is particularly significant for the most massive satellites and is (at least in part) responsible for the fact that brightest cluster galaxies in runs with gas have stellar masses which are about 25 per cent larger than those obtained from dark matter only simulations. Our results showed that gas-dynamics has only a marginal impact on the statistical properties of the galaxy population, but that its impact on the orbits and merging times of haloes strongly influences the assembly of the most massive galaxies.

■ SPH and semi-analytic modelling of cluster galaxies

In Chapter 7 we presented results from a detailed comparison between a direct SPH simulation based on the GADGET-2 code and semi-analytic predictions of the cluster galaxy population for a simulated massive cluster with $M_{200} \sim 1.14 \times 10^{15} M_{\odot}$ (Saro et al. 2009, in preparation). Both numerical predictions are based on stripped-down code versions, including only gravitational dynamics, radiative cooling and star formation. The adopted semi-analytic model was run on the merger trees directly extracted from the SPH simulation. As such, we identified a sample of “same galaxies” as the population of galaxies which are characterised by the same position in both SAM and direct simulation prediction. We found that due to the presence of a population of “orphan” Type-2 galaxies in the SAM, the overall number of galaxies is much larger than the number of galaxies predicted by the SPH simulation. This population of galaxies dominates the inner region of the cluster. We noted a

CONCLUSIONS

general trend for the SPH simulated central galaxies to be more massive than their counterparts in the SAM run. In contrast SAM satellite galaxies have larger stellar masses than their SPH counterparts. We showed that these differences are due to the diffuse stellar component lost by satellite galaxies because of tidal stripping due to the main halo. We presented a detailed comparison of the evolution of SAM and SPH "same galaxies". While we found a reasonable agreement for the predicted star formation history of galaxies living in lower density environment, a substantial discrepancy is found for galaxies lying in deeper potential wells. Indeed the predicted star formation history for the BCGs differs quite substantially. The SPH simulated BCG has a spike of star formation at high redshift which exhausts the low entropy gas. The SAM instead predicts an almost constant star formation along the whole BCG history. We argued that these differences are mainly due to an underestimate of the cold accretion mode implemented in the semi-analytic model. Finally we found that both numerical techniques predict that satellite galaxies have earlier and more intense episodes of star formation than central galaxies with similar integrated star formation rates.

8.2 FUTURE PERSPECTIVES

- [1] We statistically studied hydrodynamical cosmological predictions on the cluster galaxy population only at $z = 0$. Obviously, a more comprehensive study have to take into account also the evolution of the galactic population. Thus we plan to compare observed properties of cluster galaxies with the numerical predictions from hydrodynamical simulations also at higher redshifts. However, it is clear that before addressing the problem of the evolution of the properties of cluster galaxies out to $z \sim 1.5$ it is recommendable to reach first a good agreement with observations of nearby clusters, for which data are much more precise. Since we already know that we have a strong excess of star formation in the low- z BCGs, we believe there is little point to investigate how they would compare with observations of distant clusters.
- [2] A key ingredient to improve the description of cluster galaxies both at low and at high redshift is represented by AGN feedback. Indeed, AGN feedback is expected to play a crucial role in quenching star formation, especially in the deepest potential wells such as BCGs, where indeed we find an excess of star formation. Beside AGN feedback, we plan to adopt alternative and more physically motivated schemes of star formation and SN feedback, which should also help in providing a more realistic population of cluster galaxies, e.g. preventing the suppression of sub- L_* galaxies associated to the galactic ejecta included in the simulations presented in this Thesis.
- [3] We plan to investigate the uncertainties associated to spectro-photometric codes. In the recent literature, significant differences have emerged regarding the implementation of the Thermally-Pulsing Asymptotic Giant Branch (TP-AGB) phase of stellar evolution. When the TP-AGB phase is active, the rest-frame $V - K$ galaxy colours are redder

by almost 2 magnitudes in the redshift range $z \sim 2 \div 3$ and by 1 magnitude at $z \sim 1$ (Tonini et al. 2008). We plan to study the effect of the TP-AGB phase in the predicted simulated cluster galaxy population at redshift $z \sim 2 \div 3$.

From the results presented in this Thesis, it is quite clear that direct cosmological hydrodynamical simulations and semi-analytical techniques provide highly complementary approaches toward a complete understanding of galaxy formation process. Cosmological simulations of single galaxies are now reaching high enough resolution to provide a detailed description of their structural properties (e.g., Mayer et al. 2008, for a recent review). On the other hand, simulations of cosmological volumes necessary for a statistical description of the galaxy population are still characterised by a relatively poor resolution. There is no doubt that this situation will steadily improve in the coming years, thanks to the ever increasing super-computing power and code efficiency. These technical improvements need to be paralleled by a continuous refinement of the description of the physical processes included in the simulation codes, both at super-resolution and sub-resolution scales.

Despite these improvements, it is hard to expect in the foreseeable future that simulations will become competitive with SAMs in terms of flexibility in the exploration of the space of the parameters describing the physics of galaxy formation. However, they will play a crucial role in capturing in detail the complexity of the relevant gas-dynamical processes and, therefore, to refine the SAM ingredients.

The future generation of ground-based (e.g., ELT, ALMA) and space telescopes (e.g., JWST) will allow us to push to unprecedented redshift the study of galaxies. Fully exploiting the potentiality of SAM and of direct simulations will be necessary to provide a consistent picture of the process of galaxy formation and evolution across cosmic epochs, from the formation of first objects at $z \sim 10$ to the present, and in a variety of environments.

CONCLUSIONS

CHAPTER A

APPENDIX - Basics of Cosmology

The basic axiom of modern cosmology is a form of the Copernican idea that human beings – that is to say the Earth – have not a role in the Universe which is special in any respect. This Cosmological Principle states that the Universe is spatially isotropic and homogeneous, meaning that any observer in any place will infer for it the same general properties. Both isotropy and homogeneity are confirmed by observations of the mass distribution on large scale, the Large Scale Structure (LSS), of the Cosmic Microwave Background (CMB), of the cosmic velocity field and of the cosmological X-ray background. In spite of this, it is evident that the Universe is neither homogeneous nor isotropic on small, local scales. This discrepancy is due to a small primeval perturbation field which is superimposed to an otherwise homogeneous mass distribution. These tiny departures from homogeneity subsequently grow forming the currently observed cosmic structures. Hence, the cosmological theory must solve a twofold problem: the evolution of the Universe as a whole, and the evolution of such perturbations. This latter topic is deferred to Sec. (A.2), while in the rest of this Section we picture the dynamics of cosmological expansion. Finally in Sec. (A.3) we picture some of the key observations that constrain the cosmological model.

A.1 BASIC EQUATIONS FOR AN EXPANDING UNIVERSE

We assume that (1) the Gravitation governs the evolution of the Universe on large scales through the Einstein's Theory of General Relativity and (2) the metric tensor of the Universe is given by the Friedmann–Robertson–Walker (FRW) metric (see for e.g. Weinberg 1972):

$$ds^2 = dt^2 - a(t)^2 \left[\frac{dr^2}{1 - kr^2} + r^2 (d\theta^2 + \sin^2\theta\phi) \right] \quad (\text{A.1})$$

where the *expansion factor* $a(t)$ describes how distances scale with time as a consequence of the Hubble expansion and k is the space *curvature*. We know (Hubble & Humason 1931)

Component	Eq. of State
Relativistic Matter	$p = 1/3\rho$
Non-Relativistic Matter	$p = 0$
Vacuum energy	$p = -\rho$
Curvature	$p = -1/3\rho$

Table A.1: Equations of state for different matter–energy components in the Universe.

that an observer at rest recedes from any other given observer at rest with a velocity, given by $H(t)D$, which increases with the distance D . The *Hubble constant* $H(t)$ at a time t is defined as:

$$H(t) = \frac{d \log a(t)}{dt} \quad (\text{A.2})$$

and has the units of $\text{km s}^{-1} \text{Mpc}^{-1}$. H_0 is at present and is commonly parametrised as $H_0 = 100 h \text{ km s}^{-1} \text{Mpc}^{-1}$, where $h = 70.5 \pm 1.3$ (Komatsu et al. 2008).

As a consequence of this space expansion, a photon emitted at a time t in the past will be observed at present time $t = 0$ red-shifted by a factor $z = 1/a(t) - 1$ which is exactly called *redshift*; here we set $a(t = 0) \equiv 1$.

The Einstein’s field equation

$$G_{\mu\nu} = R_{\mu\nu} - \frac{1}{2}\mathcal{R}g_{\mu\nu} = 8\pi GT_{\mu\nu} + \Lambda g_{\mu\nu} \quad (\text{A.3})$$

relates the geometry of the Universe, with its own energy content, carried by the stress–energy tensor T , for which we assume the form of a perfect fluid:

$$T_{\mu\nu} = pg_{\mu\nu} + (p + \rho)u_\mu u_\nu. \quad (\text{A.4})$$

where p and ρ are related by an equation of state $p = p(\rho)$. The form of such equation for each component is reported in Tab. (A.1).

Substituting the FRW form of metric and the perfect fluid tensor in the field equations gives the *Friedmann’s Equations* that describe the expansion of the Universe:

$$\left(\frac{\dot{a}}{a}\right)^2 + \frac{k}{a^2} = \frac{8\pi G}{3}\rho \quad (\text{A.5})$$

$$\frac{\ddot{a}}{a} = -\frac{4\pi G}{3}(\rho + 3p) + \frac{\Lambda}{3}. \quad (\text{A.6})$$

It is useful to define the *critical density* ρ_c as the density needed for $k = 0$; then, it results:

$$\rho_c = \frac{3H^2(t)}{8\pi G} \simeq (1.9 \times 10^{-29}(\text{g cm}^{-3})h^2). \quad (\text{A.7})$$

The density ρ_x of a component x of the universe is commonly expressed in units of ρ_c defining the quantity Ω_x as

$$\Omega_x = \rho_x / \rho_c. \quad (\text{A.8})$$

The first of the Friedmann equations can be recasted as:

$$k = a^2 H^2 (\Omega - 1) \quad (\text{A.9})$$

where Ω accounts for overall the density of the matter–energy density. Hence, the Universe will be spatially *closed*, *flat* or *open* if its means density is respectively smaller, equal or larger than the critical density.

If Ω_r represents the density from the radiation field, Ω_m the density from matter (both baryonic and dark matter), Ω_Λ is due to the Cosmological Constant Λ and we set $\Omega_k = -k/H_0^2 = 1 - \Omega_0$ the second Friedmann equation can be rewritten as:

$$\frac{H(t)}{H_0} = \left[\frac{\Omega_r}{a^4} + \frac{\Omega_m}{a^3} + \frac{\Omega_k}{a^2} + \Omega_\Lambda \right]. \quad (\text{A.10})$$

The Simplest case of $\Omega_k = \Omega_\Lambda \equiv 0$ is called the *Einstein–de Sitter* model; in this case the scaling factor a varies with time as $a(t) \propto t^{2/3}$. It is note-worthy that all models with non–zero Ω_Λ and Ω_k approach the Einstein–de Sitter behaviour when

$$(1 + z) \gg \max \left[\frac{(1 - \Omega_m - \Omega_\Lambda)}{\Omega_m}, \left(\frac{\Omega_\Lambda}{\Omega_m} \right)^{1/3} \right]. \quad (\text{A.11})$$

Finally, we can express $a(t)$ as:

$$a(t) = a_0 \left[1 - H_0(t - t_0) - q_0 h_0^2 (t_0 - t)^2 + \dots \right] \quad (\text{A.12})$$

where

$$q_0 = -\frac{\ddot{a}_0 a_0}{\dot{a}_0^2} = \frac{1}{2} \Omega_{0m} - \Omega_\Lambda \quad (\text{A.13})$$

is called *deceleration parameter*.

A.2

STRUCTURE FORMATION

Besides providing a theory to describe the very early times of the universe and the general framework for the expanding universe, a Cosmological Theory must also provide a model for the formation of cosmological structures and the large scale distribution of matter. To give a comprehensive outline of that matter is far beyond the scope of this brief introduction,

so that we address the reader to dedicated reviews (e.g. Peebles & Ratra 2003, Coles 2000 and Peacock 2001), while in the following we give only few basic ideas.

The Universe shows locally a very rich hierarchical pattern of galaxies, galaxy clusters and clusters of clusters; however, the primeval universe was almost smooth with slight ‘ripples’ that can be seen as relics in the CMB spectrum. Models of structure evolution link such initial smoothness to the rich scenario observed nowadays through the effect of gravitation, which causes the initial tiny perturbations to attract more and more mass. If we define the *density contrast* δ with respect to the mean density $\bar{\rho}$ as:

$$\delta \equiv \frac{\rho - \bar{\rho}}{\bar{\rho}}. \quad (\text{A.14})$$

the initial fluctuations in the density field are likely to be a superposition of waves, which can be better expressed by a Fourier transform:

$$\tilde{\delta}(\mathbf{k}) = \frac{1}{(2\pi)^3} \int d^3x \delta(\mathbf{x}) e^{-i\mathbf{k}\cdot\mathbf{x}}. \quad (\text{A.15})$$

For later use, we also define the *Power-Spectrum* P of this field as basically the variance of amplitudes of different waves at a given value of k :

$$\langle \tilde{\delta}(\mathbf{k}_1) \tilde{\delta}(\mathbf{k}_2) \rangle = P(k_1) \delta_D^3(\mathbf{k}_1 + \mathbf{k}_2). \quad (\text{A.16})$$

where δ_D^3 is the three-dimensional Dirac’s *delta* function.

Those initial departures from a complete smoothness are supposed to have been adiabatic and scale invariant. This means (1) that fluctuations in matter and energy are coupled in such a way that the total entropy does not change, and (2) that the power-spectrum of such density fluctuation field looks like $P(k) = Ak^n$ where k has the usual meaning of a wavenumber. The favoured value as for the exponent n is $n = 1$. The fact that the universe is isotropic is expressed by $P(\mathbf{k}) = P(k)$.

Currently accepted models predict that Gaussian quantum fluctuations in a scalar field at very early times (e.g. Guth & Pi 1982) have generated the density perturbation field. Since the power-spectrum completely characterises in a statistical sense the Gaussian stochastic processes, we are provided with a complete statistical description of the initial ‘seed’ of structure formation once we have the power-spectrum of such pristine perturbation field.

Besides gravitation, other astrophysical process are affecting the growth of perturbations; they are accounted through a *Transfer Function* $T(k)$ which is simply a function of the wavenumber k . The final power spectrum relates to the original one by $P(k) = P_0(k) \times T^2(k)$. For the sake of clarity, here below we just remind some of these non-gravitational effects. As already mentioned, the coupling of baryons with the radiation field or the baryonic pressure can cause the dissipation of perturbation in the baryonic component, as well as the coupling of baryonic and radiation temperature until the time of decoupling, and fast

moving ('hot') dark matter particles can lead to kinematic suppression of growth. This latter effect is mainly important to determine the overall scenario; in fact, hot dark matter particles cancel small-scale structures just by free-streaming across the small potential wells, so that $T(k)$ vanish for large k . At the opposite, slow moving ('cold') dark matter particles suffer for a smaller dissipation at the horizon size $d_H = c/H$ at matter-radiation equality; nevertheless, a significant signal remains on small scales. Hence, two completely different scenarios results in each case: if the dark matter were 'hot' – which is called HDM scenario – the largest structures form first, and the smallest ones descend by fragmentation. In such scenario, galaxies form at late time, after galaxy clusters. On the other hand, in the CDM scenario – in which the dark matter is 'cold' – the smallest structures, namely the galaxies – are those who form first, becoming the building blocks for the largest ones. These two scenario are also called 'top-down' (the first) and 'bottom-up' (the second). There is no need to say that the HDM scenario has been ruled out by observations, which for instance definitively state, roughly speaking, that galaxies form well before clusters. The net result of perturbation growth in the CDM model is then a Power-Spectrum having a characteristic turn-over at the scale of order the horizon at matter-radiation equality with an asymptotic shape at small scale of $P(k) \propto k^{n-4}$.

In the rest of this Section, we give an outline of the linear theory of growth of structure. An extensive and complete treatment can be found elsewhere (e.g. Peebles 1980).

As we assume that at early times inhomogeneities were small, a perturbative approach can be adopted, at least as a first approximation. Furthermore, if the length scale of perturbations is smaller than the effective cosmological horizon $d_H = c/H$ a Newtonian treatment is physically grounded. If the mean free path of particles is small, matter can be treated as an ideal fluid. Hence, the equations of mass conservation, Euler's equation and Poisson's equation (see Chapter 3), must be re-written using comoving coordinates $\mathbf{x} = \mathbf{r}/a(t)$ (spatial coordinates, fixed for an observer moving along with the Hubble expansion), $\mathbf{v} = \dot{\mathbf{r}} - H\mathbf{r} = a\dot{\mathbf{x}}$ (the peculiar velocity field, which represents the proper motions of particles besides the Hubble expansion), $\rho(\mathbf{x}, t)$ (the density field) and $\phi(\mathbf{x}, t)$ (the local value of Newtonian potential, which relates to the fluctuations in the density field). For the exact equations in comoving form see, for instance Coles & Lucchin (1995).

Expanding ρ , \mathbf{v} and ϕ perturbatively and taking only terms which are linear in δ gives :

$$\ddot{\delta} + 2H\dot{\delta} - \frac{3}{2}\Omega_m H^2 \delta = 0 \quad (\text{A.17})$$

This linear equations has two independent solutions $\delta_{\pm} = D_{\pm}(t)\delta(\mathbf{x})$, where $D_{-}(t)$ is the *decaying mode* and $D_{+}(t)$ is the *growing mode* which shortly comes to dominate the evolution of δ . In an Einstein-de Sitter cosmology, for instance, the two modes are $\delta \propto t^{-1}$ and $\delta \propto t^{2/3}$ which also has $D_{+}(t) \propto a(t)$. The solution for the growth factor $D_{+}(t)$ in general cosmologies are given by Peebles (1980).

As long as each Fourier mode $\tilde{\delta}(\mathbf{k})$ is small, $\tilde{\delta}(\mathbf{k}) \ll 1$, the linear approximation can be applied and each Fourier mode evolves independently of the others, so that the Power-

Spectrum simply scales as the square of the growth factor. This is what is called the *linear regime* in which larger scales persist longer than the smallest ones, which are those entering first in the *non-linear regime*.

An important difference holds between the collapse of dark and baryonic matter. In fact, baryons suffer for more interactions than dark matter particles; we know, for instance, that the radiation drag prevent it to collapse until the recombination era. At later times, generally, what may impede the baryons to collapse is the pressure support due to baryon–baryon interaction. Jeans (1928) defined, as a function of the local temperature T and the pressure P , a critical length $\lambda_J(T, P)$ below which the pressure waves have times to propagate, then counteracting the gravitational support; his calculations were made in a Newtonian framework, for perturbations in an infinite, uniform and stationary distribution of gas. The mass scale M_J is defined as the mass encompassed in a sphere of radius $\lambda_J/2$, so that perturbation having mass below this limit are not able to undergo the collapse. A similar calculation can be made also in the framework of modern cosmology, accounting for pressure forces in the previous linear equation. The obtained result is just a lower limit to the mass that is able to collapse, since M_J is once more a perturbative result and thus it can only describe the first phases of the process.

It is worth noting that the Jeans mass represents only a necessary but not a sufficient condition for the collapse of baryons; in addition¹ one has to require that the cooling time (i.e. the characteristic time taken by the gas to loose its internal energy by radiative emission) is shorter than the Hubble Time (i.e. the characteristic expansion time of the universe). Many competing physical processes – e.g. radiative cooling, molecular cooling, heating from first sources of light, magnetic fields – affect the baryons settling in the potential wells, and the relative importance of them changes with redshift; we address the reader to Barkana & Loeb (2001), Ciardi & Ferrara (2005) and references therein.

Anyway, Dark Matter is made by collisionless particles that interact very weakly with the rest of matter and the radiation field; hence, density contrasts in this component start to collapse at earlier times than the baryonic component. When the perturbation δ becomes of order unity, the full non-linear gravitational problem must be solved; in order to do this, we must resort to numerical N-Body calculations (see Chapter 3), though a powerful approximation for the mild non-linear regime has been found by Zel’Dovich (1970). In such approximation, the first non-linear objects are sheet-like structures, resulting from the contraction along one of the principal axis. As the probability of simultaneous contraction along two (filamentary structures) or three (point-like structures) axis is much less, ‘pancakes’ dominate the first stage of non-linear evolution. At later times, the prediction of the Zel’Dovich model are no longer accurate. Then, the simplest case for which we can find an analytical solution is that of a spherically symmetric perturbation, having a top-hat distribution of uniform density δ_i inside a sphere of radius R_i . Results from this rough model surprisingly comes out to

¹In fact, the physics of baryonic collapse is not yet fully understood and all recipes are still fairly empirical.

be very useful to gain an accurate description of properties and distribution of halos in the CDM model.

The collapse of such a spherical top-hat is described, in Newtonian formalism, by:

$$\frac{d^2 r}{dt^2} = H_0^2 \Omega_\Lambda r - \frac{GM}{r^2} \quad (\text{A.18})$$

where r is the radius in a fixed coordinate frame, H_0 is the present value for the Hubble constant, M is the total mass enclosed in the radius r and the initial velocity field is given by the Hubble flow. Initially, the enclosed δ grows linearly as $\delta_i D(t)/D(t_i)$. We assume that the mass shell at radius r is bound, so that it reaches a maximum expansion and subsequently collapses. The over-density predicted by the linear theory for the collapse to a point-like structure is $\delta = 1.686$ in an Einstein-de Sitter universe (Peebles 1980). Thus, a top-hat collapse at redshift z if its linear over-density extrapolated to the present (the *critical density*) is:

$$\delta_{\text{crit}}(z) = \frac{1.686}{D(z)} \quad (\text{A.19})$$

where $D(z=0) = 1$. Instead, the halo reaches the virial equilibrium by violent relaxation (which basically means a phase mixing); using the virial theorem we obtain as for the final over-density at the redshift of collapse (Peebles 1980) :

$$\Delta_c = 18\pi^2 \simeq 178 \quad (\text{A.20})$$

that in a universe having $\Omega_\Lambda + \Omega_m = 1$ becomes (Bryan & Norman 1998):

$$\Delta_c = 18\pi^2 + 82x - 39x^2 \quad (\text{A.21})$$

where $x \equiv \Omega_m^z - 1$ is evaluated at the same collapse redshift:

$$\Omega_m^z - 1 = \frac{\Omega_m(1+z)^3}{\Omega_m(1+z)^3 + \Omega_\Lambda + \Omega_k(1+z)^2}. \quad (\text{A.22})$$

Thus $\Delta_c \simeq 100$ for $\Omega_m = 0.3$. We therefore define r_{100} as the radius encompassing a mean over-density of 100 times the critical density of the Universe and M_{100} as the total mass contained within the same radius. In general, we define M_Δ as the mass contained within a radius encompassing a mean density equal to $\Delta\rho_c$, with ρ_c the critical cosmic density. In this Thesis we often refer to other over-densities (e.g. M_{200} , M_{500}).

All in all, the following estimates are obtained as for, respectively, the virial radius and the virial temperature for a halo of mass M collapsing at redshift z :

$$r_{\text{vir}} = 0.784 \left(\frac{M}{10^8 h^{-1} \text{M}_\odot} \right)^{1/3} \left[\frac{\Omega_m}{\Omega_m^z} \frac{\Delta_c}{18\pi^2} \right]^{-1/3} \left(\frac{1+z}{10} \right)^{-1} h^{-1} \text{kpc} \quad (\text{A.23})$$

$$T_{\text{vir}} = 1.98 \times 10^4 \left(\frac{\mu}{0.6} \right) \left(\frac{M}{10^8 h^{-1} \text{M}_\odot} \right)^{2/3} \left[\frac{\Omega_m}{\Omega_m^z} \frac{\Delta_c}{18\pi^2} \right]^{1/3} \left(\frac{1+z}{10} \right) \text{K} \quad (\text{A.24})$$

where μ is the mean molecular weight ($\mu = 0.59$ for a fully ionised primordial gas, $\mu = 0.61$ for primordial gas with fully ionised Hydrogen but neutral Helium, $\mu = 1.22$ for neutral primordial gas).

Since density fluctuations may exist on all scales, in order to determine the formation of objects of a given size or mass it is useful to consider the statistical distribution of the smoothed density field. Using a window function $W(\mathbf{y})$ normalised so that $\int d^3\mathbf{y}W(\mathbf{y}) = 1$, the smoothed density perturbation field, $\int d^3\mathbf{y}\delta(\mathbf{x} + \mathbf{y})W(\mathbf{y})$, itself follows a Gaussian distribution with zero mean. For the particular choice of a spherical top-hat, in which $W = 1$ in a sphere of radius R and is zero outside, the smoothed perturbation field measures the fluctuations in the mass in spheres of radius R . The normalisation of the present power spectrum is often specified by the value of $\sigma_8 \equiv \sigma(R = 8 h^{-1}\text{Mpc})$. For the top-hat, the smoothed perturbation field is denoted δ_R or δ_M , where M is the mass related to the comoving radius R by $M = 4\pi\rho_m R^3/3$ in terms of the current mean matter density ρ_m . The function $\sigma(M)$ plays a crucial role in estimates of the abundance of collapsed objects. This is a critical test for any theory of structure formation, and it is a fundamental step toward inferring the abundances of galaxies and galaxy clusters. A simple analytic model which successfully matches most of the numerical simulations was developed by Press & Schechter (1974). The model is based on the ideas of a Gaussian random field of density perturbations, linear gravitational growth, and spherical collapse. To determine the abundance of halos at a redshift z , we use δ_M , the density field smoothed on a mass scale M , as previously defined. Although the model is based on the initial conditions, it is usually expressed in terms of redshift-zero quantities. Thus, we use the linearly extrapolated density field, i.e., the initial density field at high redshift extrapolated to the present by simple multiplication by the relative growth factor. Similarly, here the present power spectrum refers to the initial power spectrum, linearly extrapolated to the present without including non-linear evolution.

Calculations (see e.g. Press & Schechter 1974, Barkana & Loeb 2001) give the comoving number density dn of halos with mass between M and $M + dM$:

$$\frac{dn}{dM} = \sqrt{\frac{2}{\pi}} \frac{\rho_m}{M} \frac{d(-\ln \sigma)}{dM} \nu_c e^{-\nu_c^2/2} \quad (\text{A.25})$$

where $\nu_c = \delta_{\text{crit}}(z)/\sigma(M)$ is the number of standard deviations which the critical collapse over-density represents on mass scale M . Although this distribution function represents fairly well the observations and also the numerical N-Body experiments, a significantly better agreement can be achieved using an ellipsoidal collapse model instead of the simpler spherical one (Sheth & Tormen 2002).

Figure A.1 from Springel et al. (2005) shows the comparison between the predicted mass functions of dark matter haloes identified in a dark matter simulation at different redshift with two model mass functions by the Press & Schechter (1974) and by Jenkins et al. (2001), which is based on the analyses of numerical predictions of Dark Matter simulations.

We address the reader to the following references for a more extended discussion on these

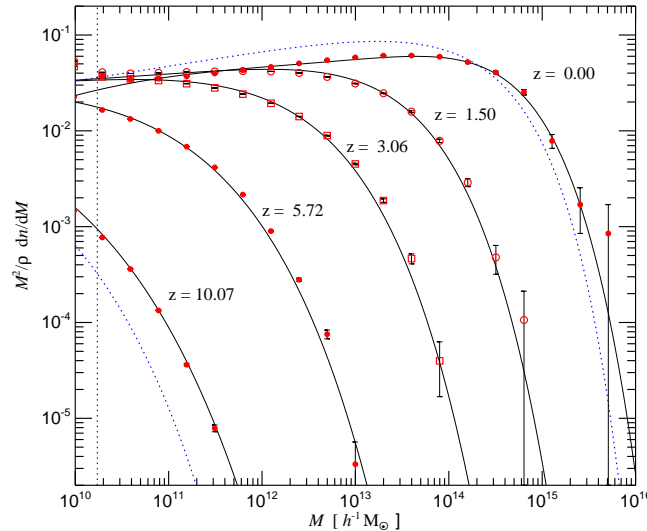


Figure A.1: Points with error-bars represent the mass function of dark matter halos identified in a dark matter simulation (Springel et al., 2005) at different redshifts. Solid and dotted curves represent two model mass functions by Press & Schechter (1974) and by Jenkins et al. (2001) respectively.

topics: Peebles (1980), Peebles (1993), Coles & Lucchin (1995), Coles (2001), Barkana & Loeb (2001) and references therein.

A.3 KEY OBSERVATIONS

The Standard Cosmological Model sketched above employs about a tenth of *a priori* free parameters for which theory does not predict preferred values. Hence, deciding whether our Universe is flat or open, whether or not there is a Dark Energy at work etc. rests upon observational constraints. The impressive technological improvement of the last twenty years has permitted very precise measures of several parameters with more independent methods; cross-combining these independent estimates leads to more certain conclusions and breaks the degeneracy among linked parameters.

What turns out is that the Model currently favoured is the so-called Λ CDM model, having $\Omega \simeq 1$, $\Omega_m \simeq 0.3$, $\Omega_\Lambda \simeq 0.7$.

It is note-worthy that the WMAP experiment (e.g. Bennett et al. 2003, Spergel et al. 2003, Spergel et al. 2007, Dunkley et al. 2008, Komatsu et al. 2008) has enormously improved the precision of our knowledge about the values of a number of cosmological parameters: the geometry of the universe, its mean density and baryonic density, the amplitude of density fluctuations, the redshift of decoupling and others have been constrained by

APPENDIX - Basics of Cosmology

measures on CMB of unprecedented precision. Although a number of discrepancies among independent methods are still there, the “concordance model” appears more and more observationally grounded.

Figure A.2 (Kowalski et al. 2008) shows the confidence regions for Ω_M and Ω_Λ from a combination of different datasets (namely the CMB, the SN-Ia and the Baryonic Acoustic Oscillations). Different and independent methods converge to the concordance model.

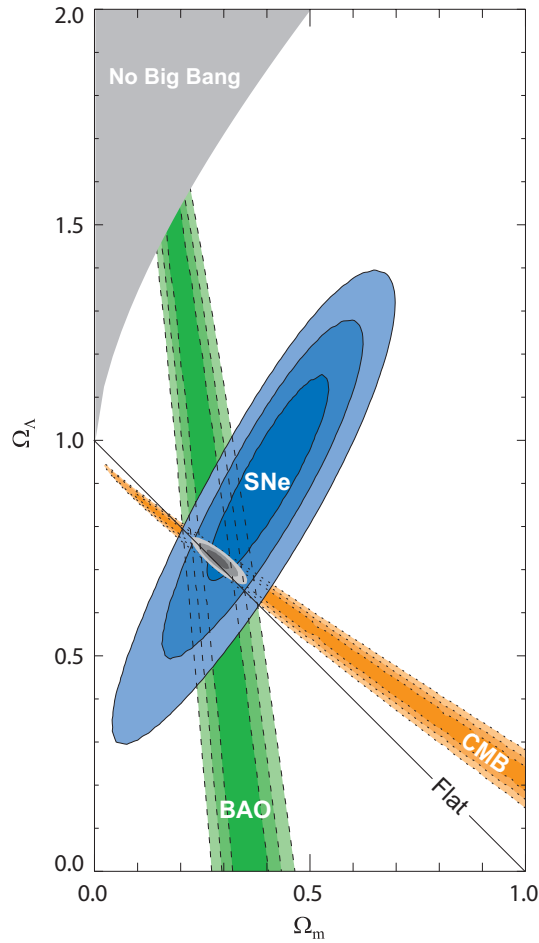


Figure A.2: 68.3 %, 95.4 % and 99.7% confidence level contours on Ω_M and Ω_Λ obtained from CMB, BAO and SN-Ia, as well as their combination (assuming $w = -1$), from the Supernova Cosmology Project (Kowalski et al., 2008).

■ The Curvature of the Universe

The most powerful technique to measure the curvature of the universe relies on the position of the acoustic peak of the CMB spectrum. Before redshift of decoupling $z_{\text{dec}} = 1089 \pm 1$ Spergel et al. (2003), the Compton scattering tightly couples the photon of CMB and the free electrons, which are in turn coupled with protons. Photon pressure impede the gravitational settling of baryons down-to the dark-matter potential well and the “photon–baryon fluid” sets up acoustic oscillations. Once the matter recombines, at $z = z_{\text{rec}}$, photon last scatter on electrons and suffer for gravitational redshift when leaving the potential well of the last scattering surface. The signature of this last scatter is a fluctuation field on the CMB spectrum which appears today as anisotropies on the sky; such fluctuations are called primary anisotropies, whereas secondary anisotropies will be due to later gravitational effects, Sachs–Wolfe effect, Rees–Sciama effects and others. On large scales the fluctuations of CMB must origin from the primordial fluctuation spectrum as no signal can had time to travel long enough distances; instead, at the characteristic scale of the sound horizon at z_{rec} acoustics oscillations mentioned above can occur and at last scattering the oscillation phase freeze. Therefore, the fluctuation spectrum should exhibit a harmonic series of fluctuation peaks whose distance in the wavenumber space is equal to the critical wavenumber corresponding at the sound horizon. The corresponding anisotropy scale projected on the sky is affected by both the curvature of the universe and the distance of the last scattering surface. Briefly, in the case of a flat space we expect the second acoustic peak at a given angular extent, which will be larger or smaller respectively for positive or negative curvatures. Before WMAP many other experiments (see for example Benoît & coauthors 2003) provided measures of the acoustic peak positions, and all estimates are in perfect agreement with the WMAP result, though its error is much smaller. Recently, Komatsu et al. (2008) from the analyses of the WMAP-5 years found:

$$\Omega_k = 1 - \Omega_m - \Omega_\Lambda = [-0.0179, 0.0081], \quad (\text{A.26})$$

within a confidence level of 95%.

■ The Cosmological Acceleration

If an observed object is nearby the observer, its luminosity distance can be well approximated by a linear function of z ; otherwise, the dependence on the redshift become important and involves the deceleration parameter. Hence, if we are provided with a set of standard candles which can be found at distances large enough that the luminosity distance is no longer a linear function of z we can infer the past values of the parameter q , then deciding whether the expansion of the universe has been accelerated or not.

Although SnIa are not standard candles in a strict sense, as their luminosity will vary as time elapses from the explosion, they can be calibrated using the characteristic brilliance

decaying–time which is instead tightly constant. Hence, we can infer the distance of an observed SNIa from its luminosity and also its receding velocity from the spectrum. In the case of unaccelerated expansion, a given SNIa at distance d is expected to recede at a velocity $v = H_0 d$, where H_0 is the present value of the Hubble constant. Instead, in case of accelerated or decelerated expansion, the value of $H(t)$ at a given time (redshift) is different than H_0 and the recession velocity will also be different than the expected value. Results on SNIa at $z \gtrsim 3$ from the *Supernova Cosmology Project* Kowalski et al. (2008) give a negative value of q_0 , indicating the presence of a positive cosmological constant:

$$\Omega_m = 0.713^{+0.027}_{-0.029}(\text{stat})^{+0.036}_{-0.039}(\text{sys}), \quad (\text{A.27})$$

for a flat, Λ CDM Universe.

■ The Matter and Baryon Density

Both the amplitude of acoustic peaks of the CMB spectrum (Bond & Efstathiou 1984) and the Deuterium abundance $[D/H]$ (Boesgaard & Steigman 1985) are sensitive to the cosmological baryon density. The comparison between the estimates obtained by such independent method provides an important test of the Big Bang model. Using the Baryon–photon ratio inferred from WMAP-5 years results $\Omega_b h^2 = 0.02267^{+0.00058}_{-0.00059}$ (Komatsu et al. 2008), the standard Big Bang nucleosynthesis gives $[D/H] = 2.62^{+0.18}_{-0.20}$. Estimates from $[D/H]$ measures in Ly α clouds and DLA give respectively $\Omega_b h^2 = 0.0214 \pm 0.0020$ and $\Omega_b h^2 = 0.025 \pm 0.001$, with a good agreement which was far to be obvious a priori. Galaxy Clusters observations provide estimates of Ω_m through the evolution with z of their number counts. Fairly different results are obtained by different author: Bahcall & Bode (2003) obtain $\sigma_8 = 0.95 \pm 0.1$ for $\Omega_m = 0.25$, Borgani et al. (2001) obtain $\sigma_8 = 0.66^{+0.05}_{-0.05}$ and $\Omega_m = 0.35^{+0.13}_{0.10}$, Reiprich & Böhringer (2002) find $\sigma_8 = 0.96^{+0.15}_{-0.12}$ and $\Omega_m = 0.12^{+0.006}_{-0.004}$. Origins of such significative discrepancy are discussed by Pierpaoli et al. (2003).

■ Baryonic Acoustic Oscillations

Baryonic Acoustic Oscillations (BAO) are predicted in the matter distribution with a calibration that depends on $\Omega_m h^2$ (Silk, 1968; Peebles & Yu, 1970; Sunyaev & Zeldovich, 1970). The oscillations arise because sound waves in the coupled baryon-photon plasma after an inflationary epoch will lead to the expansion of the baryonic material in a spherical shell around a small perturbation, reaching a radius $r_S(z_*)$, the comoving sound horizon size at recombination, before sound waves are no longer supported within the plasma (Bashinsky & Bertschinger, 2001). A baryon density $\Omega_b h^2 \simeq 0.02$, $\Omega_m = 0.24$ and $h = 0.73$ give $r_S(z_*) = 109 h^{-1} \text{Mpc}$. In real space this leads to a peak in the correlation function at $r_S(z_*)$. In Fourier space, this process leads to oscillations in the power spectrum in the same way that

the transform of a top-hat function yields a sinc function. The wavelength of these oscillations for $\Omega_M = 0.24$ and $h = 0.73$ is $k_S = 2\pi/109 = 0.06 h^{-1}\text{Mpc}^{-1}$. Percival et al. (2007b) measured the cosmological matter density by observing the positions of baryon acoustic oscillations in the clustering of galaxies in the Sloan Digital Sky Survey. They jointly analysed the main galaxies and LRGs in the SDSS DR5 sample, using over half a million galaxies in total. The oscillations were detected with 99.74% confidence (3.0σ assuming Gaussianity) compared to a smooth power spectrum. When combined with the observed scale of the peaks within the CMB, Percival et al. (2007b) found a best-fit value of $\Omega_M = 0.256^{+0.029}_{-0.024}$ (68% confidence interval), for a flat Λ cosmology when marginalising over the Hubble parameter and the baryon density.

Bibliography

- Abadi, M. G., Moore, B., & Bower, R. G.: 1999, Ram pressure stripping of spiral galaxies in clusters, *MNRAS* 308, 947–954
- Abazajian, K., Adelman-McCarthy, J. K., Agüeros, M. A., Allam, S. S., & et al.: 2004, The Second Data Release of the Sloan Digital Sky Survey, *AJ* 128, 502–512
- Abel, T., Anninos, P., Zhang, Y., & Norman, M. L.: 1997, Modeling primordial gas in numerical cosmology, *New Astron.* 2, 181–207
- Abell, G. O.: 1958, The Distribution of Rich Clusters of Galaxies., *ApJS* 3, 211–+
- Abraham, R. G., Smecker-Hane, T. A., Hutchings, J. B., Carlberg, R. G., Yee, H. K. C., Ellingson, E., Morris, S., Oke, J. B., & Rigler, M.: 1996, Galaxy Evolution in Abell 2390, *ApJ* 471, 694–+
- Adami, C., Mazure, A., Biviano, A., Katgert, P., & Rhee, G.: 1998, The ESO nearby Abell cluster survey. IV. The fundamental plane of clusters of galaxies, *A&A* 331, 493–505
- Adami, C., Ulmer, M. P., Durret, F., Nichol, R. C., Mazure, A., Holden, B. P., Romer, A. K., & Savine, C.: 2000, A turn-over in the galaxy luminosity function of the Coma cluster core?, *A&A* 353, 930–936
- Aguirre, A., Hernquist, L., Schaye, J., Weinberg, D. H., Katz, N., & Gardner, J.: 2001, Metal Enrichment of the Intergalactic Medium at $z=3$ by Galactic Winds, *ApJ* 560, 599–605
- Allen, S. W., Schmidt, R. W., & Fabian, A. C.: 2002, Cosmological constraints from the X-ray gas mass fraction in relaxed lensing clusters observed with Chandra, *MNRAS* 334, L11–L15
- Alongi, M., Bertelli, G., Bressan, A., Chiosi, C., Fagotto, F., Greggio, L., & Nasi, E.: 1993, Evolutionary sequences of stellar models with semiconvection and convective overshoot. I - $Z = 0.008$, *A&APS* 97, 851–871
- Andreon, S., Willis, J., Quintana, H., Valtchanov, I., Pierre, M., & Pcaud, F.: 2004, Galaxy evolution in clusters up to $z= 1.0$, *MNRAS* 353, 353–368

Bibliography

- Arimoto, N. & Yoshii, Y.: 1987a, Chemical and photometric properties of a galactic wind model for elliptical galaxies, *A&A* 173, 23–38
- Arimoto, N. & Yoshii, Y.: 1987b, Chemical and photometric properties of a galactic wind model for elliptical galaxies, *Astron. Astrophys.* 173, 23–38
- Arnaud, M., Pointecouteau, E., & Pratt, G. W.: 2005, The structural and scaling properties of nearby galaxy clusters. II. The M-T relation, *A&A* 441, 893–903
- Bagla, J. S.: 2005, Cosmological N-Body simulation: Techniques, Scope and Status, *Current Science* 88, 1088–1100
- Bahcall, N. A. & Bode, P.: 2003, The Amplitude of Mass Fluctuations, *Astrophys. J. Lett.* 588, L1–L4
- Bahcall, N. A., Cen, R., Davé, R., Ostriker, J. P., & Yu, Q.: 2000, The Mass-to-Light Function: Antibias and Ω_m , *ApJ* 541, 1–9
- Bahcall, N. A. & Comerford, J. M.: 2002, Antibias in Clusters: The Dependence of the Mass-to-Light Ratio on Cluster Temperature, *ApJL* 565, L5–L8
- Bahcall, N. A., Dong, F., Bode, P., Kim, R., Annis, J., McKay, T. A., Hansen, S., Schroeder, J., Gunn, J., Ostriker, J. P., Postman, M., Nichol, R. C., Miller, C., Goto, T., Brinkmann, J., Knapp, G. R., Lamb, D. O., Schneider, D. P., Vogeley, M. S., & York, D. G.: 2003, The Cluster Mass Function from Early Sloan Digital Sky Survey Data: Cosmological Implications, *ApJ* 585, 182–190
- Balestra, I., Tozzi, P., Ettori, S., Rosati, P., Borgani, S., Norman, V. M. C., & Viola, M.: 2007, Tracing the evolution in the iron content of the intra-cluster medium, *A&A* 462, 429–442
- Balogh, M. L., Morris, S. L., Yee, H. K. C., Carlberg, R. G., & Ellingson, E.: 1997, Star Formation in Cluster Galaxies at $0.2 L_X - T \propto L_X - T^{-0.55}$, *ApJL* 488, L75+
- Balogh, M. L., Pearce, F. R., Bower, R. G., & Kay, S. T.: 2001, Revisiting the cosmic cooling crisis, *MNRAS* 326, 1228–1234
- Bardeen, J. M., Bond, J. R., Kaiser, N., & Szalay, A. S.: 1986, The statistics of peaks of gaussian random fields, *ApJ* 304, 15
- Barkana, R. & Loeb, A.: 2001, In the beginning: the first sources of light and the reionization of the universe, *Phys. Rep* 349, 125–238
- Barnes, J. & Hut, P.: 1986, A Hierarchical O(NlogN) Force-Calculation Algorithm, *Nature* 324, 446–449

- Bashinsky, S. & Bertschinger, E.: 2001, Position-Space Description of the Cosmic Microwave Background and Its Temperature Correlation Function, *Physical Review Letters* 87(8), 081301–+
- Baugh, C. M.: 2006, A primer on hierarchical galaxy formation: the semi-analytical approach, *Reports on Progress in Physics* 69, 3101–3156
- Baum, W. A.: 1959, Population Inferences from Star Counts, Surface Brightness and Colors, *PASP* 71, 106–117
- Bell, E. F., Wolf, C., Meisenheimer, K., Rix, H.-W., Borch, A., Dye, S., Kleinheinrich, M., Wisotzki, L., & McIntosh, D. H.: 2004, Nearly 5000 Distant Early-Type Galaxies in COMBO-17: A Red Sequence and Its Evolution since $z \sim 1$, *ApJ* 608, 752–767
- Bennett, C. L., Halpern, M., Hinshaw, G., Jarosik, N., Kogut, A., Limon, M., Meyer, S. S., Page, L., Spergel, D. N., Tucker, G. S., Wollack, E., Wright, E. L., Barnes, C., Greason, M. R., Hill, R. S., Komatsu, E., Nolte, M. R., Odegard, N., Peiris, H. V., Verde, L., & Weiland, J. L.: 2003, First-Year Wilkinson Microwave Anisotropy Probe (WMAP) Observations: Preliminary Maps and Basic Results, *Astrophys. J. Supp.* 148, 1–27
- Benoît, A. & coauthors, .: 2003, Cosmological constraints from Archeops, *Astron. Astrophys.* 399, L25–L30
- Benson, A. J., Bower, R. G., Frenk, C. S., Lacey, C. G., Baugh, C. M., & Cole, S.: 2003, What Shapes the Luminosity Function of Galaxies?, *ApJ* 599, 38–49
- Benson, A. J., Cole, S., Frenk, C. S., Baugh, C. M., & Lacey, C. G.: 2000, The nature of galaxy bias and clustering, *MNRAS* 311, 793–808
- Benson, A. J., Frenk, C. S., Lacey, C. G., Baugh, C. M., & Cole, S.: 2002, The effects of photoionization on galaxy formation - II. Satellite galaxies in the Local Group, *MNRAS* 333, 177–190
- Benson, A. J., Kamionkowski, M., & Hassani, S. H.: 2005, Self-consistent theory of halo mergers, *MNRAS* 357, 847–858
- Benson, A. J., Pearce, F. R., Frenk, C. S., Baugh, C. M., & Jenkins, A.: 2001, A comparison of semi-analytic and smoothed particle hydrodynamics galaxy formation, *MNRAS* 320, 261–280
- Bertin, E. & Arnouts, S.: 1996, SExtractor: Software for source extraction, *A&AS* 117, 393
- Binney, J. & Tremaine, S.: 1987, *Galactic dynamics*, Princeton, NJ, Princeton University Press, 1987, 747 p.

Bibliography

- Birkinshaw, M. & Lancaster, K.: 2007, Current status of Sunyaev Zel'dovich effect measurements, *New Astronomy Review* 51, 346–349
- Biviano, A.: 2008, Galaxy systems in the optical and infrared, *ArXiv e-prints*
- Biviano, A., Durret, F., Gerbal, D., Le Fevre, O., Lobo, C., Mazure, A., & Slezak, E.: 1995, On the galaxy luminosity function in the central regions of the Coma cluster., *A&A* 297, 610–+
- Biviano, A., Katgert, P., Mazure, A., Moles, M., den Hartog, R., Perea, J., & Focardi, P.: 1997, The ESO Nearby Abell Cluster Survey. III. Distribution and kinematics of emission-line galaxies., *A&A* 321, 84–104
- Biviano, A., Murante, G., Borgani, S., Diaferio, A., Dolag, K., & Girardi, M.: 2006, On the efficiency and reliability of cluster mass estimates based on member galaxies, *ArXiv Astrophysics e-prints*
- Boesgaard, A. M. & Steigman, G.: 1985, Big bang nucleosynthesis - Theories and observations, *Annu. Rev. Astron. Astrophys.* 23, 319–378
- Bonamente, M., Joy, M., LaRoque, S. J., Carlstrom, J. E., Nagai, D., & Marrone, D. P.: 2008, Scaling Relations from Sunyaev-Zel'dovich Effect and Chandra X-Ray Measurements of High-Redshift Galaxy Clusters, *ApJ* 675, 106–114
- Bond, J. R. & Efstathiou, G.: 1984, Cosmic background radiation anisotropies in universes dominated by nonbaryonic dark matter, *Astrophys. J. Lett.* 285, L45–L48
- Borgani, S.: 2006, Cosmology with clusters of galaxies, *ArXiv Astrophysics e-prints*
- Borgani, S., Dolag, K., Murante, G., Cheng, L.-M., Springel, V., Diaferio, A., Moscardini, L., Tormen, G., Tornatore, L., & Tozzi, P.: 2006, Hot and cooled baryons in smoothed particle hydrodynamic simulations of galaxy clusters: physics and numerics, *MNRAS* 367, 1641–1654
- Borgani, S., Fabjan, D., Tornatore, L., Schindler, S., Dolag, K., & Diaferio, A.: 2008, The Chemical Enrichment of the ICM from Hydrodynamical Simulations, *Space Science Reviews* 134, 379–403
- Borgani, S. & Guzzo, L.: 2001, X-ray clusters of galaxies as tracers of structure in the Universe, *Nature* 409, 39–45
- Borgani, S., Murante, G., Springel, V., Diaferio, A., Dolag, K., Moscardini, L., Tormen, G., Tornatore, L., & Tozzi, P.: 2004, X-ray properties of galaxy clusters and groups from a cosmological hydrodynamical simulation, *MNRAS* 348, 1078–1096

- Bower, R. G., Benson, A. J., Malbon, R., Helly, J. C., Frenk, C. S., Baugh, C. M., Cole, S., & Lacey, C. G.: 2006, Breaking the hierarchy of galaxy formation, *MNRAS* 370, 645–655
- Bower, R. G., Lucey, J. R., & Ellis, R. S.: 1992, Precision Photometry of Early Type Galaxies in the Coma and Virgo Clusters - a Test of the Universality of the Colour / Magnitude Relation - Part Two - Analysis, *MNRAS* 254, 601–+
- Boylan-Kolchin, M., Ma, C.-P., & Quataert, E.: 2008, Dynamical friction and galaxy merging time-scales, *MNRAS* 383, 93–101
- Bregman, J. N., Fabian, A. C., Miller, E. D., & Irwin, J. A.: 2006, OVI Observations of Galaxy Clusters: Evidence for Modest Cooling Flows, *ArXiv Astrophysics e-prints*
- Bressan, A., Fagotto, F., Bertelli, G., & Chiosi, C.: 1993, Evolutionary sequences of stellar models with new radiative opacities. II - $Z = 0.02$, *A&AS* 100, 647–664
- Brocato, E., Matteucci, F., Mazzitelli, I., & Tornambe, A.: 1990, Synthetic colors and the chemical evolution of elliptical galaxies, *ApJ* 349, 458–470
- Bruzual, G. & Charlot, S.: 2003, Stellar population synthesis at the resolution of 2003, *MNRAS* 344, 1000–1028
- Bruzual A., G. & Charlot, S.: 1993, Spectral evolution of stellar populations using isochrone synthesis, *ApJ* 405, 538–553
- Bryan, G. L. & Norman, M. L.: 1998, Statistical Properties of X-Ray Clusters: Analytic and Numerical Comparisons, *Astrophys. J.* 495, 80–+
- Burles, S. & Tytler, D.: 1998, On the Measurements of D/H in QSO Absorption Systems Closing in on the primordial abundance of deuterium, *Space Science Reviews* 84, 65–75
- Butcher, H. & Oemler, A.: 1984, The evolution of galaxies in clusters. V - A study of populations since Z approximately equal to 0.5, *ApJ* 285, 426–438
- Buzzoni, A.: 1989, Evolutionary population synthesis in stellar systems. I - A global approach, *ApJS* 71, 817–869
- Carilli, C. L., Harris, D. E., Pentericci, L., Röttgering, H. J. A., Miley, G. K., Kurk, J. D., & van Breugel, W.: 2002, The X-Ray-Radio Alignment in the $z=2.2$ Radio Galaxy PKS 1138-262, *ApJ* 567, 781–789
- Carlberg, R. G., Yee, H. K. C., & Ellingson, E.: 1997, The Average Mass and Light Profiles of Galaxy Clusters, *ApJ* 478, 462–+
- Carlberg, R. G., Yee, H. K. C., Ellingson, E., Abraham, R., Gravel, P., Morris, S., & Pritchet, C. J.: 1996, Galaxy Cluster Virial Masses and Omega, *ApJ* 462, 32–+

Bibliography

- Carlstrom, J. E., Holder, G. P., & Reese, E. D.: 2002, Cosmology with the Sunyaev-Zel'dovich Effect, *ARA&A* 40, 643–680
- Casagrande, L. & Diaferio, A.: 2006, Clusters and Groups of Galaxies in the Simulated Local Universe, *ArXiv Astrophysics e-prints*
- Castellano, M., Salimbeni, S., Trevese, D., Grazian, A., Pentericci, L., Fiore, F., Fontana, A., Giallongo, E., Santini, P., Cristiani, S., Nonino, M., & Vanzella, E.: 2007, A Photometrically Detected Forming Cluster of Galaxies at Redshift 1.6 in the GOODS Field, *ApJ* 671, 1497–1502
- Cattaneo, A., Blaizot, J., Devriendt, J., & Guiderdoni, B.: 2005, Active Galactic Nuclei In Cosmological Simulations - I. Formation of black holes and spheroids through mergers, *MNRAS* 364, 407–423
- Cattaneo, A., Blaizot, J., Weinberg, D. H., Kereš, D., Colombi, S., Davé, R., Devriendt, J., Guiderdoni, B., & Katz, N.: 2007, Accretion, feedback and galaxy bimodality: a comparison of the GalICS semi-analytic model and cosmological SPH simulations, *MNRAS* 377, 63–76
- Cattaneo, A., Dekel, A., Devriendt, J., Guiderdoni, B., & Blaizot, J.: 2006, Modelling the galaxy bimodality: shutdown above a critical halo mass, *MNRAS* 370, 1651–1665
- Cavaliere, A., Gursky, H., & Tucker, W.: 1971, Extragalactic x-ray Sources and Associations of Galaxies, *Nature* 231, 437–+
- Cavaliere, A. & Menci, N.: 2007, Bimodal Active Nuclei in Bimodal Galaxies, *ApJ* 664, 47–52
- Chandrasekhar, S.: 1943, Dynamical Friction. I. General Considerations: the Coefficient of Dynamical Friction., *ApJ* 97, 255–+
- Charlot, S. & Fall, S. M.: 2000, A Simple Model for the Absorption of Starlight by Dust in Galaxies, *ApJ* 539, 718–731
- Chiappini, C., Matteucci, F., & Gratton, R.: 1997, The Chemical Evolution of the Galaxy: The Two-Infall Model, *ApJ* 477, 765–+
- Chieffi, A. & Limongi, M.: 2004, Explosive Yields of Massive Stars from $Z = 0$ to $Z = Z_{solar}$, *ApJ* 608, 405–410
- Ciardi, B. & Ferrara, A.: 2005, The First Cosmic Structures and Their Effects, *Space Science Reviews* 116, 625–705
- Cole, S.: 1991, Modeling galaxy formation in evolving dark matter halos, *ApJ* 367, 45–53

- Cole, S., Aragon-Salamanca, A., Frenk, C. S., Navarro, J. F., & Zepf, S. E.: 1994, A Recipe for Galaxy Formation, *MNRAS* 271, 781–+
- Cole, S., Helly, J., Frenk, C. S., & Parkinson, H.: 2008, The statistical properties of Λ cold dark matter halo formation, *MNRAS* 383, 546–556
- Cole, S., Lacey, C. G., Baugh, C. M., & Frenk, C. S.: 2000a, Hierarchical galaxy formation, *MNRAS* 319, 168–204
- Cole, S., Lacey, C. G., Baugh, C. M., & Frenk, C. S.: 2000b, Hierarchical galaxy formation, *Mon. Not. R. Astron. Soc.* 319, 168–204
- Cole, S., Norberg, P., Baugh, C. M., Frenk, C. S., Bland-Hawthorn, J., Bridges, T., Cannon, R., Colless, M., Collins, C., Couch, W., Cross, N., Dalton, G., De Propriis, R., Driver, S. P., Efstathiou, G., Ellis, R. S., Glazebrook, K., Jackson, C., Lahav, O., Lewis, I., Lumsden, S., Maddox, S., Madgwick, D., Peacock, J. A., Peterson, B. A., Sutherland, W., & Taylor, K.: 2001, The 2dF galaxy redshift survey: near-infrared galaxy luminosity functions, *MNRAS* 326, 255–273
- Coles, P.: 2000, Large-Scale Structure, in *Perspectives on Radio Astronomy: Science with Large Antenna Arrays, Proceedings of the Conference held at the Royal Netherlands Academy of Arts and Sciences in Amsterdam on 7-9 April 1999. Edited by M. P. van Haarlem. Published by ASTRON. ISBN: 90-805434-1-1, 340 pages, 2000, p.53*, pp 53–+
- Coles, P.: 2001, Large-Scale Structure, Theory and Statistics, *ArXiv Astrophysics e-prints*
- Coles, P. & Lucchin, F.: 1995, *Cosmology. The origin and evolution of cosmic structure*, Chichester: Wiley, —c1995
- Colless, M.: 1989, The dynamics of rich clusters. II - Luminosity functions, *MNRAS* 237, 799–826
- Cora, S. A.: 2006, Metal enrichment of the intracluster medium: a three-dimensional picture of chemical and dynamical properties, *MNRAS* 368, 1540–1560
- Cora, S. A., Tornatore, L., Tozzi, P., & Dolag, K.: 2008, Metal enrichment of the intracluster medium: a three-dimensional picture of chemical and dynamical properties, *MNRAS*
- Croton, D. J., Springel, V., White, S. D. M., De Lucia, G., Frenk, C. S., Gao, L., Jenkins, A., Kauffmann, G., Navarro, J. F., & Yoshida, N.: 2006, The many lives of active galactic nuclei: cooling flows, black holes and the luminosities and colours of galaxies, *MNRAS* 365, 11–28
- De Lucia, G. & Blaizot, J.: 2007, The hierarchical formation of the brightest cluster galaxies, *MNRAS* 375, 2–14

Bibliography

- De Lucia, G., Kauffmann, G., Springel, V., White, S. D. M., Lanzoni, B., Stoehr, F., Tormen, G., & Yoshida, N.: 2004a, Substructures in cold dark matter haloes, *MNRAS* 348, 333–344
- De Lucia, G., Kauffmann, G., & White, S. D. M.: 2004b, Chemical enrichment of the intracluster and intergalactic medium in a hierarchical galaxy formation model, *MNRAS* 349, 1101–1116
- De Lucia, G., Poggianti, B. M., Aragón-Salamanca, A., Clowe, D., Halliday, C., Jablonka, P., Milvang-Jensen, B., Pelló, R., Poirier, S., Rudnick, G., Saglia, R., Simard, L., & White, S. D. M.: 2004c, The Buildup of the Red Sequence in Galaxy Clusters since $z \sim 0.8$, *ApJL* 610, L77–L80
- De Lucia, G., Poggianti, B. M., Aragón-Salamanca, A., White, S. D. M., Zaritsky, D., Clowe, D., Halliday, C., Jablonka, P., von der Linden, A., Milvang-Jensen, B., Pelló, R., Rudnick, G., Saglia, R. P., & Simard, L.: 2007, The build-up of the colour-magnitude relation in galaxy clusters since $z \sim 0.8$, *MNRAS* 374, 809–822
- De Propris, R., Colless, M., Driver, S. P., & et al.: 2003, The 2dF Galaxy Redshift Survey: the luminosity function of cluster galaxies, *MNRAS* 342, 725–737
- De Propris, R., Colless, M., Peacock, J. A., & et al.: 2004, The 2dF Galaxy Redshift Survey: the blue galaxy fraction and implications for the Butcher-Oemler effect, *MNRAS* 351, 125–132
- Dekel, A., Birnboim, Y., Engel, G., Freundlich, J., Goerdt, T., Mumcuoglu, M., Neistein, E., Pichon, C., Teyssier, R., & Zinger, E.: 2008, The Main Mode of Galaxy Formation: Early Massive Galaxies by Cold Streams in Hot Haloes, *ArXiv e-prints*
- Dekel, A. & Silk, J.: 1986, The origin of dwarf galaxies, cold dark matter, and biased galaxy formation, *ApJ* 303, 39–55
- Demarco, R., Ford, H. C., & Rosati, P.: 2005, Panchromatic Studies of Distant Clusters of Galaxies, *Modern Physics Letters A* 20, 1409–1422
- Di Matteo, T., Springel, V., & Hernquist, L.: 2005, Energy input from quasars regulates the growth and activity of black holes and their host galaxies, *Nature* 433, 604–607
- Diaferio, A., Kauffmann, G., Balogh, M. L., White, S. D. M., Schade, D., & Ellingson, E.: 2001a, The spatial and kinematic distributions of cluster galaxies in a Λ CDM universe: comparison with observations, *MNRAS* 323, 999–1015
- Diaferio, A., Kauffmann, G., Balogh, M. L., White, S. D. M., Schade, D., & Ellingson, E.: 2001b, The spatial and kinematic distributions of cluster galaxies in a Λ CDM universe: comparison with observations, *MNRAS* 323, 999–1015

- Diaferio, A., Schindler, S., & Dolag, K.: 2008, Clusters of Galaxies: Setting the Stage, *Space Science Reviews* 134, 7–24
- Diemand, J., Kuhlen, M., Madau, P., Zemp, M., Moore, B., Potter, D., & Stadel, J.: 2008, Clumps and streams in the local dark matter distribution, *Nature* 454, 735–738
- Diemand, J., Moore, B., & Stadel, J.: 2004, Velocity and spatial biases in cold dark matter subhalo distributions, *MNRAS* 352, 535–546
- Dolag, K., Borgani, S., Murante, G., & Springel, V.: 2008a, Substructures in hydrodynamical cluster simulations, *ArXiv e-prints* 808
- Dolag, K., Borgani, S., Schindler, S., Diaferio, A., & Bykov, A. M.: 2008b, Simulation Techniques for Cosmological Simulations, *Space Science Reviews* 134, 229–268
- Dolag, K., Vazza, F., Brunetti, G., & Tormen, G.: 2005, Turbulent gas motions in galaxy cluster simulations: the role of smoothed particle hydrodynamics viscosity, *MNRAS* 364, 753–772
- Domainko, W., Mair, M., Kapferer, W., van Kampen, E., Kronberger, T., Schindler, S., Kimeswenger, S., Ruffert, M., & Mangete, O. E.: 2006, Enrichment of the ICM of galaxy clusters due to ram-pressure stripping, *A&A* 452, 795–802
- Dressler, A.: 1978, A comprehensive study of 12 very rich clusters of galaxies. I - Photometric technique and analysis of the luminosity function, *ApJ* 223, 765–775
- Efstathiou, G., Davis, M., White, S. D. M., & Frenk, C. S.: 1985, Numerical techniques for large cosmological N-body simulations, *Astrophys. J. Supp.* 57, 241–260
- Eisenhardt, P. R. M., Brodwin, M., Gonzalez, A. H., Stanford, S. A., Stern, D., Barmby, P., Brown, M. J. I., Dawson, K., Dey, A., Doi, M., Galametz, A., Jannuzi, B. T., Kochanek, C. S., Meyers, J., Morokuma, T., & Moustakas, L. A.: 2008a, Clusters of Galaxies in the First Half of the Universe from the IRAC Shallow Survey, *ApJ* 684, 905–932
- Eisenhardt, P. R. M., Brodwin, M., Gonzalez, A. H., Stanford, S. A., Stern, D., Barmby, P., Brown, M. J. I., Dawson, K., Dey, A., Doi, M., Galametz, A., Jannuzi, B. T., Kochanek, C. S., Meyers, J., Morokuma, T., & Moustakas, L. A.: 2008b, Clusters of Galaxies in the First Half of the Universe from the IRAC Shallow Survey, *ArXiv e-prints* 804
- Ellingson, E., Lin, H., Yee, H. K. C., & Carlberg, R. G.: 2001, The Evolution of Population Gradients in Galaxy Clusters: The Butcher-Oemler Effect and Cluster Infall, *ApJ* 547, 609–622
- Ellis, J.: 2003, Dark matter and dark energy: summary and future directions, *Royal Society of London Philosophical Transactions Series A* 361, 2607–2627

Bibliography

- Enßlin, T. A. & Kaiser, C. R.: 2000, Comptonization of the cosmic microwave background by relativistic plasma, *A&A* 360, 417–430
- Ettori, S., Tozzi, P., & Rosati, P.: 2003, Constraining the cosmological parameters with the gas mass fraction in local and $z > 0.7$ galaxy clusters, *A&A* 398, 879–890
- Evrard, A. E., Bialek, J., Busha, M., White, M., Habib, S., Heitmann, K., Warren, M., Rasia, E., Tormen, G., Moscardini, L., Power, C., Jenkins, A. R., Gao, L., Frenk, C. S., Springel, V., White, S. D. M., & Diemand, J.: 2008, Virial Scaling of Massive Dark Matter Halos: Why Clusters Prefer a High Normalization Cosmology, *ApJ* 672, 122–137
- Faber, S. M., Willmer, C. N. A., Wolf, C., Koo, D. C., Weiner, B. J., Newman, J. A., Im, M., Coil, A. L., Conroy, C., Cooper, M. C., Davis, M., Finkbeiner, D. P., Gerke, B. F., Gebhardt, K., Groth, E. J., Guhathakurta, P., Harker, J., Kaiser, N., Kassin, S., Kleinheinrich, M., Konidaris, N. P., Kron, R. G., Lin, L., Luppino, G., Madgwick, D. S., Meisenheimer, K., Noeske, K. G., Phillips, A. C., Sarajedini, V. L., Schiavon, R. P., Simard, L., Szalay, A. S., Vogt, N. P., & Yan, R.: 2007, Galaxy Luminosity Functions to $z \sim 1$ from DEEP2 and COMBO-17: Implications for Red Galaxy Formation, *ApJ* 665, 265–294
- Fabian, A. C.: 1991, On the baryon content of the Shapley Supercluster, *MNRAS* 253, 29P–+
- Fabian, A. C., Sanders, J. S., Crawford, C. S., & Ettori, S.: 2003, A deep Chandra observation of the cluster environment of the $z = 1.786$ radio galaxy 3C 294, *MNRAS* 341, 729–738
- Fabjan, D., Tornatore, L., Borgani, S., Saro, A., & Dolag, K.: 2008, Evolution of the metal content of the intracluster medium with hydrodynamical simulations, *MNRAS* 386, 1265–1273
- Fagotto, F., Bressan, A., Bertelli, G., & Chiosi, C.: 1994a, Evolutionary sequences of stellar models with new radiative opacities. III. $Z=0.0004$ and $Z=0.05$, *A&APS* 104, 365–376
- Fagotto, F., Bressan, A., Bertelli, G., & Chiosi, C.: 1994b, Evolutionary sequences of stellar models with new radiative opacities. IV. $Z=0.004$ and $Z=0.008$, *A&APS* 105, 29–38
- Fagotto, F., Bressan, A., Bertelli, G., & Chiosi, C.: 1994c, Evolutionary sequences of stellar models with very high metallicity. V. $Z=0.1$, *A&APS* 105, 39–45
- Faltenbacher, A., Kravtsov, A. V., Nagai, D., & Gottlöber, S.: 2005, Supersonic motions of galaxies in clusters, *MNRAS* 358, 139–148
- Felten, J. E., Gould, R. J., Stein, W. A., & Woolf, N. J.: 1966, X-Rays from the Coma Cluster of Galaxies, *ApJ* 146, 955–958

- Fontanot, F., Monaco, P., Cristiani, S., & Tozzi, P.: 2006, The effect of stellar feedback and quasar winds on the active galactic nucleus population, *MNRAS* 373, 1173–1187
- Fontanot, F., Monaco, P., Silva, L., & Grazian, A.: 2007, Reproducing the assembly of massive galaxies within the hierarchical cosmogony, *MNRAS* 382, 903–914
- Fontanot, F., Somerville, R. S., Silva, L., Monaco, P., & Skibba, R.: 2008, Evaluating and Improving Semi-analytic modelling of Dust in Galaxies based on Radiative Transfer Calculations, *ArXiv e-prints*
- Frenk, C. S., Evrard, A. E., White, S. D. M., & Summers, F. J.: 1996, Galaxy Dynamics in Clusters, *ApJ* 472, 460–+
- Fried, J. W., von Kuhlmann, B., Meisenheimer, K., Rix, H.-W., Wolf, C., Hippelein, H. H., Kümmel, M., Phleps, S., Röser, H. J., Thierring, I., & Maier, C.: 2001, The luminosity function of field galaxies and its evolution since $z=1$, *A&A* 367, 788–800
- Gal-Yam, A., Maoz, D., & Sharon, K.: 2002, Supernovae in deep Hubble Space Telescope galaxy cluster fields: cluster rates and field counts, *MNRAS* 332, 37–48
- Galli, D. & Palla, F.: 1998, The chemistry of the early Universe, *A&A* 335, 403–420
- Gao, L., De Lucia, G., White, S. D. M., & Jenkins, A.: 2004a, Galaxies and subhaloes in Λ CDM galaxy clusters, *MNRAS* 352, L1–L5
- Gao, L., De Lucia, G., White, S. D. M., & Jenkins, A.: 2004b, Galaxies and subhaloes in Λ CDM galaxy clusters, *MNRAS* 352, L1–L5
- Gao, L., White, S. D. M., Jenkins, A., Stoehr, F., & Springel, V.: 2004c, The subhalo populations of Λ CDM dark haloes, *MNRAS* 355, 819–834
- Ghigna, S., Moore, B., Governato, F., Lake, G., Quinn, T., & Stadel, J.: 2000a, Density Profiles and Substructure of Dark Matter Halos: Converging Results at Ultra-High Numerical Resolution, *ApJ* 544, 616–628
- Ghigna, S., Moore, B., Governato, F., Lake, G., Quinn, T., & Stadel, J.: 2000b, Density Profiles and Substructure of Dark Matter Halos: Converging Results at Ultra-High Numerical Resolution, *ApJ* 544, 616–628
- Giacconi, R., Murray, S., Gursky, H., Kellogg, E., Schreier, E., & Tananbaum, H.: 1972, The UHURU catalog of X-ray sources., *ApJ* 178, 281–308
- Gingold, R. A. & Monaghan, J. J.: 1977, Smoothed particle hydrodynamics - Theory and application to non-spherical stars, *Mon. Not. R. Astron. Soc.* 181, 375–389

Bibliography

- Girardi, L., Bressan, A., Chiosi, C., Bertelli, G., & Nasi, E.: 1996, Evolutionary sequences of stellar models with new radiative opacities. VI. $Z=0.0001$., *A&APS* 117, 113–125
- Girardi, M., Borgani, S., Giuricin, G., Mardirossian, F., & Mezzetti, M.: 2000, Optical Luminosities and Mass-to-Light Ratios of Nearby Galaxy Clusters, *ApJ* 530, 62–79
- Girardi, M., Manzato, P., Mezzetti, M., Giuricin, G., & Limboz, F.: 2002, Observational Mass-to-Light Ratio of Galaxy Systems from Poor Groups to Rich Clusters, *ApJ* 569, 720–741
- Girardi, M. & Mezzetti, M.: 2001, Evolution of the Internal Dynamics of Galaxy Clusters, *ApJ* 548, 79–96
- Gladders, M. D. & Yee, H. K. C.: 2000, A New Method For Galaxy Cluster Detection. I. The Algorithm, *AJ* 120, 2148–2162
- Gladders, M. D. & Yee, H. K. C.: 2005, The Red-Sequence Cluster Survey. I. The Survey and Cluster Catalogs for Patches RCS 0926+37 and RCS 1327+29, *ApJS* 157, 1–29
- Gladders, M. D., Yee, H. K. C., Majumdar, S., Barrientos, L. F., Hoekstra, H., Hall, P. B., & Infante, L.: 2007, Cosmological Constraints from the Red-Sequence Cluster Survey, *ApJ* 655, 128–134
- Goto, T., Okamura, S., McKay, T. A., Bahcall, N. A., Annis, J., Bernard, M., Brinkmann, J., Gómez, P. L., Hansen, S., Kim, R. S. J., Sekiguchi, M., & Sheth, R. K.: 2002, Composite Luminosity Functions Based on the Sloan Digital Sky Survey “Cut and Enhance” Galaxy Cluster Catalog, *PASJ* 54, 515–525
- Granato, G. L., De Zotti, G., Silva, L., Bressan, A., & Danese, L.: 2004, A Physical Model for the Coevolution of QSOs and Their Spheroidal Hosts, *ApJ* 600, 580–594
- Greggio, L. & Renzini, A.: 1983, The binary model for type I supernovae - Theoretical rates, *A&A* 118, 217–222
- Gunn, J. E. & Gott, J. R. I.: 1972, On the Infall of Matter Into Clusters of Galaxies and Some Effects on Their Evolution, *ApJ* 176, 1–+
- Guth, A. H. & Pi, S.-Y.: 1982, Fluctuations in the new inflationary universe, *Physical Review Letters* 49, 1110–1113
- Haardt, F. & Madau, P.: 1996, Radiative Transfer in a Clumpy Universe. II. The Ultraviolet Extragalactic Background, *ApJ* 461, 20–+
- Hatch, N. A., Overzier, R. A., Röttgering, H. J. A., Kurk, J. D., & Miley, G. K.: 2008, Diffuse UV light associated with the Spiderweb Galaxy: evidence for in situ star formation outside galaxies, *MNRAS* 383, 931–942

- Heckman, T. M.: 2003, Starburst-Driven Galactic Winds, in V. Avila-Reese, C. Firmani, C. S. Frenk, & C. Allen (eds.), *Revista Mexicana de Astronomia y Astrofisica Conference Series*, pp 47–55
- Heger, A. & Woosley, S. E.: 2002, The Nucleosynthetic Signature of Population III, *ApJ* 567, 532–543
- Helly, J. C., Cole, S., Frenk, C. S., Baugh, C. M., Benson, A., Lacey, C., & Pearce, F. R.: 2003a, A comparison of gas dynamics in smooth particle hydrodynamics and semi-analytic models of galaxy formation, *MNRAS* 338, 913–925
- Helly, J. C., Cole, S., Frenk, C. S., Baugh, C. M., Benson, A., Lacey, C., & Pearce, F. R.: 2003b, A comparison of gas dynamics in smooth particle hydrodynamics and semi-analytic models of galaxy formation, *MNRAS* 338, 913–925
- Henriksen, M. J. & Mushotzky, R. F.: 1986, The X-ray spectrum of the Coma Cluster of galaxies, *ApJ* 302, 287–295
- Hernquist, L. & Katz, N.: 1989, TREESPH - A unification of SPH with the hierarchical tree method, *Astrophys. J. Supp.* 70, 419–446
- Hockney, R. & Eastwood, J.: 1988, *Computer simulation using particles*, Bristol: Hilger, 1988
- Huang, J.-S., Glazebrook, K., Cowie, L. L., & Tinney, C.: 2003, The Hawaii+Anglo-Australian Observatory K-Band Galaxy Redshift Survey. I. The Local K-Band Luminosity Function, *ApJ* 584, 203–209
- Hubble, E. & Humason, M. L.: 1931, The Velocity-Distance Relation among Extra-Galactic Nebulae, *Astrophys. J.* 74, 43–+
- Iwamoto, K., Brachwitz, F., Nomoto, K., Kishimoto, N., Umeda, H., Hix, W. R., & Thielemann, F.-K.: 1999, Nucleosynthesis in Chandrasekhar Mass Models for Type IA Supernovae and Constraints on Progenitor Systems and Burning-Front Propagation, *ApJS* 125, 439–462
- Jeans, J. H.: 1928, *Astronomy and cosmogony*, Cambridge [Eng.] The University press, 1928.
- Jenkins, A., Frenk, C., White, S., Colberg, J., Cole, S., Evrard, A., Couchman, H., & Yoshida, N.: 2001, The mass function of dark matter haloes, *MNRAS* 321, 372
- Jiang, C. Y., Jing, Y. P., Faltenbacher, A., Lin, W. P., & Li, C.: 2008, A Fitting Formula for the Merger Timescale of Galaxies in Hierarchical Clustering, *ApJ* 675, 1095–1105

Bibliography

- Johnston, D. E., Sheldon, E. S., Wechsler, R. H., Rozo, E., Koester, B. P., Frieman, J. A., McKay, T. A., Evrard, A. E., Becker, M. R., & Annis, J.: 2007, Cross-correlation Weak Lensing of SDSS galaxy Clusters II: Cluster Density Profiles and the Mass–Richness Relation, *ArXiv e-prints*
- Johnstone, R. M., Fabian, A. C., & Nulsen, P. E. J.: 1987, The optical spectra of central galaxies in southern clusters Evidence for star formation, *MNRAS* 224, 75–91
- Jones, C. & Forman, W.: 1999, Einstein Observatory Images of Clusters of Galaxies, *ApJ* 511, 65–83
- Kaastra, J. S., Bykov, A. M., Schindler, S., Bleeker, J. A. M., Borgani, S., Diaferio, A., Dolag, K., Durret, F., Nevalainen, J., Ohashi, T., Paerels, F. B. S., Petrosian, V., Rephaeli, Y., Richter, P., Schaye, J., & Werner, N.: 2008, Clusters of Galaxies: Beyond the Thermal View, *Space Science Reviews* 134, 1–4
- Kaiser, N.: 1991, Evolution of clusters of galaxies, *Astrophys. J.* 383, 104–111
- Katz, N., Weinberg, D. H., & Hernquist, L.: 1996, Cosmological Simulations with TreeSPH, *ApJS* 105, 19–+
- Kauffmann, G. & Charlot, S.: 1998, Chemical enrichment and the origin of the colour-magnitude relation of elliptical galaxies in a hierarchical merger model, *MNRAS* 294, 705–+
- Kauffmann, G., Colberg, J. M., Diaferio, A., & White, S. D. M.: 1999a, Clustering of galaxies in a hierarchical universe - I. Methods and results at $z=0$, *MNRAS* 303, 188–206
- Kauffmann, G., Colberg, J. M., Diaferio, A., & White, S. D. M.: 1999b, Clustering of galaxies in a hierarchical universe - I. Methods and results at $z=0$, *MNRAS* 303, 188–206
- Kauffmann, G., White, S. D. M., & Guiderdoni, B.: 1993, The Formation and Evolution of Galaxies Within Merging Dark Matter Haloes, *MNRAS* 264, 201–+
- Kenney, J. D. P., van Gorkom, J. H., & Vollmer, B.: 2004, VLA H I Observations of Gas Stripping in the Virgo Cluster Spiral NGC 4522, *AJ* 127, 3361–3374
- Kennicutt, Jr., R. C.: 1998, The Global Schmidt Law in Star-forming Galaxies, *ApJ* 498, 541–+
- Kim, J., Park, C., Gott, R. I., & Dubinski, J.: 2008, The Horizon Run N-body Simulation: Baryon Acoustic Oscillations and Topology of Large Scale Structure of the Universe, *ArXiv e-prints*
- King, I.: 1962, The structure of star clusters. I. an empirical density law, *AJ* 67, 471–+

- Kochanek, C. S., Pahre, M. A., Falco, E. E., Huchra, J. P., Mader, J., Jarrett, T. H., Chester, T., Cutri, R., & Schneider, S. E.: 2001, The K-Band Galaxy Luminosity Function, *ApJ* 560, 566–579
- Kodama, T. & Arimoto, N.: 1997, Origin of the colour-magnitude relation of elliptical galaxies., *A&A* 320, 41–53
- Komatsu, E., Dunkley, J., Nolta, M. R., Bennett, C. L., Gold, B., Hinshaw, G., Jarosik, N., Larson, D., Limon, M., Page, L., Spergel, D. N., Halpern, M., Hill, R. S., Kogut, A., Meyer, S. S., Tucker, G. S., Weiland, J. L., Wollack, E., & Wright, E. L.: 2008, Five-Year Wilkinson Microwave Anisotropy Probe (WMAP) Observations: Cosmological Interpretation, *ArXiv e-prints*
- Kong, X., Charlot, S., Brinchmann, J., & Fall, S. M.: 2004, Star formation history and dust content of galaxies drawn from ultraviolet surveys, *MNRAS* 349, 769–778
- Kowalski, M., Rubin, D., Aldering, G., Agostinho, R. J., Amadon, A., Amanullah, R., Ballard, C., Barbary, K., Blanc, G., Challis, P. J., Conley, A., Connolly, N. V., Covarrubias, R., Dawson, K. S., Deustua, S. E., Ellis, R., Fabbro, S., Fadeyev, V., Fan, X., Farris, B., Folatelli, G., Frye, B. L., Garavini, G., Gates, E. L., Germany, L., Goldhaber, G., Goldman, B., Goobar, A., & coauthors: 2008, Improved Cosmological Constraints from New, Old, and Combined Supernova Data Sets, *ApJ* 686, 749–778
- Kravtsov, A. V., Berlind, A. A., Wechsler, R. H., Klypin, A. A., Gottlöber, S., Allgood, B., & Primack, J. R.: 2004, The Dark Side of the Halo Occupation Distribution, *ApJ* 609, 35–49
- Kroupa, P.: 2001, On the variation of the initial mass function, *MNRAS* 322, 231–246
- Kurk, J., Röttgering, H., Pentericci, L., Miley, G., & Overzier, R.: 2003, A study of the evolutionary state of the cluster 1138-262 on the basis of H α , Ly α and X-ray emitters and extremely red objects, *New Astronomy Review* 47, 339–342
- Kurk, J. D., Pentericci, L., Overzier, R. A., Röttgering, H. J. A., & Miley, G. K.: 2004, A search for clusters at high redshift. IV. Spectroscopy of H α emitters in a proto-cluster at $z = 2.16$, *A&A* 428, 817–821
- Kurk, J. D., Röttgering, H. J. A., Pentericci, L., Miley, G. K., van Breugel, W., Carilli, C. L., Ford, H., Heckman, T., McCarthy, P., & Moorwood, A.: 2000, A Search for clusters at high redshift. I. Candidate Ly α emitters near 1138-262 at $z=2.2$, *A&A* 358, L1–L4
- Lacey, C. & Cole, S.: 1993, Merger rates in hierarchical models of galaxy formation, *MNRAS* 262, 627–649

Bibliography

- Lanzoni, B., Guiderdoni, B., Mamon, G. A., Devriendt, J., & Hatton, S.: 2005, GALICS-VI. Modelling hierarchical galaxy formation in clusters, *MNRAS* 361, 369–384
- LaRoque, S. J., Bonamente, M., Carlstrom, J. E., Joy, M. K., Nagai, D., Reese, E. D., & Dawson, K. S.: 2006, X-Ray and Sunyaev-Zel’dovich Effect Measurements of the Gas Mass Fraction in Galaxy Clusters, *ApJ* 652, 917–936
- Larson, R. B.: 1974, Effects of supernovae on the early evolution of galaxies, *MNRAS* 169, 229–246
- Li, Y., Mo, H. J., van den Bosch, F. C., & Lin, W. P.: 2007, On the assembly history of dark matter haloes, *MNRAS* 379, 689–701
- Lin, Y., Mohr, J. J., & Stanford, S. A.: 2003, Near-Infrared Properties of Galaxy Clusters: Luminosity as a Binding Mass Predictor and the State of Cluster Baryons, *Astrophys. J.* 591, 749–763
- Lin, Y.-T., Mohr, J. J., & Stanford, S. A.: 2004, K-Band Properties of Galaxy Clusters and Groups: Luminosity Function, Radial Distribution, and Halo Occupation Number, *ApJ* 610, 745–761
- López-Cruz, O., Barkhouse, W. A., & Yee, H. K. C.: 2004, The Color-Magnitude Effect in Early-Type Cluster Galaxies, *ApJ* 614, 679–691
- Lucy, L. B.: 1977, A numerical approach to the testing of the fission hypothesis, *Astron. J.* 82, 1013–1024
- Maeder, A. & Meynet, G.: 1989, Grids of evolutionary models from 0.85 to 120 solar masses - Observational tests and the mass limits, *A&A* 210, 155–173
- Magorrian, J., Tremaine, S., Richstone, D., Bender, R., Bower, G., Dressler, A., Faber, S. M., Gebhardt, K., Green, R., Grillmair, C., Kormendy, J., & Lauer, T.: 1998, The Demography of Massive Dark Objects in Galaxy Centers, *AJ* 115, 2285–2305
- Maio, U., Dolag, K., Ciardi, B., & Tornatore, L.: 2007, Metal and molecule cooling in simulations of structure formation, *MNRAS* 379, 963–973
- Mannucci, F., Maoz, D., Sharon, K., Botticella, M. T., Della Valle, M., Gal-Yam, A., & Panagia, N.: 2008, The supernova rate in local galaxy clusters, *MNRAS* 383, 1121–1130
- Marigo, P.: 2001, Chemical yields from low- and intermediate-mass stars: Model predictions and basic observational constraints, *A&A* 370, 194–217
- Martin, C. L.: 1999, Properties of Galactic Outflows: Measurements of the Feedback from Star Formation, *Astrophys. J.* 513, 156–160

- Matteucci, F.: 2003, *The Chemical Evolution of the Galaxy*, The Chemical Evolution of the Galaxy. By Francesca Matteucci, Department of Astronomy, University of Trieste, Italy. Astrophysics and Space Science Library Volume 253 reprint Kluwer Academic Publishers, Dordrecht
- Matteucci, F. & Gibson, B. K.: 1995, Chemical abundances in clusters of galaxies., *A&A* 304, 11–+
- Matteucci, F. & Greggio, L.: 1986, Relative roles of type I and II supernovae in the chemical enrichment of the interstellar gas, *A&A* 154, 279–287
- Matteucci, F. & Recchi, S.: 2001, On the Typical Timescale for the Chemical Enrichment from Type Ia Supernovae in Galaxies, *ApJ* 558, 351–358
- Maughan, B. J., Jones, C., Forman, W., & Van Speybroeck, L.: 2008, Images, Structural Properties, and Metal Abundances of Galaxy Clusters Observed with Chandra ACIS-I at $0.1L_X-T$ z_{L_X-T} 1.3, *ApJS* 174, 117–135
- McIntosh, D. H., Zabludoff, A. I., Rix, H.-W., & Caldwell, N.: 2005, Testing the Universality of the (U-V) Color-Magnitude Relations for Nearby Clusters of Galaxies, *ApJ* 619, 193–217
- McNamara, B. R., Rafferty, D. A., Birzan, L., Steiner, J., Wise, M. W., Nulsen, P. E. J., Carilli, C. L., Ryan, R., & Sharma, M.: 2006, The Starburst in the Abell 1835 Cluster Central Galaxy: A Case Study of Galaxy Formation Regulated by an Outburst from a Supermassive Black Hole, *ArXiv Astrophysics e-prints*
- Menci, N.: 2002, The Evolution of the Galaxy Luminosity Function: Theoretical Predictions vs. Observations, *APSS* 281, 509–513
- Menci, N., Cavaliere, A., Fontana, A., Giallongo, E., & Poli, F.: 2002, Binary Aggregations in Hierarchical Galaxy Formation: The Evolution of the Galaxy Luminosity Function, *ApJ* 575, 18–32
- Menci, N., Fontana, A., Giallongo, E., Grazian, A., & Salimbeni, S.: 2006, The Abundance of Distant and Extremely Red Galaxies: The Role of AGN Feedback in Hierarchical Models, *ApJ* 647, 753–762
- Menci, N., Rosati, P., Gobat, R., Strazzullo, V., Rettura, A., Mei, S., & Demarco, R.: 2008, The Red Sequence of High-Redshift Clusters: A Comparison with Cosmological Galaxy Formation Models, *ApJ* 685, 863–874
- Metzler, C. A. & Evrard, A. E.: 1994, A simulation of the intracluster medium with feedback from cluster galaxies, *ApJ* 437, 564–583

Bibliography

- Miley, G. & De Breuck, C.: 2008, Distant radio galaxies and their environments, *A&ARv* 15, 67–144
- Miley, G. K., Overzier, R. A., Zirm, A. W., Ford, H. C., Kurk, J., Pentericci, L., Blakeslee, J. P., Franx, M., Illingworth, G. D., Postman, M., Rosati, P., Röttgering, H. J. A., Venemans, B. P., & Helder, E.: 2006, The Spiderweb Galaxy: A Forming Massive Cluster Galaxy at $z \sim 2$, *ApJL* 650, L29–L32
- Milne, M. L., Pritchet, C. J., Poole, G. B., Gwyn, S. D. J., Kavelaars, J. J., Harris, W. E., & Hanes, D. A.: 2007, The Faint End of the Luminosity Function in the Core of the Coma Cluster, *AJ* 133, 177–185
- Mobasher, B., Colless, M., Carter, D., Poggianti, B. M., Bridges, T. J., Kranz, K., Komiyama, Y., Kashikawa, N., Yagi, M., & Okamura, S.: 2003, A Photometric and Spectroscopic Study of Dwarf and Giant Galaxies in the Coma Cluster. IV. The Luminosity Function, *ApJ* 587, 605–618
- Monaco, P. & Fontanot, F.: 2005, Feedback from quasars in star-forming galaxies and the triggering of massive galactic winds, *MNRAS* 359, 283–294
- Monaco, P., Fontanot, F., & Taffoni, G.: 2007, The MORGANA model for the rise of galaxies and active nuclei, *MNRAS* 375, 1189–1219
- Monaghan, J. J.: 2006, Smoothed particle hydrodynamic simulations of shear flow, *MNRAS* 365, 199–213
- Moran, S. M., Ellis, R. S., Treu, T., Smail, I., Dressler, A., Coil, A. L., & Smith, G. P.: 2005, A Wide-Field Hubble Space Telescope Survey of the Cluster Cl 0024+16 at $z = 0.4$. III. Spectroscopic Signatures of Environmental Evolution in Early-Type Galaxies, *ApJ* 634, 977–1001
- Moscardini, L., Matarrese, S., & Mo, H. J.: 2001, Constraining cosmological parameters with the clustering properties of galaxy clusters in optical and X-ray bands, *MNRAS* 327, 422–434
- Mullis, C. R., Rosati, P., Lamer, G., Böhringer, H., Schwobe, A., Schuecker, P., & Fassbender, R.: 2005, Discovery of an X-Ray-luminous Galaxy Cluster at $z=1.4$, *ApJL* 623, L85–L88
- Murante, G., Giovalli, M., Gerhard, O., Arnaboldi, M., Borgani, S., & Dolag, K.: 2007, The importance of mergers for the origin of intracluster stars in cosmological simulations of galaxy clusters, *MNRAS* 377, 2–16
- Nagai, D. & Kravtsov, A. V.: 2005, The Radial Distribution of Galaxies in Λ Cold Dark Matter Clusters, *ApJ* 618, 557–568

- Nagamine, K., Cen, R., Hernquist, L., Ostriker, J. P., & Springel, V.: 2005, Massive Galaxies in Cosmological Simulations: Ultraviolet-selected Sample at Redshift $z=2$, *ApJ* 618, 23–37
- Navarro, J., Frenk, C., & White, S.: 1996, The structure of cold dark matter halos, *ApJ* 462, 563
- Navarro, J., Frenk, C., & White, S.: 1997, A universal density profile from hierarchical clustering, *ApJ* 490, 493
- Nesvadba, N. P. H., Lehnert, M. D., Eisenhauer, F., Gilbert, A., Tecza, M., & Abuter, R.: 2006, Extreme Gas Kinematics in the $z=2.2$ Powerful Radio Galaxy MRC 1138-262: Evidence for Efficient Active Galactic Nucleus Feedback in the Early Universe?, *ApJ* 650, 693–705
- Nomoto, K. & et al.: 2000, Type Ia supernova Progenitors, Environmental Effects, and Cosmic Supernova Rates, in J. C. Niemeyer & J. W. Truran (eds.), *Type Ia Supernovae, Theory and Cosmology. Edited by J. C. Niemeyer and J. W. Truran. Published by Cambridge University Press, 2000., p.63*, pp 63–+
- Nomoto, K., Iwamoto, K., Nakasato, N., Thielemann, F.-K., Brachwitz, F., Tsujimoto, T., Kubo, Y., & Kishimoto, N.: 1997a, Nucleosynthesis in type Ia supernovae, *Nuclear Physics A* 621, 467–476
- Nomoto, K., Iwamoto, K., Nakasato, N., Thielemann, F.-K., Brachwitz, F., Tsujimoto, T., Kubo, Y., & Kishimoto, N.: 1997b, Nucleosynthesis in type Ia supernovae, *Nuclear Physics A* 621, 467–476
- Oppenheimer, B. D. & Davé, R.: 2006, Cosmological simulations of intergalactic medium enrichment from galactic outflows, *MNRAS* 373, 1265–1292
- Ott, J., Walter, F., & Brinks, E.: 2005, A Chandra X-ray survey of nearby dwarf starburst galaxies - II. Starburst properties and outflows, *MNRAS* 358, 1453–1471
- Overzier, R. A., Bouwens, R. J., Cross, N. J. G., & et al.: 2008, Lyman Break Galaxies, Ly α Emitters, and a Radio Galaxy in a Protocluster at $z = 4.1$, *ApJ* 673, 143–162
- Padoan, P., Nordlund, Å., Kritsuk, A. G., Norman, M. L., & Li, P. S.: 2007, Two Regimes of Turbulent Fragmentation and the Stellar Initial Mass Function from Primordial to Present-Day Star Formation, *ApJ* 661, 972–981
- Padovani, P. & Matteucci, F.: 1993, Stellar Mass Loss in Elliptical Galaxies and the Fueling of Active Galactic Nuclei, *Astrophys. J.* 416, 26–+

Bibliography

- Peacock, J. A.: 2001, Clustering of Mass and Galaxies, in *NATO ASIC Proc. 565: Structure Formation in the Universe*, pp 305–+
- Pearce, F. R., Jenkins, A., Frenk, C. S., Colberg, J. M., White, S. D. M., Thomas, P. A., Couchman, H. M. P., Peacock, J. A., Efstathiou, G., & The Virgo Consortium: 1999, A Simulation of Galaxy Formation and Clustering, *ApJL* 521, L99–L102
- Peebles, P. J. & Ratra, B.: 2003, The cosmological constant and dark energy, *Reviews of Modern Physics* 75, 559–606
- Peebles, P. J. E.: 1980, *The large-scale structure of the universe*, Research supported by the National Science Foundation. Princeton, N.J., Princeton University Press, 1980. 435 p.
- Peebles, P. J. E.: 1993, *Principles of physical cosmology*, Princeton Series in Physics, Princeton, NJ: Princeton University Press, —c1993
- Peebles, P. J. E. & Yu, J. T.: 1970, Primeval Adiabatic Perturbation in an Expanding Universe, *ApJ* 162, 815–+
- Pentericci, L., Kurk, J. D., Röttgering, H. J. A., Miley, G. K., van Breugel, W., Carilli, C. L., Ford, H., Heckman, T., McCarthy, P., & Moorwood, A.: 2000, A search for clusters at high redshift. II. A proto cluster around a radio galaxy at $z=2.16$, *A&A* 361, L25–L28
- Pentericci, L., Roettgering, H. J. A., Miley, G. K., Carilli, C. L., & McCarthy, P.: 1997, The radio galaxy 1138-262 at $z=2.2$: a giant elliptical galaxy at the center of a proto-cluster?, *A&A* 326, 580–596
- Pentericci, L., Roettgering, H. J. A., Miley, G. K., Spinrad, H., McCarthy, P. J., van Breugel, W. J. M., & Macchetto, F.: 1998, HST Images of the Extremely Clumpy Radio Galaxy 1138-262 at $Z = 2.2$, *ApJ* 504, 139–+
- Pentericci, L., Röttgering, H. J. A., Miley, G. K., McCarthy, P., Spinrad, H., van Breugel, W. J. M., & Macchetto, F.: 1999, HST images and properties of the most distant radio galaxies, *A&A* 341, 329–347
- Percival, W. J., Cole, S., Eisenstein, D. J., Nichol, R. C., Peacock, J. A., Pope, A. C., & Szalay, A. S.: 2007a, Measuring the Baryon Acoustic Oscillation scale using the Sloan Digital Sky Survey and 2dF Galaxy Redshift Survey, *MNRAS* 381, 1053–1066
- Percival, W. J., Nichol, R. C., Eisenstein, D. J., Weinberg, D. H., Fukugita, M., Pope, A. C., Schneider, D. P., Szalay, A. S., Vogeley, M. S., Zehavi, I., Bahcall, N. A., Brinkmann, J., Connolly, A. J., Loveday, J., & Meiksin, A.: 2007b, Measuring the Matter Density Using Baryon Oscillations in the SDSS, *ApJ* 657, 51–55

- Pierini, D., Zibetti, S., Braglia, F., Böhringer, H., Finoguenov, A., Lynam, P. D., & Zhang, Y.-Y.: 2008, Diffuse stellar emission in X-ray luminous galaxy clusters at $z \sim 0.3$. I. Is the diffuse optical light boosted and rejuvenated in merging clusters?, *A&A* 483, 727–739
- Pierpaoli, E., Borgani, S., Scott, D., & White, M.: 2003, On determining the cluster abundance normalization, *Mon. Not. R. Astron. Soc.* 342, 163–175
- Pimblet, K. A., Smail, I., Edge, A. C., O’Hely, E., Couch, W. J., & Zabludoff, A. I.: 2006, The Las Campanas/Anglo-Australian Telescope Rich Cluster Survey - III. Spectroscopic studies of X-ray bright galaxy clusters at $z \sim 0.1$, *MNRAS* 366, 645–666
- Plionis, M., López-Cruz, O., & Hughes, D. (eds.): 2008, *A Pan-Chromatic View of Clusters of Galaxies and the Large-Scale Structure*, Vol. 740 of *Lecture Notes in Physics*, Berlin Springer Verlag
- Poincaré, H.: 1891, Mémoires et observations. Sur le problème des trois corps, *Bulletin Astronomique, Serie I* 8, 12–24
- Popesso, P., Biviano, A., Böhringer, H., & Romaniello, M.: 2006a, RASS-SDSS Galaxy cluster survey. IV. A ubiquitous dwarf galaxy population in clusters, *A&A* 445, 29–42
- Popesso, P., Biviano, A., Böhringer, H., & Romaniello, M.: 2006b, RASS-SDSS Galaxy Cluster Survey. VII. On the Cluster Mass to Light ratio and the Halo Occupation Distribution, *ArXiv Astrophysics e-prints*
- Popesso, P., Biviano, A., Böhringer, H., Romaniello, M., & Voges, W.: 2005, RASS-SDSS galaxy cluster survey. III. Scaling relations of galaxy clusters, *A&A* 433, 431–445
- Popesso, P., Böhringer, H., Brinkmann, J., Voges, W., & York, D. G.: 2004, RASS-SDSS Galaxy clusters survey. I. The catalog and the correlation of X-ray and optical properties, *A&A* 423, 449–467
- Portinari, L., Chiosi, C., & Bressan, A.: 1998, Galactic chemical enrichment with new metallicity dependent stellar yields, *A&A* 334, 505–539
- Portinari, L., Moretti, A., Chiosi, C., & Sommer-Larsen, J.: 2004, Can a “Standard” Initial Mass Function Explain the Metal Enrichment in Clusters of Galaxies?, *ApJ* 604, 579–595
- Press, W. H. & Schechter, P.: 1974, Formation of Galaxies and Clusters of Galaxies by Self-Similar Gravitational Condensation, *Astrophys. J.* 187, 425–438
- Prugniel, P. & Simien, F.: 1996, The fundamental plane of early-type galaxies: stellar populations and mass-to-light ratio., *A&A* 309, 749–759

Bibliography

- Puchwein, E., Bartelmann, M., Dolag, K., & Meneghetti, M.: 2005, The impact of gas physics on strong cluster lensing, *A&A* 442, 405–412
- Rafferty, D. A., McNamara, B. R., Nulsen, P. E. J., & Wise, M. W.: 2006, The Feedback-regulated Growth of Black Holes and Bulges through Gas Accretion and Starbursts in Cluster Central Dominant Galaxies, *ApJ* 652, 216–231
- Ramella, M., Boschin, W., Geller, M. J., Mahdavi, A., & Rines, K.: 2004, K-Band Properties of Well-Sampled Groups of Galaxies, *AJ* 128, 2022–2036
- Recchi, S., Matteucci, F., & D’Ercole, A.: 2001, Dynamical and chemical evolution of gas-rich dwarf galaxies, *MNRAS* 322, 800–820
- Reiprich, T. H. & Böhringer, H.: 2002, The Mass Function of an X-Ray Flux-limited Sample of Galaxy Clusters, *Astrophys. J.* 567, 716–740
- Renzini, A. & Voli, M.: 1981a, Advanced evolutionary stages of intermediate-mass stars. I - Evolution of surface compositions, *A&A* 94, 175–193
- Renzini, A. & Voli, M.: 1981b, Advanced evolutionary stages of intermediate-mass stars. I - Evolution of surface compositions, *Astron. Astrophys.* 94, 175–193
- Rines, K., Geller, M. J., Diaferio, A., Kurtz, M. J., & Jarrett, T. H.: 2004a, CAIRNS: The Cluster and Infall Region Nearby Survey. II. Environmental Dependence of Infrared Mass-to-Light Ratios, *AJ* 128, 1078–1111
- Rines, K., Geller, M. J., Diaferio, A., Kurtz, M. J., & Jarrett, T. H.: 2004b, CAIRNS: The Cluster and Infall Region Nearby Survey. II. Environmental Dependence of Infrared Mass-to-Light Ratios, *AJ* 128, 1078–1111
- Romeo, A. D., Napolitano, N. R., Covone, G., Sommer-Larsen, J., Antonuccio-Delogu, V., & Capaccioli, M.: 2008, The evolution of the galaxy red sequence in simulated clusters and groups, *MNRAS* pp 793–+
- Romeo, A. D., Portinari, L., & Sommer-Larsen, J.: 2005, Simulating galaxy clusters - II. Global star formation histories and the galaxy populations, *MNRAS* 361, 983–996
- Romeo, A. D., Sommer-Larsen, J., & Portinari, L.: 2004, Simulating galaxy clusters : the ICM and the galaxy populations, in R. Dettmar, U. Klein, & P. Salucci (eds.), *Baryons in Dark Matter Halos*
- Rosati, P., Borgani, S., & Norman, C.: 2002, The Evolution of X-ray Clusters of Galaxies, *ARA&A* 40, 539–577

- Rosati, P., Stanford, S. A., Eisenhardt, P. R., Elston, R., Spinrad, H., Stern, D., & Dey, A.: 1999, An X-Ray-Selected Galaxy Cluster at $Z = 1.26$, *AJ* 118, 76–85
- Rosati, P., Tozzi, P., Ettori, S., Mainieri, V., Demarco, R., Stanford, S. A., Lidman, C., Nonino, M., Borgani, S., Della Ceca, R., Eisenhardt, P., Holden, B. P., & Norman, C.: 2004, Chandra and XMM-Newton Observations of RDCS 1252.9-2927, A Massive Cluster at $z=1.24$, *AJ* 127, 230–238
- Rybicki, G. B. & Lightman, A. P.: 1986, *Radiative Processes in Astrophysics*, Radiative Processes in Astrophysics, by George B. Rybicki, Alan P. Lightman, pp. 400. ISBN 0-471-82759-2. Wiley-VCH, June 1986.
- Rykoff, E. S., Evrard, A. E., McKay, T. A., Becker, M. R., Johnston, D. E., Koester, B. P., Nord, B., Rozo, E., Sheldon, E. S., Stanek, R., & Wechsler, R. H.: 2008, The $L_X - M$ relation of clusters of galaxies, *MNRAS* 387, L28–L32
- Salpeter, E. E.: 1955, The Luminosity Function and Stellar Evolution., *ApJ* 121, 161–+
- Saro, A., Borgani, S., Tornatore, L., De Lucia, G., Dolag, K., & Murante, G.: 2009, Simulating the formation of a protocluster at $z \sim 2$, *MNRAS* 392, 795–800
- Saro, A., Borgani, S., Tornatore, L., Dolag, K., Murante, G., Biviano, A., Calura, F., & Charlot, S.: 2006, Properties of the galaxy population in hydrodynamical simulations of clusters, *MNRAS* 373, 397–410
- Saro, A., De Lucia, G., Dolag, K., & Borgani, S.: 2008, The effect of gas dynamics on semi-analytic modelling of cluster galaxies, *MNRAS* pp 1229–+
- Sawicki, M. & Thompson, D.: 2006, Keck Deep Fields. II. The Ultraviolet Galaxy Luminosity Function at $z \sim 4, 3$, and 2, *ApJ* 642, 653–672
- Schechter, P.: 1976, An analytic expression for the luminosity function for galaxies., *ApJ* 203, 297–306
- Schechter, P.: 1976, An analytic expression for the luminosity function for galaxies., *ApJ* 203, 297
- Schmidt, M.: 1959, The Rate of Star Formation., *Astrophys. J.* 129, 243–+
- Sellwood, J. A.: 2004, What is the Evidence for Dark Matter?, in *IAU Symposium*, pp 27–+
- Shandarin, S. F. & Zeldovich, Y. B.: 1989, The large-scale structure of the universe: Turbulence, intermittency, structures in a self-gravitating medium, *Reviews of Modern Physics* 61, 185–220

Bibliography

- Sharon, K., Gal-Yam, A., Maoz, D., Filippenko, A. V., & Guhathakurta, P.: 2007, Supernovae in Low-Redshift Galaxy Clusters: The Type Ia Supernova Rate, *ApJ* 660, 1165–1175
- Sheth, R. & Tormen, G.: 1999, *MNRAS* 308, 119
- Sheth, R. K. & Tormen, G.: 2002, An excursion set model of hierarchical clustering: ellipsoidal collapse and the moving barrier, *Mon. Not. R. Astron. Soc.* 329, 61–75
- Sijacki, D. & Springel, V.: 2006, Hydrodynamical simulations of cluster formation with central AGN heating, *MNRAS* 366, 397–416
- Silk, J.: 1968, Cosmic Black-Body Radiation and Galaxy Formation, *ApJ* 151, 459–+
- Silverberg, R. F., Cheng, E. S., Cottingham, D. A., Fixsen, D. J., Inman, C. A., Kowitt, M. S., Meyer, S. S., Page, L. A., Puchalla, J. L., & Rephaeli, Y.: 1997, Millimeter/Submillimeter Search for the Sunyaev-Zeldovich Effect in the Coma Cluster, *ApJ* 485, 22–+
- Smith, S.: 1936, The Mass of the Virgo Cluster, *ApJ* 83, 23–+
- Somerville, R. S. & Kolatt, T. S.: 1999, How to plant a merger tree, *MNRAS* 305, 1–14
- Somerville, R. S. & Primack, J. R.: 1999, Semi-analytic modelling of galaxy formation: the local Universe, *MNRAS* 310, 1087–1110
- Spergel, D. N., Verde, L., Peiris, H. V., Komatsu, E., Nolta, M. R., Bennett, C. L., Halpern, M., Hinshaw, G., Jarosik, N., Kogut, A., Limon, M., Meyer, S. S., Page, L., Tucker, G. S., Weiland, J. L., Wollack, E., & Wright, E. L.: 2003, First-Year Wilkinson Microwave Anisotropy Probe (WMAP) Observations: Determination of Cosmological Parameters, *Astrophys. J. Supp.* 148, 175–194
- Springel, V.: 2005, The cosmological simulation code GADGET-2, *MNRAS* 364, 1105–1134
- Springel, V. & Hernquist, L.: 2002, Cosmological smoothed particle hydrodynamics simulations: the entropy equation, *MNRAS* 333, 649–664
- Springel, V. & Hernquist, L.: 2003a, Cosmological smoothed particle hydrodynamics simulations: a hybrid multiphase model for star formation, *Mon. Not. R. Astron. Soc.* 339, 289–311
- Springel, V. & Hernquist, L.: 2003b, Cosmological smoothed particle hydrodynamics simulations: a hybrid multiphase model for star formation, *MNRAS* 339, 289–311
- Springel, V. & Hernquist, L.: 2003c, The history of star formation in a Λ cold dark matter universe, *MNRAS* 339, 312–334

- Springel, V., Wang, J., Vogelsberger, M., Ludlow, A., Jenkins, A., Helmi, A., Navarro, J. F., Frenk, C. S., & White, S. D. M.: 2008, The Aquarius Project: the subhaloes of galactic haloes, *MNRAS* 391, 1685–1711
- Springel, V., White, S., Tormen, G., & Kauffmann, G.: 2001, Populating a cluster of galaxies - i. results at $z = 0$, *MNRAS* 328, 726
- Springel, V., White, S. D. M., Jenkins, A., Frenk, C. S., Yoshida, N., Gao, L., Navarro, J., Thacker, R., Croton, D., Helly, J., Peacock, J. A., Cole, S., Thomas, P., Couchman, H., Evrard, A., Colberg, J., & Pearce, F.: 2005a, Simulations of the formation, evolution and clustering of galaxies and quasars, *Nature* 435, 629–636
- Springel, V., White, S. D. M., Jenkins, A., Frenk, C. S., Yoshida, N., Gao, L., Navarro, J., Thacker, R., Croton, D., Helly, J., Peacock, J. A., Cole, S., Thomas, P., Couchman, H., Evrard, A., Colberg, J., & Pearce, F.: 2005b, Simulations of the formation, evolution and clustering of galaxies and quasars, *Nature* 435, 629–636
- Springel, V., White, S. D. M., Tormen, G., & Kauffmann, G.: 2001, Populating a cluster of galaxies - I. Results at $z=0$, *MNRAS* 328, 726–750
- Springel, V., Yoshida, N., & White, S.: 2001, Gadget: a code for collisionless and gasdynamical cosmological simulations, *New Astronomy* 6, 79
- Springel, V., Yoshida, N., & White, S. D. M.: 2001, GADGET: a code for collisionless and gasdynamical cosmological simulations, *New Astron.* 6, 79–117
- Stadel, J. G.: 2001, Cosmological N-body simulations and their analysis, *Ph.D. Thesis*
- Stanek, R., Evrard, A. E., Böhringer, H., Schuecker, P., & Nord, B.: 2006, The X-Ray Luminosity-Mass Relation for Local Clusters of Galaxies, *ApJ* 648, 956–968
- Stanford, S. A., Eisenhardt, P. R., Brodwin, M., Gonzalez, A. H., Stern, D., Jannuzi, B. T., Dey, A., Brown, M. J. I., McKenzie, E., & Elston, R.: 2005, An IR-selected Galaxy Cluster at $z = 1.41$, *ApJL* 634, L129–L132
- Stanford, S. A., Holden, B., Rosati, P., Eisenhardt, P. R., Stern, D., Squires, G., & Spinrad, H.: 2002, An X-Ray-Selected Galaxy Cluster at $z=1.11$ in the ROSAT Deep Cluster Survey, *AJ* 123, 619–626
- Stanford, S. A., Romer, A. K., Sabirli, K., Davidson, M., Hilton, M., Viana, P. T. P., Collins, C. A., Kay, S. T., Liddle, A. R., Mann, R. G., Miller, C. J., Nichol, R. C., West, M. J., Conselice, C. J., Spinrad, H., Stern, D., & Bundy, K.: 2006, The XMM Cluster Survey: A Massive Galaxy Cluster at $z = 1.45$, *ApJL* 646, L13–L16

Bibliography

- Stoehr, F., White, S. D. M., Springel, V., Tormen, G., & Yoshida, N.: 2003, Dark matter annihilation in the halo of the Milky Way, *MNRAS* 345, 1313–1322
- Stoughton, C., Lupton, R. H., Bernardi, M., & et al.: 2002, Sloan Digital Sky Survey: Early Data Release, *AJ* 123, 485–548
- Sunyaev, R. A. & Zeldovich, Y. B.: 1970, The interaction of matter and radiation in the hot model of the Universe, II, *APSS* 7, 20–30
- Sunyaev, R. A. & Zeldovich, Y. B.: 1972, The Observations of Relic Radiation as a Test of the Nature of X-Ray Radiation from the Clusters of Galaxies, *Comments on Astrophysics and Space Physics* 4, 173–+
- Sutherland, R. S. & Dopita, M. A.: 1993, Cooling functions for low-density astrophysical plasmas, *ApJS* 88, 253–327
- Terlevich, A. I., Caldwell, N., & Bower, R. G.: 2001, The colour-magnitude relation for galaxies in the Coma cluster, *MNRAS* 326, 1547–1562
- Thielemann, F.-K., Argast, D., Brachwitz, F., Hix, W. R., Höflich, P., Liebendörfer, M., Martinez-Pinedo, G., Mezzacappa, A., Panov, I., & Rauscher, T.: 2003, Nuclear cross sections, nuclear structure and stellar nucleosynthesis, *Nuclear Physics A* 718, 139–146
- Thielemann, F.-K., Nomoto, K., & Hashimoto, M.-A.: 1996, Core-Collapse Supernovae and Their Ejecta, *ApJ* 460, 408–+
- Thomas, P. A. & Couchman, H. M. P.: 1992, Simulating the formation of a cluster of galaxies, *MNRAS* 257, 11–31
- Tonini, C., Maraston, C., Devriendt, J., Thomas, D., & Silk, J.: 2008, The impact of TP-AGB stars on hierarchical galaxy formation models, *ArXiv e-prints*
- Tormen, G., Bouchet, F. R., & White, S. D. M.: 1997, The structure and dynamical evolution of dark matter haloes, *MNRAS* 286, 865–884
- Tornatore, L., Borgani, S., Dolag, K., & Matteucci, F.: 2007a, Chemical enrichment of galaxy clusters from hydrodynamical simulations, *MNRAS* 382, 1050–1072
- Tornatore, L., Borgani, S., Dolag, K., & Matteucci, F.: 2007b, Chemical enrichment of galaxy clusters from hydrodynamical simulations, *MNRAS* 382, 1050–1072
- Tornatore, L., Borgani, S., Matteucci, F., Recchi, S., & Tozzi, P.: 2004, Simulating the metal enrichment of the intracluster medium, *MNRAS* 349, L19–L24

- van Breukelen, C., Clewley, L., Bonfield, D. G., Rawlings, S., Jarvis, M. J., Barr, J. M., Foucaud, S., Almaini, O., Cirasuolo, M., Dalton, G., Dunlop, J. S., Edge, A. C., Hirst, P., McLure, R. J., Page, M. J., Sekiguchi, K., Simpson, C., Smail, I., & Watson, M. G.: 2006, Galaxy clusters at $0.6 < L_X - T < z < L_X - T < 1.4$ in the UKIDSS Ultra Deep Survey Early Data Release, *MNRAS* 373, L26–L30
- Venemans, B. P., Röttgering, H. J. A., Miley, G. K., van Breugel, W. J. M., de Breuck, C., Kurk, J. D., Pentericci, L., Stanford, S. A., Overzier, R. A., Croft, S., & Ford, H.: 2007, Protoclusters associated with $z > 2$ radio galaxies . I. Characteristics of high redshift protoclusters, *A&A* 461, 823–845
- Viola, M., Monaco, P., Borgani, S., Murante, G., & Tornatore, L.: 2008, How does gas cool in dark matter haloes?, *MNRAS* 383, 777–790
- Voit, G. M.: 2005, Tracing cosmic evolution with clusters of galaxies, *Reviews of Modern Physics* 77, 207–258
- Vollmer, B., Cayatte, V., Balkowski, C., & Duschl, W. J.: 2001, Ram Pressure Stripping and Galaxy Orbits: The Case of the Virgo Cluster, *ApJ* 561, 708–726
- Wake, D. A., Collins, C. A., Nichol, R. C., Jones, L. R., & Burke, D. J.: 2005, The Environmental Dependence of Galaxy Colors in Intermediate-Redshift X-Ray-selected Clusters, *ApJ* 627, 186–202
- Weinberg, S.: 1972, *Gravitation and cosmology: Principles and applications of the general theory of relativity*, New York: Wiley, —c1972
- White, S.: 1996, The formation and evolution of galaxies, in R. Schaeffer, J. Silk, M. Spiro, & J. Zinn-Justin (eds.), *Cosmology and Large-Scale Structure*, p. 395, Elsevier, Dordrecht
- White, S. D. M. & Frenk, C. S.: 1991, Galaxy formation through hierarchical clustering, *ApJ* 379, 52–79
- White, S. D. M., Navarro, J. F., Evrard, A. E., & Frenk, C. S.: 1993, The Baryon Content of Galaxy Clusters - a Challenge to Cosmological Orthodoxy, *Nature* 366, 429–+
- White, S. D. M. & Rees, M. J.: 1978, Core condensation in heavy halos - A two-stage theory for galaxy formation and clustering, *MNRAS* 183, 341–358
- Wilson, G., Muzzin, A., Lacy, M., Yee, H., Surace, J., Lonsdale, C., Hoekstra, H., Majumdar, S., Gilbank, D., & Gladders, M.: 2008, Clusters of Galaxies at $1 < L_X - T < z < L_X - T < 2$: The Spitzer Adaptation of the Red-Sequence Cluster Survey, in R.-R. Chary, H. I. Teplitz, & K. Sheth (eds.), *Infrared Diagnostics of Galaxy Evolution*, Vol. 381 of *Astronomical Society of the Pacific Conference Series*, pp 210–+

Bibliography

- Woosley, S. E. & Weaver, T. A.: 1995a, The Evolution and Explosion of Massive Stars. II. Explosive Hydrodynamics and Nucleosynthesis, *Astrophys. J. Supp.* 101, 181–+
- Woosley, S. E. & Weaver, T. A.: 1995b, The Evolution and Explosion of Massive Stars. II. Explosive Hydrodynamics and Nucleosynthesis, *ApJS* 101, 181–+
- Yamada, T., Kodama, T., Akiyama, M., Furusawa, H., Iwata, I., Kajisawa, M., Iye, M., Ouchi, M., Sekiguchi, K., Shimasaku, K., Simpson, C., Tanaka, I., & Yoshida, M.: 2005, The Number Density of Old Passively Evolving Galaxies at $z=1$ in the Subaru/XMM-Newton Deep Survey Field, *ApJ* 634, 861–878
- Yee, H. K. C. & Gladders, M. D.: 2002, Optical Surveys for Galaxy Clusters, in L.-W. Chen, C.-P. Ma, K.-W. Ng, & U.-L. Pen (eds.), *AMiBA 2001: High-Z Clusters, Missing Baryons, and CMB Polarization*, Vol. 257 of *Astronomical Society of the Pacific Conference Series*, pp 109–+
- York, D. G., Adelman, J., Anderson, Jr., J. E., & et al.: 2000, The Sloan Digital Sky Survey: Technical Summary, *AJ* 120, 1579–1587
- Yoshida, N., Sheth, R. K., & Diaferio, A.: 2001, Non-Gaussian cosmic microwave background temperature fluctuations from peculiar velocities of clusters, *MNRAS* 328, 669–677
- Yoshida, N., Stoehr, F., Springel, V., & White, S.: 2002, Gas cooling in simulations of the formation of the galaxy population, *MNRAS* 334, 762
- Yoshida, N., Stoehr, F., Springel, V., & White, S. D. M.: 2002, Gas cooling in simulations of the formation of the galaxy population, *MNRAS* 335, 762–772
- Yungelson, L. R. & Livio, M.: 2000, Supernova Rates: A Cosmic History, *ApJ* 528, 108–117
- Zanni, C., Murante, G., Bodo, G., Massaglia, S., Rossi, P., & Ferrari, A.: 2005, Heating groups and clusters of galaxies: The role of AGN jets, *A&A* 429, 399–415
- Zel'Dovich, Y. B.: 1970, Gravitational instability: an approximate theory for large density perturbations., *Astron. Astrophys.* 5, 84–89
- Zibetti, S., White, S. D. M., Schneider, D. P., & Brinkmann, J.: 2005, Intergalactic stars in $z \sim 0.25$ galaxy clusters: systematic properties from stacking of Sloan Digital Sky Survey imaging data, *MNRAS* 358, 949–967
- Zirm, A. W., Stanford, S. A., Postman, M., Overzier, R. A., Blakeslee, J. P., Rosati, P., Kurk, J., Pentericci, L., Venemans, B., Miley, G. K., Röttgering, H. J. A., Franx, M., van der Wel, A., Demarco, R., & van Breugel, W.: 2008, The Nascent Red Sequence at $z \sim 2$, *ApJ* 680, 224–231

Zwicky, F.: 1933, Die Rotverschiebung von extragalaktischen Nebeln, *Helvetica Physica Acta* 6, 110–127

Zwicky, F.: 1937, On the Masses of Nebulae and of Clusters of Nebulae, *Astrophys. J.* 86, 217–+